

ABSTRACT

DUDEK, RYAN BENJAMIN. Redox Catalysts for Selective Hydrogen Combustion. (Under the direction of Dr. Fanxing Li).

The chemicals and petrochemicals sector is the largest industrial energy user and a prominent CO₂ emissions source, annually accounting for 10% of global final energy consumption (more than 40 quadrillion BTU per year) and emitting 7% of all global greenhouse gases (1.5 Gt CO_{2,eq}/year). Approximately one-fifth of all carbon emissions from the sector arise from the production of two high-volume commodity chemicals, ethylene and propylene, combining for 220 million tonnes of production in 2012. Often described as the building blocks of the industry, ethylene and propylene (also referred to as light olefins) are conventionally produced during the steam cracking of naphtha or ethane, which is the single most energy-intensive chemical manufacturing process. Oxidative reactions such as oxidative dehydrogenation (ODH) and oxidative cracking (OC) have significant advantages over steam cracking reactions in terms of energy utilization and obtainable light olefin yields; however, the implementation of these reactions in a commercial process can be difficult due to the need for pure, gaseous O₂ with a potentially hazardous hydrocarbon co-feed. Chemical looping represents a promising strategy for implementing both ODH and OC processes to convert ethane or naphtha to light olefins without the requirement of co-feeding pure oxygen, resulting in improved processes with reduced energy consumption and carbon emissions in comparison to conventional steam cracking. Both chemical looping oxidative dehydrogenation (CL-ODH) and redox oxidative cracking (ROC) rely on a metal oxide intermediate known as an oxygen carrier or redox catalyst, which enables the partial oxidation of hydrocarbon feedstocks to form light olefins and the subsequent reactive separation of oxygen from air.

The focus of this work is the development of redox catalysts which are suitable for both the CL-ODH and the ROC processes to intensify olefin production from ethane and naphtha, respectively. A critical function of redox catalysts is the ability to donate lattice oxygen and perform selective hydrogen combustion (SHC) from a mixture of H₂, C₂H₄, and other feed and product molecules; SHC by a metal oxide redox catalyst (i) enables autothermal operation through the release of *in situ* heat, (ii) increases single-pass conversion and allows for greater-than-equilibrium olefin yields by lifting thermodynamic constraints, and (iii) reduces downstream separation load by replacing H₂ with easily condensable water, while (iv) avoiding non-selective combustion of feed or product to form CO_x compounds. Metal oxides typically do not inherently possess high H₂ selectivity – instead, SHC properties must be developed and optimized during the design of redox catalysts.

Firstly, a new class of manganese oxide-based redox catalysts for selective hydrogen combustion (SHC) is presented, and a paradigm for rationally designing and evaluating redox catalysts across a range of temperatures is discussed. A redox catalyst consisting of 20 wt.% Na₂WO₄ on perovskite oxide CaMnO₃ is quickly identified as a highly selective and stable redox catalyst across the range of 550°C to 850°C using a H₂/C₂H₄ co-feed. Na₂WO₄/CaMnO₃ is subsequently demonstrated for SHC during ethane CL-ODH at 650°C using a Cr₂O₃/Al₂O₃ co-catalyst. Redox oxidative cracking (ROC) of naphtha (represented by *n*-hexane) is introduced in the next section as a more efficient alternative to naphtha steam cracking, enabled by the high selectivity of the Na₂WO₄/CaMnO₃ and Na₂WO₄/SrMnO₃ redox catalysts. Olefin yields as high as 58% are achieved at 725°C along with total H₂ combustion, and a number of characterization methods are used to evaluate the material properties impacting SHC performance. Finally, the third and fourth studies presented here provide further detail on the reduction kinetics of CaMnO₃ and Na₂WO₄/CaMnO₃, the relationship between

individual reduction rates and overall selectivity to H₂ combustion, and the impact of operating conditions and phase transformations on the kinetics of the Na₂WO₄/CaMnO₃ redox catalyst.

© Copyright 2020 by Ryan B. Dudek

All Rights Reserved

Redox Catalysts for Selective Hydrogen Combustion

by
Ryan Benjamin Dudek

A dissertation submitted to the Graduate Faculty of
North Carolina State University
in partial fulfillment of the
requirements for the degree of
Doctor of Philosophy

Chemical Engineering

Raleigh, North Carolina
2020

APPROVED BY:

Dr. Fanxing Li
Committee Chair

Dr. H. Henry Lamb

Dr. Phillip R. Westmoreland

Dr. Veronica Augustyn

DEDICATION

To my Mom and Dad, Tracey and John Dudek, for their constant love and support.

I would not be where I am today without you. 143

and

To my grandfather, Donald “Al” Higgins (March 12, 1933 – October 4, 2020).

I hope I made you proud. *Vaya con dios.*

BIOGRAPHY

Ryan Benjamin Dudek was born in Pottstown, Pennsylvania, USA, on June 3, 1993, to parents Tracey Ann Dudek and John Walter Dudek. At an early age he moved with his family to Folsom, PA, where he lived until the age of 18, and completed primary and secondary education in Ridley School District in Ridley Park, PA. Ryan attended the University of Delaware for his undergraduate studies from 2011 to 2015, graduating with an Honors Degree with Distinction in Chemical and Biomolecular Engineering and with a Minor in Computer Science. During his time at Delaware, Ryan performed undergraduate research in the lab of Prof. Christopher J. Roberts and completed an undergraduate thesis under the advisement of Prof. Prasad Dhurjati; he also worked briefly at the Catalysis Center for Energy Innovation with Prof. Dionisios Vlachos. Ryan directly entered into graduate studies in Fall 2015 at North Carolina State University in Raleigh, inspired by the collegial and collaborative environment in the Department of Chemical and Biomolecular Engineering (CBE). He joined the laboratory of Prof. Fanxing Li in December 2015 and has spent the last five years performing research on metal oxide redox catalysts for the process intensification of light olefin production. Ryan is an author of eight published manuscripts, including three as first author, and a co-inventor of one patent. In addition to his thesis research, Ryan has been active in the NC State community, serving the Graduate Student Association for four years and founding a student organization providing professional development opportunities to scientists and engineers entering the field of public policy.

ACKNOWLEDGMENTS

“And because all things have contributed to your advancement, you should include all things in your gratitude.” – Ralph Waldo Emerson

I view this dissertation as a culmination of all the education, mentorship, training, love, support, kindness, and encouragement I have received from a truly vast group of family members, friends, teachers, and professional colleagues over the years. To each and every one of these people, I want to extend a heartfelt “thank you” for playing a role in my journey, whether it was during my Ph.D. or earlier in my life. Here, I will do my best to include everyone in my gratitude, starting with my family.

Mom and Dad: Everything I have accomplished so far in my life, and anything I will accomplish in the years ahead, have all been thanks to the love and support you have given me since day one. You have made me the person I am today. I’m so lucky to have you as my parents and I hope you know how grateful I am for the care, encouragement, lessons, advantages, stability, and everything you have provided me in my life. I love you and I hope I can continue to make you proud.

Extended Family: I’m thankful for the wide network of supportive relatives I have back home in Ridley Park, PA, and Pottstown, PA. *Memom and Al:* Staying with you early in life, on Wed/Thurs and during summers, will always be a fond memory. I miss you both. Memom, I wonder if you somehow knew when you knitted me a red and black quilt that I would end up at NC State! Al, thank you for teaming up with me on crossword puzzles and Sudokus. *Grandmom:* Thank you for taking such good care of me while we stayed in Pottstown, and for giving me an enduring sweet

tooth! *Jack and Jessica*: You two are the best brother and sister that this only child could have asked for, and I'm excited to continue growing up alongside you. *Joseph*: Your accomplishments in law have always been an inspiration for me to keep going. If Jessica went for an M.D. eventually, we would have a complete set! (No pressure, Jess, but you can do whatever you set your mind to!) Thankful for my cousins Chris, Lauren, Marissa, Caitlin, Colleen, and Daniel, as well as all my aunts and uncles: Diane, Joe and Sue, Dana and Kevin, Susan and Joe, and Steve and Donna.

Next, I would like to acknowledge a host of teachers, professors, instructors, coaches, and other mentors from throughout my life who helped me hone the skills I have used to get here, as well as later figures who have helped me in professional settings – particularly in research and academia.

Ridley School District: First and foremost, I must thank *Mr. Bill Stumm* for teaching me how to study, for recognizing and nurturing my mathematics abilities, and for being the most formative teacher in my education; *Mr. Gerard Ryan*, for being a nerd, for teaching me algebra, geometry, trigonometry, statistics, and robotics, and for regaling us with tales of Princess Sochahtoa; *Dr. Samuel Valentine* and *Mr. Joseph Gagliardi*, for inspiring my early love of history and mythology; *Ms. Karen Zaino*, for helping me to develop my writing; *Mrs. Michele Jackson-Dua*, for helping me avoid shifts in verb tense and excessive semicolon usage (please don't read much of this thesis), for introducing me to Kate Bush on the moors and Joseph Conrad ("the horror..."), and for being a cool person in addition to an excellent mentor; *Mrs. Andrea Kupprion*, for nurturing my ability to study independently and introducing me to the many wonders of the French language, including *Le Comte de Monte-Cristo*; *Mrs. Cynthia Greene*, for her excellent AP courses on government and public policy, which I appreciate more and more each day; and last but far from least, *Mrs. Luann*

Crosby, who remains one of the best educators I have ever known, who challenged me like I had never been challenged before – Mrs. Crosby, you prepared me for every challenge since then, including writing this dissertation. In addition to my teachers, I need to thank my coaches who taught me important lessons outside of the classroom, starting with *Mr. Kurt Slenn*, who never gave up on me (no matter the sport) and who proved to me that hard work, perseverance, and grit, sustained over many years, can produce amazing results; *Mr. Kevin Pierce* and *Colonel Tom Reimann*, for pushing me both in and out of the pool; and finally, *Mr. Tom Kelly* who more than anyone else in my life taught me how to work through pain (“This isn’t Candy Land!”), and whose favorite refrain has been echoing in my mind as I have written this document: “Finish the race.”

University of Delaware: I had many excellent professors and instructors at my alma mater who all deserve my gratitude, both for their support at the time and for their enduring influence on my life.

Dr. John Burmeister: I cannot overstate the impact you have had on my career. Thank you for your chemistry lectures, for your enjoyable and often exothermic stories, for your immense wit, and for showing me that I belonged in the fields of chemistry and chemical engineering. Thanks also to *Justin Teesdale*, who was an excellent teaching assistant! *Dr. Christopher J. Roberts*: Thank you for welcoming me into the world of research and teaching me how to think for myself. Thanks also to the Roberts Group from 2013-2015, including *Dr. Greg Barnett*, *Dr. Chris O’Brien*, and especially *Dr. Ranendu Ghosh* – Ranendu, all of my good wet-work habits came from you! *Dr.*

Prasad Dhurjati: I will always remember your mentorship, your unparalleled sense of humor, the constant sense of wonder you brought to research, and your willingness to pull out a blank sheet of printer paper and brainstorm ideas with me for hours at a time. I’m sad that I cannot celebrate this achievement with you – Rest in Peace. *Dr. Dionisios Vlachos*: You were an excellent adviser

throughout my undergraduate years, and I am thankful for your input during my graduate school applications, and for the brief period of time I was able to perform research with you at CCEI. In addition, I would like to thank a few more instructors across a range of disciplines for the quality of their teaching and mentorship, including *Prof. Michael T. Klein*, *Dr. R. Bertram Diemer*, and *Dr. Mark Shiflett* (CHEG); *Prof. Julia Maresca* (BIOL); *Prof. Gilberto Schleiniger* (MATH); *Prof. Keith Decker* (CISC); and *Prof. Viet Dinh* (ENGL). I appreciate both the scientific and life lessons I learned from a few industry professionals I met during my time at Delaware, including *Dr. Scott Jackson* and *Dr. Bob Fallon* of DuPont and especially *Ms. Carol Eidt* of ExxonMobil, who advised me to pursue graduate studies. Finally, I will forever be indebted to *Dr. Lauren Barsky* from the Undergraduate Research Program for supporting me through the writing of my first thesis.

Committee Members: From North Carolina State University, I have so many people to thank, and I have to start with the faculty members who have advised me throughout my doctoral research. *Prof. Fanxing Li:* Thank you for this opportunity to perform research in your lab and to grow as a scientist and as a person under your guidance – it has truly been a privilege. You taught me how to look for the areas where I can do work with the most efficiency and potential impact. You know better than most that my interests have shifted over the years, and you have always supported me in my endeavors with great patience, which I will always appreciate. I have to imagine I was one of your more difficult graduate students to advise, and I hope that I have not let you down. *Prof. H. Henry Lamb*, *Prof. Phillip Westmoreland*, and *Prof. Veronica Augustyn:* I am thankful to have had your advice and guidance throughout my PhD coursework and research, and I will remember fondly all of the encouragement and feedback you gave me during and after my preliminary oral exam, which gave me the confidence to continue pursuing my degree.

Li Research Group: Next, I would like to thank everyone with whom I worked in the Li Group at NC State, without whom I could not have produced this body of work. *Prof. Luke M. Neal*: Your knowledge of redox catalysis knows no bounds, and I would not have accomplished half as much in the laboratory without being able to consult your experience and expertise – thank you. *Dr. Junshe Zhang*: I will be forever impressed by your productivity in the lab – thank you for training me on a few key skills early on. *Dr. Amit Mishra*: Special thanks to you for training me on the Setaram, which has been so critical to my work since, and for all of the office laughs. *Dr. Vasudev Haribal*: You are one of the most accomplished scientists I have ever met, and in addition to your inspiring work ethic, I will always be grateful for your camaraderie during those late nights in lab (“piece...”). *Dr. Seif Yusuf*: More than anyone else, you made my doctoral research enjoyable, and your friendship over the years has been one of the rewarding things about my NC State experience – thank you for everything. I also want to thank the rest of the members of the Li Group from over the years, including *Dr. Nathan Galinsky*, *Dr. Arya Shafiefarhood*, *Dr. Yunfei Gao*, *Michael Gerber*, *Emily Krzystowczyk*, *Daniel Jackson*, *Yuan Tian*, *Junchen Liu*, *Leo Brody*, *Dennis Chacko*, *Megan Yaffey*, *Qiongqiong Jiang*, *Dr. Jian Dou*, and *Dr. Fang Hao*. Special thanks go to *Dr. Xin Tian*, a remarkable collaborator and a brilliant researcher, and to the group of fantastic and talented undergraduate and Master’s students with whom I worked over the years, including *Toluwalashe Omotunde*, *Gaochen Jin*, and especially *Millicent Blivin Capstaff*.

CBE Department: From the Department of Chemical and Biomolecular Engineering faculty and staff, I would like to thank *Prof. Peter Fedkiw* for his excellent 711 course and his early guidance, *Prof. Michael Dickey* for playing a key role in my selection of NC State for graduate school, and *Prof. Lisa Bullard* for being a wonderful mentor, a joy to learn from and teach alongside. I also

want to thank all of the CBE staff for their hard work, dedication, and commitment to our success as students, most especially Sandra Bailey, as well as Michelle Bunce, Saundra Doby, Kathleen Berding, Christiana Boyle, Paola Cavaliere, Jolie Kajioka, and Danielle Riegel. Finally, I must thank *Joan O'Sullivan* and *Nancy Dear* for keeping us safe while we perform research, as well as *Mike Mantini* for being an incredible source of assistance and overall know-how.

Susteon, Inc.: While the work I performed in collaboration with Susteon, Inc. is not featured in this dissertation, I nonetheless grew tremendously as a researcher during our project together; the DHA work was some of the most enjoyable research I did while at NC State. I therefore need to thank *Dr. Raghubir Gupta* for leading this project and being an excellent mentor for me, as well as *Dr. Jim Zhou* and *Dr. Brian Turk* for their technical guidance during the 9-month SBIR project.

Even as all of these educational, professional, academic, and research connections have been of tremendous importance to the completion of my doctoral research and to my development up until now, my family, and especially my friends and colleagues, are the ones who got me to this point. Without close friends and confidants, without an incredible support system, I would not have made it through my first year of graduate studies, let alone an entire PhD program. It is my great pleasure to end this acknowledgements section with a roll call of the special people who have made this life wonderful and worth living, and without whom I certainly could not have produced this work.

My Pillars: I have leaned heavily on each and every one of these people, and I hope they know I am incredibly grateful for the support and will always be here for them in return. *Molly (Gartland)*
Jenkins: It was truly a godsend that you and Charlie moved to North Carolina the same year I did,

and with every year I am more thankful for our friendship. I am glad we could support each other through our respective programs. You are wonderful, and I wouldn't be here without you. *Shane Bonner*: It's impossible to imagine my life without your friendship – you've been there for me for 12 years and I am really glad we're still close, even when I've been away for nine of them. I'll be relying on you to keep me humble after I earn this degree. *Dilara Sen*: Thank you for those late-night Krispy Kreme adventures during first semester, for buying a keg with me, for making crazy pumpkin murder eyes in photos, and for being my first great friend in our program. *Yunhu Peng*: Our bubble tea and Chinese food outings have been a consistent source of enjoyment and stress relief over the years, and I'm fortunate to have you as a friend – because of you, I've learned how to “just chill.” *Minyung Song*: Thank you for being my walking buddy during quarantine, a close confidant over the years, and a wonderful friend! I hope we end up nearby in the next steps of our lives. *Seif Yusuf*: I truly would not have survived five years of laboratory research without being able to vent and joke about it all with you – thank you for being a great friend and helping me get through so much. *Leah Granger*: You are such a fun and positive and kind person, and I'm so glad we became friends! Thanks for all the swing dancing, running adventures, history brackets, awful puns, and chocolate! *Andrew Devenny*: I still refer to you as “my roommate” and people give me crazy looks because I live alone – that's because you are still central to my life, and I hope we'll move closer together soon! *Kristy Chong*: More than anyone else from college, you always check in with me to see how I'm doing and keep me involved in our group, and I will always be thankful to have you as a friend! *Anna Dye*: How much we have achieved together! I am tremendously glad that we have become such good friends in just two years, and I am superbly grateful to know you. *Lexie Malico*: You are going to do amazing things with your life, and I will be cheering for you, every step of the way. I will be thankful for the kindness and care you showed me, always.

Finally, I would like to thank many friends and close acquaintances for making this journey to the PhD enjoyable and supporting me throughout. *From Ridley*: the Quorum (Matt Strehlau, Buddy McGlashen, Tim McCrea, Kevin Acker, Anthony Murgidi), Andrew Reimann, Anthony Delsordo. *From UD*: Jill Allen, Matt McKenna, Jennifer Vitlip, Brianna Gietter, Jackie Nebbia, Molly Peters, James Craig, Meredith Steenkamer, Nicole Daly, Michael Thomas, Frank Cheng, Lauren Cordova, Elizabeth Keating, and Kaitlyn Turek. *From CBE*: Jenna Meanor, Sahand Saberi, Heather Barton, Emily Facchine, Emily Krzystowczyk, Ryan Tam, Taylor Neumann, Javier Huayta, Jason Miles, Amulya Pervaje, Amber Hubbard, Jenny Ovental, Jen Clark, Ishan Joshipura, Cathryn Conner, Amelia Chen, Rachel Nye, Chris Estridge, Matt and Rebecca Mansell, Ria Corder, Barbara Farias, Salvatore Luiso, Scott Baldwin, John Schneible, Petr Novotny, Joe McCaig, Nidhi Diwakar, Matt Melillo, Deepti and Joe Tilly, and Ryan Barton. *From life in NC*: Charlie Jenkins, Justin Peers, Melike Şen, Prakash Bhave, Jean Ritok, the Haeris (Mehdi, Shamim, Farrah), Elise Anderson, Lynn Gupton, James Moran, Dr. Becky Barnette, Dr. Lydia Miller-Anderson. *From GSA*: Nathan Corder, Judy Rivera, James Withrow, Laura Goodman, Justin Middleton, Matt Kollman, Ashling Lupiani, Andy Andis, Dr. Peter Harries. *From SciPolPack*: Alex Hsain, Ishita Kamboj, Victoria Yell, Megan Franklin, Hanna Berman, Joe Sagues, Prof. Jean Goodwin. *From NSPN*: Holly Mayton, Michaela Rikard, Avital Percher, Caitlin Short, Amanda Acosta-Ruiz, Sarah Goggin, Matthew Diasio, Danielle DaCrema, Cole Harris, Meredith Schmehl, Caroline Schuerger, and Melody Tan.

Thank you so much, everyone!

TABLE OF CONTENTS

LIST OF TABLES	xv
LIST OF FIGURES	xvi
CHAPTER 1: INTRODUCTION.....	1
1.1. The Growing Importance of Process Intensification for the Chemicals Sector	1
1.2. Chemical Looping as a Process Intensification Strategy for Light Olefins Production	8
1.3. Core-Shell Redox Catalysts for Selective Hydrogen Combustion	17
1.4. Summary	25
1.5. References	28
CHAPTER 2: MANGANESE-CONTAINING REDOX CATALYSTS FOR SELECTIVE HYDROGEN COMBUSTION UNDER A CYCLIC REDOX SCHEME	41
2.1. Abstract.....	42
2.2. Introduction.....	42
2.3. Experimental Section.....	46
2.3.1. <i>Redox Catalyst Preparation</i>	46
2.3.2. <i>Redox Catalyst Characterization</i>	47
2.3.3. <i>Reaction Testing</i>	49
2.4. Results and Discussion	51
2.4.1. <i>Structure Characterization</i>	51
2.4.2. <i>Material Screening</i>	52
2.4.3. <i>Selective Hydrogen Combustion Properties of Redox Catalysts</i>	55
2.4.4. <i>Long-Term Stability and Application in Ethane Dehydrogenation</i>	64
2.5. Conclusions.....	66
2.6. References.....	68
CHAPTER 3: PEROVSKITE OXIDES FOR REDOX OXIDATIVE CRACKING OF N- HEXANE UNDER A CYCLIC REDOX SCHEME	71
3.1. Abstract.....	72
3.2. Introduction.....	73
3.3. Experimental Section.....	77
3.3.1. <i>Synthesis of Redox Catalysts</i>	77
3.3.2. <i>Characterization of Redox Catalysts</i>	78
3.3.3. <i>n-Hexane Oxidative Cracking Test Conditions</i>	80
3.4. Results and Discussion	82
3.4.1. <i>Perovskites as Redox Catalysts</i>	82

3.4.2. Olefin Yield Comparisons	83
3.4.3. Effect of Temperature on Product Yields.....	87
3.4.4. Redox Catalyst Characterization and Mechanistic Investigation.....	91
3.4.5. Evaluation and Literature Comparison of Redox Catalyst Performance and Stability	100
3.5. Conclusions.....	103
3.6. References.....	105
CHAPTER 4: REDUCTION KINETICS OF PEROVSKITE OXIDES FOR SELECTIVE HYDROGEN COMBUSTION IN THE CONTEXT OF OLEFIN PRODUCTION	108
4.1. Abstract.....	109
4.2. Introduction.....	110
4.3. Experimental Section.....	115
4.3.1. Redox Catalyst Synthesis	115
4.3.2. Fixed-Bed Reactor Experiments.....	115
4.3.3. Kinetics Experiments	116
4.3.4. Kinetic Modeling	118
4.4. Results and Discussion	121
4.4.1. Selective Hydrogen Combustion by CaMnO_3 -Based Redox Catalysts.....	121
4.4.2. Reduction Kinetics of CaMnO_3	124
4.4.3. Kinetic Model Fitting and Parameter Estimation for CaMnO_3	129
4.4.4. Effect of Sodium Tungstate on Reduction Rates	135
4.5. Conclusions.....	141
4.6. Symbols	142
4.7. References.....	143
CHAPTER 5: REDUCTION KINETICS OF $\text{Na}_2\text{WO}_4/\text{CaMnO}_3$: INFLUENCE OF THERMAL HISTORY AND LONG-TERM REDOX CYCLING ON RATE PARAMETERS	146
5.1. Introduction.....	147
5.2. Experimental Section.....	151
5.2.1. Redox Catalyst Preparation.....	151
5.2.1. Reduction Kinetics Experiments and Modeling	151
5.2.3. In Situ X-Ray Powder Diffraction	153
5.3. Results and Discussion	153
5.3.1. Partial Pressure Dependence of CaMnO_3 Reduction Kinetics.....	153
5.3.2. Temperature Dependence of CaMnO_3 Reduction Kinetics	157
5.3.3. Reduction Kinetics of $\text{Na}_2\text{WO}_4/\text{CaMnO}_3$: Rate Crossover and Hysteresis Phenomena ...	164

5.3.4. <i>Effect of Long-Term Redox Cycling on Na₂WO₄/CaMnO₃ Reduction Rates</i>	172
5.3.5. <i>In Situ X-Ray Diffraction Study</i>	176
5.4. Conclusions.....	181
5.5. References.....	182
CHAPTER 6: CONCLUSIONS AND OUTLOOK	185
6.1. Conclusions.....	185
6.2. Outlook.....	189
6.3. Future Work.....	190
6.3.1. <i>Oxidative Aromatization (OA) of Methane and Ethane</i>	190
6.3.2. <i>Towards an Improved Understanding of Na₂WO₄/CaMnO₃ Reduction Kinetics</i>	194
6.4. References.....	196
APPENDICES	198
Appendix A: Supplementary Information for Chapter 2	199
Appendix B: Supplementary Information for Chapter 3.....	207
Appendix C: Supplementary Information for Chapter 4.....	220
Appendix D: Supplementary Information for Chapter 5	234

LIST OF TABLES

Table 1.1: Examples of the chemical looping process approach applied to a number of existing chemical processes. In each case, the CL oxidation reaction can be written as a multiple of $\text{MeO}_{x-1} + \frac{1}{2} \text{O}_2 \rightarrow \text{MeO}_x$ in which the redox catalyst can be contacted directly with air instead of pure O_2 . CLC = chemical looping combustion, CLR = chemical looping reforming, CL-ODH = chemical looping oxidative dehydrogenation, CL-OC = chemical looping oxidative cracking, CL-DHA = chemical looping dehydroaromatization. CL-ODH, CL-OC, and CL-DHA involve selective hydrogen combustion (SHC).	9
Table 2.1: BET surface areas (S_{BET} , m^2/g) for as-prepared redox catalysts.	51
Table 2.2: Reduction onset temperatures (T_o) and peak temperatures (T_p) over redox catalysts as determined by $\text{H}_2/\text{C}_2\text{H}_4$ TPR.	55
Table 2.3: Near-surface atomic percentages of metal cations on fresh and cycled redox catalysts, obtained via XPS (on an oxygen- and carbon-free basis). Dashes indicate no measurement was taken.	62
Table 3.1: Product distribution of the <i>n</i> -hexane oxy-cracking reaction over the 20 wt.% $\text{Na}_2\text{WO}_4/\text{CaMnO}_3$ redox catalyst at $\text{GHSV} = 9000 \text{ h}^{-1}$ ($m = 500 \text{ mg}$) and over a range of temperatures. Thermal background (<i>BG</i>) data at 725°C and 775°C are from an inert alumina-packed reactor.	90
Table 3.2: Surface cation atomic percentages for six redox catalyst variants from XPS analysis. Carbon and oxygen are excluded. Surface enrichment and suppression of cations, shown in parentheses, are calculated using observed percentages from XPS in combination with expected percentages from overall stoichiometry.	94
Table 4.1: The set of 15 reaction models evaluated in the current study. Each model is designated by an alphanumeric name based on its category: reaction-order models (F); geometric contraction models (R); diffusion-limited models (D); Avrami–Erofe’ev nucleation models (AE). ^[50]	119
Table 4.2: Summary of chosen kinetic models, approximate rate constants and reduction rates at 650°C , and activation energy values for reduction of CaMnO_3 and $\text{Na}_2\text{WO}_4/\text{CaMnO}_3$ redox catalysts by H_2 and C_2H_4	139
Table 5.1: Kinetic pre-factors $A = k(T) \cdot (P_{\text{H}_2})^n$ for reduction of CaMnO_3 by H_2 at six temperatures and four P_{H_2} conditions, along with apparent reaction orders <i>n</i> at each temperature.	157
Table 5.2: List of apparent activation energy and pre-exponential factor values obtained via the reduction of CaMnO_3 by H_2 . Avrami-Erofe’ev models (AE_n) were selected for parameter fitting.	162
Table 5.3: List of apparent activation energy and pre-exponential factor values obtained via the reduction of $\text{Na}_2\text{WO}_4/\text{CaMnO}_3$ by 5% H_2 . The Avrami-Erofe’ev model (AE1.5 or AE2) was selected for parameter fitting. Experiments are separated into Low Temperature (575°C and below) and High Temperature (625°C and above) to capture the bifurcation of kinetics around 600°C for certain samples.	176
Table 6.1: Effect of selective hydrogen combustion (shown as H_2 conversion) on the overall heat of reaction (positive = endothermic) and equilibrium conversion of the feed (methane or ethane) for DHA at 650°C	192

LIST OF FIGURES

Figure 1.1: Comparison of classical or co-feed oxidative dehydrogenation (ODH) with chemical looping oxidative dehydrogenation (CL-ODH), using ethane to ethylene as an example. In comparison to gaseous O ₂ used in ODH, the selectivity of the oxygen species in CL-ODH can be controlled by tuning the properties of the redox catalyst (MeO _x → MeO _{x-1}), facilitating selective hydrogen combustion and forming C ₂ H ₄ and H ₂ O.....	8
Figure 1.2: Methods of implementing CL-ODH. <i>Left:</i> A single, catalytically active ODH catalyst performs both dehydrogenation and selective H ₂ combustion at intermediate temperatures. <i>Center:</i> A dehydrogenation catalyst converts ethane to ethylene and H ₂ at lower temperatures; a selective hydrogen combustion (SHC) co-catalyst removes H ₂ as H ₂ O without oxidizing ethylene. <i>Right:</i> Ethane is cracked at high temperatures to form ethylene and H ₂ ; an SHC redox catalyst removes H ₂ as H ₂ O without oxidizing ethylene. Arrows indicate the direction of reactants and overall gas flow.	15
Figure 2.1: A simplified block flow diagram for the chemical looping-oxidative dehydrogenation scheme. In this scheme, the ODH (reduction) step at left is comprised of two reactions. The first reaction is dehydrogenation (DH), proceeding either via gas-phase thermal cracking or by heterogeneous catalysis, and the second reaction is selective hydrogen combustion of the products from the dehydrogenation reaction.....	44
Figure 2.2: XRD patterns for (a) Mg ₆ MnO ₈ (i) and 20 wt.% Na ₂ WO ₄ /Mg ₆ MnO ₈ (ii); (b) SrMnO ₃ (i) and 20 wt.% Na ₂ WO ₄ /SrMnO ₃ (ii); and (c) CaMnO ₃ (i) and 20 wt.% Na ₂ WO ₄ /CaMnO ₃ (ii).	51
Figure 2.3: H ₂ O generation based on MS signal (m/z = 18) during H ₂ /C ₂ H ₄ TPR for the three redox catalyst systems: (a) Mg ₆ MnO ₈ ; (b) SrMnO ₃ ; and (c) CaMnO ₃ . Conditions: m = 100 mg, F = 100 ml/min, H ₂ :C ₂ H ₄ = 2.5%:2.5% v/v in Ar, ramping rate = 5°C/min.	53
Figure 2.4: Hydrogen conversion (●) and selectivity towards hydrogen combustion (▲) for the unpromoted (—) and Na ₂ WO ₄ -promoted (– –) redox catalysts: (a) Mg ₆ MnO ₈ ; (b) SrMnO ₃ ; (c) CaMnO ₃ . Conversion and selectivity are determined via C and H atomic balances from GC analysis of entire pulse volumes. Conditions: m = 100 mg, F = 100 mL/min, H ₂ :C ₂ H ₄ = 40%:40% v/v in Ar, pulse duration = 10 s.	56
Figure 2.5: Selective hydrogen combustion (SHC) properties of the six redox catalyst materials. Each bar represents the temperature range within which the catalyst provides an H ₂ conversion rate of at least 40 mmol H ₂ / kg-cat·s (averaged over a 10 s pulse) and at least 95% SHC selectivity. By varying the metal oxide substrate and by promotion with Na ₂ WO ₄ , a wide range of operating temperatures is covered.	60
Figure 2.6: Effect of altering gas hourly space velocity (GHSV) through the reactor on molar H ₂ conversion and SHC selectivity; (a) lower GHSV over Na ₂ WO ₄ /Mg ₆ MnO ₈ , and; (b) higher GHSV over Na ₂ WO ₄ /CaMnO ₃ . GHSV = 6000 hr ⁻¹ corresponds to τ ≈ 0.15 s. Conditions: m = 100 mg, H ₂ :C ₂ H ₄ = 40%:40% v/v in Ar, pulse duration = 10 s, T = 850°C.	61

Figure 2.7: Near-surface enrichment (> 1) and suppression (< 1) ratios of metal atoms in as-prepared catalysts, determined via XPS narrow scan analysis. Enrichment and suppression are calculated based on the bulk atomic composition expected from the material stoichiometry.	62
Figure 2.8: Redox cycling stability of the 20 wt.% $\text{Na}_2\text{WO}_4/\text{CaMnO}_3$ redox catalyst over 50 cycles. Conversion and selectivity were calculated via C and H atomic balances of GC data. Conditions: $m = 100$ mg, $F = 100$ ml/min, $\text{H}_2:\text{C}_2\text{H}_4 = 40\%:40\%$ v/v in Ar, pulse duration = 10 s, $T = 850^\circ\text{C}$	64
Figure 2.9: Sequential bed results for $\text{Cr}_2\text{O}_3/\text{Al}_2\text{O}_3$ (ethane dehydrogenation) followed by $\text{Na}_2\text{WO}_4/\text{CaMnO}_3$ redox catalyst (selective hydrogen combustion). (a) Results of single $\text{Cr}_2\text{O}_3/\text{Al}_2\text{O}_3$ bed showing ethane dehydrogenation; (b) Sequential bed with $\text{Na}_2\text{WO}_4/\text{CaMnO}_3$. The redox catalyst consumes 84% of H_2 generated by ethane dehydrogenation. Conditions: $m_{\text{EDH}} = 250$ mg (a) or 150 mg (b), $m_{\text{SHC}} = 500$ mg, $F = 50$ mL/min, 5% C_2H_6 v/v in Ar, $T = 650^\circ\text{C}$	66
Figure 3.1: A block flow diagram for the redox oxidative cracking (ROC) of naphtha concept, using the simplified net reaction $\text{C}_6\text{H}_{14} \rightarrow 3 \text{C}_2\text{H}_4 + \text{H}_2$ to represent thermal cracking of naphtha with n -hexane as a model compound. MeO_x represents a fully oxidized perovskite-type mixed metal oxide while MeO_{x-1} indicates lattice oxygen has been donated.	75
Figure 3.2: Oxygen donation by (a) SrMnO_3 , $\text{Na}_2\text{WO}_4/\text{SrMnO}_3$, and (b) CaMnO_3 , $\text{Na}_2\text{WO}_4/\text{CaMnO}_3$, as determined by material balance on $\text{H}_2/\text{C}_2\text{H}_4$ co-feed experiments in a U-tube reactor. Conditions: $F = 100$ mL/min, $y_{\text{H}_2}/y_{\text{C}_2\text{H}_4}/y_{\text{Ar}} = 0.4/0.4/0.2$, $m = 100$ mg, step duration = 10 s.	83
Figure 3.3: Results from n -hexane TPR on four redox catalysts and accompanying thermal background, showing in STP mL/min (a) ethylene product flowrate, (b) incremental ethylene flowrate over the background, and (c) incremental CO_2 product flowrate over the background CO_2 (equal to zero). Ethylene production above the thermal background indicates n -hexane activation by the redox catalyst, while CO_2 production indicates undesired side reactions. Results were obtained via mass spectrometry. Conditions: $\text{GHSV} = 4500 \text{ h}^{-1}$ ($F_{\text{Ar}} = 75$ mL/min, $m = 500$ mg), $y_{n\text{-hexane}} \approx 0.13$, ramping rate of $5^\circ\text{C}/\text{min}$	84
Figure 3.4: A comparison of n -hexane conversion and olefin yields over the $\text{Na}_2\text{WO}_4/\text{CaMnO}_3$ redox catalyst with those from the thermal cracking background. Conditions: $\text{GHSV} = 9000 \text{ h}^{-1}$ ($F_{\text{Ar}} = 150$ mL/min, $m = 500$ mg), $y_{n\text{-hexane}} \approx 0.13$, step duration = 20 s.	87
Figure 3.5: Olefin yields achieved by four redox catalysts. From left to right: $T = 725^\circ\text{C}$, 750°C , 775°C . Constant yield contours indicate the product of n -hexane conversion and olefin selectivity for each data point, with selectivity on a carbon basis. Results obtained via GC. Conditions: $\text{GHSV} = 9000 \text{ h}^{-1}$ ($F_{\text{Ar}} = 150$ mL/min, $m = 500$ mg), $y_{n\text{-hexane}} \approx 0.13$, step duration = 20 s.	88
Figure 3.6: O_2 -TPD results of three redox catalysts. Samples were held under 10% atmosphere of the adsorbing gas for 30 min at 900°C , ramped down to 150°C at $10^\circ\text{C}/\text{min}$, and purged under an inert He environment for 60 min prior to testing. TG weight loss rates were normalized by initial sample mass. Conditions: $m = 30$ – 50 mg, $F = 180$ mL/min He, ramping rate = $5^\circ\text{C}/\text{min}$	92

- Figure 3.7:** Photoemission spectra of Sr 3*d* (a) and Ca 2*p* (b) for the SrMnO₃- and CaMnO₃-based redox catalysts, respectively, using an Al K α X-ray source (1486.7 eV). Binding energies (BE) were referenced to the C 1*s* peak for adventitious carbon at 284.6 eV. Dotted lines indicate BE value for the characteristic peaks of lattice (low BE) and surface (high BE) doublets for the unpromoted (Sr,Ca)MnO₃. 96
- Figure 3.8:** Relationship between the accommodation of surface-type Sr/Ca species and CO_x selectivity at T = 725°C and GHSV = 4500 h⁻¹ (F_{Ar} = 75 mL/min, m = 500 mg). $y_{n\text{-hexane}} \approx 0.13$, step duration = 40 s. The dashed line is used to show the general trend and does not represent a quantitative correlation. 98
- Figure 3.9:** LEIS spectra for 20 wt.% Na₂WO₄/CaMnO₃ acquired using a 3 keV He⁺ probe beam. (a) Surface scans after varying amounts of 0.5 keV Ar⁺ sputter-etching; one sputter cycle corresponds to 0.5 x 10¹⁵ Ar⁺ ions cm⁻². (b) Depth profiles of Na, W, O, Ca, and Mn, showing peak areas as a function of sputter cycle, up to a maximum dose of 5.0 x 10¹⁵ cm⁻². 99
- Figure 3.10:** A comparison of reaction characteristics over the course of 25 *n*-hexane oxy-cracking cycles for (a) Na₂WO₄/SrMnO₃ and (b) Na₂WO₄/CaMnO₃. Thermal background olefin yield is given as a dashed line. Conditions: T = 725°C, GHSV = 4500 h⁻¹ (F_{Ar} = 75 mL/min, m = 500 mg), $y_{n\text{-hexane}} \approx 0.13$, step duration = 40 s. 100
- Figure 3.11:** XRD patterns for all redox catalysts. (a) Patterns for (i) SrMnO₃, (ii) Na₂WO₄/SrMnO₃, (iii) cycled Na₂WO₄/SrMnO₃. (b) Patterns for (i) CaMnO₃, (ii) Na₂WO₄/CaMnO₃, (iii) cycled Na₂WO₄/CaMnO₃. Cycled samples tested and re-oxidized at T = 725°C, GHSV = 4500 h⁻¹ for 25 cycles. 101
- Figure 4.1:** Schematic of the ethane chemical looping – oxidative dehydrogenation (CL-ODH) process; (left) gravimetric data showing the redox catalyst MeO_x undergo reduction in H₂ to MeO_y (y < x); (right) gravimetric data representing the regeneration of MeO_y to MeO_x using oxygen from air. X corresponds to dimensionless solid conversion, with X = 0 as a fully oxidized solid and X = 1 as a fully reduced solid. 112
- Figure 4.2:** Time-on-stream measurements of the effluent gas from an ethane dehydrogenation + selective hydrogen combustion scheme (EDH+SHC), utilizing (a) CaMnO₃ and (b) Na₂WO₄/CaMnO₃ as redox catalysts. Inlet gas flowrates were chosen to simulate the effluent gas from the dehydrogenation of ethane. The dashed blue line indicates the expected flow of hydrogen gas in absence of an oxygen donor. $S_H \equiv$ selectivity towards hydrogen combustion (%), $\Delta m \equiv$ oxygen donation (wt.%). Conditions: $m_0 = 500$ mg, F_{Ar} = 40 mL/min, F_{C₂H₆} = F_{C₂H₄} = F_{H₂} = 5 mL/min, T = 650°C. 123
- Figure 4.3:** Results of three reduction kinetics experiments for CaMnO₃ using H₂, C₂H₄, and C₂H₆ at 650°C. (a) Dimensionless conversion (X) vs. time (t, min); (b) time derivative of conversion (dX/dt) vs. conversion (X). Mass measurements (in mg) were obtained via thermogravimetric analysis. Conditions: $m_0 = 20$ mg, 150–250 μ m, T = 650°C, P = 1 atm, F_{total} = 200 mL/min (20 mL/min H₂/C₂H₄/C₂H₆, 180 mL/min He or Ar). 124
- Figure 4.4:** TGA-MS data for CaMnO₃ reduction kinetics experiments utilizing C₂H₄ (solid lines) and C₂H₆ (dashed lines) individually as reducing gases. F-H₂ and F-CO₂ are volumetric flow rates from the outlet of the TGA determined via MS from m/z = 2 and 44, respectively, while X is the dimensionless solid conversion of

CaMnO ₃ by each reducing gas determined via TGA. Conditions: $m_0 = 20$ mg, 150–250 μm , $T = 650^\circ\text{C}$, $P = 1$ atm, $F_{total} = 200$ mL/min (20 mL/min C ₂ H ₄ /C ₂ H ₆ , 180 mL/min Ar).	127
Figure 4.5: Reduction of CaMnO ₃ by H ₂ during four isothermal TGA experiments. (a) Dimensionless solid conversion (X) as a function of time; (b) time derivative of conversion (dX/dt) as a function of conversion Conditions: $m_0 = 20$ mg, 150–250 μm , $T = 500$ – 650°C , $P = 1$ atm, $F_{total} = 200$ mL/min (20 mL/min H ₂ , 180 mL/min He).	128
Figure 4.6: Reduction of CaMnO ₃ by C ₂ H ₄ during six isothermal TGA experiments. (a) Dimensionless solid conversion (X) as a function of time; (b) time derivative of conversion (dX/dt) as a function of conversion. Conditions: $m_0 = 20$ mg, 150–250 μm , $T = 650$ – 700°C , $P = 1$ atm, $F_{total} = 200$ mL/min (20 mL/min C ₂ H ₄ , 180 mL/min Ar).	129
Figure 4.7: Kinetic modeling results showing the model predictions of the best-fit kinetic model, F1 (the first-order reaction model), in the (a) integral form and (b) differential form, for the reduction of CaMnO ₃ by H ₂ from 500°C to 650°C . Points represent the experimental data and dotted lines represent the F1 model predictions.	131
Figure 4.8: Kinetic modeling results showing the model predictions of the best-fit kinetic model, F1.5 (the three-halves reaction-order model), in the (a) integral form and (b) differential form, for the reduction of CaMnO ₃ by C ₂ H ₄ from 650°C to 700°C . Points represent the experimental data and dotted lines represent the F1.5 model predictions.	132
Figure 4.9: Arrhenius plot based on the rate constants for CaMnO ₃ reduction by H ₂ and by C ₂ H ₄ across the temperature range 500°C to 700°C . Rate constants k (min^{-1}) were extracted from the most well-fitting kinetic models (F1 for H ₂ , F1.5 for C ₂ H ₄) as determined via statistical analyses. Estimates for apparent activation energy, E_a (kJ mol^{-1}), were calculated from the Arrhenius slope, m , as $E_a \approx -mRT$	133
Figure 4.10: Reduction kinetics of Na ₂ WO ₄ /CaMnO ₃ by H ₂ with superimposed best-fitting kinetic model AE2 (dotted lines). (a) Solid conversion X vs. t ; (b) derivative conversion dX/dt vs. X ; (c) Arrhenius analysis of data using $k(T)$ values based on the Avrami-Erofe'ev nucleation and growth kinetic model with $n = 2$. TGA conditions: $m_0 = 20$ mg, 150–250 μm , $T = 500$ – 650°C , $P = 1$ atm, $F_{total} = 200$ mL/min (20 mL/min H ₂ , 180 mL/min He). E_a (kJ mol^{-1}) was calculated from Arrhenius slope m , as $E_a \approx -mRT$	137
Figure 4.11: Quantitative comparison for the reduction of CaMnO ₃ and Na ₂ WO ₄ /CaMnO ₃ by either H ₂ or C ₂ H ₄ at 650°C , depicted as solid conversion (wt%) vs. time (min). TGA conditions: $m_0 = 20$ mg, 150–250 μm , $T = 650^\circ\text{C}$, $P = 1$ atm, $F_{total} = 200$ mL/min (20 mL/min H ₂ or C ₂ H ₄ , 180 mL/min He or Ar).	140
Figure 5.1: Dimensionless solid conversion of the CaMnO ₃ redox catalyst (X) as a function of time (t , min) across a range of temperatures ($^\circ\text{C}$) and P_{H_2} (atm) values. All data were acquired using sample CM-05 with detailed experiment descriptions provided in Appendix D.	155
Figure 5.2: Dimensionless reduction rates of the CaMnO ₃ redox catalyst (dX/dt) as a function of conversion (X) across a range of temperatures ($^\circ\text{C}$) and P_{H_2} (atm)	

values. All data were acquired using sample CM-05 with detailed experiment descriptions provided in <i>Appendix D</i>	156
Figure 5.3: Reduction kinetics of CaMnO ₃ in 5% H ₂ . (a) Integral and (b) differential solid conversion plots, representing an average of thermogravimetric data for five independent experiments across four samples (CM-02, CM-03, CM-04, CM-05), for all six temperature conditions. (c)—(h): Individual temperature data sets, with error bars representing one sample standard deviation calculated from the five individual sets.....	160
Figure 5.4: Model-fitting method results for CaMnO ₃ reduction by 5% H ₂ , shown for (a, c) integral and (b, d) differential data at 700°C and 500°C. Four best-fitting kinetic models are presented along with associated sum of squared errors (SSE): first-order power law (F1), three-dimensional unreacted shrinking core (R3), Jander equation for three-dimensional diffusion (D3), and Avrami-Erofe'ev nucleation (AE, <i>n</i> = 1.5 or 2). The fitting data are from Experiment 2 on sample CM-03.	161
Figure 5.5: Reduction kinetics of CaMnO ₃ in 5% C ₂ H ₄ ; (a) Integral and (b) differential solid conversion plots. Data were acquired on sample CM-04.....	164
Figure 5.6: Reduction kinetics of 20 wt.% Na ₂ WO ₄ /CaMnO ₃ in 5% H ₂ . (a) Integral and (b) differential solid conversion plots, representing an average of thermogravimetric data for independent experiments across three samples (NWCM-05, NWCM-08, NWCM-09), for nine temperature conditions. (c)—(k): Individual temperature data sets, with error bars representing one sample standard deviation calculated from the three individual sets. All data were acquired in a decreasing order of temperatures.	167
Figure 5.7: Reduction kinetics of 20 wt.% Na ₂ WO ₄ /CaMnO ₃ in 5% H ₂ . (a) Integral and (b) differential solid conversion plots for seven temperature conditions, acquired on a single sample (NWCM-07, Experiment 1). All data were acquired in an increasing order of temperatures.	169
Figure 5.8: Examination of the thermal hysteresis effect on two distinct Na ₂ WO ₄ /CaMnO ₃ samples. (a)—(b): Experiments on sample NWCM-07, tested first in decreasing order from 675°C to 500°C (Exp. 2A) and then back to 675°C (Exp. 2B), comprising cycles 34–78 on the sample. (c)—(d): Experiments on sample NWCM-08, tested first in increasing order from 525°C to 700°C (Exp. 2A) and then back to 525°C (Exp. 2B), comprising cycles 33–77 on the sample. Dotted lines represent cooling; solid lines represent heating.	171
Figure 5.9: Effect of extended redox cycling on the reduction rate crossover and hysteresis phenomena of Na ₂ WO ₄ /CaMnO ₃ , all performed on sample NWCM-08: (a) Cycles 33–77; (b) Cycles 135–185; (c) Cycles 186–236. All experiments follow an increasing temperature program from 500°C/525°C to 700°C followed by a decreasing temperature program to 500°C/525°C. Reduction kinetics in 5% H ₂ are shown.	174
Figure 5.10: <i>In situ</i> XRD patterns for Na ₂ WO ₄ /CaMnO ₃ redox catalyst. (a) Heating from RT to 700°C, prior to redox cycling. (b) Cooling from 650°C to RT, following redox cycling.	178
Figure 5.11: <i>In situ</i> XRD patterns for Na ₂ WO ₄ /CaMnO ₃ redox catalyst at six operating temperatures during redox cycling. Beginning at <i>t</i> = 0 under inert N ₂ flow, the	

sample is switched to a 3% H₂ environment for 45 to 90 minutes, purged in N₂, and then re-oxidized with air. 180

Figure 6.1: Oxidative aromatization using a DHA+SHC approach with either a single DHA bed (dotted line) or a DHA bed upstream followed by an SHC bed downstream (solid line). (a) Yields of benzene (B), toluene (T), and CO₂ from DHA. (b) Hydrogen effluent flowrate from the reaction with and without the SHC bed. (c) Instantaneous benzene and toluene yields in DHA vs. DHA+SHC. 193

Figure 6.2: Core-shell composite catalyst design for the oxidative aromatization (OA) of methane or ethane using a combined SHC@DHA approach. In this OA catalyst system, a perovskite oxide (e.g. CaMnO₃) with optimal oxygen donation properties is covered by a shape-selective zeolite shell exchanged with active metal sites (e.g. Mo, Ga, Pt), rather than by a chemical promoter such as Na₂WO₄. Alkane feedstock enters the pore network of the zeolite and is activated to form aromatics and H₂; at the zeolite-perovskite interface, the SHC core selectively combusts hydrogen, and the resulting steam permeates through the zeolite shell, burning off coke in the process. 194

CHAPTER 1: INTRODUCTION

1.1. The Growing Importance of Process Intensification for the Chemicals Sector

The first two decades of the 21st century have seen the global scientific community solidify its consensus, based on extensive observational evidence, that Earth's climate is rapidly changing and that greenhouse gas emissions from human activities are playing a primary role.^[1-4] Populations and economies in the United States and throughout the world already face the risks and experience the impacts of climate change; critically, the 2020s and 2030s represent a shrinking window of opportunity to curb anthropogenic carbon emissions and limit the increase in annual average global temperature to 2°C or lower, thereby mitigating further, more drastic long-term climate impacts.^[5,6] Carbon capture, utilization, and storage (CCUS), a developing set of technologies which has the potential to reduce carbon dioxide (CO₂) emissions from coal- and natural gas-fired power plants and which is promising for emissions mitigation from other key sectors such as agriculture and manufacturing, has not yet been sufficiently deployed to impact this trajectory.^[7-9] Similarly, in the second half of this century, CO₂ direct air capture (DAC) will likely play an important role in maintaining the global atmospheric CO₂ concentration at or below pre-industrial levels; however, this technology is not mature, and significant steps are needed in the next two critical decades.^[10] The global industrial and manufacturing sector (chemicals and petrochemicals, cement, iron and steel, etc.) produces 1.5 Gt CO_{2,eq} annually and may have the most significant impact, positive or negative, on worldwide CO₂ emissions and atmospheric CO₂ concentration; despite improvements in the energy- and carbon-intensity of this sector, absolute levels of industry-related greenhouse gas emissions continue to increase.^[11] The challenge of achieving a timely and absolute reduction in CO₂ emissions from the industrial sector, while keeping processes reliable and cost-effective, requires radically innovative process schemes focused on mitigation and sustainability.^[11,12]

The chemicals and petrochemicals manufacturing sub-sector is the largest industrial energy user, accounting for 10% of all global energy use (more than 40 quadrillion BTU/year) and 7% of global greenhouse gas emissions (1.5 Gt CO₂/year).^[13-15] The adoption of sustainable chemical processes represents a historic technical challenge for the sector – as well as an economic opportunity – and an array of technological options will be needed to produce significant energy savings and reduce CO₂ emissions.^[15-17] For example, downstream technologies such as CCUS can capture CO₂ during chemicals manufacturing for use as a feedstock in other processes,^[9] while the adoption of the best available technologies will make a significant cut in energy use and emissions.^[18] Long-term decarbonization of the global chemicals sector will rely heavily on the research, development, and deployment of advanced technologies which can dramatically improve energy consumption and consequently cut emissions from high-volume chemicals production as demand grows, and this endeavor falls within the chemical engineering subdiscipline of process intensification.^[12,15,18] Reay, Ramshaw, and Harvey define process intensification as “any chemical engineering development that leads to a substantially smaller, cleaner, safer, and more energy-efficient technology,” encompassing both decreased energy consumption and reduced emissions.^[19] Process intensification will be most impactful when targeting the chemical products and processes with large and increasing production volumes, as well as high carbon emissions intensity (in ton CO_{2,eq} per ton product), most notably those for producing ammonia, ethylene, propylene, methanol, and the BTX hydrocarbons (benzene, toluene, and xylenes).^[13,15,18]

The production of light olefins (ethylene and propylene) is a particularly compelling target for process intensification, with a combined production of 220 million tonnes in 2012 resulting in 220 Mt CO_{2,eq} emissions from these two chemicals alone (18% of the sector total).^[13] Often described

as the building blocks of the chemicals industry,^[15,20] ethylene (C₂H₄) and propylene (C₃H₆) are direct precursors for the plastics polyethylene and polypropylene (each representing approximately two-thirds of the demand for the respective monomer), and demand for these materials is projected to increase nearly 70% by 2050;^[15] ethylene demand could reach 500–600 Mt/year in the same period.^[16] Steam cracking of naphtha or ethane feedstock is the state-of-the-art industrial process for producing the light olefins ethylene and propylene and is the single most energy-intensive process in chemical manufacturing.^[18,21–23] Highly endothermic cracking reactions, high operating temperatures (750–900°C), feed heating requirements (in the case of naphtha), and complex downstream separations result in (i) an energy intensity of 16–19 GJ/ton C_nH_{2n} and 14–17 GJ/ton C_nH_{2n} and (ii) a CO₂ emissions intensity of 1.0–1.2 ton CO₂/ton C_nH_{2n} and 1.6–1.8 ton CO₂/ton C_nH_{2n}, for the steam cracking of ethane and naphtha, respectively.^[21] Excellent descriptions of both steam cracking processes are available from Ren *et al.* and Zimmermann *et al.*^[21,22] After decades of process optimization, steam cracking has reached its maximum potential in terms of first-law energy efficiency (95%).^[24,25] Existing process alternatives are not well-suited to the challenge of greatly reducing energy consumption and carbon emissions from light olefins production; catalytic cracking can provide energy savings of 10–20%, while methanol-to-olefins (MTO) consumes about twice as much energy and relies on multiple chemical steps.^[21,26] As the industry seeks to intensify the manufacturing of light olefins, more material-efficient and energy-efficient process technologies are needed.

In parallel with the increased global focus on sustainability, the United States shale gas boom over the last two decades has exerted significant influence on the industry by increasing the availability of light alkane feedstocks from natural gas (methane, ethane, and propane) and altering demand

for important commodity chemicals such as ethylene and propylene.^[17,18,27–29] For example, the shift towards more abundant ethane feedstocks in steam cracking has already created a shortage of propylene, resulting in an increased reliance on on-purpose propylene production from propane.^[30] The global feedstock transition towards light alkanes, and the resulting supply gaps and changes in profit margins, provide the chemicals sector with a rare economic opportunity to develop new, efficient technologies with reduced energy and emissions footprints using cheap and abundant starting materials.^[16,17,30–32] The direct production of light olefins from alkanes is not new, but uses established process technologies which are scarcely better than steam cracking in terms of energy input due to the endothermic and equilibrium-limited nature of dehydrogenation.^[30,33] Of these processes, the most industrially mature and historically relevant route to light olefins is catalytic dehydrogenation (DH) of propane to propylene or butanes to butenes (the analogous route of ethane to ethylene is not economically viable).^[34,35] During World War II, dehydrogenation of butanes to butenes over chromia-alumina ($\text{Cr}_2\text{O}_3/\text{Al}_2\text{O}_3$) catalysts was the first step in synthesizing high-octane aviation fuels.^[36] In the following decades, a number of industrial DH processes were patented and commercialized to produce propylene from propane as well as 1-butene, isobutylene, and 1,3-butadiene from butanes, with the Catadiene process invented by Eugene J. Houdry representing one of the earliest examples.^[35] The two most industrially relevant catalytic dehydrogenation processes for the production of propylene and butenes are the Catofin process (Lummus) and the Oleflex process (UOP).^[35,37] In addition to catalytic or “classical” dehydrogenation, the related approach of oxidative dehydrogenation (or oxydehydrogenation) – where the dehydrogenation of paraffins to olefins is followed by the selective combustion of the hydrogen co-product – has seen limited commercial implementation for the synthesis of butadiene, including the Oxo-D and O-X-D processes, and for the synthesis of propylene in the Uhde STAR

process.^[23,34,35] As steam cracking of naphtha became more prominent in the late 20th century and heavier products such as propylene and 1,3-butadiene were co-produced with lighter ethylene gas, these on-purpose or ad-hoc technologies for producing C₃ and C₄ olefins became economically unviable. Now, as ethane from shale gas gains wider use as a steam cracking feedstock, dehydrogenation processes are once again becoming relevant, both as readily deployable commercial technologies for on-purpose production of C₃-C₄ olefins and as a starting point for the intensification of ethylene and propylene production utilizing light alkanes from shale gas.^[17]

Oxidative approaches to ethylene and propylene production are the most promising alternatives to steam cracking for the purposes of reducing energy consumption and carbon emissions.^[38] Among these alternative olefin production technologies, oxidative dehydrogenation (ODH) – a variation on catalytic dehydrogenation (DH) – is potentially the most well-studied.^[17,33,39–41] As depicted in **Figure 1.1**, classical ODH on a bulk metal oxide catalyst involves an oxygen-alkane co-feed (*e.g.* ethane, propane, butane) and encompasses (i) endothermic catalytic dehydrogenation of alkane to alkene and (ii) exothermic combustion of the hydrogen co-product to form water; the oxide supplies surface oxygen to the latter reaction via a Mars-van Krevelen redox mechanism with subsequent surface re-oxidation by gaseous O₂.^[42,43] The presence of O₂ and the selective oxidation of H₂ enables ODH to overcome the thermodynamic limitations of traditional alkane DH and creates a net exothermic reaction, allowing for lower-temperature operation and improved energy efficiency compared to catalytic dehydrogenation and steam cracking.^[33,34] Myriad catalyst systems have been demonstrated for the ODH of ethane and propane, with supported vanadium oxide representing the classical example.^[44,45] Most propane ODH literature has focused on either supported vanadium oxide (VO_x) or molybdenum oxide (MoO_x) catalysts which, despite decades

of research, have not yet provided sufficiently high yields of propylene to garner commercial interest.^[17,41,46–53] Boron nitride may represent a breakthrough catalyst technology for the ODH of propane,^[54] as described in a recent review by Shi *et al.*^[55] In contrast, several major categories of ethane ODH catalysts have shown >70% yield of ethylene.^[40] Supported VO_x and MO_x are once again among the most-studied catalysts for ethane ODH,^[56–62] and the related Mo-V-Te-Nb-O mixed oxide phase (“M1”) has shown high selectivity in literature studies.^[63–65] NiO with various dopants, particularly Nb, also gives excellent selectivity to ethylene and is treated in detail in a case study by McFarland and Metiu.^[66] A significant body of research has explored MgO-based catalysts with alkali promoters (*e.g.*, Li), of which a few representative efforts are referenced here.^[67–69] These Li/MgO catalysts were borrowed from the similar oxidative coupling of methane (OCM) to generate ethylene;^[70–72] OCM will be discussed in a later section as the original source of the Mn-Na₂WO₄/SiO₂ catalyst.^[73] Following from Li/MgO, a larger group of supported molten alkali chlorides (Li, Na, K, *etc.*), commonly using Dy₂O₃-doped MgO as the support, have exhibited high ethylene selectivity (>90%) during ethane ODH due to the dynamically rearranging molten catalyst surface facilitating ethylene desorption.^[74,75] Finally, platinum-group metals (PGM) supported on ceramic monoliths have been used by Schmidt *et al.* to perform ethane ODH with millisecond contact times, and this approach has been extended to propane-to-propylene and butane-to-butenes.^[76–78] More broadly, it is worth noting that ODH has been applied widely to butanes and C₆₊ hydrocarbons to produce C₄-C₆ olefins and vinyl compounds;^[45,79,80] the ODH of ethylbenzene to styrene is a prominent example.^[66,81] Despite extensive research efforts on ethane and propane ODH and the compelling environmental advantages of these reactions in comparison to state-of-the-art steam cracking, recent and authoritative reviews on ODH with both feedstocks have cited low selectivity towards and yield of olefins as the principal obstacle to industrial

investment and commercialization.^[39-41] Specifically, no low-cost and environmentally benign ODH catalyst has been identified which can selectively oxidize H₂ while avoiding the over-oxidation of alkanes or alkenes to CO and CO₂ and do so over a long catalyst lifetime; vanadium oxide, for example, introduces significant health hazards due to its toxicity. Moreover, ODH is a challenging reaction to implement from a reactor design standpoint due to the inherent safety hazards associated with hydrocarbon-oxygen co-feed, and the requirement of pure O₂ as a reactant negatively impacts the profit margin of any commercial ODH process.^[17] ODH represents one of the most promising approaches for the intensification of light olefin production and possesses significant energy-savings and emissions-reduction potential. However, in order to unlock these benefits and ease the chemical sector's reliance on steam cracking for light olefin production, novel approaches are needed in ODH catalyst design, ODH reactor and process design, or both.^[20]

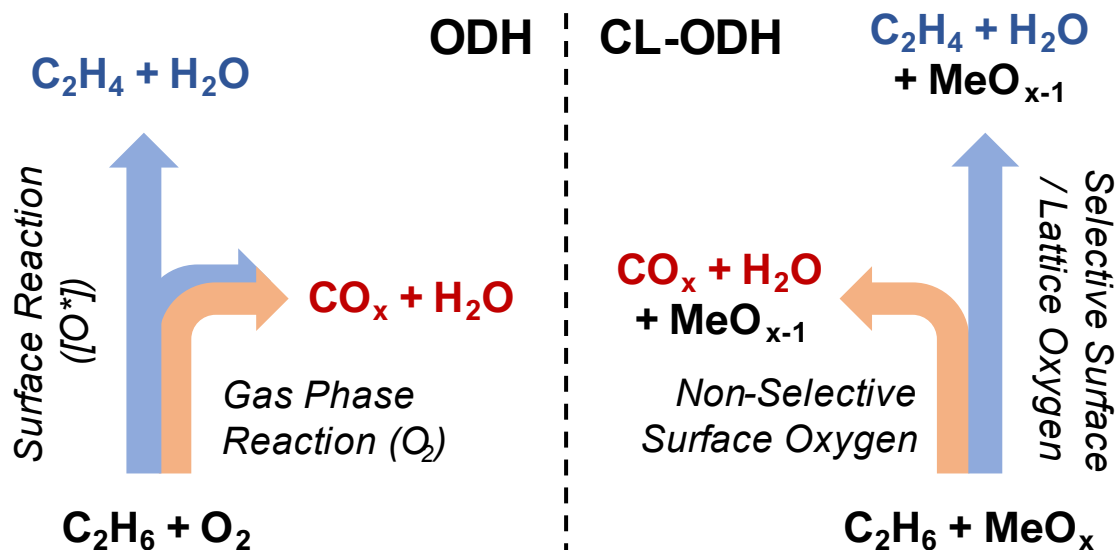


Figure 1.1: Comparison of classical or co-feed oxidative dehydrogenation (ODH) with chemical looping oxidative dehydrogenation (CL-ODH), using ethane to ethylene as an example. In comparison to gaseous O_2 used in ODH, the selectivity of the oxygen species in CL-ODH can be controlled by tuning the properties of the redox catalyst ($MeO_x \rightarrow MeO_{x-1}$), facilitating selective hydrogen combustion and forming C_2H_4 and H_2O .

1.2. Chemical Looping as a Process Intensification Strategy for Light Olefins Production

Chemical looping represents a novel, versatile, and potentially transformative technology platform to intensify processes for power generation and chemicals manufacturing through improved energy utilization and exergy loss minimization.^[14] Originally developed over the past three decades as a strategy for the conversion of carbonaceous fuels (*e.g.* coal, natural gas) for power generation with intrinsic CO_2 capture, chemical looping as a generalized approach can be applied to reduce energy consumption and carbon emissions from processes involving total or partial oxidation reactions.^[82–84] In a chemical looping process, the source of oxygen for the oxidation reaction – most typically air, though sometimes CO_2 or H_2O as steam is used – is kept separate from the fuel or chemical undergoing oxidation (**Table 1.1**). Instead, an intermediate solid oxygen carrier, known as a redox catalyst, is cycled between two spatially separate reactors, donating oxygen towards an oxidation

reaction in one reactor (often a “fuel reactor” or “reducer”) to become reduced, and then reacting with a gaseous oxidant in the other reactor (an “air reactor” or “regenerator”) to be re-oxidized. By decomposing an overall oxidation or combustion reaction into two sub-reactions via the use of a reducible intermediate, direct contact between the gaseous oxidant and the fuel or chemical is avoided. Moreover, the thermodynamically driven re-oxidation of the redox catalyst in air can be viewed as a reactive separation strategy for extracting O₂ from air, eliminating the need for energy-intensive methods of obtaining pure O₂ such as cryogenic air separation.

Table 1.1: Examples of the chemical looping process approach applied to a number of existing chemical processes. In each case, the CL oxidation reaction can be written as a multiple of $\text{MeO}_{x-1} + \frac{1}{2} \text{O}_2 \rightarrow \text{MeO}_x$ in which the redox catalyst can be contacted directly with air instead of pure O₂. CLC = chemical looping combustion, CLR = chemical looping reforming, CL-ODH = chemical looping oxidative dehydrogenation, CL-OC = chemical looping oxidative cracking, CL-DHA = chemical looping dehydroaromatization. CL-ODH, CL-OC, and CL-DHA involve selective hydrogen combustion (SHC).

Product	Feedstock	Standard Reaction	Chemical Looping Reaction (Reduction)	Process
Power, Combustion Products	Methane	$\text{CH}_4 + 2 \text{O}_2 \rightarrow \text{CO}_2 + 2 \text{H}_2\text{O}$	$\text{CH}_4 + 4 \text{MeO}_x \rightarrow \text{CO}_2 + 2 \text{H}_2\text{O} + 4 \text{MeO}_{x-1}$	CLC
Synthesis Gas	Methane	$\text{CH}_4 + \frac{1}{2} \text{O}_2 \rightarrow \text{CO} + 2 \text{H}_2$	$\text{CH}_4 + \text{MeO}_x \rightarrow \text{CO} + 2 \text{H}_2 + \text{MeO}_{x-1}$	CLR
Ethylene	Ethane	$\text{C}_2\text{H}_6 + \frac{1}{2} \text{O}_2 \rightarrow \text{C}_2\text{H}_4 + \text{H}_2\text{O}$	$\text{C}_2\text{H}_6 + \text{MeO}_x \rightarrow \text{C}_2\text{H}_4 + \text{H}_2\text{O} + \text{MeO}_{x-1}$	CL-ODH
Propylene	Propane	$\text{C}_3\text{H}_8 + \frac{1}{2} \text{O}_2 \rightarrow \text{C}_3\text{H}_6 + \text{H}_2\text{O}$	$\text{C}_3\text{H}_8 + \text{MeO}_x \rightarrow \text{C}_3\text{H}_6 + \text{H}_2\text{O} + \text{MeO}_{x-1}$	CL-ODH
Ethylene, Propylene	Naphtha	$\text{C}_6\text{H}_{14} + \frac{1}{2} \text{O}_2 \rightarrow 3 \text{C}_2\text{H}_4 + \text{H}_2\text{O}$	$\text{C}_6\text{H}_{14} + \text{MeO}_x \rightarrow 3 \text{C}_2\text{H}_4 + \text{H}_2\text{O} + \text{MeO}_{x-1}$	CL-OC
Aromatics	Methane	$6 \text{CH}_4 + 4.5 \text{O}_2 \rightarrow \text{C}_6\text{H}_6 + 9 \text{H}_2\text{O}$	$6 \text{CH}_4 + 9 \text{MeO}_x \rightarrow \text{C}_6\text{H}_6 + 9 \text{H}_2\text{O} + 9 \text{MeO}_{x-1}$	CL-DHA
Aromatics	Ethane	$3 \text{C}_2\text{H}_6 + 3 \text{O}_2 \rightarrow \text{C}_6\text{H}_6 + 6 \text{H}_2\text{O}$	$3 \text{C}_2\text{H}_6 + 6 \text{MeO}_x \rightarrow \text{C}_6\text{H}_6 + 6 \text{H}_2\text{O} + 6 \text{MeO}_{x-1}$	CL-DHA
Styrene	Ethylbenzene	$\text{C}_8\text{H}_{10} + \frac{1}{2} \text{O}_2 \rightarrow \text{C}_8\text{H}_8 + \text{H}_2\text{O}$	$\text{C}_8\text{H}_{10} + \text{MeO}_x \rightarrow \text{C}_8\text{H}_8 + \text{H}_2\text{O} + \text{MeO}_{x-1}$	CL-ODH

Of central importance in chemical looping is the redox catalyst, which consists primarily of a metal oxide capable of becoming reduced by a fuel or chemical and subsequently regaining oxygen under an oxidizing environment. Additional phases such as an inert support material or a non-reducible chemical promoter may also be present. Many reported redox catalysts are transition metal oxide-based (Ni, Cu, Fe, Mn, Co) and are either single or mixed oxides; moreover, crystal structures such as perovskites and spinels are often reported in chemical looping literature incorporating these elements along with alkaline earth or rare earth metals such as Ca or La.^[85] As the development of redox catalyst particles is a key determinant of success in chemical looping processes, much work has been done identifying materials with desirable chemical and mechanical properties for a broad range of applications.^[84,86] From a chemical reaction standpoint, the most important properties are activity, selectivity, and oxygen capacity, generally governing the rate at which the redox catalyst will donate oxygen, the extent of lattice oxygen (wt.%) that a redox catalyst can donate, and which gaseous species are or are not oxidized by the redox catalyst. Selectivity is most important for partial oxidation reactions and is highly transient, depending on the extent of depletion of the lattice oxygen at a given time.^[87,88] The stability of the redox catalyst performance over many cycles combines both chemical and mechanical aspects and is highly important for the viability of any looping process. Additional mechanical properties such as particle integrity become important when redox catalysts are used at scale in a fluidized bed reactor. For many years, NiO – both as a pure phase and supported on various inert materials – was considered one of the most effective redox catalysts for chemical looping in terms of activity, syngas selectivity, stability, and overall performance, and some of the most profoundly useful studies in the literature were performed on NiO-based redox catalysts.^[89–91] However, in recent years, NiO has lost favor compared to more benign catalyst materials.^[92] The discovery of some of these, including the perovskite SrFeO₃, was

enabled by recent advances in *in silico* screening techniques within the redox catalyst material space.^[93] Subsequent sections will go into further detail on a few distinct redox catalyst materials which are relevant to this dissertation; for an excellent summary of the current state of the broad domain of redox catalyst design, the reader should consider the review by Zeng *et al.*^[86]

There are many potential feed and effluent streams in chemical looping processes which vary depending on the application. In a total oxidation context, such as in the traditional example of chemical looping combustion (CLC), the feed is typically a fuel such as coal or gas; the primary effluent stream consists of high-purity and readily sequestrable CO₂ (plus easily condensable H₂O) and the secondary effluent from the regenerator usually contains O₂-depleted air. CLC of coal and methane for built-in CO₂ capture and sequestration was the first major application of chemical looping research and drove much of the technological innovation in the field, with pioneering developments coming from Chalmers University of Technology and Ohio State University.^[82,89,94–98] Variants of traditional CLC have also been developed such as chemical looping with oxygen uncoupling (CLOU) for improved gas-solid contact or the new application of bio-energy with carbon capture and sequestration (BECCS) for biomass conversion.^[99,100] Of equal and growing importance to CLC and total oxidation is the use of chemical looping in a partial oxidation context, most notably with chemical looping reforming (CLR) of methane to syngas.^[85,92,101] In applying the chemical looping paradigm to chemicals manufacturing, partial or selective oxidations are the most relevant reactions due to the importance of partial oxidation product CO (in synthesis gas) and of unsaturated hydrocarbons (such as olefins and aromatics) as building blocks for commodity chemicals and fuels.^[14,102] **Table 1.1** shows some of the diverse process chemistries towards which chemical looping has been applied, including CLC, CLR, and a range of selective oxidations.^[14,86]

As discussed in the authoritative review by Zhu *et al.*, chemical looping schemes have been utilized to produce a range of chemicals, including chemical looping partial oxidation (CL-PO) of methane to syngas; oxidative coupling of methane (CL-OCM) to ethylene; dehydroaromatization (CL-DHA) of methane to aromatics; water-gas shift (CL-WGS) to produce H₂; reverse water-gas shift (CL-RWGS) to produce CO; CL ammonia synthesis; air separation (CL-AS) to produce O₂; and a range of CL selective oxidations.^[14] For the production of light olefins and particularly of ethylene, the CL-OCM scheme is interesting but limited in terms of yield (~25%).^[103,104] However, significant yields of both ethylene and propylene have been observed when the chemical looping approach has been applied to the process intensification of steam cracking, leading to a novel process which resembles oxidative dehydrogenation (ODH) but removes all of its disadvantages.

As noted in previous sections, steam cracking takes primarily ethane or naphtha as feedstock, with the United States also utilizing some propane from natural gas (~15 wt.% of all cracking feeds).^[21] Ethylene and propylene production from each of these distinct processes can be intensified with chemical looping oxidative dehydrogenation (CL-ODH) or chemical looping oxidative cracking (CL-OC), the result of combining the exothermic and thermodynamically favorable ODH process with the high-value product selectivity and built-in O₂ reactive separation intrinsic to chemical looping partial oxidation processes.^[105] As shown in **Figure 1.2** using ethane as an example, CL-ODH can be implemented in a variety of ways based on the operating temperature of the reactors and the properties of the redox catalysts; the commonality among all approaches is the use of the redox catalyst to selectively combust the H₂ co-product as in conventional ODH. At relatively low temperatures (700°C and below for ethane), there is minimal ethane thermal cracking (or thermal dehydrogenation), necessitating the use of (i) a catalytically active ODH redox catalyst (pictured

in green in **Figure 1.2**) or (ii) a co-catalyst to activate and dehydrogenate ethane to form ethylene and H₂ (pictured in red); the latter may be simply called “DH+SHC” representing catalytic dehydrogenation followed by selective hydrogen combustion. Higher temperature CL-ODH (750°C and above for ethane) can rely primarily on gas-phase thermal cracking of ethane to form the majority of the ethylene and H₂, after which the H₂ is selectively combusted by the SHC redox catalyst (pictured in blue); this type of CL-ODH can also be called CL-OC as it is an enhancement of a cracking reaction. Each CL-ODH variant has been demonstrated in the literature for one of the major cracking feeds. Grasselli *et al.* explored a redox process mode for the dehydrogenation of propane using a Pt-Sn/HZSM-5 catalyst along with a Bi₂O₃/SiO₂ redox catalyst for the oxidation of hydrogen.^[106] In the same year, Creaser *et al.* used a classical V₂O₅/MgO catalyst in a cyclic implementation of propane ODH; Ballarini *et al.* soon followed with several studies using supported VO_x for the ODH of propane using a cyclic redox scheme.^[107–110] After a brief period of inactivity, two groups began to research CL-ODH of ethane and propane feedstocks. Hossain, de Lasa, *et al.* relied primarily on supported VO_x catalysts to demonstrate CL-ODH in a fluidized bed at relatively low temperatures (600°C), leveraging the catalytic activity of VO_x species for ODH.^[111–115] Modulation of bulk V₂O₅ catalyst by MoO_x was later shown to significantly improve propylene selectivity in propane CL-ODH applications, eliminating a key disadvantage of that process.^[116] Separately, Li and co-workers published a large body of work on ethane CL-ODH.^[25,105,117–128] For high-temperature CL-ODH with ethane thermal cracking followed by selective hydrogen combustion, Yusuf *et al.* developed a highly selective Na₂WO₄/Mg₆MnO₈ redox catalyst capable of providing 68% ethylene yield at 850°C.^[105,121,123] At 700°C, Gao *et al.* demonstrated a similar series of core-shell redox catalysts consisting of first of LiFeO₂ and then of molten Li₂CO₃ supported on La_{0.8}Sr_{0.2}FeO₃ perovskite oxide, which possessed both catalytic

activity for ODH and sufficient selective lattice oxygen for hydrogen combustion.^[125–127] Novotny *et al.* also tested $\text{MoO}_3/\text{Fe}_2\text{O}_3$ and $\text{MoO}_3/\text{Al}_2\text{O}_3$ redox catalysts for ethane CL-ODH at 600°C .^[118,119] Finally, for a naphtha feedstock, Hossain *et al.* used $\text{VO}_x/\text{Ce-Al}_2\text{O}_3$ to demonstrate the oxidative cracking of *n*-hexane to light olefins at 550°C ,^[129] shortly after, Li *et al.* introduced high-temperature CL-OC of *n*-hexane and cyclohexane feed streams over a $\text{Na}_2\text{WO}_4/\text{CaMnO}_3$ core-shell redox catalyst and demonstrated superior yields of both ethylene and propylene compared to naphtha steam cracking.^[130–132] Process simulation studies by Haribal *et al.* on the CL-ODH of ethane and the CL-OC of naphtha demonstrate that chemical looping can reduce process energy consumption per kg ethylene product by 82% and 52%, respectively, along with commensurate decreases in carbon emissions, confirming the considerable potential of the aforementioned CL approaches for the intensification of olefin production.^[120,133] As in any CL process, success hinges upon the redox catalyst; maintaining high selectivity and yields of olefins depends on the ability of the redox catalyst to selectively oxidize hydrogen out of the reactant mixture and avoid the over-oxidation of the feed or product molecules to form CO_x .

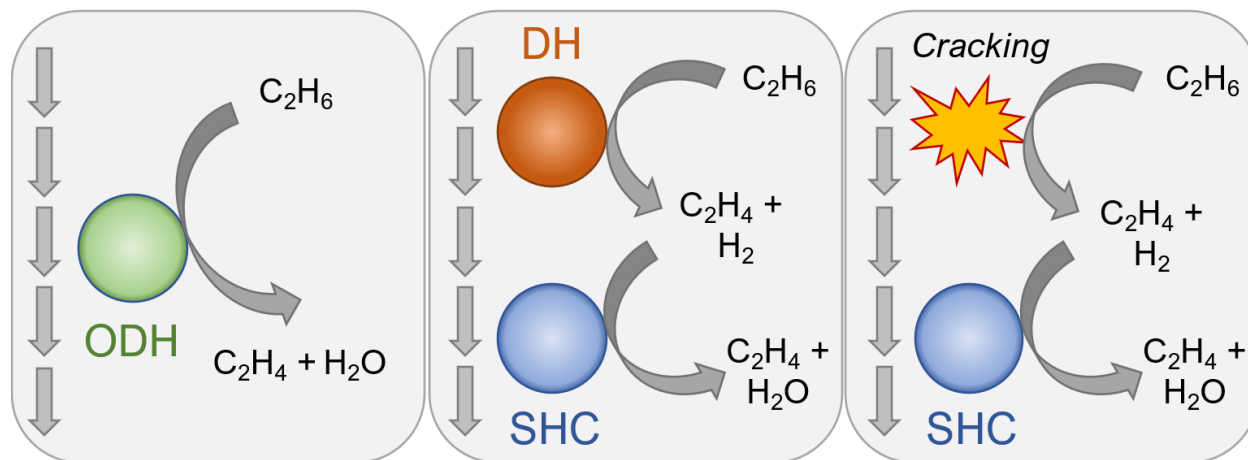


Figure 1.2: Methods of implementing CL-ODH. *Left:* A single, catalytically active ODH catalyst performs both dehydrogenation and selective H₂ combustion at intermediate temperatures. *Center:* A dehydrogenation catalyst converts ethane to ethylene and H₂ at lower temperatures; a selective hydrogen combustion (SHC) co-catalyst removes H₂ as H₂O without oxidizing ethylene. *Right:* Ethane is cracked at high temperatures to form ethylene and H₂; an SHC redox catalyst removes H₂ as H₂O without oxidizing ethylene. Arrows indicate the direction of reactants and overall gas flow.

The selective removal of hydrogen during dehydrogenation – and other endothermic, equilibrium-limited, H₂-producing processes – allows for enhanced yields of various olefins and aromatics. CL-ODH achieves H₂ removal by utilizing the active lattice oxygen of a redox catalyst for selective hydrogen combustion (SHC), which (i) minimizes the risk of product over-oxidation to CO_x, (ii) balances reactor heating requirements via an exothermic reaction, and (iii) simplifies downstream separations by forming easily condensable water.^[120] From a thermodynamic standpoint, the *in situ* combustion of H₂ for reactor heat is more exergetically efficient than the use of an external carbonaceous fuel such as methane; similarly, the combustion of the H₂ co-product is currently more economically advantageous and less carbon-intensive than purifying and transporting H₂.^[25] The concept of SHC has been a subject of industrial and academic interest for several decades. In

the 1960s, two processes by Petro-Tex Chemical Corporation and by Phillips Petroleum utilized the SHC approach to improve yields of 1,3-butadiene.^[35] Multiple patents from inventors at UOP LLC cover the dehydrogenation of ethylbenzene to styrene via the SMART process, which includes an SHC step.^[134–137] Starting from the 1990s, selective removal of hydrogen was increasingly explored for the catalytic dehydrogenation of propane, first through the use of permselective membranes and then with an oxygen-donating SHC catalyst.^[138–140] Lin *et al.* reported a series of shape-selective metal-exchanged ZSM-5 catalysts as the first materials in open literature explicitly suited for SHC, focusing on enhancing isobutylene yields from isobutane.^[141] Subsequently, a pioneering investigation by Grasselli and co-workers at Mobil identified multiple oxides and molybdates of bismuth and indium with high selectivity towards H₂ combustion in the presence of propane and propylene and was the first study to demonstrate SHC by oxygen-donating materials in a redox process mode.^[106,142–145] Rothenberg *et al.* published a comprehensive body of work on the use of doped and promoted CeO₂ (ceria) for selective hydrogen combustion in the context of both ethane and propane dehydrogenation, including a fixed-bed reactor study with a 1D transport modeling component which demonstrated the DH+SHC redox process scheme first proposed by Grasselli *et al.*^[146–154] Many of the same metal dopants and promoters chosen to enhance SHC by ceria – particularly Cr, Pb, Tl, Bi, and In – were the same elements identified by Grasselli *et al.*, and bismuth oxide on ceria is still studied for the SHC application.^[155] Similarly, gadolinium-doped ceria (GDC) was employed to great effect by Zhang *et al.* to enhance the yield of aromatics from methane dehydroaromatization, another equilibrium-limited reaction which co-produces significant H₂. A common challenge for all of the aforementioned SHC redox catalysts has been the high cost and toxicity of the promoters, which introduces a significant obstacle in the potential commercial use of these materials. SHC catalysts

consisting of supported platinum-group metals (PGM) have also been extensively studied; supported PGMs are used widely in industrial processes (*e.g.* Pt-Sn catalysts for propane dehydrogenation) and, while less toxic, are nonetheless costly.^[156–159] McFarland and Metiu, in their 2013 review of doped oxide catalysis, noted that no existing SHC catalysts performed sufficiently well to be commercialized in a combined DH+SHC process.^[66] Recent literature reports show some progress on the identification of low-cost and low-toxicity redox catalysts with high selectivity to H₂ combustion – for example, perovskite oxides LaFeO₃ and LaMnO₃, prepared from abundant lanthanum oxide and transition metal oxides, were examined by Rothenberg and coworkers and found to have high selectivity to H₂ (93%) and satisfactory cycle stability.^[160] In another recent study, the redox pair Fe₃O₄/FeO was claimed to be selective for H₂ combustion in the methane dehydroaromatization (MDA) reaction; the selective removal of H₂ during MDA represents a particularly exciting research topic and has led to greater understanding of the kinetic and thermodynamic effects of H₂ removal by combustion and other means.^[161–163] SHC remains an active area of research in both academia and industry, with several relevant patents filed on SHC redox catalyst technologies within the past three years;^[159,164,165] moreover, SHC is of central importance to the effectiveness of CL-ODH for the intensification of olefin production. The final two sections of this chapter will (i) provide further background on the materials specifically chosen for selective hydrogen combustion within the body of CL-ODH research performed by this group, and (ii) summarize the contribution of this dissertation to the state of knowledge in this field.

1.3. Core-Shell Redox Catalysts for Selective Hydrogen Combustion

A collection of successful redox catalysts will be shown throughout this dissertation for two key chemical looping schemes to produce light olefins: chemical looping oxidative dehydrogenation

(CL-ODH) and chemical looping oxidative cracking (CL-OC), also referred to as redox oxidative cracking (ROC). Subsequent chapters will describe the progression in our understanding of these redox catalyst systems, including a presentation of evidence from several characterization methods that the two primary phases of the redox catalysts – typically an oxygen-donating bulk metal oxide and a non-reducible alkali-based promoter – form a core-shell arrangement. This section aims to provide a background on each of the single components which are used together throughout the remainder of this work, specifically the perovskite oxides CaMnO_3 ^[166,167] and SrMnO_3 ^[166,168,169] and the spinel-structured alkali salt Na_2WO_4 .^[170] Brief rationale for the material selection will be given, and elements of the previous work by this research group will be described in further detail.

Throughout the majority of this work, the main component of the redox catalysts will be perovskite oxides with the structure ABO_3 , where the A-site is most commonly a Group II metal cation (*e.g.* Ca, Sr) and the B-site is occupied by a smaller d-row transition metal cation (*e.g.* Fe, Mn). Among the broader group of mixed metal oxides, perovskite oxides have proven to be excellent catalysts in a variety of contexts due to their finely tunable chemical and physical properties, a consequence of (i) the wide range of metals which are stable in the perovskite crystal structure and (ii) the ability to substitute (or “dope”) different cations into either the A- or B-site over a continuous distribution while maintaining a single phase (*e.g.* $\text{La}_{0.8}\text{Sr}_{0.2}\text{FeO}_3$, $\text{CaMn}_{0.75}\text{Fe}_{0.25}\text{O}_3$).^[171] Some established applications for perovskite oxides include automotive / three-way catalysis (CO oxidation, NO_x reduction, *etc.*),^[172] electrocatalysis (oxygen evolution and reduction reactions),^[173] and acid-base catalysis,^[174] and more recent research directions using perovskite oxides include thermochemical water splitting^[175] and air separation.^[176] For a general overview of the use of perovskite oxides across the field of catalysis, excellent reviews are available from Peña *et al.*^[171] and Zhu *et al.*^[177]

Owing to high oxygen storage capacity, fast reduction and oxidation rates, and the ability to donate substantial amounts of lattice oxygen (O^{2-}) without undergoing a phase change, perovskite oxides are exceptional base materials for redox catalysts in chemical looping processes; a recent review by Zhu *et al.* provides an overview of their application in chemical looping along with a summary of the chemical, structural, and morphological properties of importance.^[178] Two perovskite oxides ($La_{0.8}Sr_{0.2}Co_{0.2}Fe_{0.8}O_{3-\delta}$ and $CaMn_{0.875}Ti_{0.125}O_{3-\delta}$) were initially investigated by Blom, Rydén, *et al.* for the chemical looping combustion of natural gas with oxygen uncoupling (CLOU) and later for the chemical looping reforming of methane (CLR).^[179–182] Separately, Beckers *et al.* identified $LaFeO_3$ and $LaMnO_3$ as ideal oxygen carriers for selective hydrogen combustion (SHC) in their sweeping study of perovskite oxygen reservoirs.^[160] In the years since, $LaFeO_3$ and its derivatives (most notably $La_{0.8}Sr_{0.2}FeO_3$ or LSF) have been studied extensively for the CLR of methane, leading to general insights about the selectivity of perovskite oxides in partial oxidation applications, including, *e.g.* (i) the influence of the degree of oxidation on surface oxygen coverage and selectivity,^[88,183] (ii) the relative selectivity of lattice oxygen vs. surface oxygen species,^[87,184] (iii) the effects of cation substitution on selectivity,^[185] and (iv) the influence of the relative rates of bulk oxide ion diffusion vs. surface reaction.^[186] In contrast with $LaFeO_3$ and LSF, the use of $LaMnO_3$ and $CaMnO_3$ has primarily been confined to total oxidation applications, namely the CLC of methane.^[187–189] $CaMnO_3$, in particular, has been doped with a variety of elements such as Fe, Ti, and Mg for the CLC and CLOU of methane; these studies are tabulated in the review by Zhu *et al.*, which also dedicates several paragraphs to the discussion of $CaMnO_3$ as a redox catalyst.^[178] Recently, Shafieifarhood, Mishra, *et al.* began to investigate $CaMnO_3$ for the partial oxidation of methane, using a Rh promoter to reduce the reaction temperature and improve selectivity towards syngas compared to the bulk or unpromoted $CaMnO_3$.^[190,191] However, if perovskite oxides are to

be extended to higher-temperature applications such as CL-ODH, rare metal promoters would not be feasible. From over a decade of research, it is clear that CaMnO_3 has exceptional potential as a redox catalyst resulting from high oxygen capacity and stability, fast oxygen donation rates, and preparation from abundant and environmentally benign materials. In addition to CaMnO_3 , recent studies of the related $\text{Ca}_{0.8}\text{Sr}_{0.2}\text{MnO}_3$ and SrMnO_3 for thermochemical air separation have similarly demonstrated that these perovskite oxides have ideal oxygen donation properties in the temperature range of interest for dehydrogenation reactions.^[176,192,193] The challenge is to enhance these CaMnO_3 and SrMnO_3 perovskite oxides for chemical looping partial oxidations such as CL-ODH and CL-OC by improving their selectivity towards hydrogen combustion.

Following on recent advances from this group on redox catalyst design for chemical looping partial oxidation reactions, most notably for the CL-ODH of ethane, the strategy for improving hydrogen combustion selectivity on CaMnO_3 and SrMnO_3 involves the use of a sodium tungstate promoter (Na_2WO_4).^[105,121–123] Investigations by Neal, Yusuf, *et al.* employed a 20 wt.% Na_2WO_4 -promoted Mg_6MnO_8 redox catalyst for the CL-ODH of ethane at 850°C, a cyclic process scheme which involves parallel gas-phase cracking of ethane to ethylene with selective combustion of H_2 on the redox catalyst surface. At these conditions, Na_2WO_4 exists in molten form. In the first two studies by Neal *et al.* and Yusuf *et al.*, Na_2WO_4 was shown to significantly improve selectivity towards ethylene formation during ethane CL-ODH by suppressing over-oxidation of C_2H_4 and C_2H_6 by Mg_6MnO_8 to form CO_x ; non-selective surface Mn^{4+} species were suppressed by the presence of a Na_2WO_4 shell coating the Mn/MgO core.^[105,121] While the $\text{Na}_2\text{WO}_4/\text{Mg}_6\text{MnO}_8$ redox catalyst did not react with C_2 hydrocarbons, it demonstrated a propensity for H_2 combustion and removed ~80% of produced H_2 during the reaction, effectively heat-balancing the system and lifting

thermodynamic constraints to give higher ethylene yield.^[120] Subsequent studies by Yusuf *et al.* extended the selectivity enhancing effect of Na₂WO₄ to a mixed Mn/Si oxide substrate^[122] and further probed the mechanism of selective H₂ combustion by the Na₂WO₄/Mg₆MnO₈ redox catalyst; in the latter, it was determined that H₂ is oxidized at the gas-solid interface located at the surface of the molten Na₂WO₄ shell by oxide ions (O²⁻) conducted through the tungstate layer.^[123] The ability of Na₂WO₄ to conduct oxygen in crystalline (< 600°C) and molten form (> 700°C) was further confirmed in a recently published study by this group.^[131] Additional insights on the role of Na₂WO₄ as a promoter have been published in the literature and will be reported in later chapters of this dissertation.^[117,128,130]

Given the importance of Na₂WO₄ to this body of work, these final introductory paragraphs will provide additional background on the use of this material as a chemical promoter in redox catalysis and describe what is known about the Na₂WO₄ structure—property relationship in this context. Most of the relevant information on Na₂WO₄ for high-temperature redox applications comes from the oxidative coupling of methane (OCM), first reported by Keller and Bhasin.^[70] Early efforts on OCM demonstrated a highly selective Mn/SiO₂ catalyst with a sodium pyrophosphate (Na₂P₂O₇) promoter.^[194–196] Shortly thereafter, Jiang *et al.* first reported the MnO_x-Na₂WO₄/SiO₂ catalyst for OCM;^[197] the Mn-Na₂WO₄/SiO₂ system remains the highest-yield OCM catalyst in the literature, consistently achieving ~25% ethylene yield from methane. (The success of Mn-Na₂WO₄/SiO₂ and Mn-Na₂WO₄/MgO led directly to the discovery of Na₂WO₄/Mg₆MnO₈ for ethane CL-ODH; the final step of the OCM sequence is the ODH of ethane.)^[105] Interestingly, there is not yet consensus on the nature of the active site on the Mn-Na₂WO₄/SiO₂ catalyst, and the best reviews on the topic simply mention a “synergistic effect” among the Na, W, Mn, and Si metals.^[73,198] The full breadth

of OCM studies on Mn-Na₂WO₄/SiO₂ will not be summarized here, not least because of the lack of agreement on most aspects of the catalyst performance, and the review by Kiani *et al.* is highly recommended for an understanding of that application.^[73] However, several specific OCM studies provide useful insights on the use of Na₂WO₄ as a promoter. Yu and Lunsford examined CeO₂ and Pr₆O₁₁ with and without Na₂WO₄ and found that the addition of Na₂WO₄ transformed the materials from CH₄ oxidation catalysts with < 10% C₂₊ selectivity to highly effective OCM catalysts with > 70% C₂₊ selectivity (for Na₂WO₄/CeO₂) at 780°C.^[199] XPS measurements revealed that molten Na₂WO₄ completely coated the catalysts and suppressed the surface oxygen species implicated in CH₄ over-oxidation, leading to higher C₂H₄ yields and demonstrating the effectiveness of Na₂WO₄ across a variety of metal oxide substrates. Ji *et al.* noted that K₂WO₄ provided roughly the same benefits as Na₂WO₄ when incorporated into the Mn/SiO₂ catalyst, though Li₂WO₄ did not;^[200] similarly, Hou *et al.* showed that the MoO₄²⁻ oxyanion was nearly as effective as WO₄²⁻ for OCM, and taken together the studies suggest that the material space of molten salt promoters for selective hydrogen combustion could be extended beyond Na₂WO₄.^[201] A recent publication by Wang *et al.* focused on MnTiO₃ as a catalytically active phase for OCM, and the authors demonstrated that the addition of 8–15 wt.% Na₂WO₄ to the perovskite oxide gave a significant and stable improvement to olefin selectivity (73% *vs.* 29%), showing that Na₂WO₄ on perovskites can be stable over many redox cycles (500 h).^[202] In 2020, Werny *et al.* shared one of the first comprehensive operando investigations on Mn-Na₂WO₄/SiO₂ for OCM, with several interesting findings: (i) during heating, crystalline (cubic) Na₂WO₄ disappears around 600°C from *in situ* XRD; (ii) in an air environment, cubic Na₂WO₄ is replaced by a transient phase possibly representing orthorhombic Na₂WO₄, while in an inert environment a different phase is seen; (iii) during cooling, two unidentified phases appear from 660–600°C, while cubic Na₂WO₄ does not recrystallize until 450°C; (iv) the classical

OCM catalyst with 5 wt.% Na_2WO_4 and 2 wt.% Mn does not have complete surface coverage with the melt, and some surface inhomogeneities exist; (v) MnWO_4 forms under reducing conditions, but not during normal OCM operation which includes a low level of O_2 ; and (vi) Na_2O is identified as the active phase and is “stored” by the Na_2WO_4 until the introduction of O_2 creates the condition for steady-state OCM, where a $\text{Mn}_7\text{SiO}_{12}/\text{MnWO}_4$ redox pair stabilizes the mobile Na_2O phase.^[203] Finally, from a practical standpoint, Sadjadi *et al.* published a relevant study exploring whether Mn- $\text{Na}_2\text{WO}_4/\text{SiO}_2$ could be used in a fluidized bed reactor for OCM and determined an optimum Na concentration to avoid particle agglomeration while preserving C_{2+} selectivity.^[204] While these OCM studies provide relevant information about Na_2WO_4 in the form of both phase behavior and catalytic activity for C—H bond activation in CH_4 , it is noted that the primary role of Na_2WO_4 in this work is as a selective surface for hydrogen combustion in the presence of C_2H_4 and C_2H_6 , and not as a catalytically active surface; activation of C_2 hydrocarbons by Na_2WO_4 is not well studied.

Lastly, a number of references from outside the scope of OCM literature provide relevant data and insights on the Na_2WO_4 phase and its close relatives. Due to the high-temperature conditions in which Na_2WO_4 will be employed in this work, the phase composition and crystal or melt structure during heating and cooling are highly pertinent. A phase diagram for the Na/W/O system can be found in Pistorius *et al.*, which establishes $\sim 590^\circ\text{C}$ and $\sim 695^\circ\text{C}$ as the cubic-to- K_2SO_4 -type and K_2SO_4 -type-to-liquid phase transitions, respectively, at ambient pressure.^[170] Studies of Na_2WO_4 featuring *in situ* XRD report a loss of crystallinity in this region.^[131,201,203,205] Luz-Lima *et al.* found that Na_2WO_4 during heating underwent a first-order phase transition from cubic to orthorhombic crystal system at approximately 560°C , after which the WO_4^{2-} tetrahedra were partially disordered, before becoming fully disordered as a liquid.^[206] These authors also reported similarities between

Na_2WO_4 and Na_2MoO_4 phases, echoing the finding by Hou *et al.*^[201] Cortes-Jacome *et al.* studied a core-shell Na- WO_x/TiO_2 catalyst system via Raman spectroscopy and HR-TEM, finding sodium tungstate formation on the catalyst surface present in several phases including Na_2WO_4 , $\text{Na}_2\text{W}_2\text{O}_7$ (sodium ditungstate), and Na_xWO_3 (sodium tungsten bronze). Wang *et al.* recently studied the melting and re-crystallization behavior of $\text{Na}_2\text{W}_2\text{O}_7$ in detail via *in situ* Raman spectroscopy and determined that molten $\text{Na}_2\text{W}_2\text{O}_7$ consists of isolated $(\text{W}_2\text{O}_7)^{2-}$ anions (corner-sharing tetrahedra) while crystalline $\text{Na}_2\text{W}_2\text{O}_7$ shows an infinite-chain network of $[\text{WO}_6]$ octahedra and $[\text{WO}_4]$ tetrahedra; moreover, a non-crystalline phase with a different structure from either pre-heating or molten $\text{Na}_2\text{W}_2\text{O}_7$ was observed upon rapid cooling, suggesting a degree of thermal hysteresis.^[207] Xu *et al.* demonstrated that the melting of $\text{Na}_2\text{W}_2\text{O}_7$ is associated with a two-orders-of-magnitude increase in oxide ion conductivity, introducing the possibility that different mechanisms for oxide ion transport persist above and below the melting point of sodium tungstate;^[208] currently, is no analogous study on conductivity by Na_2WO_4 which includes data at or above 700°C. Na_xWO_3 was hypothesized by Yusuf *et al.* to be involved in the redox mechanism for shuttling of oxygen species through the tungstate surface layer in the $\text{Na}_2\text{WO}_4/\text{Mg}_6\text{MnO}_8$ system;^[123] a few studies on the properties of sodium tungsten bronze are cited here.^[209,210] Finally, a recent follow-up study by Takanabe *et al.* on the *in situ* formation of OH radicals by Na_2WO_4 at high temperatures included a wide assortment of characterization on the Na_2WO_4 system, including *in situ* XRD and STEM measurements which corroborated earlier reports on the molten salt state of Na_2WO_4 relating to onset temperatures of phase transitions and the coverage of the support by the melt.^[205] Many of these findings on Na_2WO_4 from the literature will be mentioned later in this dissertation as they become relevant, particularly in Chapter 5.

1.4. Summary

The intensification of the most high-volume, energy-intensive, and emissions-intensive processes in the chemical industry will provide both environmental and economic benefits as sustainability and climate risk mitigation continue to grow in importance. For intensified production of ethylene and propylene, the chemical looping oxidative dehydrogenation (CL-ODH) and chemical looping oxidative cracking (CL-OC) are promising approaches due to the improved energy and exergy efficiency and lowered carbon emissions as compared to the conventional steam cracking of ethane and naphtha, respectively. As with any chemical looping scheme, these process technologies succeed or fail based on the activity, selectivity, and long-term stability of the metal oxide redox catalyst, which must undergo thousands of cycles between reduced and oxidized states with a low degree of degradation. The redox catalyst property of most importance for chemical looping partial oxidations, which includes CL-ODH and CL-OC, is the ability to perform selective hydrogen combustion (SHC) in a mixture containing H_2 and high-value products including C_2H_4 and C_3H_6 . This dissertation focuses on the development, characterization, and demonstration of a new class of highly selective core-shell redox catalysts prepared from earth-abundant, low-cost, and benign materials, which can be used to enable CL-ODH and CL-OC processes for olefin production.

Chapter 2 introduces the design rationale and screening of a new class of Mn-containing redox catalysts for selective hydrogen combustion (SHC) in a cyclic redox scheme. The redox catalysts, which include unpromoted and Na_2WO_4 -promoted Mg_6MnO_8 , $CaMnO_3$, and $SrMnO_3$, are suitable for a range of chemical looping applications including the CL-ODH of ethane and the CL-OC of naphtha. Initial experiments using a H_2/C_2H_4 co-feed are presented, demonstrating the selectivity-enhancing effects of Na_2WO_4 promotion; moreover, the influence of Na_2WO_4 on the elemental

surface composition is explored. The best-performing redox catalyst, 20 wt.% Na₂WO₄/CaMnO₃, is further examined in the CL-ODH of ethane using a Cr₂O₃/Al₂O₃ co-catalyst for dehydrogenation of ethane at 650°C.

Chapter 3 demonstrates the high performance of the two perovskite oxide-based redox catalysts, Na₂WO₄/CaMnO₃ and Na₂WO₄/SrMnO₃, for SHC in a challenging chemical looping application: the redox oxidative cracking (ROC) of naphtha, represented by *n*-hexane, to form the light olefins ethylene and propylene. The ROC process for *n*-hexane conversion is introduced and reaction data for unpromoted and Na₂WO₄-promoted SrMnO₃ and CaMnO₃ are presented. The high selectivity and cycling stability of these oxygen-carrying materials is established. An array of spectroscopic and other methods are employed to determine the nature of the Na₂WO₄-promoted redox catalysts, and a core-shell arrangement is confirmed, with the oxygen-donating perovskite oxide serving as the core and the Na₂WO₄ forming a shell around the bulk oxide.

In Chapter 4, the CaMnO₃ and Na₂WO₄/CaMnO₃ redox catalysts are investigated from a reduction kinetics perspective via thermogravimetric analysis (TGA). A new methodology is introduced for obtaining kinetic parameters from non-dimensionalized reduction rate data, and this approach is applied to the reduction of the two redox catalysts by H₂, C₂H₄, and C₂H₆ in order to describe the selective combustion of hydrogen at the particle level. The impact of Na₂WO₄ is shown on the pre-exponential factor and apparent activation energy for lattice oxygen removal from CaMnO₃ by H₂ and C₂H₄; the reduction rate of Na₂WO₄/CaMnO₃ in C₂H₄ is shown to be three orders of magnitude lower than in H₂, supporting the use of this redox catalyst for selective hydrogen combustion.

Fixed-bed reactor data are acquired to complement the TGA kinetics information and illustrate the influence of solid conversion on H₂ selectivity.

Lastly, Chapter 5 represents a deeper dive into the reduction kinetics of Na₂WO₄/CaMnO₃ and aims to characterize more precisely the transient nature of the redox catalyst performance. Thermal history is determined to be an important influence on the reduction rate of Na₂WO₄/CaMnO₃ and significantly impacts the resulting kinetic parameters; moreover, the rates are shown to be affected by the extent of previous redox cycling. A higher degree of statistical rigor is applied to the kinetic data for reduction by both H₂ and C₂H₄. Kinetic data from H₂/C₂H₄ co-feed experiments are shown to determine whether the reduction of Na₂WO₄/CaMnO₃ by the two gases is competitive (using the same sites) or additive (using different sites).

1.5. References

- [1] National Research Council, *Climate Change Science: An Analysis of Some Key Questions*, The National Academies Press, **2001**.
- [2] N. Oreskes, *Science* (80-.). **2004**, 306, 2004–2006.
- [3] W. R. L. Anderegg, J. W. Prall, J. Harold, S. H. Schneider, *Proc. Natl. Acad. Sci.* **2010**, 107, 12107–12109.
- [4] USGCRP, *Climate Science Special Report: Fourth National Climate Assessment, Volume I*, **2017**.
- [5] USGCRP, *Impacts, Risks, and Adaption in the United States: Fourth National Climate Assessment, Volume II*, **2018**.
- [6] IPCC, *Climate Change 2014: Synthesis Report. Contribution of Working Groups I, II, and III to the Fifth Assessment Report of the Intergovernmental Panel on Climate Change.*, **2014**.
- [7] M. Bui, C. S. Adjiman, E. J. Anthony, A. Boston, S. Brown, P. S. Fennell, S. Fuss, A. Galindo, L. A. Hackett, J. P. Hallett, et al., *Energy Environ. Sci.* **2018**, 11, 1062–1176.
- [8] S. J. Davis, N. S. Lewis, M. Shaner, S. Aggarwal, D. Arent, I. L. Azevedo, S. M. Benson, T. Bradley, J. Brouwer, Y. Chiang, et al., **2018**, 9793, DOI 10.1126/science.aas9793.
- [9] A. Kästelhön, R. Meys, S. Deutz, S. Suh, A. Bardow, **2019**, c, DOI 10.1073/pnas.1821029116.
- [10] C. R. Murdock, S. A. Didas, C. W. Jones, *Chem. Rev.* **2016**, DOI 10.1021/acs.chemrev.6b00173.
- [11] M. Fishedick, J. Roy, A. Abdel-Aziz, A. Acquaye, J. M. Allwood, J. P. Ceron, Y. Geng, H. Khesghi, A. Lanza, D. Perczyk, et al., in *Clim. Chang. 2014 Mitig. Clim. Chang.*

- Contrib. Work. Gr. III to Fifth Assess. Rep. Intergov. Panel Clim. Chang.*, **2014**, pp. 739–810.
- [12] A. I. Stankiewicz, J. A. Moulijn, *Chem. Eng. Prog.* **2000**, 96.
- [13] International Energy Agency, *Technology Roadmap: Energy and GHG Reductions in the Chemical Industry via Catalytic Processes*, **2013**.
- [14] X. Zhu, Q. Imtiaz, F. Donat, *Energy Environ. Sci.* **2020**, 13, 772–804.
- [15] IEA, *The Future of Petrochemicals*, **n.d.**
- [16] R. C. Valencia, *The Future of the Chemical Industry by 2050*, **2013**.
- [17] E. E. Stangland, *Annu. Rev. Chem. Biomol. Eng.* **2018**, 9, 341–364.
- [18] DOE, *Bandwidth Study on Energy Use and Potential Energy Saving Opportunities in U.S. Chemical Manufacturing*, **2015**.
- [19] D. Reay, C. Ramshaw, A. Harvey, *Process Intensification: Engineering for Efficiency, Sustainability and Flexibility*, **2013**.
- [20] J. F. Brazdil, *Top. Catal.* **2006**, 38, 289.
- [21] T. Ren, M. Patel, K. Blok, *Energy* **2006**, 31, 425–451.
- [22] H. Zimmermann, R. Walzl, *Ullmann's Encycl. Ind. Chem.* **2012**, 466–529.
- [23] H. Zimmermann, *Ullmann's Encycl. Ind. Chem.* **2014**, 6, 45–66.
- [24] S. M. Sadrameli, *Fuel* **2015**, 140, 102–115.
- [25] L. M. Neal, V. P. Haribal, F. Li, *iScience* **2019**, 19, 894–904.
- [26] N. Rahimi, R. Karimzadeh, *Appl. Catal. A Gen.* **2011**, 398, 1–17.
- [27] R. A. Kerr, *Science (80-.)*. **2010**, 328, 1624.
- [28] J. J. Siirola, *AIChE J.* **2014**, 60, 810–819.
- [29] O. O. James, S. Mandal, N. Alele, B. Chowdhury, S. Maity, *Fuel Process. Technol.* **2016**,

- 149, 239–255.
- [30] I. Amghizar, L. A. Vandewalle, K. M. Van Geem, G. B. Marin, *Engineering* **2017**, *3*, 171–178.
- [31] E. McFarland, *Science (80-.)*. **2012**, *338*, 340–343.
- [32] E. G. Rightor, C. L. Tway, *Catal. Today* **2015**, *258*, 226–229.
- [33] F. Cavani, F. Trifirò, *Catal. Today* **1995**, *24*, 307–313.
- [34] M. M. Bhasin, J. H. McCain, B. V. Vora, T. Imai, P. R. Pujadó, *Appl. Catal. A Gen.* **2001**, *221*, 397–419.
- [35] B. V Vora, **2012**, 1297–1308.
- [36] A. V Grosse, V. N. Ipatieff, *Ind. Eng. Chem.* **1940**, 268–272.
- [37] J. J. H. B. Sattler, J. Ruiz-Martinez, E. Santillan-Jimenez, B. M. Weckhuysen, *Chem. Rev.* **2014**, *114*, 10613–10653.
- [38] Y. Gao, L. Neal, D. Ding, W. Wu, C. Baroi, A. M. Ga, F. Li, *ACS Catal.* **2019**, DOI 10.1021/acscatal.9b02922.
- [39] F. Cavani, N. Ballarini, A. Cericola, *Catal. Today* **2007**, *127*, 113–131.
- [40] C. A. Gartner, A. C. Van Veen, J. A. Lercher, *ChemCatChem* **2013**, *5*, 3196–3217.
- [41] C. A. Carrero, R. Schloegl, I. E. Wachs, R. Schomaecker, *ACS Catal.* **2014**, *4*, 3357–3380.
- [42] N. Mizuno, M. Misono, *Chem. Rev.* **1998**, 199–217.
- [43] P. Mars, D. W. Van Krevelen, *Chem. Eng. Sci.* **1954**, *3*, 41–59.
- [44] E. A. Mamedov, V. Cortes Corberan, *Appl. Catal. A, Gen.* **1995**, *127*, 1–40.
- [45] T. Blasco, J. M. Lopez-Nieto, *Appl. Catal. A Gen.* **1997**, *157*, 117–142.
- [46] A. Khodakov, J. Yang, S. Su, E. Iglesia, A. T. Bell, *J. Catal.* **1998**, *177*, 343–351.
- [47] K. Chen, A. Khodakov, J. Yang, A. Bell, E. Iglesia, *J. Catal.* **1999**, *333*, 325–333.

- [48] K. Chen, A. T. Bell, E. Iglesia, *J. Phys. Chem. B* **2000**, *104*, 1292–1299.
- [49] K. Chen, S. Xie, A. T. Bell, E. Iglesia, *J. Catal.* **2000**, *195*, 244–252.
- [50] K. Chen, S. Xie, E. Iglesia, A. T. Bell, *J. Catal.* **2000**, *189*, 421–430.
- [51] K. Chen, S. Xie, A. T. Bell, E. Iglesia, *J. Catal.* **2001**, *198*, 232–242.
- [52] K. Chen, A. T. Bell, E. Iglesia, *J. Catal.* **2002**, *209*, 35–42.
- [53] A. Christodoulakis, M. Machli, A. A. Lemonidou, S. Boghosian, *J. Catal.* **2004**, *222*, 293–306.
- [54] J. T. Grant, C. A. Carrero, F. Goeltl, J. Venegas, P. Mueller, S. P. Burt, S. E. Specht, W. P. Mcdermott, A. Chieragato, I. Hermans, *Science (80-.)*. **2016**.
- [55] L. Shi, Y. Wang, B. Yan, W. Song, D. Shao, A.-H. Lu, *Chem. Commun.* **2018**, *54*, 10936.
- [56] E. M. Thorsteinson, T. P. Wilson, F. G. Young, P. H. Kasai, *J. Catal.* **1978**, *52*, 116–132.
- [57] M. D. Argyle, K. Chen, A. T. Bell, E. Iglesia, *J. Phys. Chem. B* **2002**, *106*, 5421–5427.
- [58] E. Heracleous, A. F. Lee, I. A. Vasalos, A. A. Lemonidou, *Catal. Letters* **2003**, *88*, 47.
- [59] E. Heracleous, A. A. Lemonidou, J. A. Lercher, *Appl. Catal. A Gen.* **2004**, *264*, 73–80.
- [60] E. Heracleous, A. A. Lemonidou, *Appl. Catal. A Gen.* **2004**, *269*, 123–135.
- [61] E. Heracleous, M. Machli, A. A. Lemonidou, I. A. Vasalos, *J. Mol. Catal. A Chem.* **2005**, *232*, 29–39.
- [62] A. Christodoulakis, E. Heracleous, A. A. Lemonidou, S. Boghosian, *J. Catal.* **2006**, *242*, 16–25.
- [63] J. M. López Nieto, P. Botella, M. I. Vázquez, A. Dejoz, *Chem. Commun.* **2002**, 1906–1907.
- [64] J. M. López Nieto, P. B. Asunción, M. I. Vazquez Navarro, A. D. Garcia, *US Patent 7,319,179 B2*, **2008**.

- [65] J. S. Valente, H. Armendariz-Herrera, R. Quintana-Solorzano, P. del Angel, N. Nava, A. Masso, J. M. Lopez Nieto, *ACS Catal.* **2014**, *4*, 1292–1301.
- [66] E. W. McFarland, H. Metiu, *Chem. Rev.* **2013**, *113*, 4391–4427.
- [67] E. Morales, J. H. Lunsford, *J. Catal.* **1989**, *118*, 255–265.
- [68] S. J. Conway, J. H. Lunsford, *J. Catal.* **1991**, *131*, 513–522.
- [69] S. Fuchs, L. Leveles, K. Seshan, L. Lefferts, A. a. Lemonidou, J. a. Lercher, *Top. Catal.* **2001**, *15*, 169–174.
- [70] G. E. Keller, M. M. Bhasin, *J. Catal.* **1982**, *73*, 9–19.
- [71] Y. Amenomiya, V. I. Birss, M. Goledzinowski, J. Galuszka, A. R. Sanger, *Catal. Rev.* **1990**, *32*, 163–227.
- [72] P. Schwach, X. Pan, X. Bao, *Chem. Rev.* **2017**, *117*, 8497–8520.
- [73] D. Kiani, S. Sourav, J. Baltrusaitis, I. E. Wachs, *ACS Catal.* **2019**, *9*, 5912–5928.
- [74] C. P. Kumar, S. Gaab, T. E. Müller, J. A. Lercher, *Top. Catal.* **2008**, *50*, 156–167.
- [75] C. A. Gartner, A. C. Van Veen, J. A. Lercher, *J. Am. Chem. Soc.* **2014**, *136*, 12691–12701.
- [76] M. Huff, L. D. Schmidt, *J. Phys. Chem.* **1993**, *97*, 11815–11822.
- [77] M. Huff, L. D. Schmidt, *J. Catal.* **1994**, *149*, 127–141.
- [78] A. S. Bodke, D. Henning, L. D. Schmidt, S. S. Bharadwaj, J. J. Maj, J. Siddall, *J. Catal.* **2000**, *191*, 62–74.
- [79] J. Zhang, X. Liu, R. Blume, A. Zhang, R. Schlogl, D. S. Su, *Science (80-.)*. **2008**, *322*, 73–78.
- [80] B. Pillay, M. R. Mathebula, H. B. Friedrich, *Catal. Letters* **2011**, *141*, 1297–1304.
- [81] F. Cavani, F. Trifiro, *Appl. Catal. A Gen.* **1995**, *133*, 219–239.

- [82] F. Li, L.-S. Fan, *Energy Environ. Sci.* **2008**, *1*, 248.
- [83] L.-S. Fan, *Chemical Looping Systems for Fossil Energy Conversions*, John Wiley & Sons, Inc., Hoboken, NJ, **2010**.
- [84] L.-S. Fan, L. Zeng, W. Wang, S. Luo, *Energy Environ. Sci.* **2012**, *5*, 7254–7280.
- [85] J. Adanez, A. Abad, F. Garcia-Labiano, P. Gayan, L. F. De Diego, *Prog. Energy Combust. Sci.* **2012**, *38*, 215–282.
- [86] L. Zeng, Z. Cheng, J. A. Fan, L. Fan, J. Gong, *Nat. Rev. Chem.* **n.d.**, DOI 10.1038/s41570-018-0046-2.
- [87] L. M. Neal, A. Shafieifarhood, F. Li, *ACS Catal.* **2014**, *4*, 3560–3569.
- [88] A. Shafieifarhood, J. C. Hamill, L. M. Neal, F. Li, *Phys. Chem. Chem. Phys.* **2015**, *17*, 31297–31307.
- [89] M. M. Hossain, H. I. de Lasa, *Chem. Eng. Sci.* **2008**, *63*, 4433–4451.
- [90] K. E. Sedor, M. M. Hossain, H. I. De Lasa, *Can. J. Chem. Eng.* **2008**, *86*, 323–334.
- [91] Z. Zhou, L. Han, G. M. Bollas, *Int. J. Hydrogen Energy* **2014**, *9*, 8535–8556.
- [92] T. Mattisson, M. Keller, C. Linderholm, P. Moldenhauer, M. Rydén, H. Leion, A. Lyngfelt, *Fuel Process. Technol.* **2018**, *172*, 1–12.
- [93] C. Y. Lau, M. T. Dunstan, W. Hu, C. P. Grey, S. A. Scott, *Energy Environ. Sci.* **2017**, *10*, 818–831.
- [94] A. Lyngfelt, B. Leckner, T. Mattisson, *Chem. Eng. Sci.* **2001**, *56*, 3101–3113.
- [95] T. Mattisson, A. Järnäs, A. Lyngfelt, *Energy & Fuels* **2003**, *17*, 643–651.
- [96] P. Cho, T. Mattisson, A. Lyngfelt, *Fuel* **2004**, *83*, 1215–1225.
- [97] A. Abad, T. Mattisson, A. Lyngfelt, M. Ryde, **2006**, *85*, 1174–1185.
- [98] L. Fan, L. Zeng, S. Luo, **2015**, *61*, DOI 10.1002/aic.

- [99] Q. Imtiaz, D. Hosseini, C. Rüdiger, *Energy Technol.* **2013**, *1*, 633–647.
- [100] X. Zhao, H. Zhou, V. S. Sikarwar, M. Zhao, A.-H. A. Park, P. S. Fennell, L. Shen, L.-S. Fan, *Energy Environ. Sci.* **2017**, *10*, 1885.
- [101] D. Li, R. Xu, Z. Gu, X. Zhu, S. Qing, K. Li, **2020**, *1900925*, 1–28.
- [102] D. Li, R. Xu, X. Li, Z. Li, X. Zhu, K. Li, **2020**, DOI 10.1021/acs.energyfuels.0c01006.
- [103] S. Parishan, P. Littlewood, A. Arinchtein, V. Fleischer, R. Schomäcker, **2018**, *311*, 40–47.
- [104] V. Fleischer, U. Simon, S. Parishan, M. Gracia, O. Görke, A. Gurlo, W. Riedel, L. Thum, J. Schmidt, T. Risse, et al., *J. Catal.* **2018**, *360*, 102–117.
- [105] L. M. Neal, S. Yusuf, J. A. Sofranko, F. Li, *Energy Technol.* **2016**, *4*, 1200–1208.
- [106] R. K. Grasselli, D. L. Stern, J. G. Tsikoyiannis, **1999**, *189*, 9–14.
- [107] D. Creaser, B. Andersson, R. R. Hudgins, P. L. Silveston, **1999**, *187*, 147–160.
- [108] N. Ballarini, F. Cavani, M. Ferrari, R. Catani, U. Cornaro, **2003**, *213*, 95–102.
- [109] N. Ballarini, F. Cavani, C. Cortelli, C. Giunchi, P. Nobili, F. Trifirò, R. Catani, U. Cornaro, **2003**, *78*, 353–364.
- [110] N. Ballarini, F. Cavani, A. Cericola, C. Cortelli, M. Ferrari, F. Trifirò, G. Capannelli, A. Comite, R. Catani, U. Cornaro, *Catal. Today* **2004**, *91–92*, 99–104.
- [111] S. Al-Ghamdi, M. Volpe, M. M. Hossain, H. De Lasa, *Appl. Catal. A Gen.* **2013**, *450*, 120–130.
- [112] S. A. Al-Ghamdi, H. I. De Lasa, *Fuel* **2014**, *128*, 120–140.
- [113] I. A. Bakare, S. A. Mohamed, S. Al-ghamdi, S. A. Razzak, M. M. Hossain, H. I. De Lasa, *Chem. Eng. J.* **2015**, *278*, 207–216.
- [114] A. H. Elbadawi, M. S. Ba-shammakh, S. Al-ghamdi, S. A. Razzak, M. M. Hossain, *Chem. Eng. J.* **2016**, *284*, 448–457.

- [115] A. A. Ayandiran, I. A. Bakare, H. Binous, S. Al-Ghamdi, S. A. Razzak, M. M. Hossain, *Catal. Sci. Technol.* **2016**, *6*, 5154–5167.
- [116] S. Chen, L. Zeng, R. Mu, C. Xiong, Z. Zhao, C. Zhao, C. Pei, L. Peng, J. Luo, L. Fan, et al., *J. Am. Chem. Soc.* **2019**, *141*, 18653–18657.
- [117] R. B. Dudek, Y. Tian, G. Jin, M. Blivin, F. Li, *Energy Technol.* **2019**, *1900738*, 1–12.
- [118] P. Novotný, S. Yusuf, F. Li, H. H. Lamb, *Catal. Today* **2018**, 1–6.
- [119] P. Novotný, S. Yusuf, F. Li, H. H. Lamb, *J. Chem. Phys.* **2020**, *152*, 044713.
- [120] V. P. Haribal, L. M. Neal, F. Li, *Energy* **2017**, *119*, 1024–1035.
- [121] S. Yusuf, L. M. Neal, F. Li, *ACS Catal.* **2017**, *7*, 5163–5173.
- [122] S. Yusuf, L. Neal, V. Haribal, M. Baldwin, H. H. Lamb, F. Li, *Appl. Catal. B Environ.* **2018**, *232*, 77–85.
- [123] S. Yusuf, L. Neal, Z. Bao, Z. Wu, F. Li, *ACS Catal.* **2019**, *9*, 3174–3186.
- [124] S. Yusuf, V. Haribal, D. Jackson, L. Neal, F. Li, *Appl. Catal. B Environ.* **2019**, *257*, 117885.
- [125] Y. Gao, L. M. Neal, F. Li, *ACS Catal.* **2016**, *6*, 7293–7302.
- [126] Y. Gao, F. Haeri, F. He, F. Li, *ACS Catal.* **2018**, 1757–1766.
- [127] Y. Gao, X. Wang, J. Liu, C. Huang, K. Zhao, Z. Zhao, X. Wang, F. Li, **2020**, 1–10.
- [128] R. B. Dudek, Y. Gao, J. Zhang, F. Li, *AIChE J.* **2018**, *00*, 1–10.
- [129] A. H. Elbadawi, M. Y. Khan, M. R. Quddus, S. A. Razzak, M. M. Hossain, *AIChE J.* **2017**, *63*, 130–138.
- [130] R. B. Dudek, X. Tian, M. Blivin, L. M. Neal, H. Zhao, F. Li, *Appl. Catal. B Environ.* **2019**, *246*, 30–40.
- [131] F. Hao, Y. Gao, L. Neal, R. B. Dudek, W. Li, C. Chung, B. Guan, P. Liu, X. Liu, F. Li, *J.*

- Catal.* **2020**, 385, 213–223.
- [132] Y. Gao, S. Wang, F. Hao, Z. Dai, F. Li, *ACS Sustain. Chem. Eng.* **2020**, DOI 10.1021/acssuschemeng.0c04207.
- [133] V. P. Haribal, Y. Chen, L. Neal, F. Li, *Engineering* **2018**, 4, 714–721.
- [134] T. Imai, *US Patent 4,435,607*, **1984**.
- [135] M. J. O’Hara, T. Imai, J. C. Bricker, D. E. Mackowiak, *U.S. Pat. No. 4565898 Dehydrogenation of Dehydrogenatable Hydrocarbons*, **1986**.
- [136] J. C. Bricker, *US Patent 4,717,779*, **1988**.
- [137] G. B. Woodle, *US Patent 6,858,769*, **2005**.
- [138] J. Shu, B. P. A. Grandjean, A. V. A. N. Neste, S. Kaliaguine, **1991**, 69.
- [139] Z. D. Ziaka, R. G. Minet, T. T. Tsotsis, **1993**, 77, 221–232.
- [140] P. A. Agaskar, *US Patent 5,527,979*, **1996**.
- [141] C. H. Lin, K. C. Lee, B. Z. Wan, *Appl. Catal. A Gen.* **1997**, 164, 59–67.
- [142] R. K. Grasselli, D. L. Stern, J. G. Tsikoyiannis, **1999**, 189, 1–8.
- [143] J. G. Tsikoyiannis, D. L. Stern, R. K. Grasselli, **1999**, 86, 77–86.
- [144] R. K. Grasselli, D. L. Stern, J. G. Tsikoyiannis, *Stud. Surf. Sci. Catal.* **2000**, 130, 773–778.
- [145] L. Låte, J. I. Rundereim, E. A. Blekkan, *Appl. Catal. A Gen.* **2004**, 262, 63–68.
- [146] L. M. van der Zande, E. A. de Graaf, G. Rothenberg, *Adv. Synth. Catal.* **2002**, 344, 884–889.
- [147] G. Rothenberg, E. A. De Graaf, A. Bliet, *Angew. Chemie - Int. Ed.* **2003**, 42, 3366–3368.
- [148] E. A. De Graaf, A. Andreini, E. J. M. Hensen, A. Bliet, *Appl. Catal. A Gen.* **2004**, 262, 201–206.
- [149] E. A. De Graaf, G. Zwanenburg, G. Rothenberg, A. Bliet, *Org. Process Res. Dev.* **2005**,

- 9, 397–403.
- [150] J. H. Blank, J. Beckers, P. F. Collignon, F. Clerc, G. Rothenberg, *Chem. - A Eur. J.* **2007**, *13*, 5121–5128.
- [151] J. H. Blank, J. Beckers, P. F. Collignon, G. Rothenberg, *ChemPhysChem* **2007**, *8*, 2490–2497.
- [152] J. Beckers, F. Clerc, H. Blank, G. Rothenberg, *Adv. Synth. Catal.* **2008**, *350*, 2237–2249.
- [153] J. Beckers, A. F. Lee, G. Rothenberg, *Adv. Synth. Catal.* **2009**, *351*, 1557–1566.
- [154] J. Beckers, G. Rothenberg, *Green Chem.* **2009**, *11*, 1550–1554.
- [155] M. S. C. Chan, H. G. Baldovi, J. S. Dennis, **2018**, 887–897.
- [156] L. Låte, J. Rundereim, E. A. Blekkan, **2004**, *262*, 53–61.
- [157] S. Kaneko, T. Arakawa, M. Ohshima, H. Kurokawa, H. Miura, **2009**, *356*, 80–87.
- [158] Y. Shan, Z. Sui, Y. Zhu, J. Zhou, X. Zhou, D. Chen, *Angew. Chemie Int. Ed. English* **2018**, *130*, 1–6.
- [159] Y. Xie, I. N. Odeh, *WO 2018/025117 A1*, **2018**.
- [160] J. Beckers, R. Drost, I. Van Zandvoort, P. F. Collignon, G. Rothenberg, *ChemPhysChem* **2008**, *9*, 1062–1068.
- [161] C. Brady, B. Murphy, B. Xu, **2017**, *2*, 4–8.
- [162] A. Kumar, K. Song, L. Liu, Y. Han, A. Bhan, *Angew. Chemie - Int. Ed.* **2018**, *57*, 15577–15582.
- [163] N. K. Razdan, A. Kumar, A. Bhan, *J. Catal.* **2019**, *372*, 370–381.
- [164] F. Li, L. M. Neal, Y. Gao, *WO 2018/232133 A1*, **2018**.
- [165] B. W. Goodfellow, M. Sharma, D. F. Yancey, A. Malek, E. E. Stangland, *WO 2020/046898 A1*, **2020**.

- [166] L. Rørmark, A. B. Mørch, K. Wiik, S. Stølen, *Chem. Mater.* **2001**, *13*, 4005–4013.
- [167] E. I. Leonidova, I. A. Leonidov, M. V Patrakeev, V. L. Kozhevnikov, *J. Solid State Electrochem.* **2011**, *15*, 1071–1075.
- [168] T. Negas, R. S. Roth, *J. Solid State Chem.* **1970**, *1*, 409–418.
- [169] R. Kriegel, N. Preuss, *Thermochim. Acta* **1996**, *285*, 91–98.
- [170] C. W. F. T. Pistorius, *J. Chem. Phys.* **1966**, *44*, 4532.
- [171] M. A. Pena, J. L. G. Fierro, *Chem. Rev.* **2001**, *101*, 1981–2017.
- [172] H. Tanaka, M. Misono, **2001**, *5*, 381–387.
- [173] J. Hwang, R. R. Rao, L. Giordano, Y. Katayama, Y. Yu, Y. Shao-horn, *Science (80-.)*. **2017**, *358*, 751–756.
- [174] F. Polo-Garzon, Z. Wu, *J. Mater. Chem. A* **2018**, *6*, 2877–2894.
- [175] A. A. Emery, J. E. Saal, S. Kirklin, V. I. Hegde, C. Wolverton, *Chem. Mater.* **2016**, *28*, 5621–5634.
- [176] J. Vieten, B. Bulfin, F. Call, M. Lange, M. Schmucker, A. Francke, M. Roeb, C. Sattler, *J. Mater. Chem. A* **2016**, *4*, 13652–13659.
- [177] J. Zhu, H. Li, L. Zhong, P. Xiao, X. Xu, X. Yang, Z. Zhao, J. Li, *ACS Catal.* **2014**, *4*, 2917–2940.
- [178] X. Zhu, K. Li, L. Neal, F. Li, *ACS Catal.* **2018**, *8*, 8213–8236.
- [179] J. E. Readman, A. Olafsen, Y. Larring, R. Blom, *J. Mater. Chem.* **2005**, *15*, 1931–1937.
- [180] M. Ryden, A. Lyngfelt, T. Mattisson, D. Chen, A. Holmen, E. Bjørgum, *Int. J. Greenh. Gas Control* **2008**, *2*, 21–36.
- [181] H. Leion, Y. Larring, E. Bakken, R. Bredesen, T. Mattisson, A. Lyngfelt, *Energy & Fuels* **2009**, *23*, 5276–5283.

- [182] M. Rydén, A. Lyngfelt, T. Mattisson, *Int. J. Greenh. Gas Control* **2011**, *5*, 356–366.
- [183] O. Mihai, D. Chen, A. Holmen, *J. Catal.* **2012**, *293*, 175–185.
- [184] F. He, X. Li, K. Zhao, Z. Huang, G. Wei, H. Li, *Fuel* **2013**, *108*, 465–473.
- [185] K. Zhao, F. He, Z. Huang, G. Wei, A. Zheng, H. Li, Z. Zhao, *Appl. Energy* **2016**, *168*, 193–203.
- [186] H. Chang, E. Bjørgum, O. Mihai, J. Yang, H. L. Lein, T. Grande, S. Raaen, Y. Zhu, A. Holmen, D. Chen, *ACS Catal.* **2020**, *10*, 3707–3719.
- [187] Z. Sarshar, S. Kaliaguine, *Ind. Eng. Chem. Res.* **2013**, *52*, 6946–6955.
- [188] L. F. De Diego, A. Abad, A. Cabello, P. Gaya, F. Garc, J. Ada, *Ind. Eng. Chem. Res.* **2014**, *53*, 87–103.
- [189] N. Galinsky, M. Sendi, L. Bowers, F. Li, *Appl. Energy* **2016**, *174*, 80–87.
- [190] A. Shafiefarhood, J. Zhang, L. M. Neal, F. Li, *J. Mater. Chem. A* **2017**, *5*, 11930–11939.
- [191] A. Mishra, A. Shafiefarhood, J. Dou, F. Li, *Catal. Today* **2020**, *350*, 149–155.
- [192] B. Bulfin, J. Vieten, D. E. Starr, A. Azarpira, C. Zachaus, M. Havecker, K. Skorupska, M. Schmucker, M. Roeb, C. Sattler, et al., *J. Mater. Chem. A* **2017**, *5*, 7912–7919.
- [193] J. Vieten, B. Bulfin, M. Senholdt, M. Roeb, C. Sattler, M. Schmücker, *Solid State Ionics* **2017**, *308*, 149–155.
- [194] C. A. Jones, J. J. Leonard, J. A. Sofranko, *J. Catal.* **1987**, *103*, 311–319.
- [195] J. A. Sofranko, J. J. Leonard, C. A. Jones, *J. Catal.* **1987**, *103*, 302–310.
- [196] J. A. Sofranko, J. J. Leonard, C. A. Jones, A. M. Gaffney, H. P. Withers, *Catal. Today* **1988**, *3*, 127–135.
- [197] Z. C. Jiang, C. J. Yu, X. P. Fang, S. B. Li, H. L. Wang, *J. Phys. Chem.* **1993**, *97*, 12870–12875.

- [198] S. Arndt, T. Otremba, U. Simon, M. Yildiz, H. Schubert, R. Schomäcker, *Appl. Catal. A, Gen.* **2012**, 425–426, 53–61.
- [199] Z. Q. Yu, X. M. Yang, J. H. Lunsford, M. P. Rosynek, *J. Catal.* **1995**, 154, 163–173.
- [200] S. Ji, T. Xiao, S. Li, L. Chou, B. Zhang, C. Xu, R. Hou, A. P. E. York, M. L. H. Green, *J. Catal.* **2003**, 220, 47–56.
- [201] S. Hou, Y. Cao, W. Xiong, H. Liu, Y. Kou, *Ind. Eng. Chem. Res.* **2006**, 45, 7077–7083.
- [202] P. Wang, G. Zhao, Y. Wang, Y. Lu, *Sci. Adv.* **2017**, 3, 1–9.
- [203] M. J. Werny, Y. Wang, F. Girgsdies, R. Schlögl, A. Trunschke, *Angew. Chemie Int. Ed.* **2020**, 59, 14921–14926.
- [204] S. Sadjadi, H. R. Godini, S. Arndt, M. Wollgarten, R. Blume, G. Wozny, U. Simon, *Catal. Sci. Technol.* **2015**, 5, 942–952.
- [205] K. Takanebe, A. M. Khan, Y. Tang, L. Nguyen, A. Ziani, B. W. Jacobs, A. M. Elbaz, S. M. Sarathy, F. F. Tao, *Angew. Chemie Int. Ed.* **2017**, 56, 10403–10407.
- [206] C. Luz Lima, G. D. Saraiva, P. T. C. Freire, M. Maczka, W. Paraguassu, F. F. de Sousa, J. Mendes Filho, *J. Raman Spectrosc.* **2011**, 42, 799–802.
- [207] J. Wang, J. L. You, A. A. Sobol, L. M. Lu, M. Wang, J. Wu, X. M. Lv, S. M. Wan, *J. Raman Spectrosc.* **2017**, 48, 298–304.
- [208] J. Xu, Y. Li, J. Wang, H. Bao, J. Wang, C. Zhu, *Adv. Electron. Mater.* **2018**, 4, 1800352.
- [209] S. Yue, Y. Zhang, *J. Mater. Sci. Technol.* **2012**, 28, 569–571.
- [210] X. Li, R. Xie, X. Cao, L. Liu, L. Xu, Y. Wang, C. Meng, Q. Wu, *J. Am. Ceram.* **2018**, 101, 4458–4462.

CHAPTER 2: MANGANESE-CONTAINING REDOX CATALYSTS FOR SELECTIVE HYDROGEN COMBUSTION UNDER A CYCLIC REDOX SCHEME

is an updated print of a manuscript written by R. B. Dudek, Y. Gao, J. Zhang, F. Li, and
published in *AIChE Journal* **2018**, *64* (8), 3141–3150.

The supplementary information is reproduced in Appendix A.

2.1. Abstract

Selective hydrogen combustion (SHC) in the presence of light hydrocarbons was demonstrated with a series of Mn-containing mixed oxide redox catalysts in the context of a chemical looping-oxidative dehydrogenation (CL-ODH) scheme. Unpromoted and 20 wt.% Na_2WO_4 -promoted Mg_6MnO_8 , SrMnO_3 , and CaMnO_3 exhibited varying SHC capabilities at temperatures between 550°C – 850°C . Reduction temperature of unpromoted redox catalysts increased in the order $\text{Mg}_6\text{MnO}_8 < \text{SrMnO}_3 < \text{CaMnO}_3$. Promotion with 20 wt.% Na_2WO_4 resulted in more selective redox catalysts capable of high-temperature SHC. XPS analysis revealed a correlation between suppression of near-surface Mn and SHC selectivity. $\text{Na}_2\text{WO}_4/\text{CaMnO}_3$ showed steady SHC performance (89% H_2 conversion, 88% selectivity) at 850°C over 50 redox cycles. In series with a $\text{Cr}_2\text{O}_3/\text{Al}_2\text{O}_3$ ethane dehydrogenation catalyst, $\text{Na}_2\text{WO}_4/\text{CaMnO}_3$ combusted 84% of H_2 produced while limiting CO_x yield below 2%. The redox catalysts reported can be suitable for SHC in a cyclic redox scheme for the production of light olefins from alkanes.

2.2. Introduction

Cracking and dehydrogenation processes, which convert alkane feedstocks to high-value, unsaturated hydrocarbons, are of significant importance to the chemical industry. These processes are used to produce light olefins such as ethylene and propylene, two essential chemical building blocks with a combined global production of 220 million metric tons in 2012.^[1] The production of polyethylene, ethylene oxide, polypropylene, acrylonitrile, and many other critical industrial intermediates relies on these light olefins as feed chemicals.^[2,3] At present, ethylene and propylene are primarily produced via these energy-intensive processes, consuming approximately 8% of total primary energy use in the chemicals sector.^[1,4] The increased availability of natural gas in recent

years has created an economic incentive to convert ethane and propane into the corresponding alkenes.^[5,6] As an alternative to the endothermic cracking and dehydrogenation processes, oxidative dehydrogenation (ODH) offers excellent potential to reduce primary energy consumption and pollutant emissions (CO₂ and NO_x) from olefin production.^[7]

ODH has been the subject of substantial research since the early 1990s due to its promising characteristics: (i) the ODH reaction is net exothermic and consumes less energy than steam cracking or catalytic dehydrogenation; (ii) the thermodynamic constraints on cracking and dehydrogenation reactions can be mitigated by oxidizing the hydrogen co-product; (iii) the presence of oxygen minimizes coke deposition and subsequent deactivation of the catalyst.^[8–11] In the classical ODH literature, the most well-studied catalyst systems for ethane and propane ODH are those containing vanadium oxide and molybdenum oxide.^[12–16] Platinum-group metals have also received attention for the ODH of various alkanes.^[17,18] Most ODH reactions are operated between 400°C and 700°C and use co-fed gaseous oxygen. Although the ODH scheme provides numerous advantages, the safety concerns with oxygen-hydrocarbon mixing and the cost of O₂ via cryogenic air separation limit its commercial attractiveness. Novel ODH approaches that preserve the advantages of conventional ODH while addressing its limitations are therefore highly desirable.

Chemical looping-oxidative dehydrogenation (CL-ODH) is a process scheme for ODH without the need for gaseous O₂.^[19–22] The CL-ODH scheme consists of two process steps in a cyclic reduction-oxidation (redox) mode (**Figure 2.1**). In the ODH step, the alkane feedstock is converted to alkene and water by lattice oxygen donated from an oxide-based redox catalyst. The subsequent

regeneration step involves re-oxidizing the reduced redox catalyst with air to complete the redox cycle. This regeneration step releases heat, which is stored and transferred by the catalyst particles to satisfy the energetic requirements of the ODH step. Although the overall reaction for CL-ODH is identical to that of conventional ODH (**Figure 2.1**), the use of the metal oxide redox catalyst facilitates the separation of oxygen from air and provides lattice oxygen to the ODH reaction in a controlled manner. CL-ODH eliminates the need for purified O₂ from cryogenic air separation and minimizes explosion hazards from co-feeding oxygen with hydrocarbons. Moreover, the use of lattice oxygen can potentially inhibit non-selective oxidation reactions while reducing energy consumption and CO₂/NO_x emissions.^[7] Due to the critical role of the redox catalyst, its performance (i.e. activity, selectivity, oxygen capacity, and durability) is the key to realizing the aforementioned advantages of CL-ODH.^[23–25]

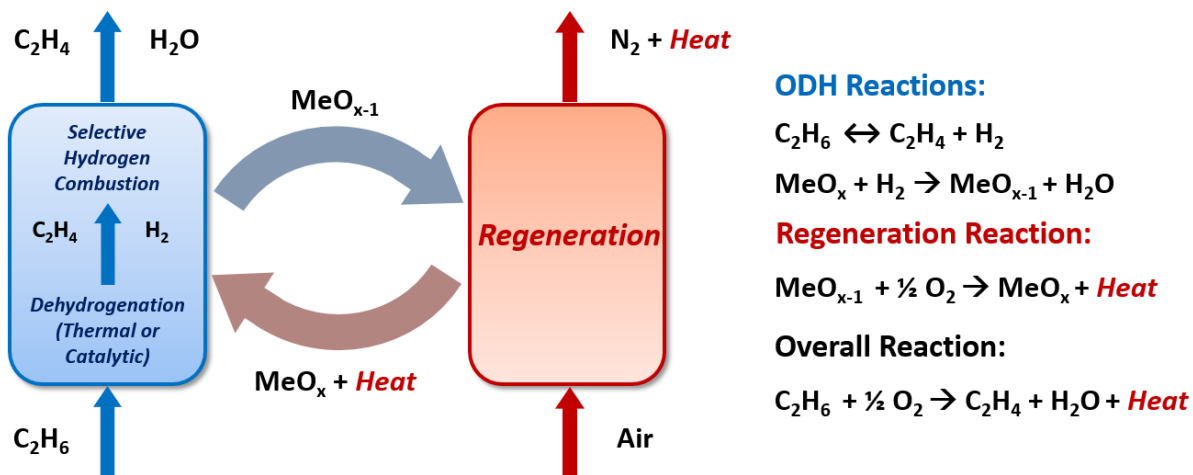


Figure 2.1: A simplified block flow diagram for the chemical looping-oxidative dehydrogenation scheme. In this scheme, the ODH (reduction) step at left is comprised of two reactions. The first reaction is dehydrogenation (DH), proceeding either via gas-phase thermal cracking or by heterogeneous catalysis, and the second reaction is selective hydrogen combustion of the products from the dehydrogenation reaction.

As presented in **Figure 2.1**, the ODH step of the overall CL-ODH process can be implemented by coupling alkane dehydrogenation with selective hydrogen combustion (SHC). This approach to CL-ODH involves the use of the redox catalyst to selectively combust the hydrogen co-product from alkane dehydrogenation (DH); the DH reaction can occur either catalytically via a co-catalyst or through thermal cracking. The redox catalyst is not intended to interact with the fed alkane and should be relatively inert towards hydrocarbons in general, a difference which distinguishes this method from catalytic ODH.^[21,26-29] Combustion of the hydrogen co-product not only provides heat to the endothermic dehydrogenation reaction but also can shift the dehydrogenation equilibrium towards the product side. Early studies of the catalytic DH+SHC approach investigated the use of a Pt-Sn-ZSM-5 dehydrogenation catalyst in the presence of bismuth, indium, and lead oxides or molybdates.^[30-33] Rothenberg et al. further explored SHC by cerium oxides in CL-ODH processes, identifying the importance of SHC to achieving improved olefin yields; in the absence of a DH co-catalyst, these studies relied on simulated ethane DH or propane DH effluent streams containing H₂ and olefins.^[34-40] However, the attractiveness of these SHC materials is hindered by their high cost (cerium, bismuth, and indium oxides), toxicity (lead, molybdenum, and vanadium oxides), and lack of stability under continuous redox cycles. More recently, Yusuf et al. implemented CL-ODH by coupling thermal cracking of ethane with SHC and reported up to 68% ethylene yield with manganese-containing redox catalysts, which was among the highest yields reported in literature.^[22] The use of low-cost and low-toxicity manganese-based redox catalysts is advantageous; however, the reported process relies on high-temperature cracking (800°C and higher) to generate ethylene and hydrogen. High operating temperatures can lead to increased energy consumption and reactor costs as well as challenges in controlling product selectivity due to complex gas-phase reactions. Therefore, extending the SHC

properties of manganese-containing materials into the lower-temperature region can potentially provide greater flexibility in CL-ODH process design, especially in combination with the well-established literature on catalytic dehydrogenation.^[6]

The current study aims to systematically investigate the SHC properties of three Mn-containing mixed oxides. Mn-containing mixed oxides including perovskite structured CaMnO_3 and rock salt structured Mg_6MnO_8 have demonstrated excellent oxygen donation properties for chemical looping.^[20,41,42] Our recent work showed that promoting Mg_6MnO_8 with sodium tungstate (Na_2WO_4) results in enhanced selectivity for hydrogen combustion while inhibiting activation of fed ethane or produced ethylene by the metal oxide.^[20] Here, we further investigate and extend the effect of Na_2WO_4 promotion for SHC properties to other Mn-containing oxides. Importantly, we determine that SHC properties of Mn-containing oxides can be optimized for specific operating temperature ranges in redox ODH by varying the metal oxide substrate and promoter content. As such, the SHC redox catalysts developed in this study can be suitable for CL-ODH under a variety of operating conditions.

2.3. Experimental Section

2.3.1. Redox Catalyst Preparation

Six redox catalysts including unpromoted and 20 wt.% Na_2WO_4 -promoted Mg_6MnO_8 , SrMnO_3 , and CaMnO_3 were prepared. Magnesium manganese oxide (Mg_6MnO_8) was synthesized using a wet impregnation method, and 20 wt.% Na_2WO_4 -promoted Mg_6MnO_8 was further obtained using a second wet impregnation step, both as reported elsewhere.^[22] Strontium manganate (SrMnO_3) and calcium manganate (CaMnO_3) were synthesized via a modified Pechini method.^[43]

Stoichiometric amounts of $\text{Mn}(\text{NO}_3)_2 \cdot 4\text{H}_2\text{O}$ (97.0%, Sigma-Aldrich) and either $\text{Sr}(\text{NO}_3)_2$ (99.0%, Noah) or $\text{Ca}(\text{NO}_3)_2 \cdot 4\text{H}_2\text{O}$ (99.0%, Sigma-Aldrich) were dissolved in deionized water with citric acid (99.5%, Sigma-Aldrich) in a 2.5:1 molar proportion of citric acid to metal ions (Mn^{4+} and either Sr^{2+} or Ca^{2+}). The resulting solution was stirred at 500 rpm and 40°C for 30 min. Next, to aid the formation of a gel, ethylene glycol (99.8%, Sigma-Aldrich) was added to the mixture in a 1.5:1 molar proportion of ethylene glycol to citric acid. The solution was heated to 80°C and stirred at 500 rpm until gel formation, then transferred to an oven and dried overnight at 120°C . Calcination was subsequently conducted in two steps. First, the gel was heated in the muffle furnace to 450°C at $5^\circ\text{C}/\text{min}$ and held for 3 h to burn off nitrates, leaving a uniform metal oxide powder precursor. Second, the powder was calcined in a tube furnace (GSL-15 0X, MTI Corporation) under continuous air flow at 1000°C for 12 h ($3^\circ\text{C}/\text{min}$ ramping rate). The high temperature led to the formation of perovskite oxide phase SrMnO_3 and CaMnO_3 . To synthesize promoted SrMnO_3 or CaMnO_3 , sodium tungstate (Na_2WO_4) was added to the as-obtained perovskite oxide substrates in the amount of 20 w.t.% via wet impregnation as described in the previous paragraph, followed by drying overnight at 80°C . Finally, both $\text{Na}_2\text{WO}_4/\text{SrMnO}_3$ and $\text{Na}_2\text{WO}_4/\text{CaMnO}_3$ were calcined at 900°C . All redox catalysts were ground and sieved into the 250–425 μm range for reaction testing. Powders finer than 250 μm were used for characterization techniques.

2.3.2. Redox Catalyst Characterization

Crystal phases of as-prepared redox catalysts were confirmed via powder X-ray diffraction (XRD) using a Rigaku SmartLab X-ray diffractometer (monochromatic $\text{Cu K}\alpha$ radiation with $\lambda = 0.1542$, operated at 40 kV and 44 mA). XRD patterns were generated over a scanning range of $2\theta = 10$ –

80° with 0.05° step size, holding at each step for 3 s. Phases were matched to reference patterns from the International Center for Diffraction Data (ICDD) database in the HighScore Plus software package. Specific surface areas of redox catalysts were obtained via BET analysis of N₂ physisorption isotherms on a Micromeritics ASAP 2020 instrument at 77 K. All samples were degassed at 200°C under vacuum prior to adsorption measurements.

Near-surface compositional information was obtained using X-ray photoelectron spectroscopy (XPS). For each as-prepared redox catalyst, XPS narrow scans were taken for all metal cations present (Mg 2s, Sr 3d, Ca 2p, Mn 2p, Na 1s, W 4f), along with C 1s and O 1s. Scans were also taken for cycled CaMnO₃ and Na₂WO₄/CaMnO₃. The XPS system used a Thermo-Fisher Alpha 110 hemispherical energy analyzer and XR3 300 W dual-anode X-ray source, and samples were excited using an Al anode (1486.7 eV). Data processing and analysis were performed in the CasaXPS program (Casa Software Ltd., U.K.). All binding energies were calibrated to the adventitious C 1s peak at 284.6 eV, and narrow scans were processed with a 21-point smoothing function. Peak areas for the metal atoms were normalized by their relative sensitivity factors to C 1s in CasaXPS and totaled in order to calculate surface atomic percentages; this calculation was done on a carbon- and oxygen-free basis.

Co-feed H₂/C₂H₄ TPR (temperature-programmed reaction) was used to screen the SHC properties of the redox catalysts. TPR experiments were carried out over 100 mg of redox catalyst loaded in a fixed-bed quartz U-tube reactor; further details on the reactor configuration are given in *Section 2.3.3*. Prior to TPR runs, catalyst samples were heated to 900°C, held there for 30 min, and allowed to cool, all under 10% O₂ in Ar (100 mL/min total). The redox catalysts were then heated from

350°C to 850°C at a ramping rate of 5°C/min under 100 mL/min ($\text{H}_2:\text{C}_2\text{H}_4 = 2.5\%:2.5\%$ v/v in Ar). Products formed during TPR runs were analyzed by a quadrupole mass spectrometer (MKS Cirrus II). H_2O peaks and CO/CO_2 (CO_x) signals were analyzed to quantify oxidation of H_2 and C_2H_4 , respectively; in most cases, CO_x signals were negligible. CO was calculated from mass 28 by subtracting contributions by CO_2 and C_2H_4 using characteristic ratios of 44/28 and 26/28 determined from three-point MS calibrations.

2.3.3. Reaction Testing

To evaluate SHC properties in a simulated CL-ODH setting, isothermal redox cycling experiments were carried out in a fixed-bed quartz microtubular reactor (ID = 1/8 in.) at atmospheric pressure. Quartz wool was placed on either side of a 0.1 g bed of redox catalyst (sized 250–425 μm). Aluminum oxide grit (16 mesh) filled the remaining void space to limit gas volume in the heated zone of the reactor. The reactor tube was secured in a tube furnace a K-type thermocouple and a temperature controller. Inlet gas flow rate and composition were set with a panel of valves and mass flow controllers (MFCs), and the redox cycles were implemented with an automated valve switching program.

Prior to any TPR or redox cycling experiments, samples were pre-treated with six ethane ODH redox cycles, three at 900°C followed by three at 850°C. During the reduction step, 60 mL/min C_2H_6 and 15 mL/min Ar were flowed for 3 min, followed by a 75 mL/min Ar purge for 5 min, then a regeneration step at 75 mL/min Ar and 15 mL/min O_2 for 3 min, and finally another 75 mL/min Ar purge for 5 min. A second type of redox cycle was used to evaluate SHC properties of the redox catalysts by simulating the product composition from ethane dehydrogenation.^[35,36] The

reduction step consisted of 40%:40% H₂:C₂H₄ v/v in Ar at 100 mL/min total. This reducing mixture flowed for 10 s to create a reducing gas volume of 13.3 mL. 17% O₂ v/v in Ar was subsequently flowed at 120 mL/min for 3 min to re-oxidize the sample. Between each step, Ar was flowed for 5 min at 100 mL/min. Using a manual valve switch, effluent gas from the reducing step was flowed into a sample bag for quantitative analysis via GC. At each temperature, two redox cycles were completed first before the effluent was sampled.

Gas chromatography (GC, Agilent Technologies 7890B) was used to analyze the outlet gas from the reactor. A flame ionization detector (FID) channel identified and quantified hydrocarbons, while Ar and He thermal conductivity detectors (TCD) identified H₂ and CO_x gases, respectively. GC signals were calibrated using a refinery-grade gas standard, and volume percentages were calculated by integrating signal peaks. An atomic C balance was used to determine ethylene conversion as well as yields of all observed hydrocarbons; carbon losses to coking were determined to be less than 2% for all cycle experiments. H₂O formation during the reduction step was calculated based on an atomic H balance, which was then used to calculate molar conversion of H₂ and C₂H₄ by combustion reactions, and SHC selectivity, defined as (H₂ conversion) / (H₂ + C₂H₄ conversion). H₂ formed as a byproduct of C₂H₄ combustion was not included in calculating H₂ conversion. All cycles not analyzed with GC were sent downstream to the mass spectrometer (MS) for confirmation of GC results and for quantification of coke formation.

2.4. Results and Discussion

2.4.1. Structure Characterization

All six redox catalysts investigated in this study were characterized via X-ray powder diffraction (XRD) to confirm the presence of expected phases. **Figure 2.2** shows the XRD patterns for the as-prepared samples. Structural matches were obtained for Mg_6MnO_8 (ICDD PDF# 01-074-1903), SrMnO_3 (PDF# 00-024-1213), and CaMnO_3 (PDF# 04-016-1860). Sodium tungstate manifested in a crystalline phase for each material promoted with 20 wt.% Na_2WO_4 (PDF# 04-008-8508). All of the redox catalysts exhibited low surface area ($< 10 \text{ m}^2/\text{g}$) as determined by BET analysis, and Na_2WO_4 promotion further lowered the surface areas (**Table 2.1**).

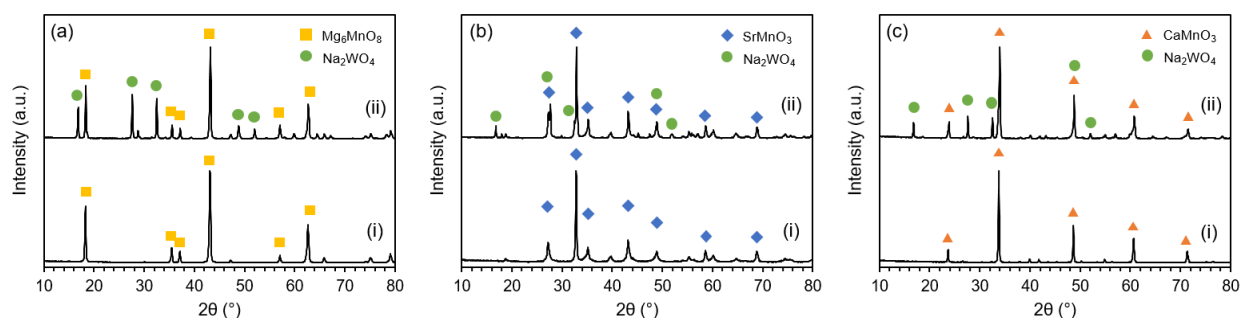


Figure 2.2: XRD patterns for (a) Mg_6MnO_8 (i) and 20 wt.% $\text{Na}_2\text{WO}_4/\text{Mg}_6\text{MnO}_8$ (ii); (b) SrMnO_3 (i) and 20 wt.% $\text{Na}_2\text{WO}_4/\text{SrMnO}_3$ (ii); and (c) CaMnO_3 (i) and 20 wt.% $\text{Na}_2\text{WO}_4/\text{CaMnO}_3$ (ii).

Table 2.1: BET surface areas (S_{BET} , m^2/g) for as-prepared redox catalysts.

Redox Catalyst	S_{BET} (m^2/g)
Mg_6MnO_8	7.3
$\text{Na}_2\text{WO}_4/\text{Mg}_6\text{MnO}_8$	2.7
SrMnO_3	6.8
$\text{Na}_2\text{WO}_4/\text{SrMnO}_3$	3.1
CaMnO_3	2.2
$\text{Na}_2\text{WO}_4/\text{CaMnO}_3$	2.0

2.4.2. Material Screening

The primary function of the redox catalysts is to enhance ethylene or propylene yields from dehydrogenation reactions via selective hydrogen combustion. Throughout this work, ethane to ethylene/H₂ was used as the model reaction. Prior to reactivity testing in a cyclic redox reaction, temperature-programmed reaction (TPR) experiments were conducted to screen the materials and determine temperature ranges at which these materials facilitated SHC.

The reducibility of the redox catalysts is illustrated in **Figure 2.3**. In all cases, reduction of the metal oxide by C₂H₄, which can be quantified by CO_x areas, was found to be insignificant (less than 5% of total peak area, including H₂O). Therefore, only the H₂O signal ($m/z = 18$) is shown here, with complete MS signal data (H₂, C₂H₄, CO, CO₂) relegated to **Figures A1–A6** in *Appendix A*. **Figure 2.3a** shows the oxygen release behavior of the Mg₆MnO₈ system with and without Na₂WO₄. The unpromoted Mg₆MnO₈ was active for H₂ combustion at as low as 550°C. In comparison to the unpromoted sample, Mg₆MnO₈ promoted with 20 wt.% Na₂WO₄ behaved significantly differently, in general agreement with previous literature.^[20] With Na₂WO₄ promotion, Mg₆MnO₈ showed notable hydrogen combustion activity only at 750°C and above. We note that gas phase reactions also became significant at 750°C and above, with C₂H₄ conversion \geq 3%. However, no CO_x formation was observed, a result later supported by isothermal redox cycling at these temperatures.

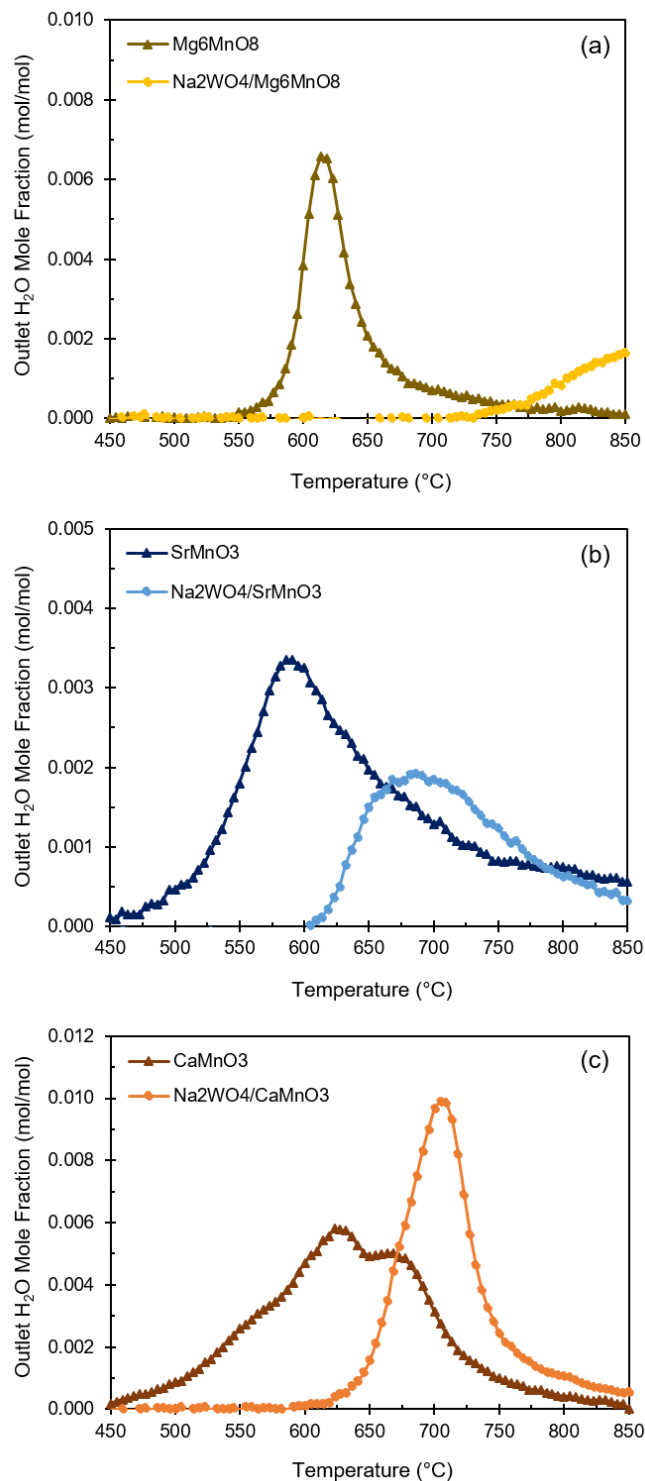


Figure 2.3: H₂O generation based on MS signal ($m/z = 18$) during H₂/C₂H₄ TPR for the three redox catalyst systems: (a) Mg₆MnO₈; (b) SrMnO₃; and (c) CaMnO₃. Conditions: $m = 100$ mg, $F = 100$ ml/min, H₂:C₂H₄ = 2.5%:2.5% v/v in Ar, ramping rate = 5°C/min.

Figure 2.3b shows the reducibility of the SrMnO₃ system. SrMnO₃ became active for H₂ combustion around 450°C, peaking around 590°C, and exhibited slower oxygen release compared to Mg₆MnO₈, apparent from the wider H₂O peak. Upon promotion with Na₂WO₄, the material became less reducible, and H₂O did not appear until 605°C, peaking near 685°C. The presence of Na₂WO₄ had two effects: it increased the initial reduction temperature but leads to a narrower peak at a higher temperature. **Figure 2.3c** demonstrates the effect of Na₂WO₄ on the reduction of the CaMnO₃ system. The bulk material exhibited similar behavior to bulk SrMnO₃, including a wide temperature range for H₂ combustion and a peak appearing around 600°C. However, the H₂O peak had a shoulder extending to 665°C, possibly indicating phase change during the reduction reaction. Promotion CaMnO₃ with Na₂WO₄ altered the H₂ combustion properties significantly; reduction did not occur until 620°C, and the peak for H₂O shifted to 705°C.

Table 2.2 summarizes the peak temperatures for all samples. Addition of Na₂WO₄ increased the initial reduction and peak temperatures for H₂ combustion. The effect of Na₂WO₄ was similar for the two perovskite materials, i.e. addition of Na₂WO₄ increased the peak temperature by 85–95°C. In comparison, Na₂WO₄ suppressed the SHC activity for the rock salt structured Mg₆MnO₈ in a much more significant manner, with a more than 235°C increase in the peak temperature. Moreover, four of the catalysts exhibited sharp reduction peaks with the following order: Mg₆MnO₈ < Na₂WO₄/SrMnO₃ < Na₂WO₄/CaMnO₃ < Na₂WO₄/Mg₆MnO₈. This indicates that the SHC properties of redox catalysts can potentially be adjusted by careful selection of substrate and promoter. The main body of cyclic redox-mode reactivity testing presented in the remainder of this study was designed to validate the possibility of tuning SHC properties (i.e. H₂ conversion and SHC selectivity) for the redox catalysts.

Table 2.2: Reduction onset temperatures (T_o) and peak temperatures (T_p) over redox catalysts as determined by H_2/C_2H_4 TPR.

Redox Catalyst	T_o ($^{\circ}C$)	T_p ($^{\circ}C$)
Mg_6MnO_8	545	615
Na_2WO_4/Mg_6MnO_8	740	> 850
$SrMnO_3$	450	590
$Na_2WO_4/SrMnO_3$	605	685
$CaMnO_3$	435	620; 665
$Na_2WO_4/CaMnO_3$	620	705

2.4.3. Selective Hydrogen Combustion Properties of Redox Catalysts

Cycling at isothermal conditions can better represent typical CL-ODH operating modes. As such, a series of redox experiments was carried out to assess the SHC properties of the six redox catalysts within the temperature range $550^{\circ}C$ to $850^{\circ}C$. This temperature range was selected based on the TPR results shown in **Figure 2.3**. Equimolar H_2 and C_2H_4 was fed to the reactor in 10-second step injections at a flowrate of $100\text{ cm}^3\text{ STP/min}$, as described in *Section 2.3.3*. The reactions included combustion of H_2 to H_2O and combustion of C_2H_4 to CO and CO_2 , though gas phase reactions can occur at high temperatures. Reaction testing results for the six redox catalysts are presented in **Figure 2.4**. Estimated oxygen release or oxygen carrying capacity (in wt.%) from each redox catalyst as a function of temperature, calculated based on material balance across the experiments shown in **Figure 2.4**, are included in **Figures A7–A9** of *Appendix A*.

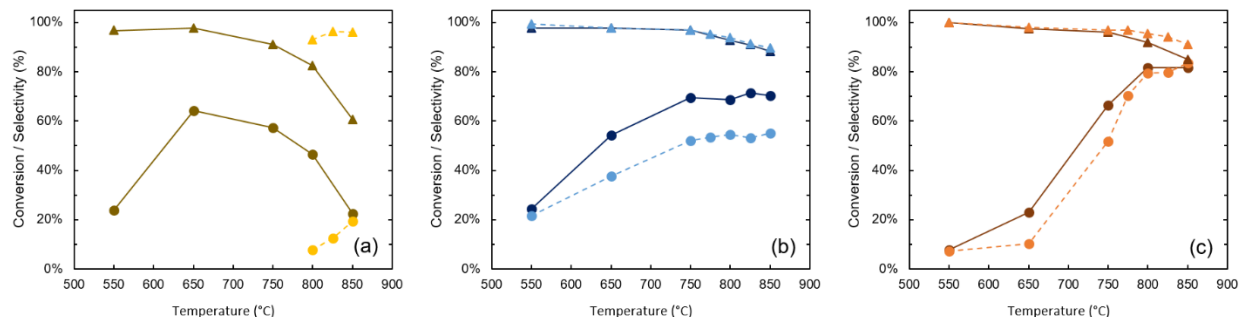


Figure 2.4: Hydrogen conversion (●) and selectivity towards hydrogen combustion (▲) for the unpromoted (—) and Na₂WO₄-promoted (---) redox catalysts: (a) Mg₆MnO₈; (b) SrMnO₃; (c) CaMnO₃. Conversion and selectivity are determined via C and H atomic balances from GC analysis of entire pulse volumes. Conditions: $m = 100 \text{ mg}$, $F = 100 \text{ mL/min}$, $\text{H}_2:\text{C}_2\text{H}_4 = 40\%:40\% \text{ v/v}$ in Ar, pulse duration = 10 s.

Figure 2.4a illustrates the SHC performance of the Mg₆MnO₈ redox catalyst system. As previously observed in the TPR screening experiments, Mg₆MnO₈ activates hydrogen gas beginning around 550°C and exhibits ~20% oxidative conversion of H₂ at 550°C. The peak of H₂ conversion occurs around 650°C, after which the observed oxidation of H₂ begins to decline as a result of decreasing SHC selectivity—the relative rate of hydrogen combustion decreases, while that of ethylene combustion increases. At 850°C, unpromoted Mg₆MnO₈ shows an SHC selectivity of 60%. Addition of sodium tungstate results in a significant change in SHC properties. Na₂WO₄-promoted Mg₆MnO₈ does not exhibit significant activity (i.e. achieve greater than 5% H₂ conversion) until 800°C, in agreement with TPR results, and at 850°C the activity is approximately 20% towards H₂ conversion. This is comparable to the activity of Mg₆MnO₈ at the same temperature, but Na₂WO₄ increases the selectivity to hydrogen combustion by more than 30% to a total SHC selectivity of 96%. This is the highest SHC selectivity of all six materials examined herein at 850°C.

Results from isothermal cycling on the SrMnO₃ redox catalyst system are shown in **Figure 2.4b**. It is apparent that materials based on SrMnO₃ are suitable for selective hydrogen combustion over much of the tested temperature range; both SrMnO₃ and 20 wt.% Na₂WO₄-promoted SrMnO₃ show over 90% SHC selectivity up to 825°C even as the activity towards hydrogen conversion is 50% or greater. Significant and selective activation of hydrogen is seen at 550°C for both materials, and this conversion remains selective at higher temperatures, indicating that SrMnO₃ is an effective redox catalyst for SHC around 700°C. Most notably, a significant difference between the Mg₅MnO₈ system and the SrMnO₃ system is the lack of significant effect of the Na₂WO₄ promoter in the latter material. The increase in SHC selectivity by adding Na₂WO₄ to the base material is countered by a marked decrease (15-20%) in overall H₂ conversion.

Figure 2.4c shows cycling results for the CaMnO₃ system of redox catalysts. Both unpromoted and Na₂WO₄-promoted CaMnO₃ are active in the upper region of the tested temperature range (~700°C and greater). This is in agreement with screening results from TPR experiments in which the H₂ oxidation peaks manifested at an average of 650°C and 700°C for the bulk and promoted sample, respectively. The effect of promotion is more evident for this perovskite than for SrMnO₃ in terms of the selectivity increase. Sodium tungstate impregnation results in an only marginally less active material (the greatest difference in H₂ conversion between materials is approximately 15% at 750°C); however, the Na₂WO₄-promoted sample is much more selective towards hydrogen combustion (SHC selectivity increases by 5% at 850°C with equal H₂ conversion). Generally, the CaMnO₃-based materials are the most suitable for hydrogen combustion out of the materials examined in this study, particularly in terms of oxygen capacity. However, neither the CaMnO₃ nor Na₂WO₄-promoted CaMnO₃ converts as much H₂ as the SrMnO₃ materials at temperatures

below 750°C. At temperatures near 850°C, Na₂WO₄-promoted Mg₆MnO₈ becomes a more desirable material for SHC due to its greater selectivity. Therefore, the utility of Na₂WO₄/CaMnO₃ for SHC lies between these two aforementioned materials, at temperatures from about 750°C to 850°C. Promotion with Na₂WO₄ enables selective H₂ combustion at temperatures slightly higher than bulk CaMnO₃ is capable of (up to 800°C).

Figures 2.4a–c show several trends. Firstly, SHC is facile at low temperatures (650°C), where five of the six materials (excluding Na₂WO₄/Mg₆MnO₈) achieve a molar hydrogen combustion selectivity of 97% or greater. As indicated in the figures, the apparent activation energy for hydrogen combustion is significantly lower than that for ethylene combustion. Secondly, the addition of sodium tungstate via wet impregnation has the consistent effect of suppressing oxygen donation from the redox catalysts, which manifests as (i) higher reduction peak temperatures and active ranges, (ii) decreased activity at identical temperatures compared to unpromoted materials, and (iii) greater selectivity towards hydrogen combustion. This effect is far more pronounced for the Mg₆MnO₈ system. Thirdly, while the selectivity towards hydrogen combustion and the magnitude of the combustion activity are inversely related, high values for H₂ combustion (greater than 70%) may still be realized while maintaining an SHC selectivity of 90% or greater, as evidenced by the Na₂WO₄-promoted CaMnO₃ data. This is beneficial for a cyclic ethane ODH scheme; a previous simulation study on the topic indicated that 71% H₂ combustion by an oxygen carrier was ideal for obtaining high ethylene yields.⁷ This relationship between activity and selectivity is highly dependent on the metal oxide substrate.

It is evident that the three redox catalyst systems in this study can be selective for hydrogen combustion via lattice oxygen donation at varying temperature ranges. Moreover, the addition of sodium tungstate increases the SHC selectivity in all cases. One can therefore envision that SHC materials may be designed via a combination of a metal oxide substrate and an alkali tungstate promoter to meet specific operating temperature ranges of a process application. As an example, an ethane ODH reactor operated at 850°C and a residence time of 0.1 s with 70% ethane conversion would require approximately 71% *in-situ* combustion of H₂ from a process heat balance standpoint.^[7] This corresponds to an H₂ combustion rate of 39.4 mmol H₂ per kg catalyst per second. A similar specific combustion “rate” can be derived from the experimental GC results of this study by calculating a time-averaged combustion rate of H₂, taking into account the feed flowrates and bed mass. **Figure 2.5** thus presents the SHC properties of the six redox catalysts by temperature, using a threshold of 40 mmol H₂/kg-cat·s to represent a useful H₂ combustion activity, along with a selectivity towards SHC of 95% or higher.

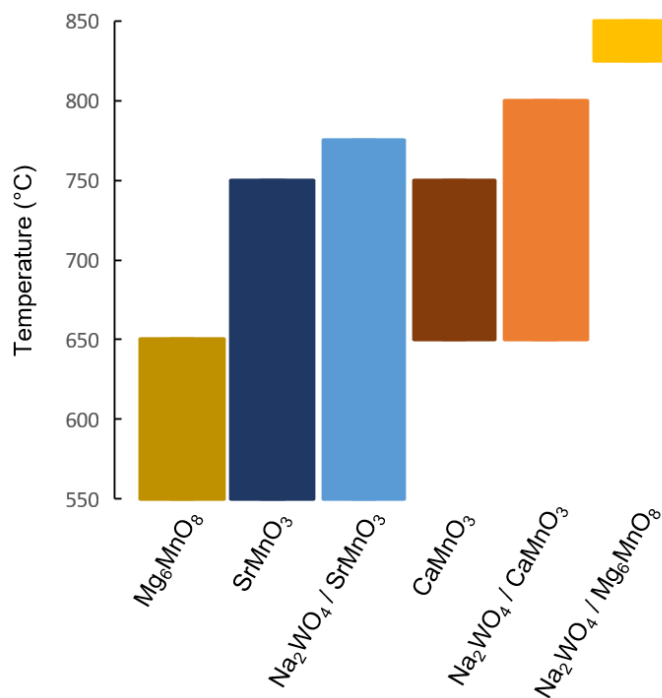


Figure 2.5: Selective hydrogen combustion (SHC) properties of the six redox catalyst materials. Each bar represents the temperature range within which the catalyst provides an H_2 conversion rate of at least 40 mmol $\text{H}_2 / \text{kg-cat}\cdot\text{s}$ (averaged over a 10 s pulse) and at least 95% SHC selectivity. By varying the metal oxide substrate and by promotion with Na_2WO_4 , a wide range of operating temperatures is covered.

Gas hourly space velocity (GHSV, hr^{-1}) is an important process condition to consider. Typical ethane steam cracking units operate at a GHSV range of 1800–8000 hr^{-1} STP.^[2,11] **Figure 2.6** illustrates the effect of changing space velocity with the relatively less active $\text{Na}_2\text{WO}_4/\text{Mg}_6\text{MnO}_8$ redox catalyst (**Figure 2.6a**) and the more active $\text{Na}_2\text{WO}_4/\text{CaMnO}_3$ redox catalyst (**Figure 2.6b**). The change in space velocity results in more moderate levels of hydrogen combustion without any loss in SHC selectivity for either redox catalyst. Interestingly, the decrease in fractional H_2 conversion for $\text{Na}_2\text{WO}_4/\text{CaMnO}_3$ was minimal (less than 10%) even when space velocity and total H_2 volume was increased by 50%, indicating that the material has both a large oxygen capacity

and fast kinetics. Along with operating temperature, gas contact time or feed flowrate requirements should be included in the design parameters for the SHC redox catalysts.

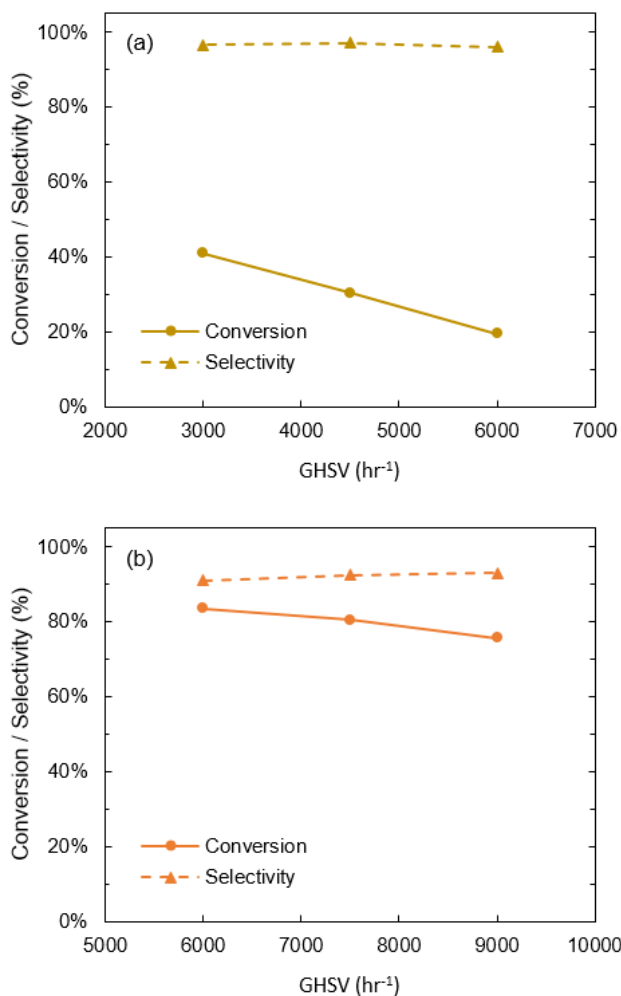


Figure 2.6: Effect of altering gas hourly space velocity (GHSV) through the reactor on molar H₂ conversion and SHC selectivity; **(a)** lower GHSV over Na₂WO₄/Mg₆MnO₈, and; **(b)** higher GHSV over Na₂WO₄/CaMnO₃. GHSV = 6000 hr⁻¹ corresponds to $\tau \approx 0.15$ s. Conditions: m = 100 mg, H₂:C₂H₄ = 40%:40% v/v in Ar, pulse duration = 10 s, T = 850°C.

With the goal of correlating redox catalyst SHC properties to near-surface atomic composition, we obtained X-ray photoelectron spectra (XPS) for each of the six redox catalysts investigated. Near-

surface atomic percentages were calculated using the total of the corrected areas for each metal spectrum. Results of near-surface composition analysis are presented in **Table 2.3**. From the observed atomic percentages, an enrichment or suppression for each metal cation was derived based on the average atomic composition of the bulk material. **Figure 2.7** presents these enrichment (greater than 1) and suppression (less than 1) ratios for the redox catalysts.

Table 2.3: Near-surface atomic percentages of metal cations on fresh and cycled redox catalysts, obtained via XPS (on an oxygen- and carbon-free basis). Dashes indicate no measurement was taken.

Redox Catalyst	Mg 2s (%)	Sr 3d (%)	Ca 2p (%)	Mn 2p (%)	Na 1s (%)	W 4f (%)
Mg ₆ MnO ₈	59.5	--	--	40.5	0.0	0.0
Na ₂ WO ₄ /Mg ₆ MnO ₈	38.8	--	--	18.4	25.0	17.9
SrMnO ₃	--	73.0	--	27.0	0.0	0.0
Na ₂ WO ₄ /SrMnO ₃	--	57.5	--	19.9	12.8	9.7
CaMnO ₃	--	--	67.5	32.5	0.0	0.0
Na ₂ WO ₄ /CaMnO ₃	--	--	42.2	22.6	16.0	19.2

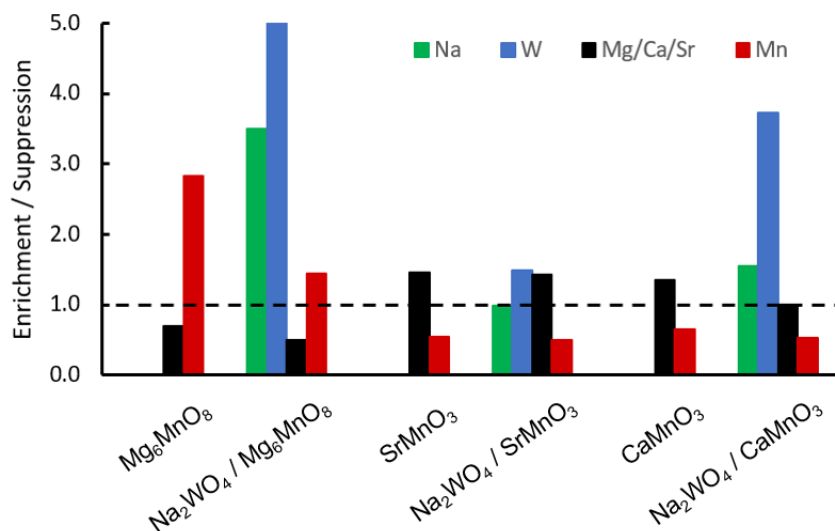


Figure 2.7: Near-surface enrichment (> 1) and suppression (< 1) ratios of metal atoms in as-prepared catalysts, determined via XPS narrow scan analysis. Enrichment and suppression are calculated based on the bulk atomic composition expected from the material stoichiometry.

Atomic percentages and enrichment behavior obtained for the Mg_6MnO_8 system are in good agreement with the XPS results reported by Yusuf et al.^[22] In particular, manganese content in the near-surface of Mg_6MnO_8 is greater than the bulk formulation ratio of Mg/Mn; Mn exhibits an enrichment of 2.84. Upon promotion by Na_2WO_4 , near-surface manganese is suppressed significantly. Moreover, sodium (25.0 at%, 3.50) and tungsten (17.9 at%, 5.01) are present in such quantities as to suggest enrichment of Na_2WO_4 on the surface. These results together with cycling data suggest that this surface enrichment is at least in part responsible for the selectivity of the catalyst towards hydrogen combustion.^[22] To date, the effect of Na_2WO_4 promotion on the near-surface composition of perovskite oxide structures has not been studied. As seen in **Figure 2.7**, the Na (0.98) and W (1.49) near-surface enrichment on promoted SrMnO_3 is only slight, and Mn suppression is also insignificant. In conjunction with reaction data, these results suggest that Na_2WO_4 does not create a radically different near-surface environment from the unpromoted formulation of SrMnO_3 . These surface composition results are consistent with experimental findings that Na_2WO_4 promotion does not significantly change the SHC properties of the SrMnO_3 redox catalyst.

In the CaMnO_3 system, a greater degree of Na and W enrichment (Na = 1.56, W = 3.73) is seen than in the SrMnO_3 system, along with slightly more significant Mn suppression. This correlates with more noticeably altered SHC behavior between the bulk and Na_2WO_4 -promoted samples of this system; promoted CaMnO_3 retains its selectivity towards SHC at higher temperature (~800°C). It can be surmised from these data and from the effects of Na_2WO_4 promotion in the Mg_6MnO_8 system that Na and W enrichment on the material surfaces is related to high-temperature SHC capability. Both Sr and Ca are enriched relative to Mn in the near-surface for their respective

perovskite oxides, regardless of promoter content; this Mn suppression may create a suitable structure for SHC activity by SrMnO₃ and CaMnO₃. Another noteworthy feature of the XPS data is a relative enrichment of W compared to Na in the promoted materials.

2.4.4. Long-Term Stability and Application in Ethane Dehydrogenation

To obtain further understanding of the effects of redox cycles on the SHC-active redox catalysts and particularly on the Na₂WO₄ promoter, the promoted CaMnO₃ redox catalyst was cycled 50 times. A high operating temperature of 850°C was selected to investigate the stability of the redox catalyst. As can be seen in **Figure 2.8**, the SHC properties of the Na₂WO₄/CaMnO₃ redox catalyst were stable, with slight decrease in SHC selectivity and increase in activity over 50 cycles. These results indicate that Na₂WO₄-promoted CaMnO₃ can be suitable for SHC under continuous redox cycles in a CL-ODH scheme.

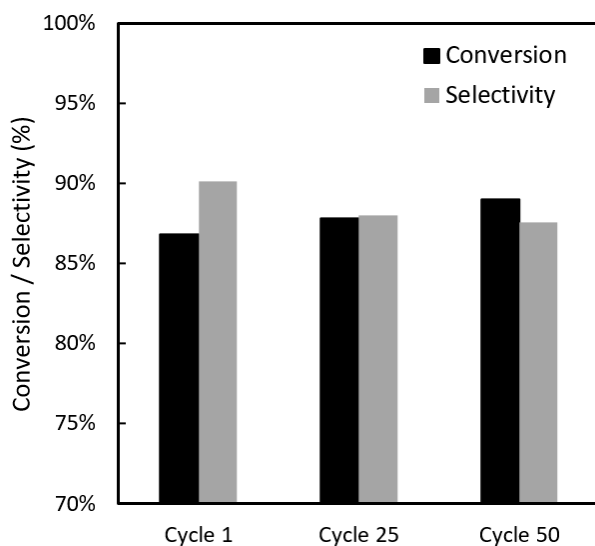


Figure 2.8: Redox cycling stability of the 20 wt.% Na₂WO₄/CaMnO₃ redox catalyst over 50 cycles.

Conversion and selectivity were calculated via C and H atomic balances of GC data. Conditions: m = 100 mg,

F = 100 ml/min, H₂:C₂H₄ = 40%:40% v/v in Ar, pulse duration = 10 s, T = 850°C.

In combination with cracking or dehydrogenation, redox catalysts possessing SHC properties can selectively oxidize the H₂ co-product. In the case of dehydrogenation with selective hydrogen combustion (DH+SHC), the redox catalyst for SHC can be loaded either in series with, or as part of a physical mixture with, a catalytic dehydrogenation catalyst.^[30,31] The latter approach was adopted in this study to demonstrate the SHC properties of 20 wt.% Na₂WO₄/CaMnO₃ in series with Cr₂O₃/Al₂O₃, an ethane dehydrogenation catalyst.

The results of a single-bed ethane dehydrogenation experiment (250 mg Cr₂O₃/Al₂O₃) and a sequential bed DH+SHC experiment (150 mg Cr₂O₃/Al₂O₃ followed by 500 mg Na₂WO₄/CaMnO₃) at 650°C are presented in **Figure 2.9**. Consistent with previous SHC experiments with this redox catalyst, the Na₂WO₄/CaMnO₃ selectively combusted over 84% of the H₂ co-product. CO_x yield was less than 2% and C₂H₄ yield was unchanged from the Cr₂O₃/Al₂O₃ single bed experiment (approximately 45% at 650°C after 30 min). These preliminary results demonstrate that redox catalysts for SHC such as those developed in this study can be combined with catalytic dehydrogenation catalysts to facilitate the selective combustion of hydrogen under a CL-ODH scheme.

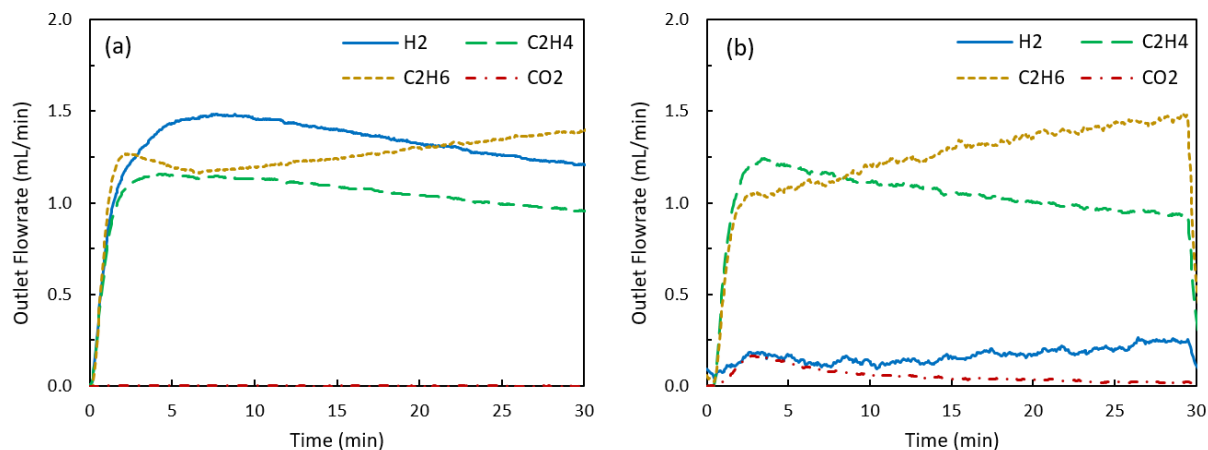


Figure 2.9: Sequential bed results for Cr₂O₃/Al₂O₃ (ethane dehydrogenation) followed by Na₂WO₄/CaMnO₃ redox catalyst (selective hydrogen combustion). **(a)** Results of single Cr₂O₃/Al₂O₃ bed showing ethane dehydrogenation; **(b)** Sequential bed with Na₂WO₄/CaMnO₃. The redox catalyst consumes 84% of H₂ generated by ethane dehydrogenation. Conditions: $m_{EDH} = 250$ mg (a) or 150 mg (b), $m_{SHC} = 500$ mg, $F = 50$ mL/min, 5% C₂H₆ v/v in Ar, $T = 650$ °C.

2.5. Conclusions

Six Mn-containing redox catalysts were investigated and found to exhibit varying selective hydrogen combustion properties across the temperature range of 550°C to 850°C. Generally, H₂ conversion increased and SHC selectivity decreased at higher temperatures. Without a promoter, the base materials were capable of SHC in different temperature ranges, increasing in the order Mg₆MnO₈ < SrMnO₃ < CaMnO₃. Promotion by Na₂WO₄ increased the SHC selectivity of the mixed oxides but suppressed the H₂ combustion activity; this effect was most significant on the Na₂WO₄-promoted Mg₆MnO₈, which was found to be the only redox catalyst suitable for SHC above 800°C. The selectivity enhancement effect of Na₂WO₄ promotion was also significant for the CaMnO₃ redox catalyst. XPS analysis of the redox catalysts indicated that SHC selectivity was inversely related to the surface Mn content. Addition of the Na₂WO₄ promoter led to varying

degrees of Mn suppression near the surface; promoted Mg_6MnO_8 exhibited significant Na and W enrichment which was positively correlated with SHC selectivity results obtained from cyclic reaction testing. Na_2WO_4 -promoted CaMnO_3 showed stable SHC performance over 50 redox cycles. When placed downstream of an ethane dehydrogenation catalyst bed, this redox catalyst is suitable for selective hydrogen combustion with over 84% hydrogen conversion and less than 2% CO_x yield.

2.6. References

- [1] International Energy Agency, *Technology Roadmap: Energy and GHG Reductions in the Chemical Industry via Catalytic Processes*, **2013**.
- [2] H. Zimmermann, R. Walzl, *Ullmann's Encycl. Ind. Chem.* **2012**, 466–529.
- [3] H. Zimmermann, *Ullmann's Encycl. Ind. Chem.* **2014**, 6, 45–66.
- [4] T. Ren, M. Patel, K. Blok, *Energy* **2006**, 31, 425–451.
- [5] M. M. Bhasin, J. H. McCain, B. V. Vora, T. Imai, P. R. Pujadó, *Appl. Catal. A Gen.* **2001**, 221, 397–419.
- [6] J. J. H. B. Sattler, J. Ruiz-Martinez, E. Santillan-Jimenez, B.M. Weckhuysen, *Chem. Rev.* **2014**, 114 (20), 10613–10653.
- [7] V. P. Haribal, L. M. Neal, F. Li, *Energy* **2017**, 119, 1024–1035.
- [8] E.A. Mamedov, V. Cortes-Corberan, *Appl. Catal. A Gen.* **1995**, 127 (1–2), 1–40.
- [9] F. Cavani, F. Trifiro, *Catal. Today* **1995**, 24 (3), 307–313.
- [10] F. Cavani, N. Ballarini, A. Cericola, *Catal. Today* **2007**, 127, 113–131.
- [11] C. A. Gartner, A. C. VanVeen, J. A. Lercher, *ChemCatChem* **2013**, 5, 3196–3217.
- [12] T. Blasco, J. M. Lopez-Nieto, *Appl. Catal. A Gen.* **1997**, 157 (1–2), 117–142.
- [13] D. L. Stern, R. K. Grasselli, *J. Catal.* **1997**, 167, 550–559.
- [14] R. Grabowski, B. Grzybowska, K. Samson, J. Stoczyfiski, J. Stoch, K. Wcisto, *Appl. Catal. A Gen.* **1995**, 125, 129–144.
- [15] K. Chen, A. T. Bell, E. Iglesia, *J. Phys. Chem. B* **2000**, 104 (6), 1292–1299.
- [16] K. Chen, S. Xie, A. T. Bell, E. Iglesia, *J. Catal.* **2000**, 195 (2), 244–252.
- [17] M. Huff, L. D. Schmidt, *J. Phys. Chem.* **1993**, 97 (45), 11815–11822.
- [18] M. Huff, L. D. Schmidt, *J. Catal.* **1994**, 149, 127–141.

- [19] N. Ballarini, F. Cavani, A. Cericola, et al., *Catal. Today* **2004**, 91–92, 99–104.
- [20] L. M. Neal, S. Yusuf, J. A. Sofranko, F. Li, *Energy Technol.* **2016**, 4, 1200–1208.
- [21] Y. Gao, L. M. Neal, F. Li, *ACS Catal.* **2016**, 6, 7293–7302.
- [22] S. Yusuf, L. M. Neal, F. Li, *ACS Catal.* **2017**, 7, 5163–5173.
- [23] F. Li, L. S. Fan, *Energy Environ. Sci.* **2008**, 1 (2), 248.
- [24] L. S. Fan, *Chemical Looping Systems for Fossil Energy Conversions*, **2010**.
- [25] J. Adanez, A. Abad, F. Garcia-Labiano, P. Gayan, L. F. De Diego, *Prog. Energy Combust. Sci.* **2012**, 38 (2), 215–282.
- [26] S. Al-Ghamdi, M. Volpe, M. M. Hossain, H. I. De Lasa, *Appl. Catal. A Gen.* **2013**, 450, 120–130.
- [27] S. Al-Ghamdi, H. I. De Lasa, *Fuel* **2014**, 128, 120–140.
- [28] I. A. Bakare, S. A. Mohamed, S. Al-Ghamdi, S. A. Razzak, M. M. Hossain, H. I. De Lasa, *Chem. Eng. J.* **2015**, 278, 207–216.
- [29] A. H. Elbadawi, M. S. Ba-shammakh, S. Al-ghamdi, S. A. Razzak, M. M. Hossain, *Chem. Eng. J.* **2016**, 284, 448–457.
- [30] R. K. Grasselli, D. L. Stern, J. G. Tsikoyiannis, **1999**, 189, 1–8.
- [31] R. K. Grasselli, D. L. Stern, J. G. Tsikoyiannis, **1999**, 189, 9–14.
- [32] J. G. Tsikoyiannis, D. L. Stern, R. K. Grasselli, **1999**, 86, 77–86.
- [33] L. Låte, J. I. Rundereim, E. A. Blekkan, *Appl. Catal. A Gen.* **2004**, 262, 53–61.
- [34] L. M. van der Zande, E. A. de Graaf, G. Rothenberg, *Adv. Synth. Catal.* **2002**, 344, 884–889.
- [35] G. Rothenberg, E. A. De Graaf, A. Bliet, *Angew. Chemie - Int. Ed.* **2003**, 42, 3366–3368.

- [36] E. A. De Graaf, A. Andreini, E. J. M. Hensen, A. Bliiek, *Appl. Catal. A Gen.* **2004**, 262, 201–206.
- [37] E. A. De Graaf, G. Zwanenburg, G. Rothenberg, A. Bliiek, *Org. Process Res. Dev.* **2005**, 9, 397–403.
- [38] J. Beckers, R. Drost, I. Van Zandvoort, P. F. Collignon, G. Rothenberg, *ChemPhysChem* **2008**, 9, 1062–1068.
- [39] J. H. Blank, J. Beckers, P. F. Collignon, G. Rothenberg, *ChemPhysChem* **2007**, 8, 2490–2497.
- [40] J. H. Blank, J. Beckers, P. F. Collignon, F. Clerc, G. Rothenberg, *Chem. - A Eur. J.* **2007**, 13, 5121–5128.
- [41] T. Mattisson, D. Jing, A. Lyngfelt, M. Ryden, *Fuel* **2016**, 164, 228–236.
- [42] J. A. Sofranko, J. J. Leonard, C. A. Jones, A. M. Gaffney, H. P. Withers, *Catal. Today* **1988**, 3 (2–3), 127–135.
- [43] A. Shafiefarhood, N. Galinsky, Y. Huang, Y. Chen, F. Li, *ChemCatChem* **2014**, 6 (3), 790–799.

**CHAPTER 3: PEROVSKITE OXIDES FOR REDOX OXIDATIVE CRACKING OF N-
HEXANE UNDER A CYCLIC REDOX SCHEME**

is an updated print of a manuscript written by R. B. Dudek, X. Tian, M. Blivin Capstaff, L. M.

Neal, H. Zhao, F. Li, and published in *Appl. Catal. B Env.* **2019**, *246*, 30–40.

The supplementary information is reproduced in Appendix B.

3.1. Abstract

Steam cracking of naphtha is a commercially proven technology for light olefin production and the primary source of ethylene in the Europe and Asia-Pacific markets. However, its significant energy consumption and high CO₂ intensity (up to 2 tons CO₂/ton C₂H₄), stemming from endothermic cracking reactions and complex product separations, make this state-of-the-art process increasingly undesirable from an environmental standpoint. We propose a redox oxidative cracking (ROC) approach as an alternative pathway for naphtha conversion. Enabled by perovskite oxide-based redox catalysts, the ROC process converts naphtha (represented by *n*-hexane) in an auto-thermal, cyclic redox mode. The addition of 20 wt.% Na₂WO₄ to SrMnO₃ and CaMnO₃ created highly selective redox catalysts capable of achieving enhanced olefin yields from *n*-hexane oxy-cracking. This was largely attributed to the redox catalysts' high activity, selectivity, and stability towards selective hydrogen combustion (SHC) under a redox mode. Na₂WO₄/CaMnO₃ demonstrated significantly higher olefin yield (55–58%) when compared to that from thermal cracking (34%) at 725°C and 4500 h⁻¹. CO_x yield as low as 1.7% was achieved along with complete combustion of H₂ over 25 cycles. Similarly, Na₂WO₄/SrMnO₃ achieved 41% olefin yield, 0.4% CO_x yield, and 73% H₂ combustion at this condition. Oxygen-temperature-programmed desorption (O₂-TPD) indicated that Na₂WO₄ hindered gaseous oxygen release from CaMnO₃. Low-energy ion scattering (LEIS) and X-ray photoelectron spectroscopy (XPS) revealed an outermost perovskite surface layer covered by Na₂WO₄, which suppressed near-surface Mn and alkaline earth metal cations. The formation of non-selective surface oxygen species was also inhibited. XPS analysis further confirmed that promotion of SrMnO₃ with Na₂WO₄ suppressed surface Sr species by 90%, with a similar effect also observed on CaMnO₃. These findings point to the promoting

effect of Na_2WO_4 and the potential of promoted SrMnO_3 and CaMnO_3 as selective redox catalysts for efficient production of light olefins from naphtha via the ROC process.

3.2. Introduction

Ethylene is a critical building block in the chemical industry, with a worldwide market totaling 148 million tonnes in 2014.^[1,2] Steam cracking of hydrocarbon feedstocks (ethane, naphtha, *etc.*) is the leading technology for ethylene production, but it is also one of the most energy- and CO_2 -intensive processes in the chemical industry; in 2010, 1.9 exajoules of energy were consumed and 120 Mt CO_2 -eq emitted solely as a result of ethylene production via steam cracking.^[3,4] With the global ethylene market projected to grow by as much as 400% by 2050, new process technologies are needed to maintain this growth while reducing the environmental impacts of ethylene production.^[5]

In Europe and the Asia-Pacific region, steam cracking of full-range naphtha (boiling point range of 35–180°C) is the primary source of ethylene production; worldwide, naphtha constitutes 55% of all steam cracking feedstocks.^[1,3] In a typical naphtha steam cracking process, naphtha is vaporized and pre-heated in the convective zone of the furnace and mixed with diluting steam (0.4–0.5 kg/kg feed) before entering the radiant tube (750–900°C) and cracking into smaller molecules via free-radical reactions.^[1,3,6] A subsequent quenching step preserves the light olefins formed. Steam cracking requires significant heat for steam generation, naphtha vaporization, and the endothermic cracking reactions. This heat requirement is met by combusting carbonaceous fuels such as fuel oil and/or natural gas, resulting in significant energy usage and up to 2 ton CO_2 / ton ethylene produced.^[3,7] Aside from heat supplied for cracking, the wide range of gaseous

products generated through steam cracking necessitates an extensive separation train which consumes additional energy. Novel approaches that can reduce the energy- and CO₂-intensity for light olefin production from naphtha are highly desirable.

While catalytic cracking in the presence of heterogeneous catalysts (*e.g.* zeolites) can decrease the temperature of the cracking reactions, the heat requirements associated with naphtha vaporization and pyrolysis are still present.^[8,9] To balance these heat requirements, multiple process alternatives have been proposed in recent years. Liu et al. proposed a gas phase oxidative cracking process which gave 50% yield of light alkenes from *n*-hexane (as a model compound for naphtha) in the presence of gaseous oxygen at 750°C, but combustion reactions led to 12-13% CO_x yield.^[10,11] Boyadjian et al. used Li/MgO catalysts in combination with gaseous O₂ in a catalytic oxidative cracking process to achieve 17% light olefin yield from *n*-hexane at 575°C; the corresponding CO_x yield was 7%.^[12] In a subsequent process analysis, feedstock loss to CO_x was shown to significantly harm the process economics.^[13] In both studies, co-feeding of gaseous oxygen with hydrocarbons introduces an inherent flammability hazard and reduces olefin yields. Oxygen production via cryogenic air separation is also energy- and capital-intensive.

Chemical looping provides a strategy for separating oxidative processes into two-step, cyclic redox processes in spatially separate reactors to mitigate the challenges related to oxygen co-feed.^[14,15] In this study, we demonstrate a redox oxidative cracking (ROC) concept for naphtha conversion in absence of O₂.^[7] In the ROC process, as illustrated in **Figure 3.1**, vaporized naphtha is cracked at temperatures above 500°C to form light olefins and hydrogen.^[7,16] The resulting hydrogen is selectively combusted by the lattice oxygen of a metal oxide redox catalyst to form water.^[7] The

reduced redox catalyst is then re-oxidized with air in a separate regeneration reactor, completing the redox cycle. In a study by Elbadawi et al., lattice oxygen from $\text{VO}_x/\text{Ce-Al}_2\text{O}_3$ was used to drive a combined *n*-hexane cracking and oxidative dehydrogenation (ODH) reaction between 525°C and 600°C in an oxidative cracker, with a separate regenerator reactor restoring the lattice oxygen. While this redox catalyst showed stable behavior over many redox cycles at 550°C, the olefin selectivity (60%) and hexane conversion (30%) were relatively limited.^[16] In contrast, we recently showed that ROC of naphtha with a manganese-containing redox catalyst has the potential to reduce thermal energy demand by 52% and CO_2 emissions by over 50% in comparison to steam cracking while slightly improving light olefin yields.^[7,17] Given the importance of redox catalysts to the overall performance of ROC, further development and optimization of redox catalysts is highly desirable.

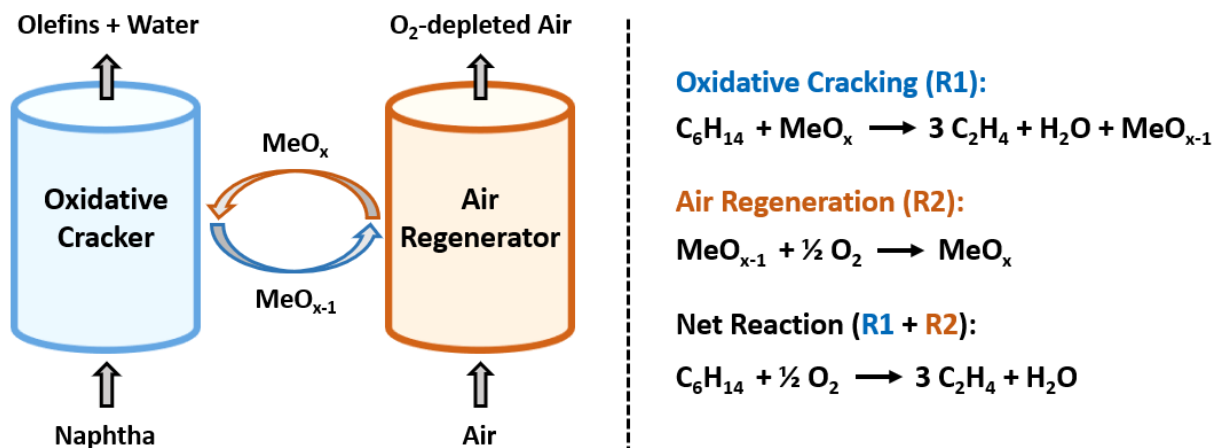


Figure 3.1. A block flow diagram for the redox oxidative cracking (ROC) of naphtha concept, using the simplified net reaction $\text{C}_6\text{H}_{14} \rightarrow 3 \text{C}_2\text{H}_4 + \text{H}_2$ to represent thermal cracking of naphtha with *n*-hexane as a model compound. MeO_x represents a fully oxidized perovskite-type mixed metal oxide while MeO_{x-1} indicates lattice oxygen has been donated.

Our recent studies on chemical looping-oxidative dehydrogenation (CL-ODH) of ethane indicate that manganese-based redox catalysts capable of selective hydrogen combustion (SHC) can enhance olefin yields from ethane cracking by 25% at 850°C.^[18,19] In addition to increasing yields, combustion of the hydrogen co-product in CL-ODH enabled auto-thermal operation of the ethane cracking reactor.^[20] While a similar strategy can be applied for naphtha cracking, lower operating temperatures are required than those for ethane cracking. Recently, we identified a promising set of Mn-containing perovskite oxides capable of performing SHC in the presence of ethylene across a wide range of temperatures. With demonstrably high selectivity and activity values in the range from 650°C to 800°C, SrMnO₃- and CaMnO₃-based redox catalysts are potentially suitable for the ROC of naphtha.^[21]

In this work, we investigated the merits of perovskite oxides applied in the redox oxidative cracking of *n*-hexane as a model compound for naphtha. Strontium manganate (SrMnO₃) and calcium manganate (CaMnO₃) were synthesized both in as-prepared forms and with sodium tungstate promotion (20 wt.% Na₂WO₄). The performance of these redox catalysts was explored across a range of temperatures and gas flowrates. Na₂WO₄-promoted SrMnO₃ and CaMnO₃ were capable of achieving olefin yields in excess of the thermal background (*e.g.* 57% vs. 41% olefin yield at 750°C) while maintaining low CO_x yields (4% at 750°C) and combusting most of the H₂ produced during cracking (83%). Characterization including O₂-TPD, XPS, LEIS, and XRD were used to study interactions between each perovskite oxide and the Na₂WO₄ dopant and correlate the structure and near-surface composition with reaction performance. Furthermore, Na₂WO₄/SrMnO₃ and Na₂WO₄/CaMnO₃ were evaluated in terms of their cycling stability and long-term performance for ROC of *n*-hexane under a cyclic redox scheme.

3.3. Experimental Section

3.3.1. Synthesis of Redox Catalysts

SrMnO₃ (strontium manganate) and CaMnO₃ (calcium manganate) were prepared via a modified Pechini method described elsewhere.^[21] Briefly, stoichiometric amounts of Mn(NO₃)₂·4H₂O (97.0%, Sigma-Aldrich) and either Sr(NO₃)₂ (99.0%, Noah) or Ca(NO₃)₂·4H₂O (99.0%, Sigma-Aldrich) were dissolved in deionized water and stirred at 40°C. Citric acid (99.5%, Sigma-Aldrich) was then added into the solution at a molar ratio of 2.5:1 to metal ions (Mn²⁺ and either Sr²⁺ or Ca²⁺). The solution was kept stirring at 500 rpm and 40°C for 30 min. Afterwards, ethylene glycol (99.8%, Sigma-Aldrich) in a molar ratio of 1.5:1 to citric acid was introduced to the mixture to promote gel formation. The solution was heated to 80°C with continuous stirring until a viscous gel formed, then dried overnight at 100°C in an oven. The dried precursor was first pre-treated in a muffle furnace at 450°C for 3 h to burn off nitrates, and then calcined in a tube furnace (GSL-15 0X, MTI Corporation) at 1000°C for 12 h under continuous air flow. The high temperature sintering contributed to the formation of SrMnO₃ and CaMnO₃ perovskite oxides.

Promotion of the as-obtained SrMnO₃ and CaMnO₃ materials with 20 wt.% Na₂WO₄ was done by wet impregnation. Calculated amount of Na₂WO₄·2H₂O (99.0%, Sigma-Aldrich) was mixed with deionized water and added dropwise to the base perovskite oxides. After being stirred every 15 min until dry, it was kept overnight at 80°C in an oven. Finally, the promoted samples, namely Na₂WO₄/SrMnO₃ and Na₂WO₄/CaMnO₃, were calcined again at 900°C for 6 h. All catalysts were ground and sieved into the size range of 250-850 μm for reaction testing. Powders smaller than 250 μm were used for characterization.

3.3.2. Characterization of Redox Catalysts

Powder X-ray diffraction (XRD) experiments were conducted to determine the crystal phase of both the as-prepared and cycled redox catalysts, using a Rigaku SmartLab X-ray diffractometer. The radiation source was monochromatic Cu K α with $\lambda = 0.1542$ nm, operated at 40 kV and 44 mA. A continuous scan method within a 2θ range of 10-80° was adopted to generate XRD patterns, with a step size of 0.05° and holding at each step for 3 s. The crystal phases were determined using the International Center for Diffraction Data (ICDD) database in HighScore Plus software.

X-ray photoelectron spectroscopy (XPS) was adopted for near-surface composition analysis of the fresh and cycled redox catalysts. The XPS system consisted of a Thermo-Fisher Alpha 110 hemispherical energy analyzer, a Thermo-Fisher XR3 and 300 W dual-anode X-ray source, with Al anode (1486.7 eV) as the excitation source. For each catalyst, XPS narrow scans were taken for all metal cations present (Sr 3*d*, Ca 2*p*, Mn 2*p* and 3*s*, Na 1*s*, W 4*f*), along with C 1*s* and O 1*s*. XPS patterns were analyzed by the CasaXPS program (Casa Software Ltd., U.K.). An adventitious C 1*s* peak at 284.6 eV was used for calibration of all binding energies.

Low-energy ion scattering (LEIS) was conducted at the Surface Analysis Center at Lehigh University on an ION-TOF Qtac¹⁰⁰ spectrometer to obtain surface compositional information. A 3 keV He⁺ (2×10^{14} ions cm⁻², 1.0 x 1.0 mm raster) primary ion beam was used at 3000 eV pass energy, while a 0.5 keV Ar⁺ sputtering source (0.5 or 1.0×10^{15} cm⁻² cyc⁻¹, 2.0 x 2.0 mm or 1.5 x 1.5 mm raster) was used at 30° angle to the sample surface for depth profiling; during spectra acquisition and sputtering, charge neutralization was invoked. Prior to analysis, sample powders were dispersed into a sample holder and compressed by 2000 psi.

To investigate the reducibility of the catalysts as well as the onset temperature of reaction, *n*-hexane temperature-programmed reaction (TPR) experiments of the four as-prepared catalysts were carried out using a 1/8 in. ID fixed-bed quartz U-tube reactor. Heat was provided to the reactor externally by a tube furnace equipped with a K-type thermocouple. In each run, 0.5 g of catalyst (250–850 μm) was loaded into the reactor. For comparison, a blank *n*-hexane TPR with inert Al_2O_3 (16 mesh) was also conducted. Prior to TPR tests, the samples were first pre-treated at 900°C in 10 vol.% O_2 (balance Ar, with a total flowrate of 100 mL/min) for 30 min to fully oxidize and clean the surface of the catalyst. After cooling down to room temperature, the catalyst samples were then heated from 450°C to 750°C at 5°C/min under ~13 vol.% *n*-hexane flow. 75 mL/min Ar carrier gas (a relatively low flowrate as compared to later tests) was used in order to amplify product signals on the mass spectrometer. Gas products generated in the reaction were analyzed by an MKS Cirrus II mass spectrometer, and volumetric flowrates of several primary gases (H_2 , C_2H_4 , CO_2 , C_6H_{14}) were calculated using three-point calibrations ($m/z = 2, 26, 44, \text{ and } 57$, respectively; $m/z = 26$ from ethylene was deconvoluted from ethane and *n*-hexane).

Oxygen and carbon dioxide temperature-programmed desorption experiments (O_2 -TPD and CO_2 -TPD) were performed on a SETARAM Setsys Evolution Thermal Gravimetric Analyzer (TGA-DTA/DSC) using redox catalyst samples in the particle size range 150–250 μm . In a typical O_2 -TPD experiment, 40–60 mg of catalyst was cycled three times between 10% H_2 / 10% O_2 using a carrier gas flow of 180 mL/min He at 750°C. The sample was then maintained under 10% O_2 , ramped to 900°C at 20°C/min, held at 900°C for 30 min, and cooled to 150°C at 10°C/min. After purging for 1 h in He, the sample was ramped to 900°C at 5°C/min and mass loss was recorded. For CO_2 -TPD experiments, 40–50 mg redox catalyst was heated to 900°C at 20°C/min under 10%

CO₂ (with 180 mL/min He) and held there for 30 min, then cooled to 150°C at 10°C/min. The sample was then purged in He for 1 h and ramped to 900°C at 5°C/min.

3.3.3. *n*-Hexane Oxidative Cracking Test Conditions

Oxidative cracking experiments with *n*-hexane were conducted in a 1/8 in. ID fixed-bed quartz U-tube reactor heated externally by a furnace controlled with a K-type thermocouple. Cycling between reduction and oxidation steps were achieved using an automated valve switching system. Each experiment used 0.5 g (approximately 1 mL volume) of redox catalyst sized 250-850 μm, with 16 mesh Al₂O₃ grit loaded into the remaining void space on either side of the fixed bed to limit the gas volume in the heated zone. For quantification of thermal background conversion and yields, the redox catalyst was replaced with Al₂O₃ grit at the same testing conditions.

Prior to *n*-hexane oxy-cracking tests, samples were pre-treated at 750°C with five redox cycles comprising a 3 min reduction step of 80 vol.% ethane/Ar (total flowrate of 75 mL/min) and a 3 min oxidation step of 17 vol.% O₂/Ar (total flowrate of 90 mL/min) to achieve stabilized redox characteristics. During a typical *n*-hexane cracking experiment, up to 6 different temperature conditions (650-775°C, 25°C increments) were evaluated at a constant gas hourly space velocity, GHSV = 9000 h⁻¹. A lowered GHSV = 4500 h⁻¹ was also used during redox catalyst stability experiments to achieve deeper reduction and greater redox stress, conditions which are more likely to expose stability or coke resistance issues. Vapor-phase *n*-hexane was introduced into the reactor by flowing the inlet Ar stream into a stainless steel bubbler containing liquid *n*-hexane maintained at 20°C. Condensation of liquid *n*-hexane was avoided throughout the procedure by saturating the Ar stream at several degrees below room temperature and by diluting the saturated stream (y_{hexane}

= 0.159) with pure Ar in a 4:1 ratio prior to the reactor, resulting in a final *n*-hexane concentration of $y_{\text{hexane}} = 0.127$, below the saturation limit at 23°C. In a typical test at GHSV = 9000 h⁻¹, 120 mL/min Ar was introduced into the bubbler to generate saturated *n*-hexane/Ar flow and another 30 mL/min Ar was added before entering the U-tube reactor for 20 s reaction duration. During the oxidation step, 150 mL/min Ar + 30 mL/min O₂ (resulting in 16.7 vol.% O₂) was used to regenerate the reduced catalyst for 3 min. A five-minute purge step with 150 mL/min Ar was introduced before and after each reduction step. For each condition, four redox cycles were conducted and the effluent gas from the third reduction step was collected in a sample gas bag for gas chromatography. Furthermore, to verify the stable cyclic redox characteristics of the two promoted samples, longer-term experiments with 25 redox cycles were conducted at 4500 h⁻¹ GHSV and 725°C. To ensure a constant volume of *n*-hexane injection at 4500 h⁻¹ compared to 9000 h⁻¹, the injection time was doubled.

A gas chromatograph (GC, Agilent Technologies 7890B), with a flame ionization detector (FID) channel for hydrocarbon analysis and two thermal conductivity detector (TCD) channels for H₂ (Ar/TCD channel) and CO_x (He/TCD channel) identification, was used to analyze the outlet gas (collected by a gas sampling bag) during the reduction step. Before measurements, a refinery-grade gas calibration standard was used to calibrate the GC signals. The volume percentage of different gas species was calculated by integrating the signal peak. The conversion of *n*-hexane and selectivity to all carbonaceous products were calculated on a molar carbon basis. H₂O formation was calculated on the basis of atomic H balance of all observed products. The whole product distribution was used to calculate the approximate oxygen donation (in wt.%) by the redox catalyst at each condition via the method given in *Appendix B*. All cycles not analyzed via GC were

measured by the MKS Cirrus II mass spectrometer and used to quantify coke (i.e. CO_x upon regeneration) as well as to verify GC results.

3.4. Results and Discussion

3.4.1. Perovskites as Redox Catalysts

Ethylene is the major hydrocarbon species produced from the *n*-hexane cracking reaction, while hydrogen is a byproduct that can be selectively combusted to provide the energy for the endothermic cracking reaction. Our previous work has demonstrated the effectiveness of SrMnO₃ and CaMnO₃ as oxygen donors capable of selective H₂ combustion (SHC) in the presence of ethylene and hydrogen.^[21] Therefore, these redox catalysts are investigated here for ROC applications. Na₂WO₄ was selected as a “promoter” since it was shown to be effective for inhibiting undesired CO_x formation in ODH and SHC reactions.^[18,19,21,22] Unlike conventional heterogenous catalysts, an important function of the redox catalyst is to carry and donate its active lattice oxygen in the oxidative cracking reaction. As such, oxygen storage capacities of both the unpromoted and Na₂WO₄-promoted perovskite redox catalysts were determined first. The oxygen storage capacity of redox catalysts is independent of specific surface area; values for the latter are given in supplementary **Table B1**.

Figure 3.2 shows the oxygen donation achieved by four redox catalysts during 10-second step experiments in the presence of a H₂/C₂H₄ mixture. As can be seen, oxygen carrying capacities of Na₂WO₄-promoted redox catalysts are lower than their unpromoted counterparts. Nevertheless, all four redox catalysts exhibited satisfactory oxygen capacity within the temperature range of interest. Moreover, the lattice oxygen of redox catalysts employed in partial oxidation processes

such as ROC can be utilized more effectively compared to complete combustion processes, e.g. chemical looping combustion (CLC). For instance, CLC of *n*-hexane would consume up to 19 times more lattice oxygen than *n*-hexane ROC (see *Appendix B*). Therefore, the oxygen capacities demonstrated by the four redox catalysts become potentially more attractive when lattice oxygen utilization in ROC is considered.

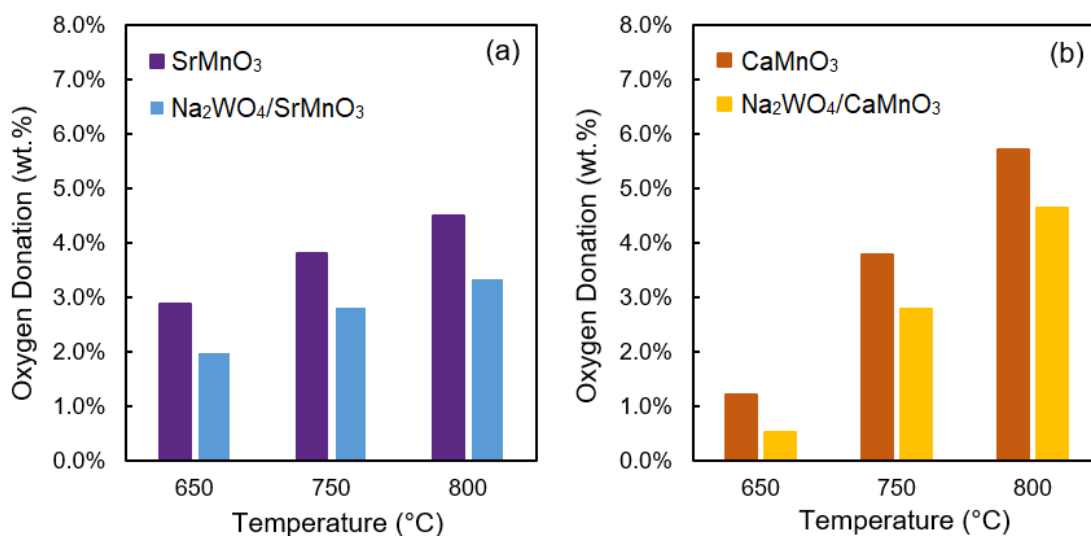


Figure 3.2. Oxygen donation by (a) SrMnO₃, Na₂WO₄/SrMnO₃, and (b) CaMnO₃, Na₂WO₄/CaMnO₃, as determined by material balance on H₂/C₂H₄ co-feed experiments in a U-tube reactor. Conditions: F = 100 mL/min, y_{H₂}/y_{C₂H₄}/y_{Ar} = 0.4/0.4/0.2, m = 100 mg, step duration = 10 s.

3.4.2. Olefin Yield Comparisons

Accurate evaluation of the role of catalysts, including redox catalysts, for ODH and oxy-cracking reactions can be affected by potential contributions from thermal cracking, especially at higher operating temperatures. While redox catalysts can significantly enhance single-pass olefin yield through SHC even if they are largely inactive for C-H bond activation,^[18,19] catalytic activity for alkane activation is nevertheless desirable for redox catalysts due to the possibility of lowering the

operating temperature and/or residence time.^[23,24] We employed a combination of temperature-programmed and isothermal experiments to establish that SrMnO₃- and CaMnO₃-based redox catalysts are capable of generating ethylene yields in excess of the thermal background in an *n*-hexane cracking setting. Temperature-programmed reaction (TPR) experiments were first conducted to assess the activity and reducibility of four redox catalysts under *n*-hexane flow in comparison to a thermal background TPR over inert alumina grit. The results of the five *n*-hexane TPR experiments are shown in **Figure 3.3** in the form of ethylene product flow, incremental ethylene flow over the background, and incremental CO₂ product flow over the background.

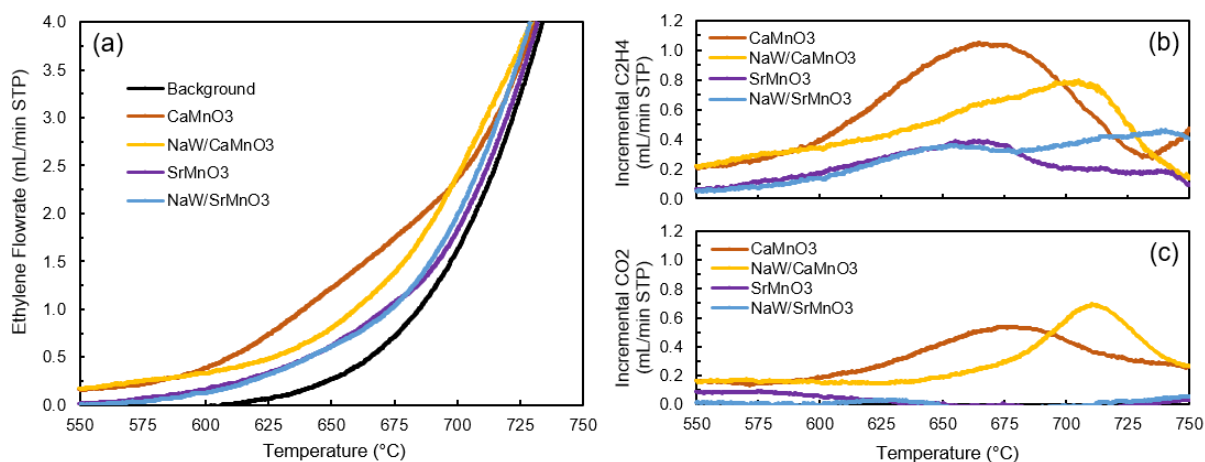


Figure 3.3. Results from *n*-hexane TPR on four redox catalysts and accompanying thermal background, showing in STP mL/min (a) ethylene product flowrate, (b) incremental ethylene flowrate over the background, and (c) incremental CO₂ product flowrate over the background CO₂ (equal to zero). Ethylene production above the thermal background indicates *n*-hexane activation by the redox catalyst, while CO₂ production indicates undesired side reactions. Results were obtained via mass spectrometry. Conditions: GHSV = 4500 h⁻¹ (F_{Ar} = 75 mL/min, m = 500 mg), y_{*n*-hexane} ≈ 0.13, ramping rate of 5°C/min.

Figure 3.3a–b indicates that each of the four redox catalysts initiates ethylene formation at a lower temperature compared to *n*-hexane thermal cracking. *n*-Hexane reacts on the redox catalysts to produce ethylene at temperatures as low as 600°C, and the ethylene yield improvement over the background is the most significant around 650°C; for CaMnO₃ vs. thermal background, this difference is 1.2 mL/min C₂H₄ vs. 0.3 mL/min C₂H₄, or 4 C% yield towards C₂H₄ vs. 1 C% C₂H₄ yield. Thermal cracking of *n*-hexane to its products becomes dominant over surface-initiated reactions (*i.e.* over a redox catalyst) at temperatures of 700°C and above.

Formation of CO_x is important in identifying the selectivity of redox catalysts towards hydrogen combustion (*i.e.* SHC) relative to oxidation of hydrocarbons (*n*-hexane fed, C₂H₄ produced, *etc.*). Loss via non-selective combustion would lead to CO_x formation and hence decrease the selectivity of desired olefin products. Generally, CO yields were insignificant compared to those of CO₂ in both TPR and isothermal experiments. **Figure 3.3c** shows that in the case of the CaMnO₃ redox catalyst, lower-temperature activation of *n*-hexane resulted in both C₂H₄ and CO₂ (*e.g.* for CaMnO₃ at 650°C, 0.6 C% CO₂ yield vs. 3.8 C% C₂H₄ yield). Promotion of CaMnO₃ with 20 wt.% Na₂WO₄ led to a higher onset temperature for C₂H₄ formation and suppression of CO₂ generation until above 700°C. Meanwhile, SrMnO₃ and Na₂WO₄/SrMnO₃ did not yield appreciable amounts of CO₂ at temperatures below 750°C during the TPR; however, the observed low CO_x selectivity from TPR experiments cannot be directly used to predict the redox catalyst performance at high-temperature isothermal conditions, due to the gradual removal of both selective and non-selective oxygen species at lower temperatures during the TPR.^[21]

Isothermal *n*-hexane oxy-cracking experiments over Na₂WO₄/CaMnO₃ feature olefin yields significantly higher than those from the background thermal cracking between 650°C and 775°C (**Figure 3.4**). Comprehensive reaction data for several background thermal cracking conditions are given in **Table B2**. The improvement in olefin yield by Na₂WO₄/CaMnO₃ is most significant at 750°C, where the yield increases by 35% over the background (55% vs. 41%). The yield increase observed across these conditions is mostly attributed to a commensurate increase in *n*-hexane conversion (66% vs. 48% at 750°C); selectivity towards olefins decreased only slightly over the redox catalyst due to non-selective combustion (CO_x selectivity below 3% across this temperature range). Na₂WO₄/CaMnO₃ achieved an olefin yield of 67% at T = 775°C with 2.3% CO_x yield. Moreover, at the conditions shown, 88% or more of the H₂ produced was combusted, which can provide heat to the overall reaction and may contribute to the increase in *n*-hexane conversion.

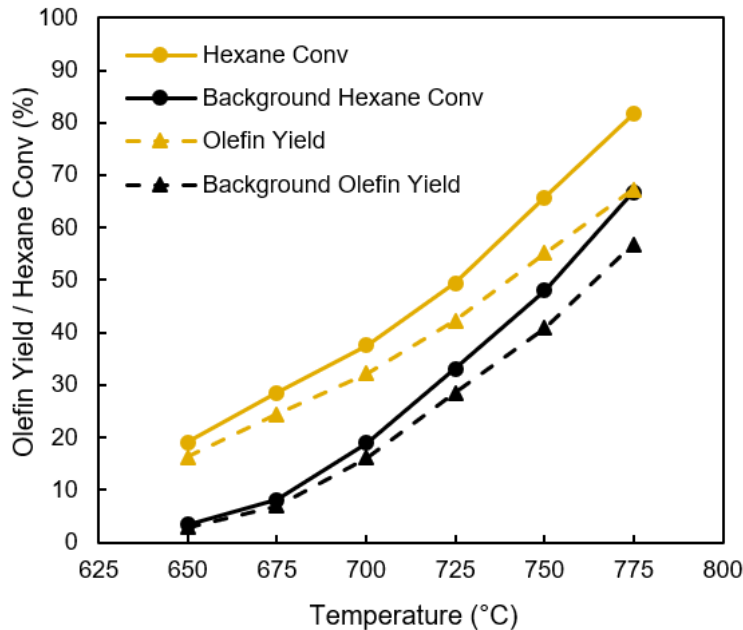


Figure 3.4. A comparison of *n*-hexane conversion and olefin yields over the Na₂WO₄/CaMnO₃ redox catalyst with those from the thermal cracking background. Conditions: GHSV = 9000 h⁻¹ (F_{Ar} = 150 mL/min, m = 500 mg), y_{*n*-hexane} ≈ 0.13, step duration = 20 s.

3.4.3. Effect of Temperature on Product Yields

A series of tests were conducted to assess the applicability of the four redox catalysts to *n*-hexane ROC and to study the resulting product distributions. Conversion of *n*-hexane proceeds largely via thermal cracking at the conditions tested (725°C to 775°C), and olefin yields (*i.e.* ethylene, propylene, and C₄₊) are therefore strongly dependent on temperature. **Figure 3.5** illustrates the relationships between *n*-hexane conversion, olefin selectivity, and temperature for each of the redox catalysts, at a fixed GHSV = 9000 h⁻¹. Olefin yields are differentiated by constant-yield contours.

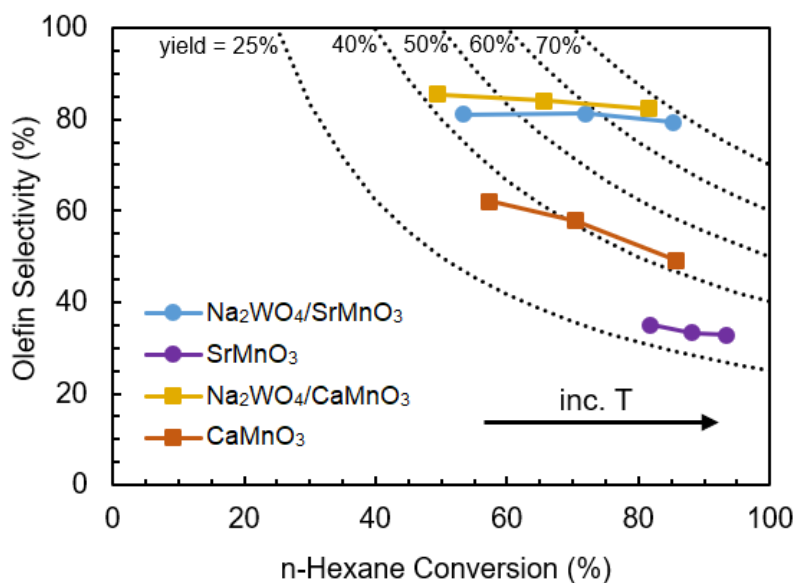


Figure 3.5. Olefin yields achieved by four redox catalysts. From left to right: $T = 725^{\circ}\text{C}$, 750°C , 775°C .

Constant yield contours indicate the product of *n*-hexane conversion and olefin selectivity for each data point, with selectivity on a carbon basis. Results obtained via GC. Conditions: GHSV = 9000 h^{-1} ($F_{\text{Ar}} = 150\text{ mL/min}$,

$$m = 500\text{ mg}), y_{n\text{-hexane}} \approx 0.13, \text{ step duration} = 20\text{ s}.$$

SrMnO₃ showed the highest *n*-hexane conversion among the four redox catalysts, even at relatively low temperatures (82% at $T = 725^{\circ}\text{C}$), along with the highest CO_x selectivity (43%), indicating that its lattice oxygen participates significantly in non-selective combustion. SrMnO₃ was the only redox catalyst in this study to exhibit coke formation (**Tables B3, B5**; coke determination methods are described in **Figure B1**). Unpromoted CaMnO₃ converted less *n*-hexane but was more inherently selective to olefins, though olefin selectivity decreased significantly with increasing temperature. The activity towards *n*-hexane conversion and the significant CO_x selectivity of the base SrMnO₃ and CaMnO₃ redox catalysts is not surprising, given that perovskite oxide-based catalysts have been explored for catalytic combustion or degradation of various hydrocarbons.^[25,26]

Promotion by 20 wt.% Na₂WO₄ consistently improves selectivity to olefins for both SrMnO₃ and

CaMnO₃. CO_x yield from CaMnO₃ dropped by over 96% upon Na₂WO₄ promotion and olefin yield increased by 19% at 725°C, indicating that Na₂WO₄ suppressed the non-selective combustion of *n*-hexane and olefins by CaMnO₃ and facilitated olefin yields in excess of the thermal background yields, as shown in **Figure 3.4**. Similarly, Na₂WO₄/SrMnO₃ exhibited a 130–140% increase in olefin selectivity compared to SrMnO₃ at all temperatures tested. Complete reaction testing results can be found in **Table B3**.

To further understand the effect of temperature on the oxy-cracking reaction, we examined the products formed over the Na₂WO₄-promoted CaMnO₃, focusing on two aspects: (1) the combustion (via the redox catalyst) of any resulting hydrogen, to form H₂O, and; (2) the formation of light olefins compared to that of CO_x compounds. On the first point, the ability to perform selective hydrogen combustion (SHC) is a key functionality for metal oxides employed in ROC; moreover, SHC has a complex dependence on reaction temperature. Selective combustion of H₂ to H₂O shifts the dehydrogenation equilibrium towards the olefin product and provides internal heat to the reactor, closing the heat balance and enabling auto-thermal cracking operation. On the other hand, the formation of easily condensable water facilitates separation with reduced energy consumption. These benefits lie in contrast to non-selective combustion, which would lead to CO_x formation and decrease the yield of olefin products.

Table 3.1 summarizes the performance of the Na₂WO₄/CaMnO₃ redox catalyst in terms of key characteristics from the *n*-hexane oxy-cracking reaction at temperatures from 725°C to 775°C. Thermal background data are also given for T = 725°C and 775°C. At all three temperatures, in the presence of the redox catalyst, >88% of the H₂ co-produced in cracking reactions was

combusted. Despite the significant combustion capability of Na₂WO₄/CaMnO₃, there is relatively little generation of CO_x compounds at any of the temperatures studied, indicating that this redox catalyst is capable of performing SHC under *n*-hexane oxy-cracking conditions. CO₂ selectivity reached a maximum of 2.8% at 775°C compared to a total olefin selectivity of 82.4%, and CO was never detected. While the olefin selectivity remained generally constant (from 85.5% at 725°C to 82.4% at 775°C), the selectivity towards longer chain olefins decreased with increasing temperature due to the higher cracking severity. Ethylene was the favored product at each temperature, most significantly at 775°C, while propylene and the C₄ olefins (*e.g.* 1-butene, 1,3-butadiene) had greater selectivity at the low-temperature end of the range (25.0% and 18.1%, respectively). Neither coke nor aromatic compounds were detected in these experiments (verified via MS on-stream analysis, **Figure B1**).

Table 3.1. Product distribution of the *n*-hexane oxy-cracking reaction over the 20 wt.% Na₂WO₄/CaMnO₃ redox catalyst at GHSV = 9000 h⁻¹ (m = 500 mg) and over a range of temperatures. Thermal background (*BG*) data at 725°C and 775°C are from an inert alumina-packed reactor.

	725°C (<i>BG</i>)	725°C	750°C	775°C	775°C (<i>BG</i>)
Conversion (mol %)					
<i>n</i> -hexane	33.6	49.4	65.7	81.7	66.7
H ₂ (to H ₂ O)	--	89.0	100.0	89.0	--
Selectivity (carbon mol %)					
CH ₄	9.7	9.1	10.0	10.5	10.4
C ₂ H ₄	36.9	36.8	40.3	43.2	42.8
C ₃ H ₆	25.9	25.0	24.0	21.9	24.1
butenes	15.9	14.9	12.2	9.5	11.0
1,3-butadiene	1.9	3.2	4.6	6.2	4.2
C ₂ -C ₄ paraffins	4.2	4.3	4.0	3.7	4.1
C ₅₊ (paraffins, olefins)	4.8	4.6	3.1	1.6	2.3
CO	--	0.0	0.0	0.0	--
CO ₂	--	1.1	1.6	2.8	--

3.4.4. Redox Catalyst Characterization and Mechanistic Investigation

Redox catalysts are unique in that both the surface and bulk properties can affect reaction performance—the surface facilitates both desired and undesired chemical reactions, whereas the bulk supplies active lattice oxygen as the oxidant. In this section, we endeavor to explain the performance of Na₂WO₄-promoted SrMnO₃ and CaMnO₃ via characterization of as-prepared and cycled variants of these redox catalysts as well as the unpromoted perovskite oxides. The results shown in **Figure 3.3** and **Figure 3.5** indicate that perovskite oxide promotion by Na₂WO₄ alters the oxygen donation properties of SrMnO₃ and CaMnO₃ redox catalysts, leading to enhanced olefin yields. Generally, the increase in ethylene and propylene yields for the promoted samples was due to increased olefin selectivity rather than higher *n*-hexane conversion when compared to their unpromoted counterparts; in fact, conversion was suppressed by the presence of Na₂WO₄ for both redox catalyst systems whereas selectivity was significantly enhanced (**Figure 3.5**). Therefore, it can be instructive to investigate the effect of Na₂WO₄ on the oxygen donation and surface properties of the redox catalysts. We begin by assessing the ability of the redox catalysts to release oxygen directly into the gas phase (oxygen uncoupling) via oxygen temperature-programmed desorption (O₂-TPD) experiments. It is worth noting that oxygen uncoupling determined via O₂-TPD is distinct from oxygen donation capacity under a reducing gas (i.e. as in **Figure 3.2**), and the two cannot be directly correlated.

The effect of Na₂WO₄ promotion on oxygen release was characterized using O₂-TPD, with redox catalyst mass loss measured on a SETARAM TGA instrument (**Figure 3.6**). O₂-TPD results for SrMnO₃ did not show significant desorption of oxygen species until a rise starting at 800°C which was attributed to the release of lattice oxygen resulting from oxygen vacancy formation and

reduction of Mn cations.^[27,28] Conversely, significant O₂ loss from CaMnO₃ was detected beginning at 625°C, in agreement with previous reports showing that CaMnO₃ will spontaneously release its lattice oxygen under inert atmospheres as low as 600°C.^[27] Desorbed surface or chemisorbed oxygen species, while potentially present, could not be differentiated from released lattice oxygen. Oxygen desorption and lattice oxygen release were suppressed by promotion with Na₂WO₄ as indicated by the O₂-TPD curve for Na₂WO₄/CaMnO₃ in **Figure 3.6**; loss of oxygen from CaMnO₃ fell by 41% (from 1.9 to 1.1 wt.%) upon Na₂WO₄ promotion. Na₂WO₄/SrMnO₃ was not tested due to the lack of meaningful oxygen release by SrMnO₃

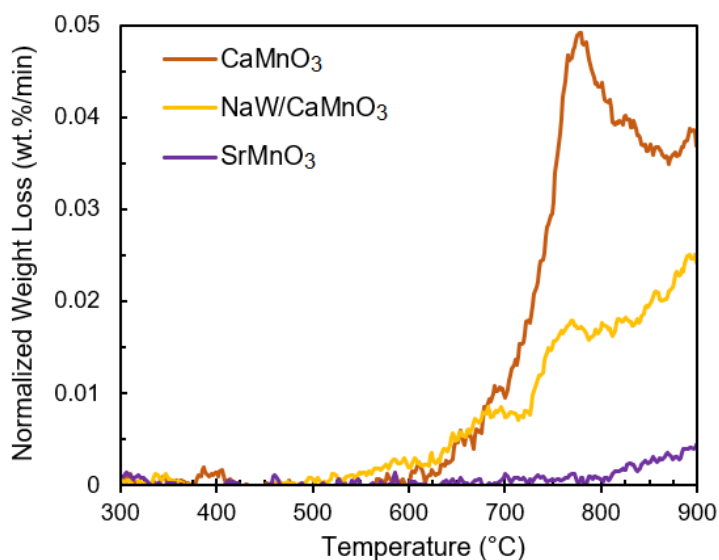


Figure 3.6. O₂-TPD results of three redox catalysts. Samples were held under 10% atmosphere of the adsorbing gas for 30 min at 900°C, ramped down to 150°C at 10°C/min, and purged under an inert He environment for 60 min prior to testing. TG weight loss rates were normalized by initial sample mass.

Conditions: $m = 30\text{--}50$ mg, $F = 180$ mL/min He, ramping rate = 5°C/min.

The O₂-TPD results could explain both the lowered *n*-hexane conversion of Na₂WO₄/CaMnO₃ compared to CaMnO₃ and (in part) the increased selectivity towards olefins (**Figure 3.5**), as

electrophilic oxygen species and more readily available oxygen evolved from the bulk would provide an abundance of non-selective oxidant for undesirable CO_x formation (as observed in the *n*-hexane TPR for CaMnO₃ in **Figure 3.3**). Consistent with previous reports on ethane ODH with Ruddlesden-Popper-structured redox catalysts,^[23,24] the O₂-TPD and isothermal ROC reaction results indicate that inhibiting oxygen release properties from a mixed oxide can improve its selectivity towards olefins at the expense of lowered activity. However, such a principle cannot be used to compare different mixed oxides with varying compositions and hence surface properties. For instance, unpromoted SrMnO₃, with inferior oxygen donation properties compared to unpromoted CaMnO₃, gave higher *n*-hexane conversion and lower olefin selectivity. This was likely a result of their distinct surface properties, as will now be discussed.

Near-surface atomic percentages found via X-ray photoelectron spectroscopy (XPS) for six SrMnO₃- and CaMnO₃-based redox catalysts exhibited a relative enrichment of Na and W atoms compared to Sr, Ca, and Mn (**Table 3.2**). In this context, enrichment (or suppression) was defined as the ratio of the observed near-surface metal content (in atomic percent) to the expected metal percentage based on the overall sample stoichiometry. W atoms were enriched in the near-surfaces of as-prepared Na₂WO₄/CaMnO₃ (W = 3.3) and Na₂WO₄/SrMnO₃ (W = 2.6), while Na enrichment was significant for the promoted CaMnO₃ (Na = 2.9) and more modest for the promoted SrMnO₃ (Na = 1.1). After 25 redox cycles, Na₂WO₄ remained prominent in the near-surface of each redox catalyst (**Table 3.2**), rather than moving into the bulk in response to repeated redox stresses or volatilizing due to high-temperature operation. As such, the XPS analysis for each sample indicates a significant Na₂WO₄ enrichment on the redox catalyst surface which is resistant to change after 25 redox cycles with *n*-hexane. Due to the escape depth of XPS measurements (~10 atomic layers),

the degree of Na₂WO₄ enrichment on the immediate surface is likely to be much stronger than indicated, as suggested in studies on related systems.^[19,22] Carbon and oxygen were not included in enrichment and suppression calculations; C 1s and O 1s XPS spectra for all samples are provided in **Figures B2–B5**.

Table 3.2. Surface cation atomic percentages for six redox catalyst variants from XPS analysis. Carbon and oxygen are excluded. Surface enrichment and suppression of cations, shown in parentheses, are calculated using observed percentages from XPS in combination with expected percentages from overall stoichiometry.

Redox Catalyst	Sr 3d / Ca 2p	Mn 2p	Na 1s	W 4f
SrMnO ₃ (<i>fresh</i>)	74.9% (1.5)	25.2% (0.5)	--	--
Na ₂ WO ₄ /SrMnO ₃ (<i>fresh</i>)	52.9% (1.3)	16.1% (0.4)	14.2% (1.1)	16.7% (2.6)
Na ₂ WO ₄ /SrMnO ₃ (<i>cycled</i>)	52.3% (1.3)	17.3% (0.4)	16.5% (1.3)	13.9% (2.1)
CaMnO ₃ (<i>fresh</i>)	67.8% (1.4)	32.2% (0.6)	--	--
Na ₂ WO ₄ /CaMnO ₃ (<i>fresh</i>)	41.9% (1.0)	19.1% (0.5)	22.2% (2.2)	16.7% (3.3)
Na ₂ WO ₄ /CaMnO ₃ (<i>cycled</i>)	44.7% (1.1)	20.1% (0.5)	20.4% (2.0)	14.9% (2.9)

The selectivity of perovskites for partial oxidation reactions such as methane to syngas and ethane oxidative dehydrogenation has previously been related to the relative amounts of lattice oxygen to surface oxygen species, often estimated from the XPS O 1s spectra.^[24,29,30] While these species were clearly present in the asymmetric O 1s spectra of as-prepared SrMnO₃ and CaMnO₃ (with SrMnO₃ showing slightly higher surface oxygen species), the presence of WO₄²⁻ species obfuscated the relevant peaks in the Na₂WO₄-promoted samples (**Figures B3–B4**). Surface Mn was under-represented in both unpromoted samples, though Na₂WO₄ promotion further decreased the near-surface Mn cations in both cases (**Table 3.2**). Mn 2p spectra of the as-prepared and Na₂WO₄-promoted redox catalysts are presented in **Figures B6–B7**.

To understand the differences in olefin selectivity between as-prepared and Na₂WO₄-promoted redox catalysts, we examined the Sr 3*d* and Ca 2*p* XPS spectra of SrMnO₃ and CaMnO₃ for changes in (Sr,Ca) surface species upon promotion. The characteristic XPS peaks of these alkaline earth ions, particularly Sr, indicated a suppression of surface species upon promotion with Na₂WO₄. **Figure 3.7** shows the fitted XPS spectra for Sr 3*d* (**Figure 3.7a**) and Ca 2*p* (**Figure 3.7b**) on SrMnO₃-based and CaMnO₃-based redox catalysts, respectively. Details of the fit peaks are given in **Tables B6–B7**. All spectra were well fit by a pair of doublets, with one doublet consistent with bulk oxide species and another consistent with surface species.^[31] Line shape fitting for the Sr 3*d* spectra of SrMnO₃ required two doublets: the Sr 3*d*_{5/2} peak at 132.3 eV binding energy (BE) was assigned to bulk Sr from the SrMnO₃ lattice,^[32–35] while a second doublet with its characteristic Sr 3*d*_{5/2} peak at 132.8 eV was attributed to a combination of Sr bonded with surface oxygen species (SrCO₃, Sr(OH)₂)^[31,36,37] and a near-surface SrO/Sr₂MnO₄ region (Sr/Mn = 3.0 for the SrMnO₃ near-surface).^[38,39] Each doublet exhibited an energy separation of 1.7 eV, consistent with previous literature.^[33,36,40] Upon promotion of SrMnO₃ with 20 wt.% Na₂WO₄, the presence of free SrO, Sr(OH)₂, and SrCO₃ in the near-surface was diminished by over 90%, evident from the drastic reduction of the higher BE Sr 3*d* doublet for surface Sr and the drop in overall near-surface Sr enrichment (1.5 to 1.3), which corresponds to the 40% increase in olefin selectivity of the Na₂WO₄/SrMnO₃ redox catalyst. CO₂-TPD results confirmed an absence of strongly chemisorbed CO₂ species on Na₂WO₄/SrMnO₃, whereas CO₂ adsorbed on unpromoted SrMnO₃ was significantly more stable and amounted to nearly 1 wt.% of the sample after exposure (see **Figure B5**). The suppression of Sr surface species resulting from Na₂WO₄ surface enrichment, and the subsequent inhibition of hydrocarbon combustion activity, was critical to achieving the high olefin yields demonstrated in **Figure 3.5**. This finding is consistent with previous literature

identifying the important role of surface Sr^{2+} in catalytic combustion reactions over Sr-containing perovskite catalysts.^[25]

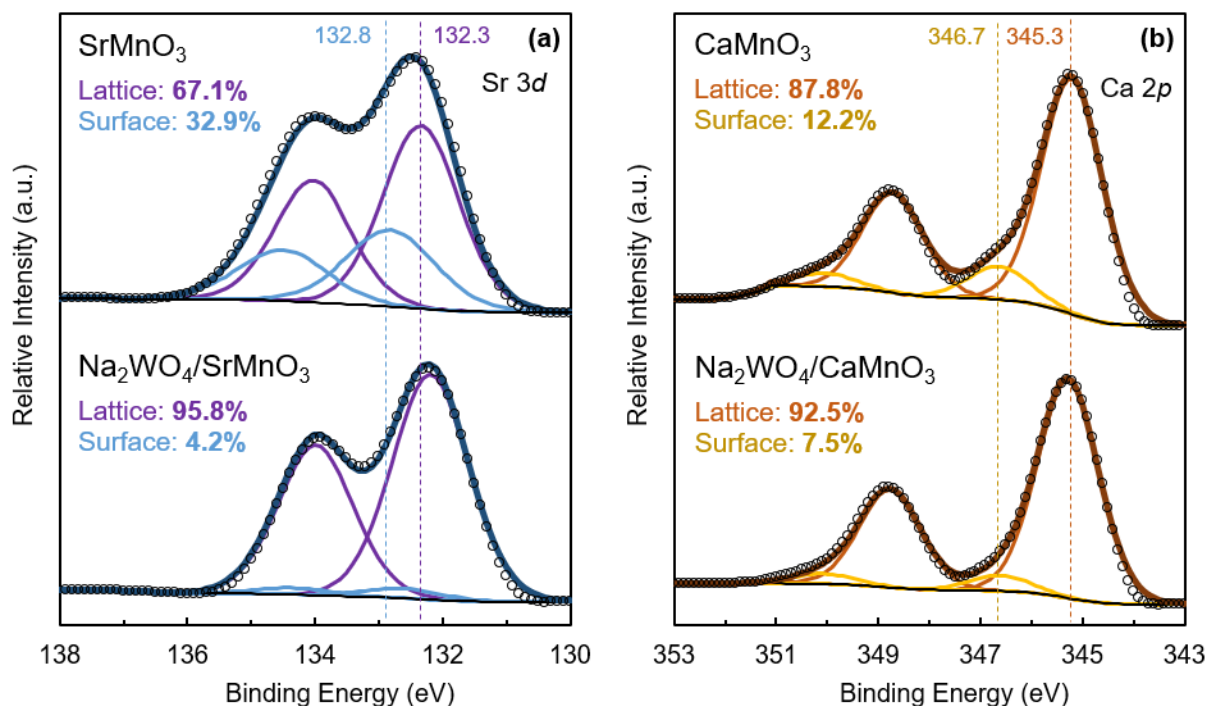


Figure 3.7. Photoemission spectra of Sr 3d (a) and Ca 2p (b) for the SrMnO₃- and CaMnO₃-based redox catalysts, respectively, using an Al K α X-ray source (1486.7 eV). Binding energies (BE) were referenced to the C 1s peak for adventitious carbon at 284.6 eV. Dotted lines indicate BE value for the characteristic peaks of lattice (low BE) and surface (high BE) doublets for the unpromoted (Sr,Ca)MnO₃.

Surface oxides, hydroxides, and carbonates were significantly less prominent for the undoped CaMnO₃ system than for the SrMnO₃ (accounting for 12.2% of Ca ions vs. 32.9% of Sr ions), and therefore the suppression of such species by Na₂WO₄ was less significant, as depicted in **Figure 3.7b**. The Ca 2p spectra exhibited a primary feature at around 345.3 eV consistent with the characteristic Ca 2p_{3/2} peak for lattice Ca from CaMnO₃.^[32] A high BE shoulder located at 346.7

eV indicated the presence of surface-type Ca, which can be assigned to CaO, CaCO₃, Ca(OH)₂, or a combination thereof,^[32,26,41] as would be expected from the surface enrichment of Ca from the CaMnO₃ lattice (1.4, **Table 3.2**). Upon promotion with 20 wt.% Na₂WO₄, surface-type Ca species decreased from 12.2% to 7.5% of all detected Ca which, combined with the near-surface depletion of Ca upon promotion with Na₂WO₄ (1.4 to 1.0), gave an overall decrease in Ca surface species of 62%. The suppression of surface species resulting from Na₂WO₄ enrichment may inhibit deep oxidation, resulting in greater olefin selectivity for the *n*-hexane oxy-cracking reaction in the presence of Na₂WO₄/CaMnO₃ as compared to CaMnO₃ (**Figure 3.5**).^[23,30]

After 25 redox cycles under *n*-hexane, the Ca 2*p* spectra of the Na₂WO₄/CaMnO₃ were unchanged. For cycled Na₂WO₄/SrMnO₃, the Sr 3*d* spectra reveal only a slight reemergence of surface-type Sr (11.2%), indicating that the cycled sample maintained a significant suppression of the surface Sr species from SrMnO₃ (32.9%). Additional spectra for the cycled samples are presented in **Figures B8–B10**. The presence of significantly more surface hydroxides and carbonates on as-prepared SrMnO₃ compared to CaMnO₃ can be attributable to both the stronger basicity of SrO, which strongly chemisorbs H₂O and CO₂,^[36,42] and to an elevated presence of Sr in the near-surface due to its surface separation, as reported in multiple studies of Sr-containing perovskites.^[38–40,42] (XRD patterns indicated that such phase separation did not affect the bulk, as will be discussed later.) For both SrMnO₃ and CaMnO₃, the suppression of surface-type Sr and Ca species upon Na₂WO₄ promotion was associated with a significant decline in CO_x selectivity at reaction conditions, as shown in **Figure 3.8**.

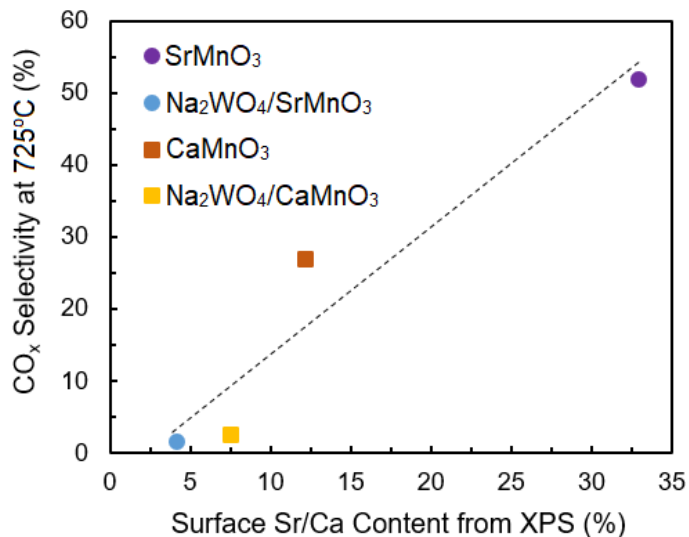


Figure 3.8. Relationship between the accommodation of surface-type Sr/Ca species and CO_x selectivity at T = 725°C and GHSV = 4500 h⁻¹ (F_{Ar} = 75 mL/min, m = 500 mg). *y*_{*n*-hexane} ≈ 0.13, step duration = 40 s. The dashed line is used to show the general trend and does not representative quantitative correlation.

Surface enrichment of Na₂WO₄ was shown to have a significant suppression effect on surface cation and oxygen species, which resulted in greater olefin selectivity and improved yields from *n*-hexane ROC. The nature of this enrichment was further studied with low-energy ion scattering spectroscopy (LEIS), and we determined that Na₂WO₄ comprised the outermost surface layer of the Na₂WO₄/CaMnO₃ redox catalyst upon promotion. **Figure 3.9a** shows LEIS spectra for the 20 wt.% Na₂WO₄/CaMnO₃ redox catalyst surface with increasing doses of sputter-etching using 0.5 keV Ar⁺ sputtering source (1 x 10¹⁵ Ar⁺ ions/cm² corresponding to the removal of approximately one atomic monolayer) and with a 3 keV He⁺ probe beam.^[24] Initial sputtering with 0.5 x 10¹⁵ cm⁻² (green) revealed an outermost surface layer composed of O, Na, and W, with a slight shoulder in the vicinity of Ca and a less significant shoulder where a Mn peak would be expected, altogether indicating the predominance of Na₂WO₄ in the surface monolayer. Subsequent removal of the first few atomic monolayers revealed a Ca peak, but not a Mn peak; this may indicate that the CaMnO₃

substrate terminates in a CaO plane or Ca-rich phase (*e.g.* CaO, Ca₂MnO₄) or that Ca from the CaMnO₃ lattice migrates and reacts with Na₂WO₄ to form a calcium tungstate (*e.g.* CaWO₄) phase near the surface. A cumulative dosing of $20 \times 10^{15} \text{ cm}^{-2}$ was sufficient to reveal a Mn peak. Depth profiling of the main elements shown in **Figure 3.9b** featured Na and W signals which rose more rapidly than those of Ca and particularly Mn with increasing sputtering, also indicating that the Na₂WO₄ promoter was at a higher concentration than CaMnO₃ near the immediate surface. Taken together, the surface-sensitive characterization and reaction performance data of (Sr,Ca)MnO₃-based redox catalysts have revealed the crucial role of the Na₂WO₄ surface layer in achieving high olefin yields for *n*-hexane ROC.

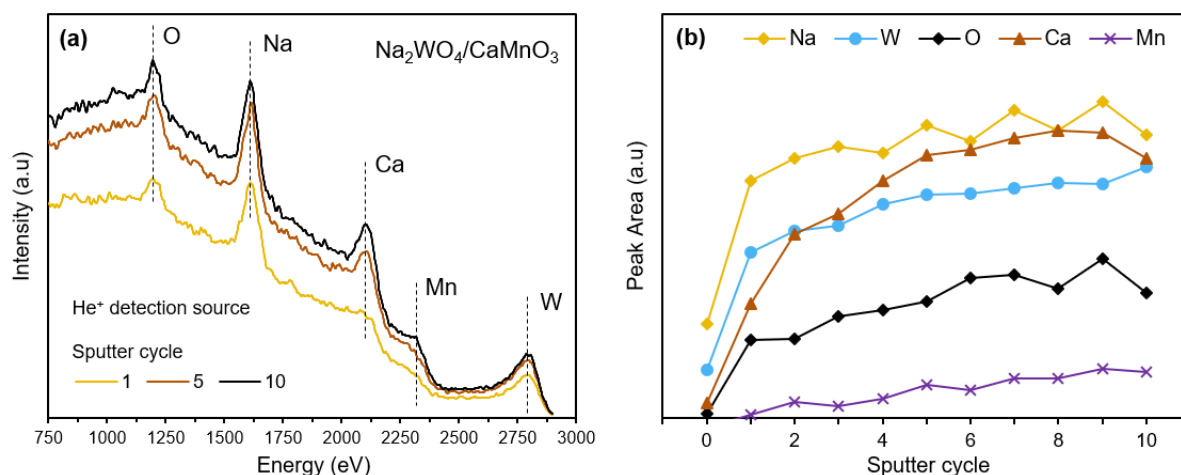


Figure 3.9. LEIS spectra for 20 wt.% Na₂WO₄/CaMnO₃ acquired using a 3 keV He⁺ probe beam. **(a)** Surface scans after varying amounts of 0.5 keV Ar⁺ sputter-etching; one sputter cycle corresponds to $0.5 \times 10^{15} \text{ Ar}^+$ ions cm⁻². **(b)** Depth profiles of Na, W, O, Ca, and Mn, showing peak areas as a function of sputter cycle, up to a maximum dose of $5.0 \times 10^{15} \text{ cm}^{-2}$.

3.4.5. Evaluation and Literature Comparison of Redox Catalyst Performance and Stability

Lastly, we demonstrate with XRD after 25 cycles of *n*-hexane ROC that the Na₂WO₄/SrMnO₃ and Na₂WO₄/CaMnO₃ redox catalysts are structurally stable and capable of maintaining desirable properties (*n*-hexane conversion, olefin selectivity, SHC). **Figure 3.10** gives key reaction characteristics for multiple *n*-hexane oxy-cracking cycles using Na₂WO₄/SrMnO₃ (**Figure 3.10a**) and Na₂WO₄/CaMnO₃ (**Figure 3.10b**) at T = 725°C and GHSV = 4500 h⁻¹. Each sample was pre-treated under ethane at 750°C. Both redox catalysts show stable conversion of *n*-hexane and of hydrogen as well as olefin yields that are consistently higher than the thermal background (given by the dashed line), with Na₂WO₄/CaMnO₃ showing the greater activity (and slightly lower selectivity).

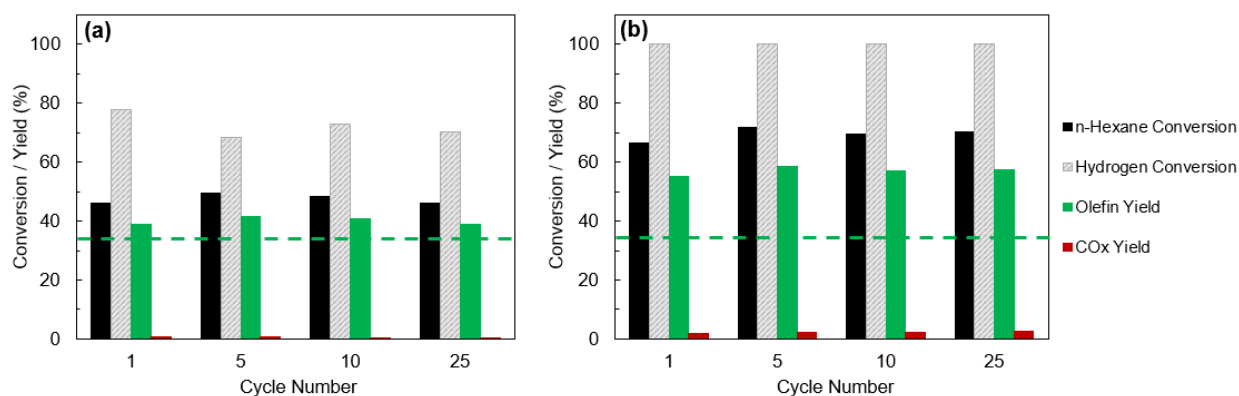


Figure 3.10. A comparison of reaction characteristics over the course of 25 *n*-hexane oxy-cracking cycles for (a) Na₂WO₄/SrMnO₃ and (b) Na₂WO₄/CaMnO₃. Thermal background olefin yield is given as a dashed line.

Conditions: T = 725°C, GHSV = 4500 h⁻¹ (F_{Ar} = 75 mL/min, m = 500 mg), y_{*n*-hexane} ≈ 0.13, duration = 40 s.

Na₂WO₄/SrMnO₃ preserves its high selectivity towards hydrogen combustion over the 25 cycles, with the last cycle showing low CO_x formation (0.28% CO_x yield). The slight decline in CO_x generation over 25 cycles may be explained by a decrease in available oxygen, as evidenced by

the XRD pattern for the cycled $\text{Na}_2\text{WO}_4/\text{SrMnO}_3$ redox catalyst (**Figure 3.11a**). Non-selective combustion of *n*-hexane or olefins to CO_x may be exacerbated by a fully restored oxygen carrier and the presence of surface α -oxygen species. Nonetheless, the hydrogen conversion and SHC capability by this material is not negatively affected, and $\text{Na}_2\text{WO}_4/\text{SrMnO}_3$ remains an attractive material for the application.

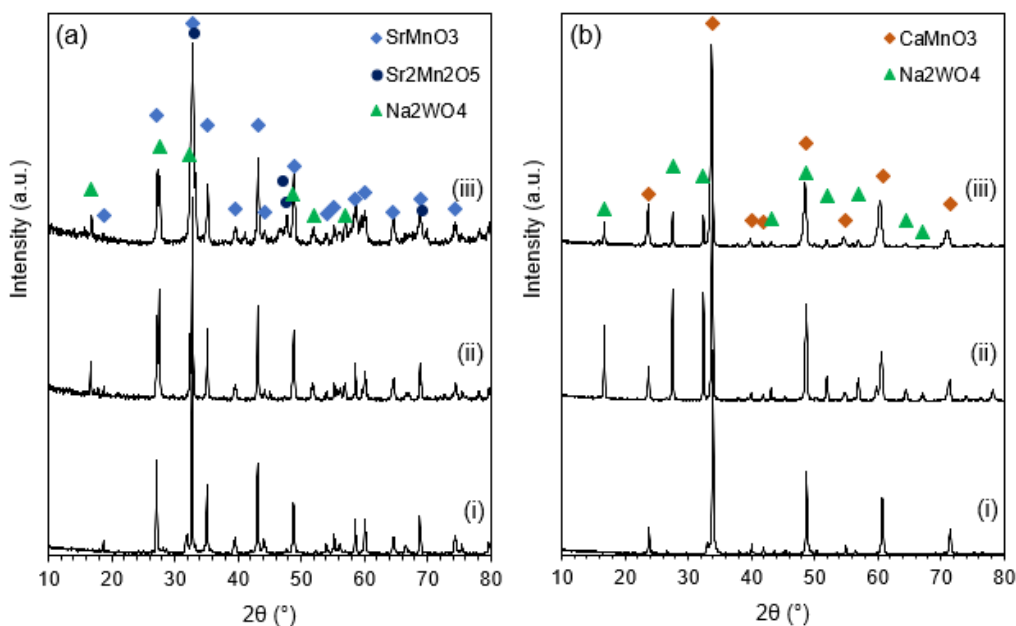


Figure 3.11. XRD patterns for all redox catalysts. **(a)** Patterns for (i) SrMnO_3 , (ii) $\text{Na}_2\text{WO}_4/\text{SrMnO}_3$, (iii) cycled $\text{Na}_2\text{WO}_4/\text{SrMnO}_3$. **(b)** Patterns for (i) CaMnO_3 , (ii) $\text{Na}_2\text{WO}_4/\text{CaMnO}_3$, (iii) cycled $\text{Na}_2\text{WO}_4/\text{CaMnO}_3$.

Cycled samples tested and re-oxidized at $T = 725^\circ\text{C}$, $\text{GHSV} = 4500 \text{ h}^{-1}$ for 25 cycles.

$\text{Na}_2\text{WO}_4/\text{CaMnO}_3$ shows greater oxygen donation and higher conversions in general than the SrMnO_3 -based material, leading to higher CO_x yields (1.7–2.8%); this redox catalyst is capable of combusting 100% of the generated H_2 in the system. This total combustion of H_2 may contribute to the elevated *n*-hexane conversion over this redox catalyst (69–71% for $\text{Na}_2\text{WO}_4/\text{CaMnO}_3$, compared to 48–50% for $\text{Na}_2\text{WO}_4/\text{SrMnO}_3$) and the higher olefin yields which result (55–58% vs.

39–41% at 725°C). The results obtained for Na₂WO₄/CaMnO₃ compare favorably with the catalyst developed by Liu et al., which produced approximately 12–13% CO_x yield along with 50% olefin yield at 750°C; for 20 wt.% Na₂WO₄/CaMnO₃ at 725°C, a maximum of 58% olefin yield was achieved along with only 2.8% maximum CO_x yield while also decreasing the temperature requirement.^[10,11] In another study by Boyadjian et al., Li/MgO catalysts achieved 17% light olefin yield from *n*-hexane at 575°C while producing 7% CO_x yield.^[12] The performance of Na₂WO₄/CaMnO₃ as compared to literature catalysts is best encapsulated in the ratio of carbon utilization for light olefin yield vs. CO_x yield, which was approximately 21:1 in this work, compared to 4.2:1 (Liu et al.) and 2.5:1 (Boyadjian et al.). Na₂WO₄/CaMnO₃ is thus a stable and very promising redox catalyst for *n*-hexane oxidative cracking when operated at or near 725°C.

Figure 3.11a–b shows results from XRD experiments on as-prepared and cycled samples based on SrMnO₃ and CaMnO₃, respectively. These patterns indicate that both Na₂WO₄/SrMnO₃ and Na₂WO₄/CaMnO₃ were resistant to promoter-oxide interactions during cycling at T = 725°C. Multiple phases were observed in the SrMnO₃ system: a minor Sr₂MnO₄ impurity was present which was later undetectable after promotion with Na₂WO₄, and the brownmillerite phase Sr₂Mn₂O₅ was present in nearly equal proportion to SrMnO₃ for the cycled Na₂WO₄/SrMnO₃ sample. The latter phase indicated an incomplete regeneration of the perovskite structure. Lower operating temperatures therefore have the effect of lowering the oxygen capacity of the redox catalyst by limiting phase regeneration, but increasing selectivity towards hydrogen combustion, as supported by the results of **Figure 3.10**. The presence of Sr₂Mn₂O₅ also suggests that complete regeneration of the perovskite phase is a slower process for the hexagonal SrMnO₃ than for the cubic CaMnO₃.

3.5. Conclusions

In this work, we demonstrated the effectiveness of several redox catalysts for the redox oxidative cracking (ROC) of naphtha using *n*-hexane as a model compound. At 725°C and 4500 h⁻¹, Na₂WO₄-promoted CaMnO₃ achieved over 72% increase in olefin yields, on a relative basis, over thermal cracking while completely combusting H₂. The redox catalyst exhibited < 3% CO_x yield and maintained excellent stability over 25 redox cycles. Na₂WO₄-promoted SrMnO₃ also demonstrated superior olefin yield compared to thermal cracking with CO_x formation as low as 0.28%. The greater olefin yields and low CO_x selectivity were attributed primarily to the selective combustion of H₂ by Na₂WO₄/(Sr,Ca)MnO₃. Promotion by 20 wt.% Na₂WO₄ was highly effective to improve the selectivity of the redox catalysts, which was attributed to a surface enrichment of Na and W and significant alteration of the surface sites of SrMnO₃ and CaMnO₃.

XRD analysis confirmed the phase stability, and promoter-oxide interactions were not observed after cycling. Surface-sensitive LEIS and XPS characterization revealed an outermost surface layer of was covered by Na₂WO₄, and near-surface regions for Na₂WO₄/(Sr,Ca)MnO₃ were significantly enriched in Na and W but deficient in Mn. Sr 3*d* spectra from XPS showed a 90% decrease in SrO/Sr(OH)₂/SrCO₃ surface species from SrMnO₃ upon promotion with Na₂WO₄, while similar Ca-containing surface species on CaMnO₃ were diminished by 62% with promotion. Correspondingly, we observed 97% suppression in CO_x selectivity with Na₂WO₄-promoted SrMnO₃ and 90% suppression for Na₂WO₄/CaMnO₃. Na₂WO₄ promotion also inhibited lattice oxygen release from CaMnO₃. Such effects, resulting from the surface enrichment of Na₂WO₄, suppressed non-selective combustion reactions and significantly enhanced olefin yields. Through the combination of reaction and characterization, the role of Na₂WO₄ was determined, and

Na₂WO₄-promoted perovskite oxides are identified as promising redox catalysts for the oxidative cracking of *n*-hexane.

3.6. References

- [1] H. Zimmermann, R. Walzl, *Ullmann's Encycl. Ind. Chem.* **2012**, 466–529.
- [2] J. V. Moreira, *Steam Cracking: Kinetics and Feed Characterisation*, **2015**.
- [3] T. Ren, M. Patel, K. Blok, *Energy* **2006**, *31*, 425–451.
- [4] International Energy Agency, *Technology Roadmap: Energy and GHG Reductions in the Chemical Industry via Catalytic Processes*, **2013**.
- [5] R.C. Valencia, *The Future of the Chemical Industry by 2050*, **2013**.
- [6] S. M. Sadrameli, *Fuel* **2015**, *140*, 102–115.
- [7] V. P. Haribal, Y. Chen, L. Neal, F. Li, *Engineering* **2018**, *4*, 714–721.
- [8] S. M. Sadrameli, *Fuel* **2016**, *173*, 285–297.
- [9] N. Rahimi, R. Karimzadeh, *Appl. Catal. A Gen.* **2011**, *398*, 1–17.
- [10] X. Liu, W. Li, H. Zhu, Q. Ge, Y. Chen, H. Xu, *Catal. Letters* **2004**, *94*, 31–36.
- [11] X. Liu, W. Li, H. Xu, Y. Chen, *React. Kinet. Catal. Lett.* **2004**, *81*, 203–209.
- [12] C. Boyadjian, L. Lefferts, K. Seshan, *Appl. Catal. A Gen.* **2010**, *372*, 167–174.
- [13] C. Boyadjian, K. Seshan, L. Lefferts, A. G. J. van der Ham, H. van der Berg, *Ind. Eng. Chem. Res.* **2011**, *50*, 342–351.
- [14] J. Adanez, A. Abad, F. Garcia-Labiano, P. Gayan, L. F. De Diego, *Prog. Energy Combust. Sci.* **2012**, *38* (2), 215–282.
- [15] N. Ballarini, F. Cavani, A. Cericola, C. Cortelli, M. Ferrari, F. Trifiro, G. Capannelli, A. Comite, R. Catani, U. Cornaro, *Catal. Today* **2004**, *91–92*, 99–104.
- [16] A. H. Elbadawi, M. Y. Khan, M. R. Quddus, S. A. Razzak, M. M. Hossain, *AIChE J.* **2017**, *63*, 130–138.

- [17] F. Li, L. M. Neal, J. Zhang, *Redox Catalysts for the Oxidative Cracking of Hydrocarbons, Methods of Making, and Methods of Use Thereof*, WO 2018/049389 A1, **2018**.
- [18] L. M. Neal, S. Yusuf, J. A. Sofranko, F. Li, *Energy Technol.* **2016**, *4*, 1200–1208.
- [19] S. Yusuf, L. M. Neal, F. Li, *ACS Catal.* **2017**, *7*, 5163–5173.
- [20] V. P. Haribal, L. M. Neal, F. Li, *Energy* **2017**, *119*, 1024–1035.
- [21] R. B. Dudek, Y. Gao, J. Zhang, F. Li, *AIChE J.* **2018**, *64* (8), 3141–3150.
- [22] S. Yusuf, L. Neal, V. Haribal, M. Baldwin, H. H. Lamb, F. Li, *Appl. Catal. B Environ.* **2018**, *232*, 77–85.
- [23] Y. Gao, L. M. Neal, F. Li, *ACS Catal.* **2016**, *6*, 7293–7302.
- [24] Y. Gao, F. Haeri, F. He, F. Li, *ACS Catal.* **2018**, 1757–1766.
- [25] F. Polo-Garzon, V. Fung, X. Liu, Z. D. Hood, E. E. Bickel, *ACS Catal.* **2018**, *8*, 10306–10315.
- [26] J. Chen, Z. He, G. Li, T. An, H. Shi, Y. Li, *Appl. Catal. B Environ.* **2017**, *209*, 146–154.
- [27] N. Galinsky, A. Mishra, J. Zhang, F. Li, *Appl. Energy* **2015**, *157*, 358–367.
- [28] J. Vieten, B. Bulfin, F. Call, M. Lange, M. Schmucker, A. Francke, M. Roeb, C. Sattler, *J. Mater. Chem. A* **2016**, *4*, 13652–13659.
- [29] L. M. Neal, A. Shafiearhood, F. Li, *ACS Catal.* **2014**, *4*, 3560–3569.
- [30] N. A. Merino, B. P. Barbero, P. Eloy, L. E. Cadus, *Appl. Surf. Sci.* **2006**, *253*, 1489–1493.
- [31] E. J. Crumlin, E. Mutoro, Z. Liu, M. E. Grass, M. D. Biegalski, Y. L. Lee, D. Morgan, H. M. Christen, H. Bluhm, Y. Shao-Horn, *Energy Environ. Sci.* **2012**, *5*, 6081–6088.
- [32] V. Celorrio, L. Calvillo, G. Granozzi, A. E. Russell, D. J. Fermin, *Top. Catal.* **2018**, *61*, 154–161.

- [33] S. Mno, E. Z. Kurmaev, M. A. Korotin, V. R. Galakhov, L. D. Finkelstein, E. I. Zabolotzky, N. N. Efremova, J. Mitchell, *Phys. Rev. B* **1999**, *59*, 799–806.
- [34] T. Saitoh, T. Mizokawa, A. Fujimori, M. Abbate, *Phys. Rev. B* **1997**, *56*, 1290–1295.
- [35] D. G. Popescu, N. Barrett, C. Chirila, I. Pusuk, M. A. Husanu, *Phys. Rev. B* **2015**, *92*, 1–11.
- [36] J. Dupin, D. Gonbeau, P. Vinatier, A. Levasseur, *Phys. Chem. Chem. Phys.* **2000**, *2*, 1319–1324.
- [37] R. P. Vasquez, *J. Electron Spectros. Relat. Phenomena* **1991**, *56*, 217–240.
- [38] H. Dulli, P. A. Dowben, S. H. Liou, E. W. Plummer, *Phys. Rev. B* **2000**, *62*, 14629–14632.
- [39] W. Lee, J. W. Han, Y. Chen, Z. Cai, B. Yildiz, *J. Am. Chem. Soc.* **2013**, *135*, 7909–7925.
- [40] P. Decorse, E. Quenneville, S. Poulin, M. Meunier, A. Yelon, F. Morin, *J. Vac. Sci. Technol. A Vacuum* **2001**, *19*, 910–915.
- [41] V. Celorrio, L. Calvillo, E. Dann, G. Granozzi, A. Aguadero, D. Kramer, A. E. Russell, D. J. Fermin, *Catal. Sci. Technol.* **2016**, *6*, 7231–7238.
- [42] V. Young, T. Otagawa, *Appl. Surf. Sci.* **1985**, *20*, 228–248.

CHAPTER 4: REDUCTION KINETICS OF PEROVSKITE OXIDES FOR SELECTIVE HYDROGEN COMBUSTION IN THE CONTEXT OF OLEFIN PRODUCTION

is an updated print of a manuscript written by R. B. Dudek, Y. Tian, G. Jin, M. Blivin Capstaff,

F. Li, and published in *Energy Tech.* **2019**, 1900738.

The supplementary information is reproduced in Appendix C.

4.1. Abstract

Steam cracking and catalytic dehydrogenation are the primary industrial routes to ethylene and propylene, but the high energy consumption and CO₂ emission intensity of these processes have created a need for more sustainable alternatives in light olefin production. Chemical looping represents a novel approach for generating light olefins in which thermal cracking or catalytic dehydrogenation is coupled with selective hydrogen combustion (SHC) by a metal oxide redox catalyst, which enables autothermal operation, increased per-pass conversion, and greater-than-equilibrium yields. Recent studies indicate that Na₂WO₄-promoted perovskite oxides are effective redox catalysts with high olefin selectivity; however, the underlying redox reaction kinetics have yet to be investigated. Here we report kinetic parameters, rates, and reaction models for the reduction of unpromoted and Na₂WO₄-promoted CaMnO₃ redox catalysts by H₂, C₂H₄, and C₂H₆. Reduction rates of CaMnO₃ under ethylene and ethane were significantly lower than under H₂. Model fitting of reduction kinetics (dimensionless solid conversion X vs. t , and dX/dt vs. X) showed good agreement with reaction order-controlled models for CaMnO₃ reduction and predicted greater oxygen site dependence and higher activation energy for CaMnO₃ reduction by C₂H₄ as compared to H₂. Avrami-Erofe'ev nucleation and growth models provided the best statistical fit to the reduction of Na₂WO₄/CaMnO₃ in H₂ and in C₂H₄; after Na₂WO₄ promotion, the reduction rate of CaMnO₃ was three orders of magnitude lower in ethylene in comparison to hydrogen, consistent with its superior selectivity to hydrogen combustion (S_H). Kinetic modeling results were consistent with time-on-stream fixed-bed experiments in H₂/C₂H₄/C₂H₆, which showed enhanced S_H value (99.0% vs. 93.2%) for Na₂WO₄/CaMnO₃ compared to CaMnO₃. The kinetic models developed for H₂ and hydrocarbon combustion by CaMnO₃-based redox catalysts can be applied towards reactor

design and optimization in the context of enhanced olefin production via selective hydrogen combustion under a cyclic redox scheme.

4.2. Introduction

Plastics and petrochemicals manufacturing consume more energy than any other industrial sector, and direct GHG emissions from the petrochemicals industry are projected to increase 30% by 2050.^[1] For most petrochemical products, the significant energy consumption and CO₂ emissions during manufacturing stem primarily from the production of olefinic starting materials (e.g. ethylene, propylene) via highly endothermic steam cracking processes.^[2-5] Oxidative dehydrogenation (ODH) of light paraffins to the corresponding olefins, such as ethane ODH to ethylene using gaseous oxygen, represent a promising alternative route for olefin production which can reduce energy usage and CO₂ generation.^[6-8] Compared to conventional ODH, the chemical looping oxidative dehydrogenation (CL-ODH) process has the potential to integrate O₂ separation with ODH for lowered energy- and CO₂-intensity as compared to steam cracking.^[9-11]

In contrast with the conventional ethane ODH using gaseous O₂, the CL-ODH scheme relies upon solid oxygen carriers, or redox catalysts, as the source of oxygen for redox reactions.^[8,9] CL-ODH thus comprises two half-reactions occurring in spatially separate reactors which sum to the overall ethane ODH reaction, as depicted in **Figure 4.1**. We have shown in recent studies that redox catalysts in CL-ODH can function merely as oxygen carrying agents for *in-situ* selective hydrogen combustion (SHC).^[10,12-14] Under this operating mode, ethane is dehydrogenated in the ODH reactor to ethylene and hydrogen gases, and hydrogen is preferentially combusted by the lattice oxygen of the redox catalyst to H₂O, which reduces the oxidation state of the solid. Besides

hydrogen combustion, a small fraction of hydrocarbons can also be non-selectively oxidized by the redox catalyst to form CO_x byproducts. The reduced redox catalyst is subsequently re-oxidized by air in the regenerator, consuming O_2 and forming a N_2 -rich effluent mixture, and the fully oxidized solid is circulated back into the reducer to close the cycle. Compared with conventional ODH of ethane, the CL-ODH scheme preserves the major advantages of the original ODH scheme — the net exothermicity of the reaction set, the removal of equilibrium limitations via H_2 removal, and the suppression of coke deposition due to the active lattice oxygen species — and addresses the crucial concerns about ODH, by eliminating gaseous oxygen co-feed conditions and providing built-in air separation via the regeneration reaction. For high-temperature CL-ODH operation in which the dehydrogenation of ethane occurs primarily via thermal cracking, ethylene yields up to 68% have been reported from ethane at 850°C using manganese oxide-based redox catalysts.^[10,12] Compared to industrial steam cracking of ethane, the CL-ODH of ethane can decrease energy consumption and CO_2 emissions by up to 82%.^[11] Similarly, ethane CL-ODH operated at 700°C using an alkali-promoted lanthanum strontium ferrite (LSF) redox catalyst achieved up to 52% ethylene yield.^[15,16] In the latter studies, ethane dehydrogenation occurred catalytically on the promoted LSF surface. While these results are promising, the CL-ODH performance depends strongly on the selection of metal oxide materials for the redox catalyst, as non-selective combustion by lattice oxygen would result in CO_x formation and loss of valuable ethylene or ethane.^[14,17] In both previously cited examples, the propensity of the redox catalyst towards selective hydrogen combustion (over hydrocarbon combustion) enabled high ethylene yield and mitigated the thermodynamic constraints on the $\text{C}_2\text{H}_6/\text{C}_2\text{H}_4/\text{H}_2$ equilibrium.^[10,13,15] Selectivity towards hydrogen combustion (S_{H}) is ultimately one of the most important considerations for redox catalyst development.

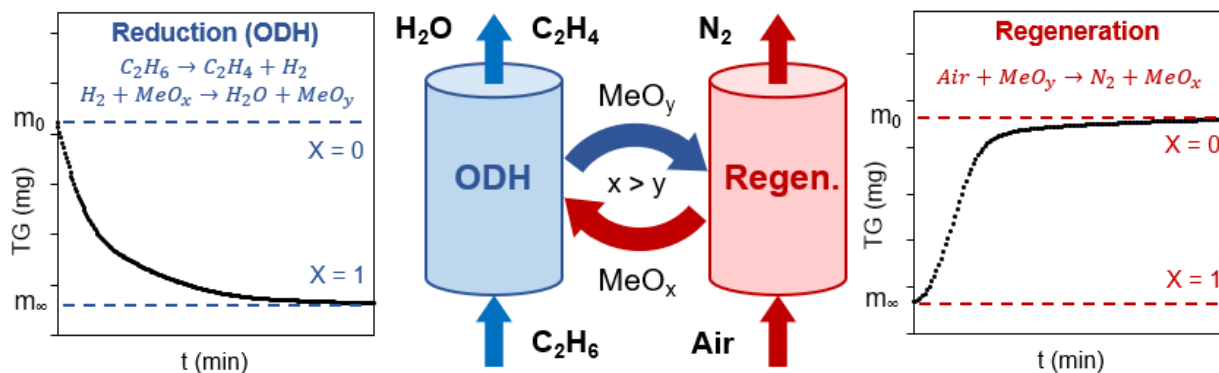


Figure 4.1. Schematic of the ethane chemical looping – oxidative dehydrogenation (CL-ODH) process; (*left*) gravimetric data showing the redox catalyst MeO_x undergo reduction in H_2 to MeO_y ($y < x$); (*right*) gravimetric data representing the regeneration of MeO_y to MeO_x using oxygen from air. X corresponds to dimensionless solid conversion, with $X = 0$ as a fully oxidized solid and $X = 1$ as a fully reduced solid.

Since the late 1980s, several studies have explored selective hydrogen combustion (SHC) as a promising potential strategy to achieve greater-than-equilibrium yields from dehydrogenation (DH) of ethane, propane, and butane.^[18,19] Pioneering contributions by Grasselli and coworkers identified a set of highly selective metal oxide-based catalysts capable of enhancing propylene yields from propane, including a supported Bi_2O_3 catalyst which enabled a 140% increase in propylene generation at 540°C .^[20–22] Subsequent research has focused on the incorporation of SHC catalysts into alkane dehydrogenation processes to improve the yields of ethylene,^[23–25] propylene,^[26–30] etc. Recent work within the chemical looping community showcased improved olefin yields from the conversion of ethane (via CL-ODH) and *n*-hexane feedstocks resulting from hydrogen combustion by highly selective redox catalysts.^[9,10,15–17,31] In these works, the alkali tungstate Na_2WO_4 emerged as a beneficial chemical promoter capable of enhancing selectivity towards hydrogen combustion in multiple systems, including rock salt-structured Mg_6MnO_8 and

perovskite-structured CaMnO_3 and SrMnO_3 .^[9,10,17,31] In summary, a number of promising redox catalysts have been discovered for the SHC reaction, and their effects on olefin yields have been well described. However, despite the multitude of studies demonstrating the SHC properties of various metal oxides via reaction testing, a rigorous investigation of the process variables affecting selective hydrogen combustion has not been attempted. Specifically, to the best of our knowledge, a systematic study focusing on kinetic modeling and parameter estimation of SHC materials in the context of light olefin production has yet to be performed.

In principle, selective hydrogen combustion by a solid oxygen carrier can be described as the preferential reduction of the metal oxide by hydrogen as compared to other hydrocarbons, i.e. materials with high S_H would exhibit rapid reduction rates under H_2 and slower kinetics under ethylene, propylene, etc.^[22] It follows that if the reduction kinetics of a redox catalyst could be modeled and parametrized for multiple gases (for ethane CL-ODH: H_2 , C_2H_4 , C_2H_6), the dynamic S_H of the catalyst could be estimated as a function of key process variables such as temperature (T), reactant gas partial pressure (P_i), and extent of solid conversion or oxygen donation (X), as in traditional solid-state reaction kinetics.^[32] Fortunately, systems for modeling and understanding redox catalyst kinetics have recently begun to emerge for the most well-studied systems (e.g. NiO).^[33,34] Pioneering work by such authors as Evans, Sohn, and Szekely provided much of the basis for contemporary studies of redox catalyst kinetics.^[35–38] Subsequent developments detailing the solid-state kinetics of oxygen carriers under reducing conditions can be found from the chemical looping combustion (CLC) and reforming (CLR) literature, encompassing both supported metal oxides (e.g. $\text{NiO}/\text{Al}_2\text{O}_3$)^[39–44] and bulk metal oxides, including perovskite oxides (e.g. LaMnO_3).^[45–48] In terms of ethane ODH, Elbadawi and coworkers recently described the

reduction kinetics of supported vanadium oxide under a cyclic scheme.^[49] However, the reduction kinetics of bulk mixed oxides in CL-ODH of ethane has not been investigated to date. Moreover, as previously mentioned, no studies have fully investigated the comparative reduction kinetics of an oxygen carrier under two or more gases (H_2 , C_2H_4 , etc.). In the current study, we model the reduction of $CaMnO_3$ based redox catalysts by H_2 , C_2H_4 , and C_2H_6 , with the goal to establish a complete kinetic description of selective hydrogen combustion during the CL-ODH of ethane.

In the present study, we comprehensively examined the selective hydrogen combustion properties of a promising SHC redox catalyst, the perovskite oxide $CaMnO_3$ (with and without a Na_2WO_4 promoter phase),^[17,31] through a combination of fixed-bed reaction testing and thermogravimetric (TG) experiments. We endeavor to quantify the reduction rates of the solid redox catalyst by three gases – hydrogen, ethylene, and ethane – as a function of dynamic process variables. Satisfactory fits were obtained for $CaMnO_3$ and $Na_2WO_4/CaMnO_3$ reduction reactions, with reaction-order models describing the former process and Avrami-Erofe'ev models fitting well to the latter process. Our results demonstrate that $CaMnO_3$ reduction is highly dynamic and dependent upon the extent of solid conversion. On a relative basis, more facile activation of H_2 at later stages of reduction in comparison to C_2H_4 was observed. Moreover, C_2H_6 cannot be combusted by $CaMnO_3$ after partial removal of lattice oxygen. Na_2WO_4 increases the energy barrier for $CaMnO_3$ reduction by both H_2 and C_2H_4 , but reduction rates in H_2 was three orders of magnitude higher than in C_2H_4 , supporting the high selectivity of the $Na_2WO_4/CaMnO_3$ redox catalyst towards hydrogen combustion in the presence of ethylene and ethane.

4.3. Experimental Section

4.3.1. Redox Catalyst Synthesis

Perovskite-structured CaMnO_3 was synthesized using a solid state reaction method (SSR). Stoichiometric amounts of powdered CaCO_3 (Noah) and MnO_2 (Materion) were physically blended in a ceramic jar and mixed for 24 h at 250 rpm in a planetary ball mill. The powder mixture was pressurized to 20 MPa using a pellet press, and the resulting mixed oxide pellets were heated up to 1200°C under air flow at $5^\circ\text{C}/\text{min}$ in a tube furnace and calcined for 12 h to form the cubic perovskite oxide structure. Finally, the sintered CaMnO_3 pellets were crushed by mortar and pestle and sieved into the 150–250 μm particle size range for TGA experiments; powders finer than 150 μm were used for characterization of as-prepared samples.

In addition to the base CaMnO_3 redox catalyst, 20 wt% Na_2WO_4 -promoted CaMnO_3 ($\text{Na}_2\text{WO}_4/\text{CaMnO}_3$) was prepared via wet impregnation. Sodium tungstate dihydrate ($\text{Na}_2\text{WO}_4 \cdot 2\text{H}_2\text{O}$, Sigma-Aldrich) was dissolved in a small amount of water and added dropwise to the as-prepared CaMnO_3 sample. The resulting wet powder was alternately hand-stirred and dried at 90°C until all water had evaporated, then kept at 90°C overnight. Lastly, the $\text{Na}_2\text{WO}_4/\text{CaMnO}_3$ sample was heated at $5^\circ\text{C}/\text{min}$ to 900°C and calcined for 8 h in a muffle furnace, and the powder was re-sieved into the 150–250 μm particle size range. X-ray diffraction (XRD) patterns confirming the phases of the redox catalysts can be found in **Figure C8**.

4.3.2. Fixed-Bed Reactor Experiments

500 mg loadings of CaMnO_3 and $\text{Na}_2\text{WO}_4/\text{CaMnO}_3$ were tested in a fixed-bed configuration using a reactor apparatus detailed in our previous work.^[17] Briefly, gas mixtures were delivered from an

automated gas switching system into a quartz micro-tubular reactor (ID = 1/8") containing the redox catalyst, suspended inside a furnace. Effluent gas from the microreactor was analyzed using a downstream quadrupole mass spectrometer (MKS Cirrus II). In the current study, the selectivity of the redox catalysts was examined in the presence of a H₂/C₂H₄/C₂H₆ mixture. A total flowrate of 55 mL/min, in the ratios of Ar:H₂:C₂H₄:C₂H₆ = 40:5:5:5, served as the inlet gas. At the operating temperature of 650°C, this mixture was thermally equilibrated based on thermodynamic calculations and experimental observations. In a typical fixed-bed cycling experiment, the redox catalyst was exposed to the reducing mixture for 10 min, followed by a 5 min purge (50 mL/min Ar), a 5 min regeneration step (50 mL/min Ar, 10 mL/min O₂), and a second, identical purge.

The effluent gas concentrations from the reduction step were analyzed at ambient conditions using an online MS and converted from m/z signals into volumetric flowrates using pre-determined sensitivity factors. Values of $m/z = 2, 26, 30, 40,$ and 44 were processed for H₂, C₂H₄, C₂H₆, Ar, and CO₂, respectively; ethylene was quantified after first subtracting the $m/z = 26$ contribution from ethane. H₂O formation (and consequently, total lattice oxygen donation) was estimated by determining the actual flowrate of H₂ (over 10 min) at room temperature and integrating the area between this expected H₂ curve and the experimental observation. CO₂ was included in the oxygen balance, while CO formation was insignificant throughout the experiments, as confirmed via gas chromatography.

4.3.3. Kinetics Experiments

Reduction kinetics of CaMnO₃ and Na₂WO₄/CaMnO₃ were determined by measuring the change in mass of the redox catalysts via thermogravimetric analysis (TGA) on a SETARAM Setsys

Evolution TGA-DTA/DSC (hanging basket configuration with a quartz crucible). Experiments were performed on 20 mg of redox catalyst in the 150–250 μm particle size range; 20 mg was selected to keep a thin sample layer (~ 1 mm height) and minimize the limiting effects of external mass transfer on reduction kinetics. Prior to each kinetic experiment, the sample was cycled five times at 750°C between reducing (20 mL/min H_2) and oxidizing (20 mL/min O_2) gas flows, with a constant inert purge stream (180 mL/min He), to ensure material stability and kinetic reproducibility while minimizing external mass transfer effects. The effectiveness of these conditions for avoiding mass transfer effects are demonstrated in **Figures C9–C11** of *Appendix C*. In addition, phase compositions of reduced CaMnO_3 and $\text{Na}_2\text{WO}_4/\text{CaMnO}_3$ redox catalysts, subjected to the above stabilizing procedure and ending with two full cycles and one reduction half-cycle at 650°C, are available in the **Figure C12**.

In a typical cycling experiment, a pre-cycled sample was maintained at isothermal conditions and reduced under 10% of a single reducing gas for 20 minutes (20 mL/min H_2 , C_2H_4 , or C_2H_6 , in 180 mL/min He or Ar carrier gas), purged in pure inert for 10 minutes, re-oxidized in 10% O_2 (20 mL/min O_2 in 180 mL/min He or Ar), and purged again in inert flow. At least four temperature conditions were examined for every combination of sample and reducing gas, with three cycles recorded at each temperature. Reduction kinetics experiments using hydrogen were conducted between 500°C and 650°C at 50°C increments. Experiments using ethylene and ethane were conducted across a narrower temperature range of 650°C to 700°C, with four intermediate conditions at 665°C, 675°C, 685°C, and 695°C. Lastly, each experiment was performed in an identical manner on an empty crucible to account for the buoyancy and drag effects. Background TG data obtained from blank crucible experiments was aligned with and subtracted from the TG

data in the main experiment. A mass spectrometer located downstream of the TGA provided additional information about the combustion products, with data analysis proceeding as described in the preceding section.

Corrected TG data from kinetic experiments, in the form of mass against time (m , mg vs. t , min), were transformed into a dimensionless solid conversion, X vs. t , using the following equation:

$$X(t) = \frac{m_0 - m(t)}{m_0 - m_\infty}$$

In the above calculation, m_0 represents the fully oxidized sample mass prior to introduction of the reducing gas, m_∞ represents the final sample mass after 20 minutes of reduction, and $m(t)$ is the sample mass (mg) at time t (min) during the reduction step. $t = 0$ is defined as the point at which the reducing gas enters the TGA chamber. $X = 0$ thus indicates a fully oxidized redox catalyst, while $X = 1$ is reached when the solid has been completely reduced.

4.3.4. Kinetic Modeling

Processed experimental TGA data in the form X vs. t and dX/dt vs. X were next compared to predictions from 15 kinetic reaction models to empirically describe the reduction behavior of CaMnO_3 and $\text{Na}_2\text{WO}_4/\text{CaMnO}_3$ and evaluate the key kinetic parameters. The set of 15 reaction models in **Table 4.1** draws from the solid state reaction models typically employed in the chemical looping literature to model kinetics of oxygen carrier reduction and oxidation.^[33,34,50] Four types of single-parameter kinetic models were considered in the present study: reaction-order models (F), geometric contraction models (R), diffusion-limited models (D), and the Avrami–Erofe’ev nucleation and nuclei growth models (AE). More complex reaction models with two or more

parameters were not considered. In all cases, the single fitting parameter was the kinetic rate constant k (min^{-1}).

Table 4.1. The set of 15 reaction models evaluated in the current study. Each model is designated by an alphanumeric name based on its category: reaction-order models (F); geometric contraction models (R); diffusion-limited models (D); Avrami–Erofe’ev nucleation models (AE).^[50]

Name	Reaction model description	Differential form $f(X) = 1/k \, dX/dt$	Integral form $g(X) = kt$
F1	First-order or Avrami–Erofe’ev ($n = 1$)	$(1-X)$	$-\ln(1-X)$
F1.5	Three-halves order	$(1-X)^{3/2}$	$2[((1-X)^{-1/2} - 1]$
F2	Second-order	$(1-X)^2$	$1/(1-X) - 1$
F3	Third-order	$(1-X)^3$	$(1/2)[(1-X)^{-2} - 1]$
R1	Zero-order	1	X
R2	Contracting area	$2(1-X)^{1/2}$	$1 - (1-X)^{1/2}$
R3	Contracting volume	$3(1-X)^{2/3}$	$1 - (1-X)^{1/3}$
D1	1-D diffusion	$1/(2X)$	X^2
D2	2-D diffusion, Valensi equation	$1/[-\ln(1-X)]$	$(1-X) \ln(1-X) + X$
D3	3-D diffusion, Jander equation	$3(1-X)^{1/3}/[2(1-X)^{-1/3} - 1]$	$[1 - (1-X)^{1/3}]^2$
D4	Ginstling–Bronshtein equation	$3/[2(1-X)^{-1/3} - 1]$	$1 - 2X/3 - (1-X)^{2/3}$
AE0.5	Avrami–Erofe’ev ($n = 0.5$)	$(1/2)(1-X)[-\ln(1-X)]^{-1}$	$[-\ln(1-X)]^2$
AE1.5	Avrami–Erofe’ev ($n = 1.5$)	$(3/2)(1-X)[-\ln(1-X)]^{1/3}$	$[-\ln(1-X)]^{2/3}$
AE2	Avrami–Erofe’ev ($n = 2$)	$2(1-X)[-\ln(1-X)]^{1/2}$	$[-\ln(1-X)]^{1/2}$
AE3	Avrami–Erofe’ev ($n = 3$)	$3(1-X)[-\ln(1-X)]^{2/3}$	$[-\ln(1-X)]^{1/3}$

The results of each isothermal TGA experiment were fitted to the 15 reaction models according to the following approach. Processed TGA data in the form X vs. t were aligned with predictions for $X(t)$ from each reaction model based on the same values of the independent variable t (min) according to its integral function $g(X) = kt$. The value of the kinetic model fitting parameter k (min^{-1}) was reached by minimizing the residual sum of squares (RSS) between the predicted value for X and the experimentally measured X , with the RSS calculated as below:

$$RSS = \sum_{i=1}^n (y_{model} - y_{experimental})^2$$

Minimization of RSS was achieved using the Generalized Reduced Gradient (GRG) Nonlinear algorithm. Each model took an initial estimate of $k = 1 \text{ min}^{-1}$; identical convergence was reached using the initial value of $k = 0.2 \text{ min}^{-1}$. The summation of errors for calculating RSS was evaluated only for the range $0.15 \leq X \leq 0.6$ to avoid instrumental artifacts during the initial entrance of gas to the TGA chamber as well as sample geometrical factors in the later stages of reduction.^[51] For ethylene kinetics, $0.15 \leq X \leq 0.5$ was selected to balance the high frequency of sampling during the later stage of conversion. The resulting value for the kinetic rate constant k gave the greatest fit of each reaction model to the experimental kinetic data. Following the determination of the fitting parameter using the integral form, the approach was repeated to fit TGA results of dX/dt vs. X against the model predictions $dX/dt = k f(X)$. The value for k determined from the differential form was averaged with that from the integral form to give the final estimate for k in min^{-1} .

The fitting procedure described previously was applied separately to each isothermal condition, resulting in four k values across the range 500°C to 650°C for H_2 and six k values across 650°C to 700°C for C_2H_4 . The reaction model with the smallest RSS among the 15 candidate models was selected for each temperature. Generally, the overall selected model provided the smallest or second-smallest RSS across the entire range of temperatures, indicating the general goodness of fit achieved by the model; see *Appendix C* for details. The set of k values obtained using the overall best-fit reaction model over the range of temperatures was linearized against $1/T$ (K^{-1}) via the Arrhenius relation to obtain empirical estimates for the activation energy (E_a , kJ mol^{-1}) and pre-exponential factor (k_0 , min^{-1}) for the reduction of CaMnO_3 by each gas.

4.4. Results and Discussion

4.4.1. Selective Hydrogen Combustion by CaMnO₃-Based Redox Catalysts

Previous studies have demonstrated the effectiveness of CaMnO₃ as a redox catalyst for selective hydrogen combustion (SHC) in the presence of light hydrocarbons (e.g. ethylene, propylene); moreover, the addition of 20 wt% Na₂WO₄ to CaMnO₃ (forming Na₂WO₄/CaMnO₃), has been shown to significantly increase the selectivity of base CaMnO₃ through creation of a Na- and W-rich surface layer which suppresses surface-bound oxygen species.^[17,31] The promising performance of CaMnO₃ and Na₂WO₄/CaMnO₃ at temperatures around 650°C potentially makes the redox catalysts suitable for a sequential process featuring ethane dehydrogenation followed by selective hydrogen combustion (EDH+SHC). Using the proposed EDH+SHC process as a case study, we endeavor in the present work to quantitatively explain the high selectivity of CaMnO₃ and Na₂WO₄/CaMnO₃ by studying their reduction kinetics in the presence of H₂, C₂H₄, and C₂H₆.

Experimental investigations of SHC performance typically have compared redox catalysts on the basis of an overall selectivity towards H₂ combustion, S_H , though the definition of S_H varies depending on the technique used for its determination (TGA, GC, MS, etc.).^[22,23] Here, we base our calculation of S_H on the experimentally measured inlet and outlet molar amounts of H₂ and CO₂, which are determined via mass spectrometry, as defined below:

$$S_H = \frac{(n_{H_2,in} - n_{H_2,out})}{(n_{H_2,in} - n_{H_2,out}) + \frac{1}{2}n_{CO_2,out}} \equiv \frac{\text{mol } H_2 \text{ converted}}{\text{mol } H_2 + C_2H_4 + C_2H_6 \text{ converted}}$$

The proposed definition of S_H is applied to the results of **Figure 4.2**, which illustrates the selective oxidation of H_2 versus C_2H_4 and C_2H_6 feed gases by (a) $CaMnO_3$ and (b) $Na_2WO_4/CaMnO_3$, as well as the subsequent reduction of each redox catalyst represented by the oxygen donation Δm (wt%). As shown in **Figure 4.2a**, $CaMnO_3$ possesses significant activity towards H_2 combustion; $CaMnO_3$ combusted more than 90% of the inlet H_2 during the first 2 min (the dashed blue line indicates inlet H_2), while approximately 72% of H_2 is converted throughout the complete 10 min. The presence of notable CO_2 flow at the beginning of the experiment indicates that $CaMnO_3$ by itself is not entirely selective ($S_H = 93.2\%$); however, CO_2 disappears after $t = 5$ min while instantaneous H_2 combustion remains greater than 50%, showing that the reduction of $CaMnO_3$ by ethylene or ethane is relatively difficult at higher solid conversion as compared to reduction by hydrogen.

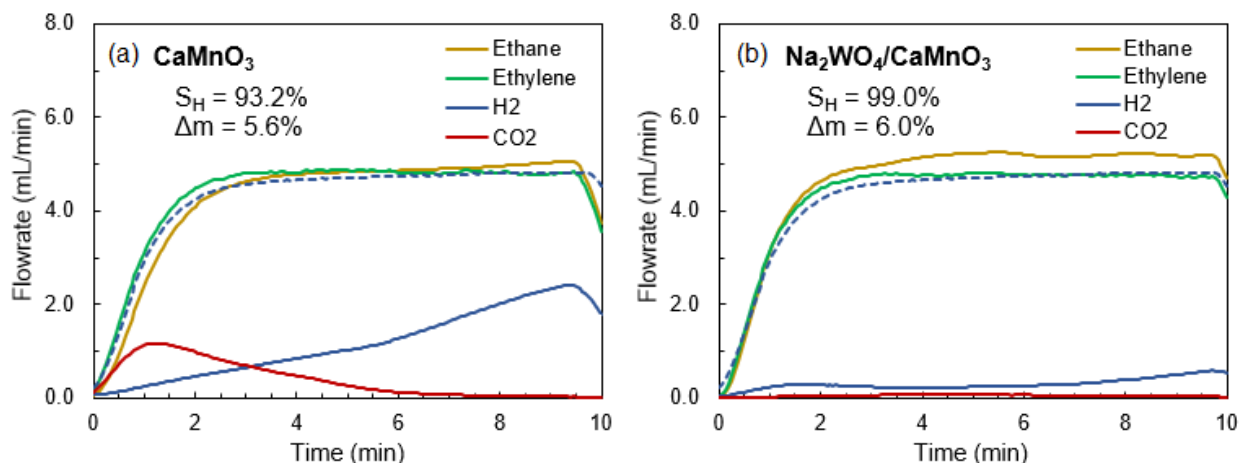


Figure 4.2. Time-on-stream measurements of the effluent gas from an ethane dehydrogenation + selective hydrogen combustion scheme (EDH+SHC), utilizing (a) CaMnO_3 and (b) $\text{Na}_2\text{WO}_4/\text{CaMnO}_3$ as redox catalysts. Inlet gas flowrates were chosen to simulate the effluent gas from the dehydrogenation of ethane. The dashed blue line indicates the expected flow of hydrogen gas in absence of an oxygen donor. $S_H \equiv$ selectivity towards hydrogen combustion (%), $\Delta m \equiv$ oxygen donation (wt.%). Conditions: $m_0 = 500$ mg, $F_{Ar} = 40$ mL/min,

$$F_{C_2H_6} = F_{C_2H_4} = F_{H_2} = 5 \text{ mL/min}, T = 650^\circ\text{C}.$$

Promotion of CaMnO_3 with 20 wt% Na_2WO_4 resulted in a noteworthy increase in selectivity ($S_H = 99.0\%$ vs. 93.2%) as well as slightly greater activity ($\Delta m = 6.0$ wt% vs. 5.6 wt%), as pictured in **Figure 4.2b**. CO_2 formation over the course of 10 min was nearly undetectable, which indicates that the reduction of $\text{Na}_2\text{WO}_4/\text{CaMnO}_3$ by C_2H_4 or C_2H_6 was not favored in the presence of H_2 co-feed. Moreover, the extremely low H_2 signal suggests that $\text{Na}_2\text{WO}_4/\text{CaMnO}_3$ possesses rapid kinetics for H_2 combustion at 650°C , such that the consumption of hydrogen was limited only by the inlet H_2 flowrate. Overall, the results shown in **Figure 4.2b** agree with our previous findings related to the SHC performance of $\text{Na}_2\text{WO}_4/\text{CaMnO}_3$ in an EDH+SHC sequential reaction scheme at 650°C .^[17]

4.4.2. Reduction Kinetics of CaMnO_3

Perovskite oxide-structured CaMnO_3 has been shown to donate lattice oxygen towards the combustion of hydrogen starting around 500°C and towards the activation and total combustion of hydrocarbons starting around 650°C . Kinetics information for the reduction of CaMnO_3 was thus obtained via TGA measurements between 500°C and 700°C ; at greater temperatures, thermal cracking of ethane becomes significant, leading to coke deposition on the TGA crucible or the redox catalyst and interference with TG weight loss and gain. At 650°C , CaMnO_3 is reduced by each of the three gases under consideration – H_2 , C_2H_4 , and C_2H_6 . Thus, the single-gas reduction kinetics of CaMnO_3 can be compared effectively at 650°C in terms of dimensionless conversion (X vs. t) and its derivative (dX/dt vs. X).

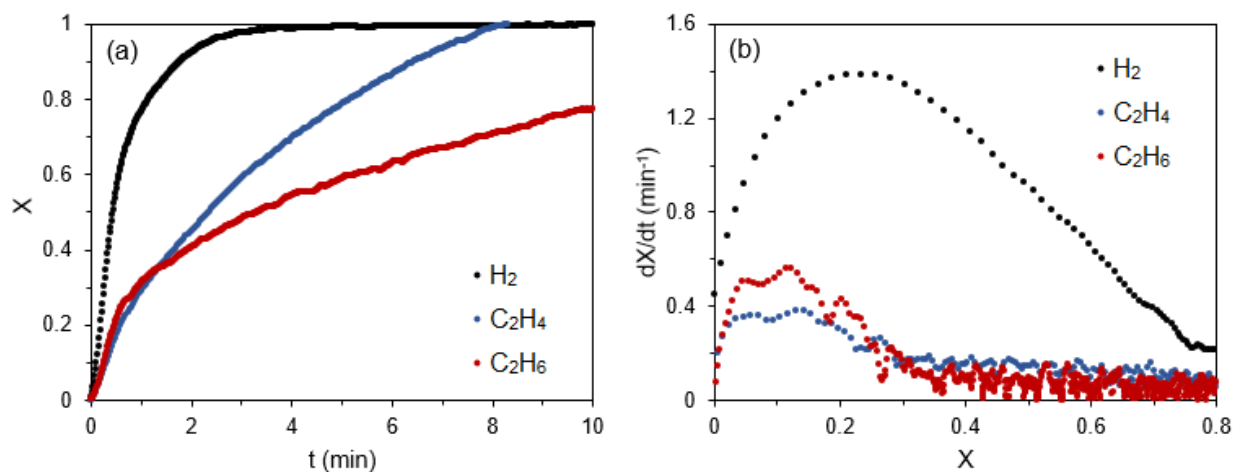


Figure 4.3. Results of three reduction kinetics experiments for CaMnO_3 using H_2 , C_2H_4 , and C_2H_6 at 650°C .

(a) Dimensionless conversion (X) vs. time (t , min); (b) time derivative of conversion (dX/dt) vs. conversion (X). Mass measurements (in mg) were obtained via thermogravimetric analysis. Conditions: $m_0 = 20$ mg, $150\text{--}250$ μm , $T = 650^\circ\text{C}$, $P = 1$ atm, $F_{\text{total}} = 200$ mL/min (20 mL/min $\text{H}_2/\text{C}_2\text{H}_4/\text{C}_2\text{H}_6$, 180 mL/min He or Ar).

Figure 4.3a–b illustrates the differences in the kinetics of reduction for CaMnO_3 under 10% H_2 , 10% C_2H_4 , and 10% C_2H_6 gas environments at 650°C . Hydrogen reduced CaMnO_3 more rapidly than either ethylene or ethane, as shown in **Figure 4.3a**; the dimensionless conversion X reached a value of 0.95 around $t = 3$ min during reduction with H_2 , whereas C_2H_4 reached $X = 0.95$ around the $t = 7$ min mark and C_2H_6 could not deplete the lattice oxygen of CaMnO_3 past approximately $X = 0.75$ after 10 min. In **Figure 4.3b**, the reduction rates (dX/dt) are directly compared across the three gases as a function of the dimensionless conversion. The rates of CaMnO_3 reduction by C_2H_4 and C_2H_6 were significantly lower than the reduction rate under H_2 over the entire range of conversion, which was consistent with previous findings identifying CaMnO_3 as a selective redox catalyst for H_2 combustion. Moreover, H_2 was capable of sustaining a rapid rate of oxygen removal from the CaMnO_3 lattice until $\sim 75\%$ solid conversion, whereas both C_2 hydrocarbons experienced a sharp decrease in reduction rate after only 30% removal of the CaMnO_3 lattice oxygen. Ethylene maintained a slightly higher activation and reduction rate of CaMnO_3 as compared to ethane for $X > 0.3$, potentially due to the relatively greater adsorption energy of alkenes on oxide surfaces.^[52] It is worth noting that ethylene and ethane displayed sluggish kinetics for CaMnO_3 reduction without the presence of H_2 . **Figure 4.3** therefore indicates that selective hydrogen combustion (SHC) is likely not a sole consequence of competitive activation and reduction of a metal oxide in the presence of H_2 , C_2H_4 , etc., but is at least partially due to the intrinsic characteristics of each individual gas reacting with the oxide.

By combining TGA data for CaMnO_3 reduction under ethylene and ethane gases with downstream MS measurements, a more complete understanding of the combustion reactions was obtained. **Figure 4.4** shows coupled TGA-MS results for the reduction of CaMnO_3 by C_2H_4 (solid lines) and

by C_2H_6 (dashed lines), with the dimensionless conversion X for each solid-gas reaction reproduced from **Figure 4.3**. For the case of $CaMnO_3$ reduction by ethylene, the curve of dimensionless conversion X aligns as expected with the 10-minute duration of CO_2 generation, suggesting the combustion of C_2H_4 to CO_2 and H_2O through a direct reaction between C_2H_4 and $CaMnO_3$, which removes lattice oxygen from the perovskite oxide. The small yet consistent amount of H_2 was due either to desorption of H_2 formed during the ethylene conversion or as a byproduct of ethylene decomposition to coke. In the case of ethane, however, TGA-MS revealed that $CaMnO_3$ was only able to directly react with ethane at the beginning of the reaction ($X < 0.3$); for $X > 0.3$, ethane was not combusted by $CaMnO_3$, as evident from the decline in $F-CO_2$. This point also coincided with the crook in the $X(t)$ curve for the reduction of $CaMnO_3$ by ethane near $t = 1$ min, suggesting a change in the $CaMnO_3$ reduction mechanism. The presence of substantial background H_2 from gas phase ethane dehydrogenation (~ 0.35 mL/min H_2 detected throughout) suggested that the remaining 70% of solid conversion during the ethane experiment was not likely to be due to reduction by ethane but instead was a result of hydrogen combustion. Owing to the largely insignificant activation of $CaMnO_3$ by C_2H_6 compared to the more reactive C_2H_4 , and to the difficulties imposed by ethane dehydrogenation even at relatively low temperatures, we chose to focus the remainder of this study on C_2H_4 as a model hydrocarbon reactant.

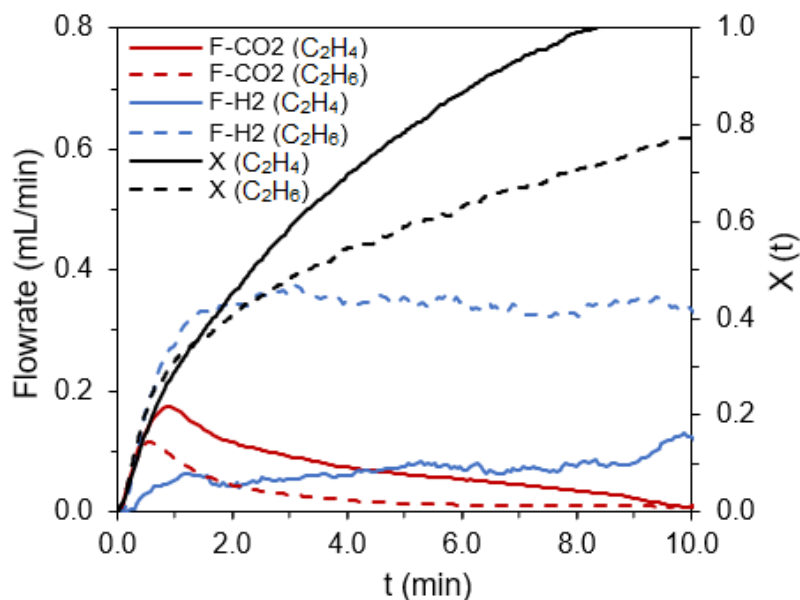


Figure 4.4. TGA-MS data for CaMnO_3 reduction kinetics experiments utilizing C_2H_4 (solid lines) and C_2H_6 (dashed lines) individually as reducing gases. $F\text{-H}_2$ and $F\text{-CO}_2$ are volumetric flow rates from the outlet of the TGA determined via MS from $m/z = 2$ and 44, respectively, while X is the dimensionless solid conversion of CaMnO_3 by each reducing gas determined via TGA. Conditions: $m_0 = 20$ mg, $150\text{--}250$ μm , $T = 650^\circ\text{C}$, $P = 1$ atm, $F_{\text{total}} = 200$ mL/min (20 mL/min $\text{C}_2\text{H}_4/\text{C}_2\text{H}_6$, 180 mL/min Ar).

Multiple isothermal experiments were conducted across a range of operating temperatures using the CaMnO_3 redox catalyst under H_2 and C_2H_4 gas environments in order to obtain temperature-dependent kinetic information. **Figure 4.5** presents the reduction of CaMnO_3 by H_2 at four temperatures from 500°C to 650°C , in terms of X (**Figure 4.5a**) and dX/dt (**Figure 4.5b**). The lattice oxygen of CaMnO_3 was easily extracted by hydrogen gas as low as $T = 500^\circ\text{C}$, with 80% solid conversion reached within 3 min. The kinetics of CaMnO_3 reduction by H_2 exhibit a strong dependence on temperature across the range of conditions examined; the peak rate of reduction at 650°C ($dX/dt \approx 1.4$) was more than twice that of the highest reduction rate at 550°C ($dX/dt \approx 0.6$). At all four temperatures, the reduction rate passes through an elbow near $X = 0.5\text{--}0.6$ and the

remaining solid conversion is a considerably slower process, indicating the relative difficulty of oxygen removal once the original cubic perovskite CaMnO_3 is reduced beyond the brownmillerite phase ($\text{Ca}_2\text{Mn}_2\text{O}_5$).

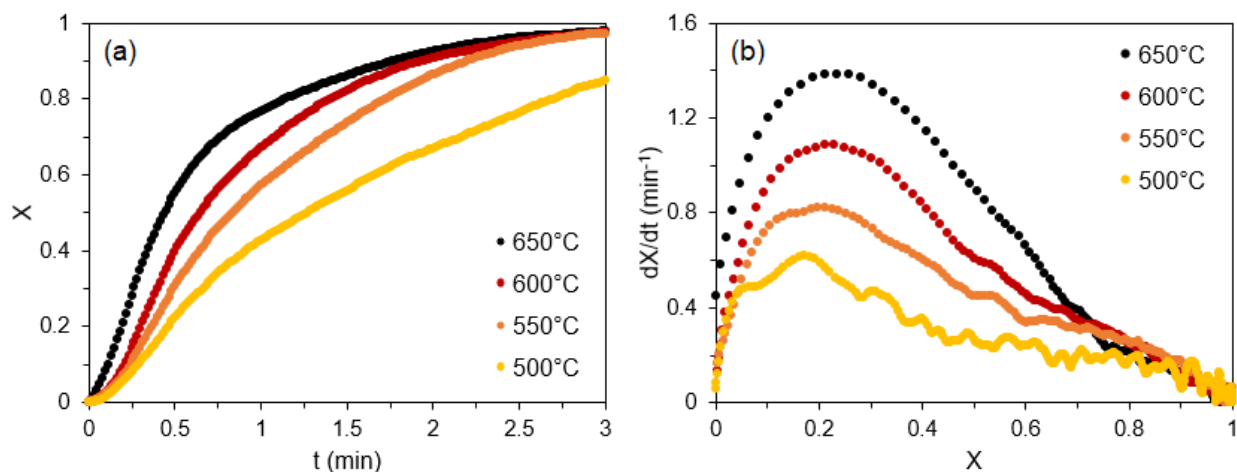


Figure 4.5. Reduction of CaMnO_3 by H_2 during four isothermal TGA experiments. **(a)** Dimensionless solid conversion (X) as a function of time; **(b)** time derivative of conversion (dX/dt) as a function of conversion. Conditions: $m_0 = 20$ mg, $150\text{--}250$ μm , $T = 500\text{--}650^\circ\text{C}$, $P = 1$ atm, $F_{\text{total}} = 200$ mL/min (20 mL/min H_2 , 180 mL/min He).

Figure 4.6a–b shows results from analogous reduction kinetic experiments using ethylene over a range of isothermal conditions (650°C to 700°C). Reduction kinetics for CaMnO_3 under C_2H_4 are consistently dependent on temperature, both in the initial reduction region ($0 \leq X \leq 0.3$) and in the remaining duration of solid conversion up until $X = 1.0$. The decrease in reduction rate around $X = 0.3$, demonstrated most clearly in the derivative dX/dt curves of **Figure 4.6b**, likely resulted from the initial removal of near-surface lattice oxygen and consequent drop in effective concentration of surface oxygen sites during the remainder of the reduction step. However, as noted previously during the comparison of H_2 , C_2H_4 , and C_2H_6 kinetics at 650°C (**Figure 4.3**), the reduction rates

for CaMnO_3 were faster and more stable for hydrogen than for ethylene, even at intermediate to high solid conversion X where the surface oxygen concentration was necessarily lower for both. The implications of this key difference will be further explored in the analyses that follow.

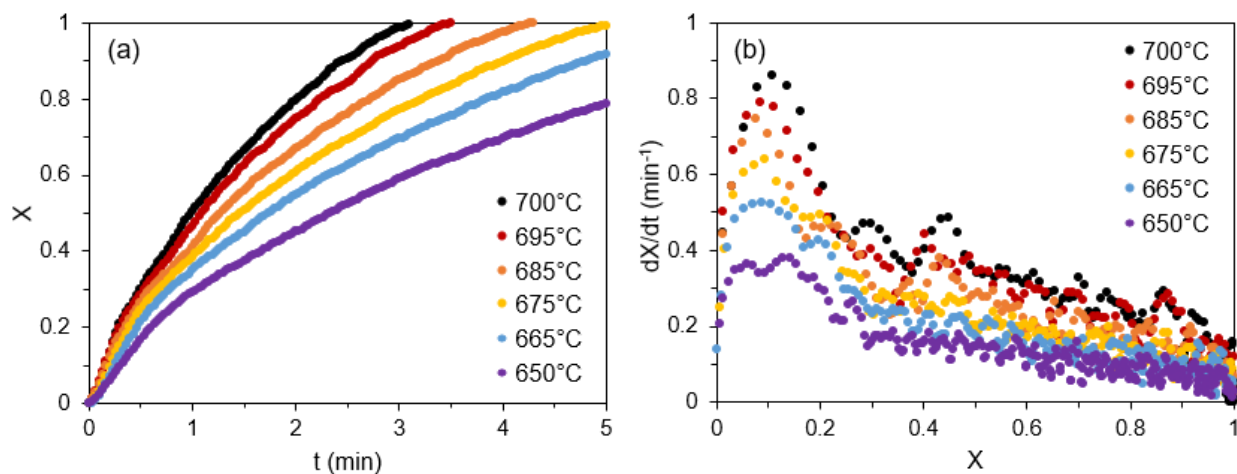


Figure 4.6. Reduction of CaMnO_3 by C_2H_4 during six isothermal TGA experiments. **(a)** Dimensionless solid conversion (X) as a function of time; **(b)** time derivative of conversion (dX/dt) as a function of conversion.

Conditions: $m_0 = 20$ mg, $150\text{--}250$ μm , $T = 650\text{--}700^\circ\text{C}$, $P = 1$ atm, $F_{\text{total}} = 200$ mL/min (20 mL/min C_2H_4 , 180 mL/min Ar).

4.4.3. Kinetic Model Fitting and Parameter Estimation for CaMnO_3

Empirical kinetic modeling analyses were performed on the processed TGA data, in integral form X vs. t and in differential form dX/dt vs. X , in order to obtain approximate kinetic parameters (activation energy E_a , pre-exponential factor k_0) and qualitative insights for the reduction of CaMnO_3 by H_2 and by C_2H_4 . 15 solid-state reaction models were screened for the CaMnO_3 reduction reaction (see **Table 4.1** in Section 4.3.4), and the residual sum of squares (RSS) for each prediction was used as the statistical indicator to assess the fit quality of the candidate kinetic

models. The best-fit RSS values accompanying all 15 kinetic models at each temperature condition, and for several combinations of reducing gas and redox catalyst, are collected in **Tables C1–C3**.

Figure 4.7 illustrates the TGA data for the reduction of CaMnO_3 by H_2 from 500°C to 650°C along with the prediction of the best-fitting kinetic model, F1. **Table C1** provides the fitting statistics for the 15 kinetic models considered. Of the four categories examined, the reaction-order type model (F) was most well-suited to describing the reduction of CaMnO_3 by H_2 , and the first-order reaction model predictions (F1) generally provided the lowest RSS compared to the experimental data. In evaluating various types of kinetic models (see **Figure C1**), the geometric contraction models fit the integral form of the reduction data reasonably well, but failed to accurately predict the rate of change of the solid conversion; the opposite can be said of the diffusion models, which matched the slope of the dX/dt curves well but were not suitable to describe the conversion over time. In contrast, the F1 model – which predicts a decelerating rate of reduction based on the decreasing availability of reactant (in this case, the available lattice oxygen) – more closely matched both the integral and differential data.^[32] As discussed in *Section 4.3.4*, the fitting methodology excludes data from $X < 0.15$ to avoid instrumental effects weighing on the fit. The values of k vs. T derived from the F1 model predictions were therefore chosen to evaluate the Arrhenius temperature dependence of CaMnO_3 reduction with H_2 and to estimate the apparent kinetic parameters.

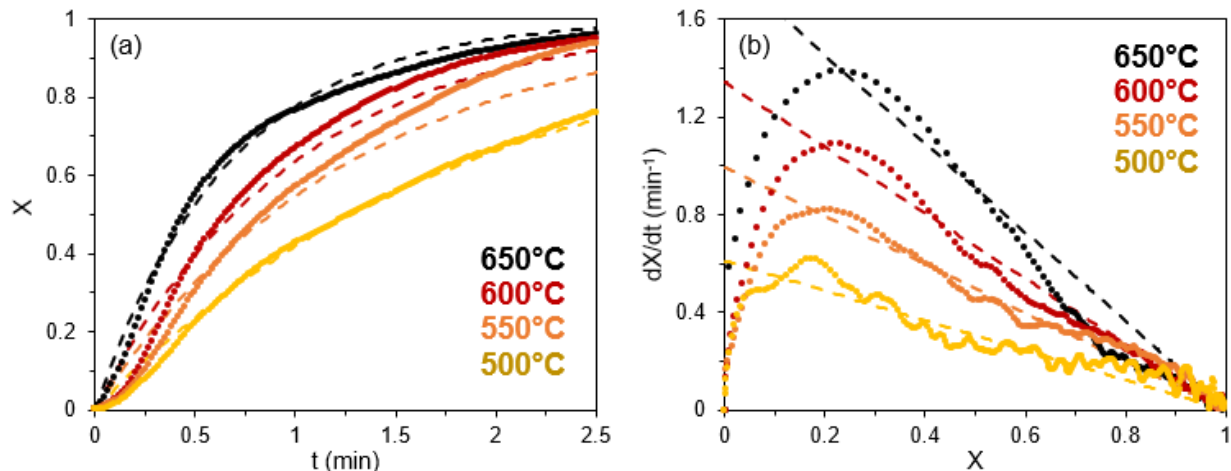


Figure 4.7. Kinetic modeling results showing the model predictions of the best-fit kinetic model, F1 (the first-order reaction model), in the (a) integral form and (b) differential form, for the reduction of CaMnO_3 by H_2 from 500°C to 650°C. Points represent the experimental data and dotted lines represent the F1 model predictions.

Experimental data and best-fit reaction models for the reduction kinetics of CaMnO_3 under C_2H_4 flow are provided in **Figure 4.8**, with the accompanying statistical values for all 15 kinetic models collected in **Table C2**. As with the kinetics under H_2 , the integral and differential conversion data for CaMnO_3 reduction by ethylene were fit best by a kinetic model from the reaction-order category (F), though all types were considered (see **Figure C2**). In contrast to H_2 , which matched to F1, the activation of C_2H_4 and subsequent extraction of lattice oxygen are described better by the F2 and F1.5 models near 650°C and 700°C, respectively—neither model was best for all six temperatures. The difference in best-fit across this temperature range may be explained by the relative availability of surface oxygen sites on CaMnO_3 during the reaction; at lower temperatures, the conduction of oxygen through the lattice to the CaMnO_3 surface would be slower and the surface concentration of oxygen sites correspondingly lower, giving the impression of a reaction more limited by surface oxygen concentration (i.e. a higher exponent to the $[1-X]$ term). The three-

halves reaction-order model (F1.5), with a conversion dependence of $(1-X)^{3/2}$, possessed superior fit quality to F2 over the entire range from 650°C to 700°C (see **Table C2**), and was therefore selected to model the reduction of CaMnO_3 by ethylene (**Figure 4.8**).

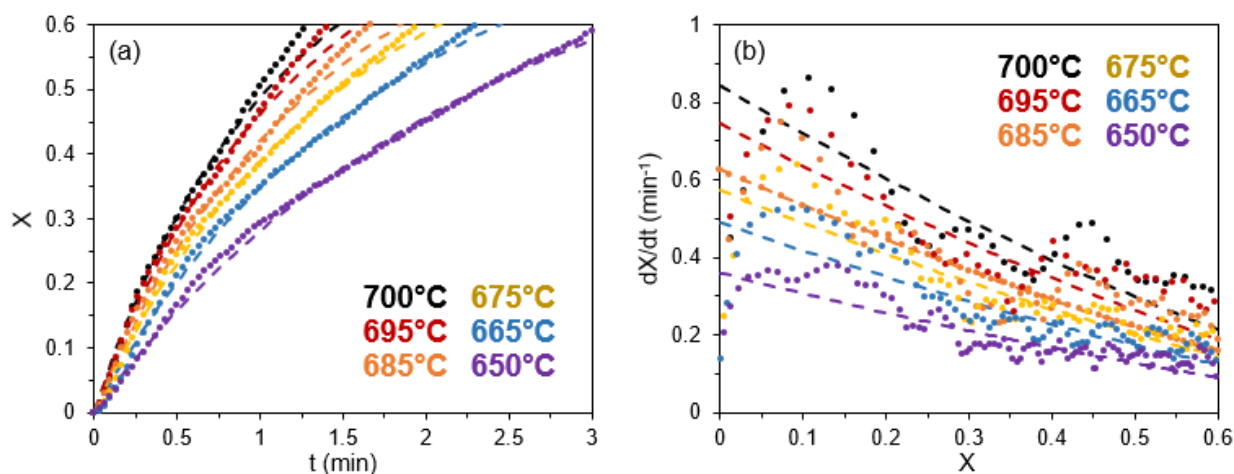


Figure 4.8. Kinetic modeling results showing the model predictions of the best-fit kinetic model, F1.5 (the three-halves reaction-order model), in the (a) integral form and (b) differential form, for the reduction of CaMnO_3 by C_2H_4 from 650°C to 700°C. Points represent the experimental data and dotted lines represent the F1.5 model predictions.

A direct comparison of the best-fit kinetic models determined to describe CaMnO_3 reduction kinetics—F1 for reduction in H_2 and F1.5 for C_2H_4 —provides useful information about the dynamic combustion behavior of CaMnO_3 in $\text{H}_2/\text{C}_2\text{H}_4$ mixtures. At constant temperature of 650°C and equal partial pressures of H_2 and C_2H_4 , CaMnO_3 in a fixed-bed configuration was shown to continuously combust H_2 in the presence of C_2H_4 and C_2H_6 while at intermediate solid conversion, despite the decrease in activity towards the hydrocarbons by this point (see **Figure 4.2**). This observation is partially explained by the empirical description of the reduction rate in C_2H_4 – a function of $(1-X)^{3/2}$ – that is, the reduction rate in C_2H_4 should deteriorate more quickly than the

reduction rate of H₂ (dependent on [1-X]) when measured at the same solid conversion, X, which is supported also by the data of **Figure 4.3**. One potential explanation for the varying dependence on solid conversion is that H₂ requires only one surface oxygen site, whereas C₂H₄ requires two or more adjacent sites being available.

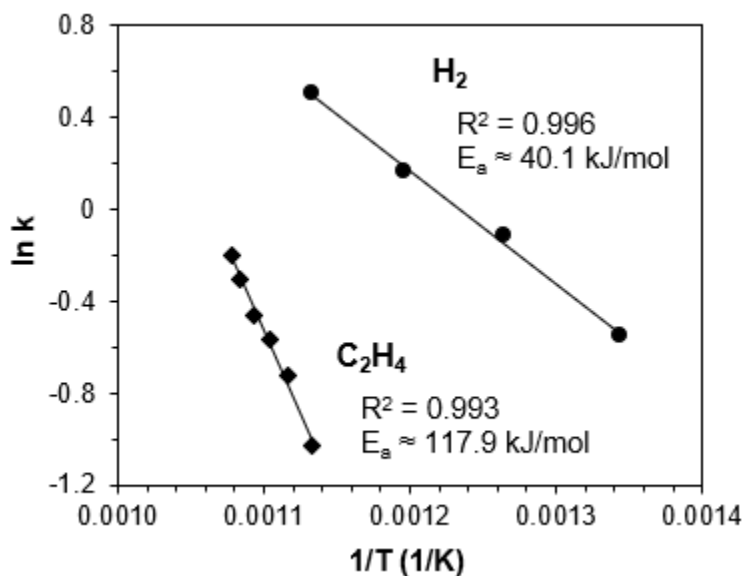


Figure 4.9. Arrhenius plot based on the rate constants for CaMnO₃ reduction by H₂ and by C₂H₄ across the temperature range 500°C to 700°C. Rate constants k (min⁻¹) were extracted from the most well-fitting kinetic models (F1 for H₂, F1.5 for C₂H₄) as determined via statistical analyses. Estimates for apparent activation energy, E_a (kJ mol⁻¹), were calculated from the Arrhenius slope, m , as $E_a \approx -mRT$.

By evaluating the reduction rates of CaMnO₃ in H₂ and C₂H₄ gas environments across appropriate temperature ranges (500°C to 650°C, and 650°C to 700°C, respectively), and using the most well-fitting kinetic models as determined via statistical analysis (F1 and F1.5, respectively), two sets of rate constants were derived for the reduction of CaMnO₃. **Figure 4.9** shows the Arrhenius relation between k (min⁻¹) and $1/T$ (K⁻¹) for the reduction rates using H₂ and C₂H₄. Results for both gases demonstrate excellent linearity, supporting the choice of the F1 and F1.5 models for the data sets.

The Arrhenius slope provides additional information regarding the relative ease of reduction for CaMnO_3 in the presence of hydrogen gas as compared to ethylene; for the former case, CaMnO_3 exhibits an apparent activation energy of 40.1 kJ mol^{-1} in H_2 . In the latter case, the apparent reduction energy barrier for C_2H_4 shows an approximate value of $117.9 \text{ kJ mol}^{-1}$, nearly three times greater than the value for H_2 , indicating that C_2H_4 combustion by CaMnO_3 is relatively more sensitive to temperature. The difference in apparent activation energy and solid conversion dependence for H_2 vs. C_2H_4 together provide a quantitative measure of the inherent propensity of the CaMnO_3 redox catalyst for selective hydrogen combustion.

Having determined the explicit dependence of CaMnO_3 reduction on solid conversion X (via the choice of reaction model) and on temperature (via the apparent E_a) for both H_2 and C_2H_4 , as well as the rate dependence on partial pressure P_i , a complete reduction rate equation may be assembled using the form:^[32]

$$\frac{dX}{dt} = k(T) f(X) h(P_i)$$

For conversion of the CaMnO_3 solid by H_2 gas, the following equation may be applied:

$$\frac{dX}{dt} = (3.42 \times 10^2 \text{ min}^{-1}) \exp\left(\frac{-40.1 \frac{\text{kJ}}{\text{mol}}}{8.314 \times 10^{-3} \frac{\text{kJ}}{\text{mol K}} T (\text{K})}\right) (1 - X) \left(\frac{P_{\text{H}_2}}{P}\right)^{0.61}$$

CaMnO_3 reduction by C_2H_4 can be described with the below variation:

$$\frac{dX}{dt} = (1.73 \times 10^6 \text{ min}^{-1}) \exp\left(\frac{-117.9 \frac{\text{kJ}}{\text{mol}}}{8.314 \times 10^{-3} \frac{\text{kJ}}{\text{mol K}} T (\text{K})}\right) (1 - X)^{3/2} \left(\frac{P_{\text{C}_2\text{H}_4}}{P}\right)^{0.28}$$

As discussed in *Appendix C (Figures C3–C6)*, the reduction of CaMnO_3 in H_2 was of higher order ($n = 0.61$) than that for reduction by C_2H_4 ($n = 0.28$). The provided single-gas CaMnO_3 reduction equations provide a basis for subsequent investigations to develop a solid conversion model describing the reduction of CaMnO_3 in gas mixtures including H_2 , C_2H_4 , and other hydrocarbons, and ultimately to predict CaMnO_3 selectivity towards hydrogen combustion at a variety of temperatures and partial pressures as a function of solid conversion. The remainder of this study deals with the addition of Na_2WO_4 to CaMnO_3 and its effect on these kinetics.

4.4.4. Effect of Sodium Tungstate on Reduction Rates

In our previous studies on selective hydrogen combustion, we have demonstrated that the addition of Na_2WO_4 to various metal oxides provides enhanced selectivity towards H_2 combustion in the presence of ethylene and ethane.^[10,12,13,17,31] Here, we show that the enhanced selectivity of Na_2WO_4 -promoted CaMnO_3 is not likely to be a consequence of any competitive effect between H_2 and C_2H_4 adsorption, but rather results from the near complete inhibition of C_2H_4 reaction at the redox catalyst surface when it is covered by Na_2WO_4 . In particular, the rates of $\text{Na}_2\text{WO}_4/\text{CaMnO}_3$ reduction in C_2H_4 were drastically lowered relative to unpromoted CaMnO_3 .

Figure 4.10a–c provides the X vs. t data with model fitting, dX/dt vs. X data with model fitting, and Arrhenius plot obtained from the fitting procedure for the reduction of the $\text{Na}_2\text{WO}_4/\text{CaMnO}_3$ redox catalyst by H_2 . For a complete statistical analysis of these data with 15 kinetic fitting models, see **Table C3**. The reduction kinetics in H_2 are significantly different—both in quantitative terms and in the qualitative behavior—for the $\text{Na}_2\text{WO}_4/\text{CaMnO}_3$ as compared to CaMnO_3 , indicating that the Na_2WO_4 layer alters the mechanism of oxygen donation from the CaMnO_3 lattice. In

particular, the X vs. t data appeared sigmoidal rather than deceleratory throughout, with a long induction period, while the derivative dX/dt vs. X was parabolic and not monotonically decreasing as with the CaMnO_3 results. Rather than fitting the F1 model for solid conversion, $\text{Na}_2\text{WO}_4/\text{CaMnO}_3$ was fit best by an Avrami-Erofe'ev model describing slow nucleation and subsequent nuclei growth. While the single most optimal value of the Avrami exponent was not constant over the range of temperatures examined, the model AE2 with Avrami exponent $n = 2$ was selected as the best representative model based on its close fitting to the X vs. t data and its intermediate position among the well-fitting models (AE1.5, AE2, AE3). The results of **Figure 4.10**, especially when viewed in contrast with those of **Figure 4.5** for unpromoted CaMnO_3 , show that Na_2WO_4 changes the physical process of lattice oxygen extraction by H_2 , possibly by inhibiting the access by H_2 to the CaMnO_3 surface.

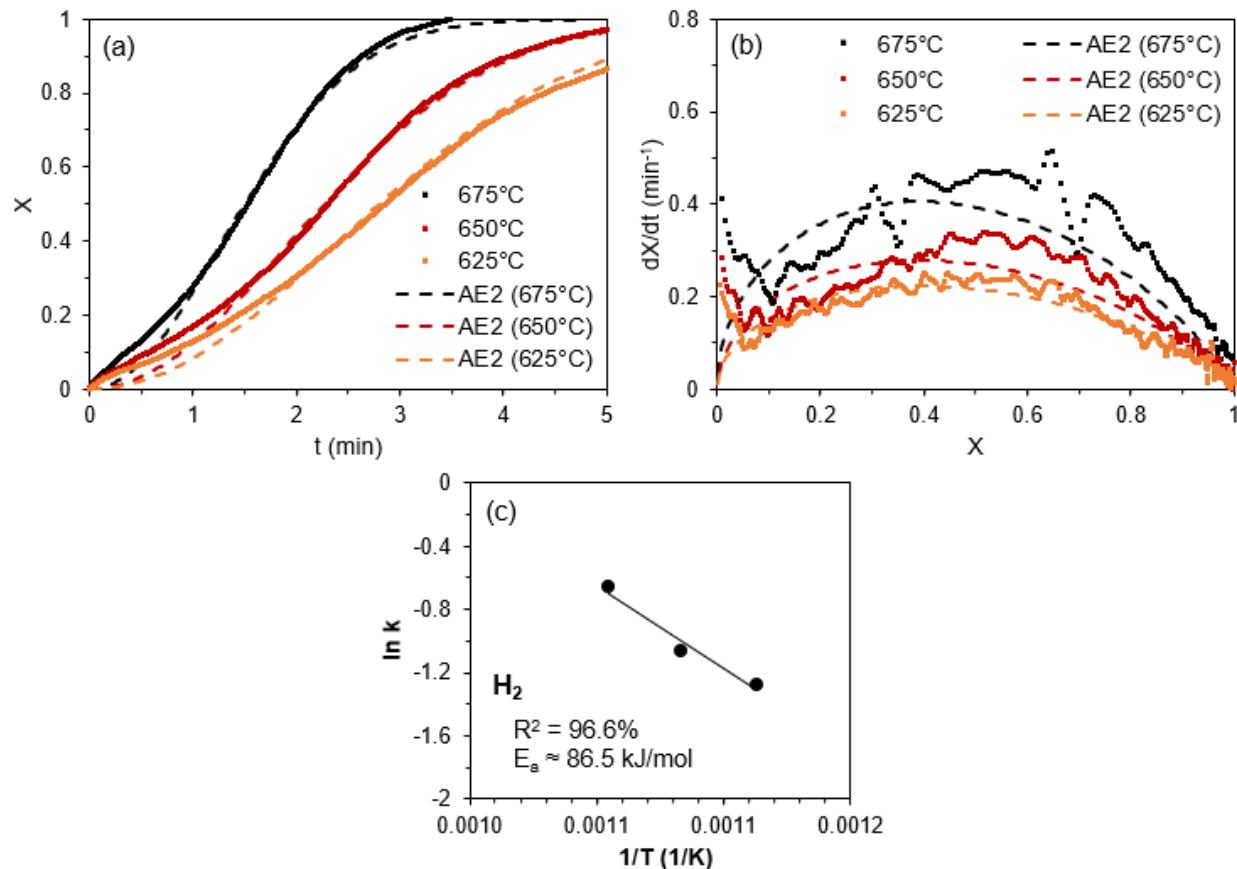


Figure 4.10. Reduction kinetics of $\text{Na}_2\text{WO}_4/\text{CaMnO}_3$ by H_2 with superimposed best-fitting kinetic model AE2 (dotted lines). (a) Solid conversion X vs. t ; (b) derivative conversion dX/dt vs. X ; (c) Arrhenius analysis of data using $k(T)$ values based on the Avrami-Erofe'ev nucleation and growth kinetic model with $n = 2$. TGA conditions: $m_0 = 20 \text{ mg}$, $150\text{--}250 \text{ }\mu\text{m}$, $T = 500\text{--}650^\circ\text{C}$, $P = 1 \text{ atm}$, $F_{\text{total}} = 200 \text{ mL/min}$ (20 mL/min H_2 , 180 mL/min He). E_a (kJ mol^{-1}) was calculated from Arrhenius slope m , as $E_a \approx -mRT$.

Compared with the reaction rate constants of CaMnO_3 reduction by H_2 (Figure 4.9), the rate constants for $\text{Na}_2\text{WO}_4/\text{CaMnO}_3$ were also observed at lower values (Figure 4.10c), chiefly the result of a higher apparent activation energy for oxygen donation from the redox catalyst (86.5 kJ mol^{-1} vs. 40.1 kJ mol^{-1} for $\text{Na}_2\text{WO}_4/\text{CaMnO}_3$ and CaMnO_3 , respectively). An additional oxygen conduction step through the Na_2WO_4 layer may potentially contribute to this raised energy barrier.^[13] As a result of suppressed rate constants, the total rates of solid reduction by H_2 decreased

from CaMnO_3 to $\text{Na}_2\text{WO}_4/\text{CaMnO}_3$ (see later **Figure 4.11**). At 650°C , the maximum instantaneous rate of oxygen donation and subsequent reduction achieved by CaMnO_3 , in 10% H_2 , was 13.3 wt%/min, occurring at fractional solid conversion $X = 0.23$. For $\text{Na}_2\text{WO}_4/\text{CaMnO}_3$ at the same conditions, the maximum rate of reduction was 2.37 wt%/min, coinciding with $X = 0.52$; meanwhile, at a matched solid conversion $X = 0.23$, the reduction rate of $\text{Na}_2\text{WO}_4/\text{CaMnO}_3$ was 1.54 wt%/min, a decrease in rate of over 88% compared to the base CaMnO_3 . A major influence of Na_2WO_4 was therefore to prevent the ease of oxygen donation from the CaMnO_3 lattice during reduction, even by H_2 .

For the case of 10% C_2H_4 , the rate of $\text{Na}_2\text{WO}_4/\text{CaMnO}_3$ reduction was so insignificant that the first 10 min of the reduction step at 675°C extracted less than 10% of the available oxygen ($X = 0.059$ at $t = 10$ min), and the derivative form dX/dt vs. X could not be separated from instrumental noise. As a result, the applicability of kinetic models was limited to a small range of X values (0.01 to 0.04), and the rate constants and kinetic parameters are of lower confidence than the three other gas-solid combinations reported here. The X vs. t data and Arrhenius curve are provided in **Figure C7**, based on the predictions of the half-order Avrami-Erofe'ev model (AE0.5), which was found to be the best statistical fit to the data. Upon promotion with Na_2WO_4 , the apparent activation energy of solid reduction in C_2H_4 increased ~18% to $135.9 \text{ kJ mol}^{-1}$ from $117.9 \text{ kJ mol}^{-1}$ for unpromoted CaMnO_3 . This was a less significant change compared to that for H_2 — 40.1 kJ mol^{-1} vs. 86.5 kJ mol^{-1} , a 115% increase — and demonstrates that the addition of Na_2WO_4 nearly equalizes the energy barrier for reduction in H_2 and in C_2H_4 . Meanwhile, the pre-exponential factor (k_0) for Na_2WO_4 -promoted CaMnO_3 increased by nearly two orders of magnitude in the case of H_2 combustion while decreased by two orders of magnitude for ethylene combustion. The net

result is significantly increased hydrogen combustion selectivity (vs. unpromoted CaMnO_3), especially at higher temperatures. The selected kinetic models, rate constants, and activation energy values for each combination of gas and solid are summarized in **Table 4.2**.

Table 4.2. Summary of chosen kinetic models, approximate rate constants and reduction rates at 650°C, and activation energy values for reduction of CaMnO_3 and $\text{Na}_2\text{WO}_4/\text{CaMnO}_3$ redox catalysts by H_2 and C_2H_4 .

c	CaMnO_3 (H_2)	CaMnO_3 (C_2H_4)	$\text{Na}_2\text{WO}_4/\text{CaMnO}_3$ (H_2)	$\text{Na}_2\text{WO}_4/\text{CaMnO}_3$ (C_2H_4)
Kinetic Model	F1	F1.5	AE2	AE0.5
E_{app}	40.1 kJ mol ⁻¹	117.9 kJ mol ⁻¹	86.5 kJ mol ⁻¹	139.5 kJ mol ⁻¹
k_0	3.42 x 10 ² min ⁻¹	1.73 x 10 ⁶ min ⁻¹	2.92 x 10 ⁴ min ⁻¹	1.24 x 10 ⁴ min ⁻¹
k (650°C)	1.66 x 10 ⁰ min ⁻¹	3.58 x 10 ⁻¹ min ⁻¹	3.46 x 10 ⁻¹ min ⁻¹	1.68 x 10 ⁻⁴ min ⁻¹

We lastly present dimensional conversion data to emphasize the effect of Na_2WO_4 on suppressing non-selective combustion reactions. **Figure 4.11** shows the conversion vs. time data for both CaMnO_3 and $\text{Na}_2\text{WO}_4/\text{CaMnO}_3$ in H_2 and C_2H_4 gases, restored to dimensional terms as X (wt%) vs. t (min). As discussed previously, the rate of reduction by H_2 was significantly impeded by the introduction of Na_2WO_4 , but full conversion of the solid was reached after a lengthened period of time ($t \approx 6$ min vs. $t \approx 3$ min for promoted vs. unpromoted CaMnO_3 , respectively). The final weight percent conversion of 20 wt% $\text{Na}_2\text{WO}_4/\text{CaMnO}_3$ (i.e. its oxygen capacity) was lower than for unpromoted CaMnO_3 (7.03 wt% vs. 9.61 wt%) due to the insignificant reducibility of Na_2WO_4 .

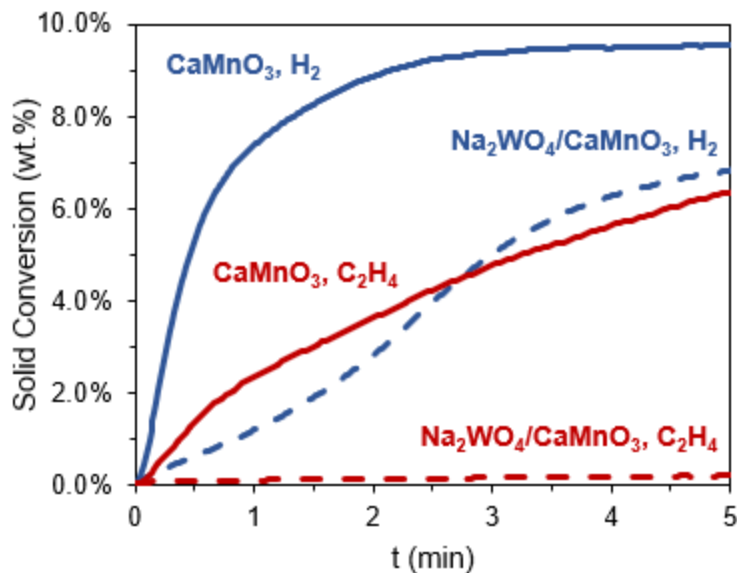


Figure 4.11. Quantitative comparison for the reduction of CaMnO_3 and $\text{Na}_2\text{WO}_4/\text{CaMnO}_3$ by either H_2 or C_2H_4 at 650°C , depicted as solid conversion (wt%) vs. time (min). TGA conditions: $m_0 = 20$ mg, $150\text{--}250$ μm , $T = 650^\circ\text{C}$, $P = 1$ atm, $F_{\text{total}} = 200$ mL/min (20 mL/min H_2 or C_2H_4 , 180 mL/min He or Ar).

The presence of Na_2WO_4 on CaMnO_3 allowed for the donation of lattice oxygen towards H_2 combustion, albeit at a slower rate than the unpromoted CaMnO_3 , while almost completely inhibiting the reduction of the redox catalyst by C_2H_4 . Between the H_2 and C_2H_4 gases, the rate constants for reduction of $\text{Na}_2\text{WO}_4/\text{CaMnO}_3$ differ by over three orders of magnitude, explaining the ability of the $\text{Na}_2\text{WO}_4/\text{CaMnO}_3$ redox catalyst to perform selective hydrogen combustion. Relative to unpromoted CaMnO_3 – with H_2 and C_2H_4 rate constants differing by only one order of magnitude – $\text{Na}_2\text{WO}_4/\text{CaMnO}_3$ can be anticipated to degrade less significantly at higher temperatures in terms of selectivity towards H_2 combustion (and consequently, towards the preservation of ethylene yields), due to the proximity of the apparent activation energy barriers for H_2 and C_2H_4 activation. In the case of $\text{H}_2/\text{C}_2\text{H}_4$ mixtures, and moreover with the addition of C_2H_6 , the presence of hydrocarbons would likely not affect the selectivity of $\text{Na}_2\text{WO}_4/\text{CaMnO}_3$ towards

H₂ combustion given the difference in H₂ and hydrocarbon reaction orders, and particularly given the large difference in CaMnO₃ reduction rates for the individual gases, especially after Na₂WO₄ promotion.

4.5. Conclusions

The present study reports the reduction kinetics of CaMnO₃ and Na₂WO₄/CaMnO₃ redox catalysts suitable for the chemical looping-oxidative dehydrogenation (CL-ODH) of ethane, via a combination of redox TGA experiments and statistical analyses applied to commonly reported kinetic models. Both redox catalysts were cycled in H₂ and C₂H₄ (as the more reactive C₂ hydrocarbon); the resulting TGA conversion data were made dimensionless (X vs. t), differentiated into the rate form (dX/dt vs. X), and fitted against 15 solid-state kinetic models in order to obtain appropriate empirical rate equations and kinetic parameters (E_a , k_0). The rate parameters obtained for CaMnO₃ reduction by H₂ and C₂H₄, and the predicted greater dependence of C₂H₄ combustion upon oxygen site density (expressed as the reaction-order exponent; 1.5 vs. 1), were consistent with fixed-bed experiments on CaMnO₃ showing selective H₂ combustion relative to C₂H₄ at intermediate to high solid conversion (X).

The addition of Na₂WO₄ to CaMnO₃ increased the activation energy for reaction with both H₂ and C₂H₄. It also led to significantly greater selectivity towards hydrogen combustion, evident from the three orders of magnitude difference in the rate constants for H₂ vs. C₂H₄. Na₂WO₄/CaMnO₃ is also predicted to have greater resilience to a degradation in selectivity at high temperatures, compared to CaMnO₃, based on the relative values of the apparent activation energy, E_{app} , for reduction by the two reactants. The kinetic model equations and parameters reported herein for

reduction of CaMnO_3 -based redox catalysts in multiple gas environments enable the rational design and optimization of redox processes that employ these materials, such as the ethane CL-ODH process.

4.6. Symbols

AE	[unitless]	designates an Avrami-Erofe'ev nucleation and nuclei growth kinetic model
D	[unitless]	designates a diffusion-limited kinetic model
dX/dt	$[\text{min}^{-1}]$	derivative of solid conversion (X) against time (t)
E_{app}	$[\text{kJ mol}^{-1}]$	apparent activation energy
F	[unitless]	designates a reaction-order kinetic model
k	$[\text{min}^{-1}]$	rate constant
k_0	$[\text{min}^{-1}]$	pre-exponential factor
m_0	[mg]	initial mass of (fully oxidized) redox catalyst
m_∞	[mg]	final mass of (fully reduced) redox catalyst
R	[unitless]	designates a geometric contraction kinetic model
P	[atm]	total pressure
P_i	[atm]	partial pressure of reactant i
S_H	[percentage]	selectivity towards hydrogen combustion
t	[min]	time
T	$[\text{°C}]$	temperature
X	[percentage]	dimensionless solid conversion

4.7. References

- [1] International Energy Agency, *The Future of Petrochemicals*, **2018**.
- [2] International Energy Agency, *Technology Roadmap: Energy and GHG Reductions in the Chemical Industry via Catalytic Processes*, **2013**.
- [3] T. Ren, M. Patel, K. Blok, *Energy* **2006**, *31*, 425–451.
- [4] H. Zimmermann, R. Walzl, *Ullmann's Encycl. Ind. Chem.* **2012**, 466–529.
- [5] H. Zimmermann, *Ullmann's Encycl. Ind. Chem.* **2014**, *6*, 45–66.
- [6] M. M. Bhasin, J. H. McCain, B. V. Vora, T. Imai, P. R. Pujadó, *Appl. Catal. A Gen.* **2001**, *221*, 397–419.
- [7] F. Cavani, N. Ballarini, A. Cericola, *Catal. Today* **2007**, *127*, 113–131.
- [8] C. A. Gartner, A. C. VanVeen, J. A. Lercher, *ChemCatChem* **2013**, *5*, 3196–3217.
- [9] L. M. Neal, S. Yusuf, J. A. Sofranko, F. Li, *Energy Technol.* **2016**, *4*, 1200–1208.
- [10] S. Yusuf, L. M. Neal, F. Li, *ACS Catal.* **2017**, *7*, 5163–5173.
- [11] V. P. Haribal, L. M. Neal, F. Li, *Energy* **2017**, *119*, 1024–1035.
- [12] S. Yusuf, L. Neal, V. Haribal, M. Baldwin, H. H. Lamb, F. Li, *Appl. Catal. B Environ.* **2018**, *232*, 77–85.
- [13] S. Yusuf, L. Neal, Z. Bao, Z. Wu, F. Li, *ACS Catal.* **2019**, *9*, 3174–3186.
- [14] X. Zhu, K. Li, L. Neal, F. Li, *ACS Catal.* **2018**, *8*, 8213–8236.
- [15] Y. Gao, L. M. Neal, F. Li, *ACS Catal.* **2016**, *6*, 7293–7302.
- [16] Y. Gao, F. Haeri, F. He, F. Li, *ACS Catal.* **2018**, 1757–1766.
- [17] R. B. Dudek, Y. Gao, J. Zhang, F. Li, *AIChE J.* **2018**, *00*, 1–10.
- [18] M. J. O'Hara, T. Imai, J. C. Bricker, D. E. Mackowiak, *U.S. Pat. No. 4565898*
Dehydrogenation of Dehydrogenatable Hydrocarbons, **1986**.

- [19] C. H. Lin, K. C. Lee, B. Z. Wan, *Appl. Catal. A Gen.* **1997**, *164*, 59–67.
- [20] R. K. Grasselli, D. L. Stern, J. G. Tsikoyiannis, **1999**, *189*, 1–8.
- [21] R. K. Grasselli, D. L. Stern, J. G. Tsikoyiannis, **1999**, *189*, 9–14.
- [22] J. G. Tsikoyiannis, D. L. Stern, R. K. Grasselli, **1999**, *86*, 77–86.
- [23] L. M. van der Zande, E. A. de Graaf, G. Rothenberg, *Adv. Synth. Catal.* **2002**, *344*, 884–889.
- [24] G. Rothenberg, E. A. De Graaf, A. Bliet, *Angew. Chemie - Int. Ed.* **2003**, *42*, 3366–3368.
- [25] E. A. De Graaf, A. Andreini, E. J. M. Hensen, A. Bliet, *Appl. Catal. A Gen.* **2004**, *262*, 201–206.
- [26] L. Låte, J. I. Rundereim, E. A. Blekkan, *Appl. Catal. A Gen.* **2004**, *262*, 53–61.
- [27] E. A. De Graaf, G. Zwanenburg, G. Rothenberg, A. Bliet, *Org. Process Res. Dev.* **2005**, *9*, 397–403.
- [28] J. H. Blank, J. Beckers, P. F. Collignon, F. Clerc, G. Rothenberg, *Chem. - A Eur. J.* **2007**, *13*, 5121–5128.
- [29] J. H. Blank, J. Beckers, P. F. Collignon, G. Rothenberg, *ChemPhysChem* **2007**, *8*, 2490–2497.
- [30] J. Beckers, R. Drost, I. Van Zandvoort, P. F. Collignon, G. Rothenberg, *ChemPhysChem* **2008**, *9*, 1062–1068.
- [31] R. B. Dudek, X. Tian, M. Blivin, L. M. Neal, H. Zhao, F. Li, *Appl. Catal. B Environ.* **2019**, *246*, 30–40.
- [32] S. Vyazovkin, K. Chrissa, M. Laura, D. Lorenzo, N. Koga, M. Pijolat, B. Roduit, N. Sbirrazzuoli, J. Josep, *Thermochim. Acta* **2014**, *590*, 1–23.
- [33] H. Kruggel-Emden, F. Stepanek, A. Munjiza, *Chem. Eng. Res. Des.* **2011**, *89*, 2714–2727.

- [34] Z. Zhou, L. Han, G. M. Bollas, *Int. J. Hydrogen Energy* **2014**, *39*, 8535–8556.
- [35] H. Y. Sohn, J. Szekely, *Chem. Eng. Sci.* **1972**, *27*, 763–778.
- [36] H. Y. Sohn, J. Szekely, **1973**, *28*.
- [37] J. Szekely, C. I. Lin, H. Y. Sohn, *Chem. Eng. Sci.* **1973**, *28*, 1975–1989.
- [38] J. W. Evans, S. Song, C. E. Leon-Sucre, *Metall. Trans. B* **1976**, *7*, 55–65.
- [39] T. Mattisson, A. Järnäs, A. Lyngfelt, *Energy and Fuels* **2003**, *17*, 643–651.
- [40] K. E. Sedor, M. M. Hossain, H. I. De Lasa, *Can. J. Chem. Eng.* **2008**, *86*, 323–334.
- [41] M. M. Hossain, H. I. de Lasa, *Chem. Eng. Sci.* **2010**, *65*, 98–106.
- [42] I. Iliuta, R. Tahoces, G. S. Patience, S. Rifflart, F. Luck, *AIChE J.* **2010**, *56*, 1063–1079.
- [43] L. Silvester, D. Ipsakis, A. Antzara, E. Heracleous, A. A. Lemonidou, D. B. Bukur, *Energy & Fuels* **2016**, *30*, 8597–8612.
- [44] D. Ipsakis, E. Heracleous, L. Silvester, D. B. Bukur, A. A. Lemonidou, *Chem. Eng. J.* **2017**, *308*, 840–852.
- [45] Z. Sarshar, S. Kaliaguine, *Ind. Eng. Chem. Res.* **2013**, *52*, 6946–6955.
- [46] X. Dai, J. Cheng, Z. Li, M. Liu, Y. Ma, X. Zhang, *Chem. Eng. Sci.* **2016**, *153*, 236–245.
- [47] E. Ksepko, P. Babiński, L. Nalbandian, *Appl. Energy* **2017**, *190*, 1258–1274.
- [48] H. Ebrahimi, M. Rahmani, *Int. J. Hydrogen Energy* **2018**, *43*, 5231–5248.
- [49] A. H. Elbadawi, M. S. Ba-shammakh, S. Al-ghamdi, S. A. Razzak, M. M. Hossain, *Chem. Eng. J.* **2016**, *284*, 448–457.
- [50] A. Khawam, D. R. Flanagan, *J. Phys. Chem. B* **2006**, *110*, 17315–17328.
- [51] J. D. Hancock, J. H. Sharp, **n.d.**, 74–77.
- [52] K. Chen, S. Xie, A. T. Bell, E. Iglesia, *J. Catal.* **2001**, *198*, 232–242.

**CHAPTER 5: REDUCTION KINETICS OF $\text{Na}_2\text{WO}_4/\text{CaMnO}_3$: INFLUENCE OF
THERMAL HISTORY AND LONG-TERM REDOX CYCLING ON RATE
PARAMETERS**

5.1. Introduction

Chemical looping oxidative dehydrogenation (CL-ODH) represents a promising route for intensification of olefin production from light alkanes, offering substantial reductions (>80%) in energy consumption and CO₂ emissions compared to conventional steam cracking processes.^[1,2] Building upon the well-established advantages of light alkane oxidative dehydrogenation (*e.g.* of ethane to ethylene) over steam cracking,^[3] CL-ODH provides further reduction in energy intensity by spatially separating the C_nH_{2n+2} and O₂ reactants and decoupling the hydrogen oxidation reaction from the provision of gaseous O₂ *via* a solid oxygen-donating reaction intermediate.^[4] A properly selected solid oxygen carrier in CL-ODH facilitates reactive separation of O₂ from air at temperatures compatible with oxy-dehydrogenation and oxy-cracking reactions, towards which the oxygen is subsequently donated.^[5,6] Therefore, CL-ODH with a solid oxygen carrier directly addresses several key limitations of the conventional C_nH_{2n+2}/O₂ co-feed approach to oxidative dehydrogenation, including (i) the operational risk associated with co-feeding oxygen, (ii) the over-oxidation of alkane and alkene to CO_x, and (iii) the requirement for costly, high-purity O₂.

Substantial attention has been paid in the literature to the design and evaluation of solid oxygen carriers, also known as redox catalysts, due to the central role of oxygen donation in chemical looping processes; the product distribution and overall process energy efficiency largely depend upon the selection of the redox catalyst, and hence the corresponding operating conditions.^[1,7,8] Effective redox catalysts must be low-cost and low-toxicity materials possessing long-term redox stability, high mechanical strength, sufficient oxygen-donating capacity (in wt.%), and both high activity and selectivity towards the oxidation of hydrogen. The latter is referred to as selective hydrogen combustion (SHC) and determines whether an oxy-dehydrogenation or oxy-cracking

process will generate the preferred light olefins or undesirable CO_x side products.^[1,6,9] Previously reported redox catalysts providing high olefin yields from CL-ODH include supported vanadium and molybdenum oxides,^[10–14] MoO₃/Fe₂O₃,^[15,16] and Li₂CO₃-promoted La_{0.8}Sr_{0.2}FeO₃ perovskite.^[17–19] Recently, Yusuf *et al.* reported an ethylene yield of 68% from CL-ODH of ethane at 850°C using a Na₂WO₄-promoted Mg₆MnO₈ redox catalyst and attributed the high yield to the exceptional SHC properties of the Na₂WO₄/Mg₆MnO₈ system.^[5,20] The high selectivity to H₂ combustion afforded by the Na₂WO₄ promoter has since been extended to additional metal oxide substrates, most notably the perovskite oxide CaMnO₃, which forms a core-shell composite with Na₂WO₄ covering the redox catalyst surface; the core functions as the oxygen storage component whereas the shell inhibits non-selective oxidation.^[6,21–24] Given the significant benefits provided by the Na₂WO₄ promoter in high-temperature redox applications, there is value in pursuing a deeper understanding of Na₂WO₄, its material properties under CL-ODH operating conditions, and its impact on the activity, selectivity, stability, and overall performance of redox catalysts, especially when CaMnO₃ is used as the oxygen carrying component.

The exploration of sodium tungstate (Na₂WO₄) as a structural promoter to metal oxide-based redox catalysts in olefin production schemes has stemmed from the successful demonstration of various Na₂WO₄-promoted catalysts by Jiang *et al.* and subsequently by Lunsford and coworkers for the oxidative coupling of methane (OCM), a process involving CH₄/O₂ co-feed.^[25–28] The study by Jiang introduced the MnO_x-Na₂WO₄/SiO₂ catalyst system, which remains the best-performing OCM catalyst in the literature, achieving a C₂ yield of 25% from methane.^[29,30] Yu *et al.* in a later study demonstrated that by promoting a typically non-selective metal oxide (CeO₂ or Pr₆O₁₁) with a small amount of Na₂WO₄, the resulting composite catalyst became highly selective for OCM due

to its increased ability to desorb ethylene prior to total oxidation.^[26] Importantly, at the OCM conditions (780°C) and also at typical CL-ODH temperatures, Na₂WO₄ is molten and covers the surface of the oxide.^[31,32] Multiple studies have therefore examined the properties of molten Na₂WO₄, both within and outside of the OCM literature, providing useful insights which will be relied upon later in this work.^[32–36] Na₂W₂O₇, a closely related phase, has also received attention and these insights may be useful based on the similarity of the monotungstate (Na₂WO₄) to the ditungstate or pyrotungstate.^[37,38] However, while some of the cited studies have addressed oxygen ion mobility through the salt under both crystalline and molten working states, the use of oxide ions for a surface reaction (*e.g.* hydrogen combustion in the case of CL-ODH) was not examined. One of the goals of the present study is therefore to connect an understanding of the material properties of Na₂WO₄ during high-temperature operation (*e.g.* in CL-ODH) to an assessment of the influence of Na₂WO₄ on the selective hydrogen combustion reaction, with active oxygen provided from the lattice of the metal oxide substrate.

As with any chemical process, an understanding of the kinetics is highly important for rational design of the reactor. For chemical looping processes, whether in a fixed bed or a fluidized bed reactor setting, the reduction kinetics of the oxygen carrier must be adequately characterized in order to make decisions about gas-solid contact time, total solid oxygen carrier inventory, reactant gas partial pressure, extent of regeneration, and a range of other factors.^[39–41] Chemical looping oxygen carrier kinetics have been extensively studied, most commonly for the chemical looping combustion (CLC) of coal or methane. The typical approach adopted for these redox catalyst kinetics investigations has been to reduce (and then re-oxidize) the material and to non-dimensionalize the extent of the solid conversion using the fully reduced ($X = 1$) and fully re-

oxidized states ($X = 0$) as the boundary conditions.^[42–44] The resulting dimensionless conversion curves (X vs. time) have been subsequently fitted to a variety of common solid-state kinetics models such as unreacted shrinking core models or nucleation and nuclei growth models.^[43,45] We recently adopted this methodology to study the reduction kinetics of CaMnO_3 and 20 wt.% $\text{Na}_2\text{WO}_4/\text{CaMnO}_3$ redox catalysts, with and without Fe doping, with an emphasis on the reduction rates of each material by hydrogen, ethylene, and ethane gases as the major components of an ethane CL-ODH effluent stream.^[46,47] In these investigations, the activation of C_2H_6 by the redox catalysts was deemed to be negligible, while the undesirable activation of C_2H_4 was inherently lower than that of H_2 on the CaMnO_3 redox catalyst and could be further suppressed by several orders of magnitude with the addition of the Na_2WO_4 promoter. However, several questions related to the reduction kinetics of the $\text{Na}_2\text{WO}_4/\text{CaMnO}_3$ remain unanswered, including the impact of a crystalline or a molten Na_2WO_4 working state on the reduction kinetics, the importance of the thermal history of the sample, and the long-term kinetic behavior of the redox catalysts.

In this study, we aim to perform a more rigorous investigation on the reduction kinetics of the CaMnO_3 and $\text{Na}_2\text{WO}_4/\text{CaMnO}_3$ redox catalysts, with a particular focus on capturing changes in the reduction rates which result from phase change of the Na_2WO_4 surface layer.^[22,24] Moreover, here we place the rates and kinetic parameters we determined for this system in our previous work into a more firm context by assessing the variability and repeatability of the rates and evaluating the impact of extended redox cycling on the observed kinetics. As we have noted elsewhere, redox catalysts based on CaMnO_3 with a molten salt promoter can find suitable application in chemical looping oxidative dehydrogenation (CL-ODH) of ethane, as well as other processes in which H_2 is produced alongside higher-value hydrocarbon products.^[1,48] The improved understanding of

$\text{Na}_2\text{WO}_4/\text{CaMnO}_3$ reduction kinetics afforded by this work can potentially enable the rational design and optimization of CL-ODH processes in fixed-bed and fluidized-bed reactors utilizing these materials.

5.2. Experimental Section

5.2.1. Redox Catalyst Preparation

Perovskite oxide CaMnO_3 was synthesized following a modified Pechini method as described in previous reports.^[6,22] In brief, stoichiometric amounts of $\text{Mn}(\text{NO}_3)_2 \cdot 4\text{H}_2\text{O}$ (97.0%, Sigma-Aldrich), $\text{Ca}(\text{NO}_3)_2 \cdot 4\text{H}_2\text{O}$ (99.0%, Sigma-Aldrich), and citric acid (99.5%, Sigma-Aldrich) were dissolved in deionized water at 40°C while stirring, followed by the addition of ethylene glycol (99.8%, Sigma-Aldrich). The solution was then heated to 80°C and stirred until the formation of a gel, then dried overnight at 100°C. Two calcination steps were used, the first at 450°C to decompose nitrates (3 h) and the second at 1000°C to form the CaMnO_3 phase (12 h). To make 20 wt.% $\text{Na}_2\text{WO}_4/\text{CaMnO}_3$, an appropriate mass of $\text{Na}_2\text{WO}_4 \cdot 2\text{H}_2\text{O}$ (99.0%, Sigma-Aldrich) was dissolved in deionized water and added dropwise to the CaMnO_3 powder, then dried overnight. The mixture was then calcined at 900°C for 8 h to form the final $\text{Na}_2\text{WO}_4/\text{CaMnO}_3$ redox catalyst. Powders in the size range 150-250 μm were used for kinetics experiments.

5.2.1. Reduction Kinetics Experiments and Modeling

The determination of reduction kinetics for the CaMnO_3 and $\text{Na}_2\text{WO}_4/\text{CaMnO}_3$ redox catalysts was performed in a similar manner to our previous work, and this section will primarily describe changes to this methodology; further details can be found in Dudek *et al.*^[46] As before, thermogravimetric analysis (TGA) experiments using a SETARAM Setsys Evolution TGA-

DTA/DSC instrument formed the basis of the kinetics data. All samples were cycled at least five times between 5% H₂ and 5% O₂ at 750°C, using He as the inert carrier gas; some samples were more extensively pre-treated, and some samples were utilized over multiple experiments. **Table S1** provides a thorough description of the five CaMnO₃ samples used in this study, and **Table S2** provides similar information on nine Na₂WO₄/CaMnO₃ samples which are used throughout. Kinetic data were non-dimensionalized by the total weight change in order to produce the dimensionless solid conversion, X:

$$X(t) = \frac{m_0 - m(t)}{m_0 - m_\infty}$$

The trend of X vs. time was then fitted to a reaction model f(X). Temperature dependence k(T) and partial pressure dependence h(P_i) were extracted by selecting a reaction model, keeping either T or P_i constant, and varying the other condition:

$$\frac{dX}{dt} = k(T) f(X) h(P_i)$$

The complete list of 15 solid-state kinetic models considered in this work are provided in **Table D3** and are the same models considered in Dudek *et al.*^[46] For the kinetic modeling approaches, one significance difference from the previous work is that each type of single-parameter kinetic model – reaction-order models (F), geometric contraction models (R), diffusion-limited models (D), and the Avrami–Erofe’ev nucleation and nuclei growth models (AE) – was fully fitted and evaluated to the point of determining Arrhenius relations and extracting kinetic parameters E_a (kJ mol⁻¹) and k₀ (s⁻¹). In every case considered, the Avrami-Erofe’ev family of models was the best fitting, and either AE1.5 or AE2 models were used to remove the X dependence of dX/dt in order to determine k(T) or h(P_i). A comparison of the four modeling types is provided for one sample

within the main manuscript (see **Figure 5.4**). The statistical approaches for the kinetic modeling are the same as discussed in Dudek *et al.*^[46]

5.2.3. *In Situ X-Ray Powder Diffraction*

In situ powder X-ray diffraction (XRD) experiments were performed on compressed powders of 20 wt.% Na₂WO₄/CaMnO₃ using a PANalytical Empyrean X-ray diffractometer with an XRK900 reactor chamber (Anton Parr) at the Analytical Instrumentation Facility (AIF) of North Carolina State University. Diffraction patterns were collected in the 2θ range 15° to 50° with 3 minutes per scan. Na₂WO₄/CaMnO₃ samples were heated or cooled at a rate of approximately 3°C/min leading to one full scan per 10°C during temperature ramping. For isothermal *in situ* XRD measurements with a redox cycling component, the gas atmosphere was switched from an inert N₂ gas to a 3% H₂ (balance N₂) reducing environment and an air environment, separated by purge steps of 12 min.

5.3. Results and Discussion

5.3.1. *Partial Pressure Dependence of CaMnO₃ Reduction Kinetics*

The primary body of experimental work in this study involved a systematic evaluation of the reduction kinetics of five CaMnO₃ (CM) samples and nine Na₂WO₄/CaMnO₃ (NWCM) samples. A variety of temperature and partial pressure conditions, testing programs, and catalyst lifetimes were considered, and presented in greater detail in **Tables D1–D2**. While not every sample and experiment are discussed in the main text, the remainder are presented in *Appendix D*. We begin by describing the reduction of CaMnO₃ perovskite by hydrogen gas as a reference point for the later discussion of the 20 wt.% Na₂WO₄/CaMnO₃ redox catalyst. The data presented here for the reduction kinetics of CaMnO₃ build upon previously published kinetic data in four important ways,

providing an improved understanding of (i) the reaction order with regards to P_{H_2} , (ii) the margin of error on TGA measurements and derived rates, (iii) the effect of performing reaction testing in a decreasing order vs. an increasing order of temperatures, and (iv) the impact of extensive redox cycling on the reduction rates and kinetic parameters for $CaMnO_3$.^[46]

Figure 5.1 presents the dimensionless solid conversion (or percentage reduction) of $CaMnO_3$ as a function of time for four partial pressures of H_2 across a range of six operating temperatures. As in Chapter 4, solid conversion X is non-dimensionalized by dividing the mass differential (in mg) at a given time t with the overall change in oxygen content after 20 minutes of reduction (also in mg); the latter quantity can also be divided by the total sample mass to arrive at the material oxygen capacity (wt.%). Similarly, **Figure 5.2** shows the time derivative of the solid conversion (dX/dt) as a function of solid conversion (X). The $CaMnO_3$ sample used for these experiments (designated as CM-05) was cycled 45 times at $750^\circ C$ prior to acquisition of kinetics information to determine dependences on P_{H_2} (reaction order) and T (activation energy and pre-exponential factor). The data of **Figure 5.1** and **Figure 5.2** are consistent with our previously reported data for the reduction of $CaMnO_3$ in 10% H_2 and provide a more complete understanding of the reduction kinetics across a wider range of conditions. Of particular note is the shoulder in the reduction rate observed at lower temperature ($600^\circ C$, $550^\circ C$, $500^\circ C$), which becomes more pronounced with decreasing temperature but is independent of the partial pressure of H_2 ; given its location near $X = 0.5$ (corresponding to an approximate stoichiometry of $CaMnO_{2.5}$), the rate shoulder likely represents the decomposition of the brownmillerite phase into the solid solution of CaO and MnO , which dominates the overall rate at higher conversion.

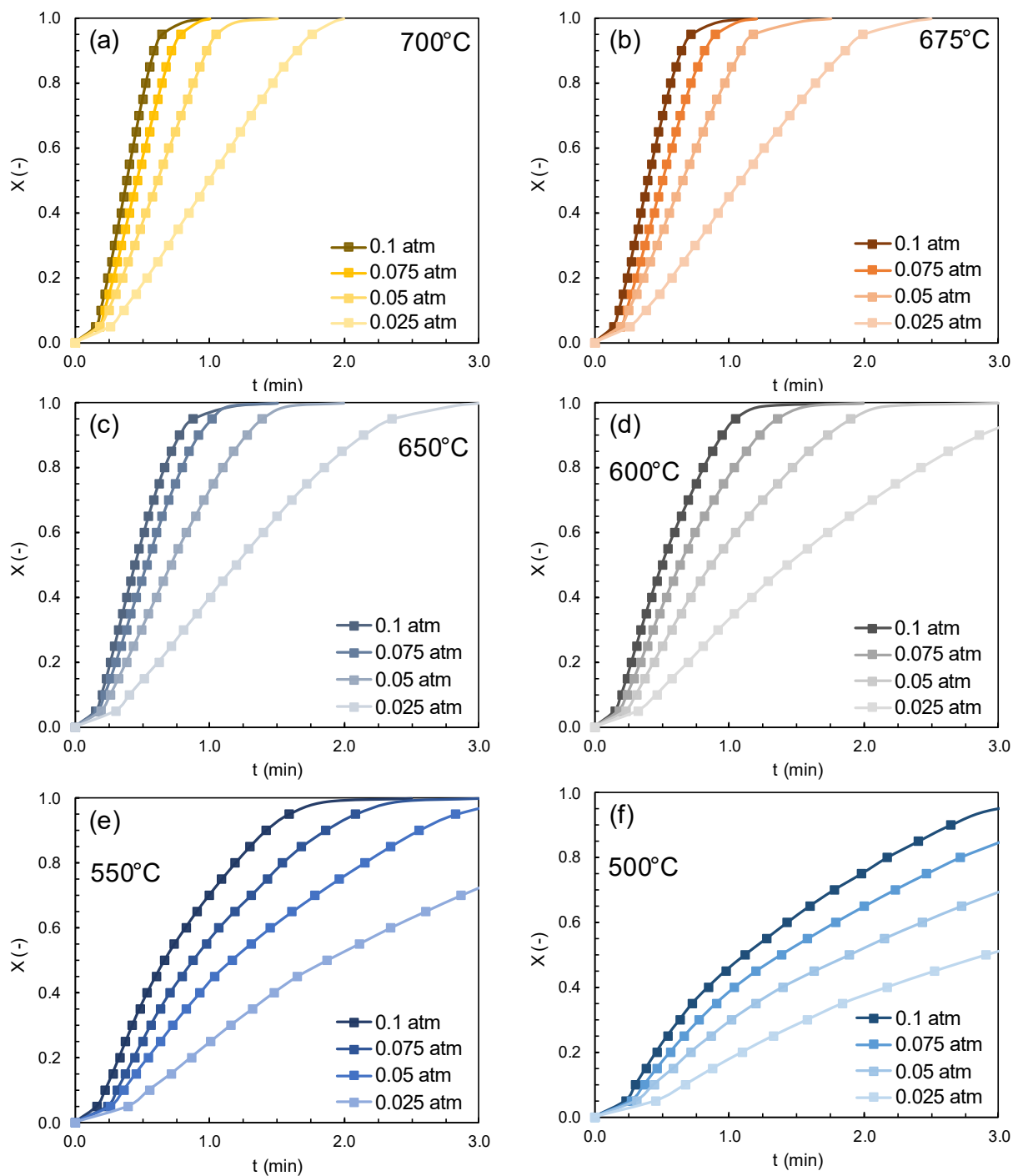


Figure 5.1: Dimensionless solid conversion of the CaMnO_3 redox catalyst (X) as a function of time (t , min) across a range of temperatures ($^{\circ}\text{C}$) and P_{H_2} (atm) values. All data were acquired using sample CM-05 with detailed experiment descriptions provided in *Appendix D*.

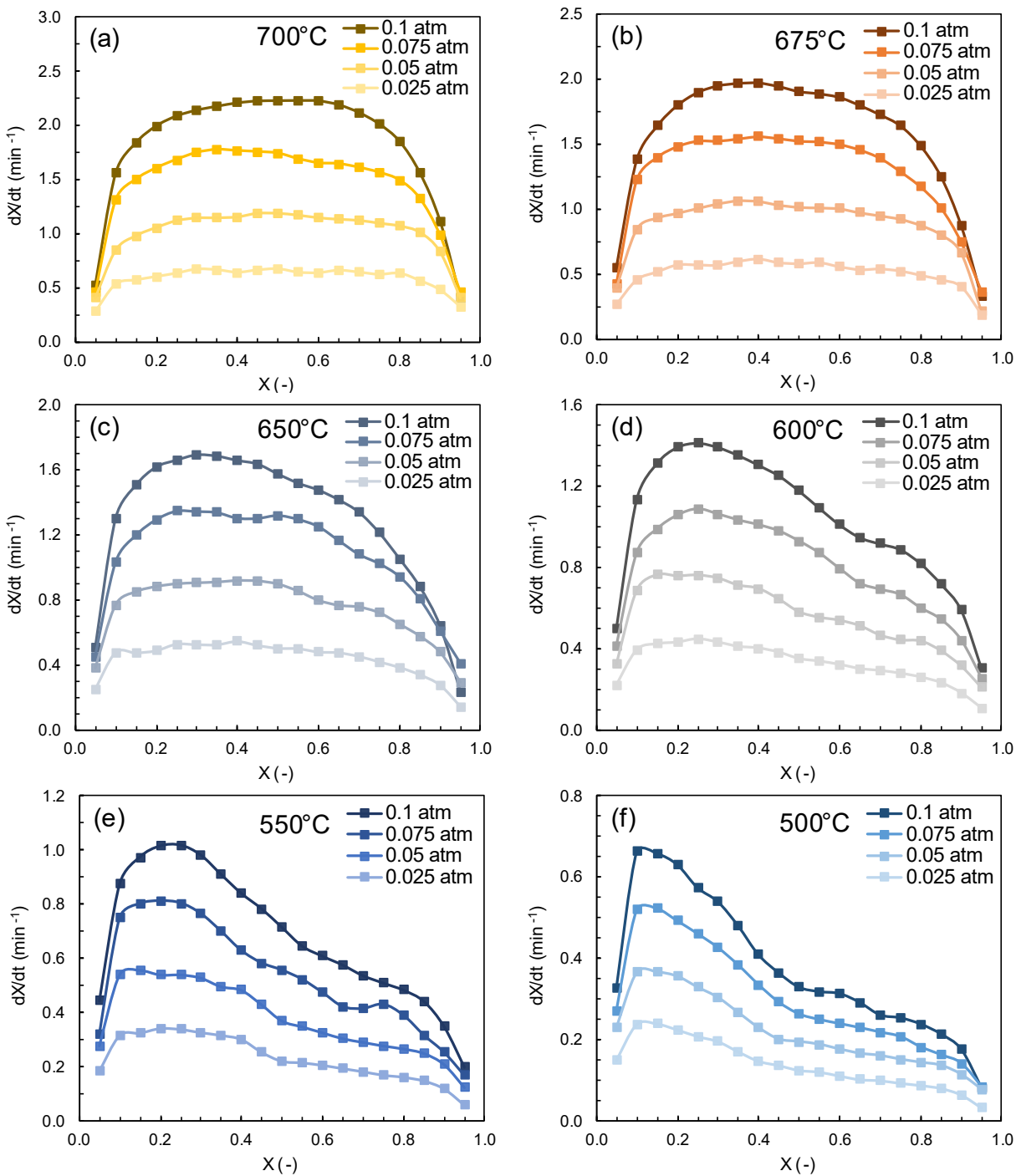


Figure 5.2: Dimensionless reduction rates of the CaMnO_3 redox catalyst (dX/dt) as a function of conversion (X) across a range of temperatures ($^\circ\text{C}$) and P_{H_2} (atm) values. All data were acquired using sample CM-05 with detailed experiment descriptions provided in *Appendix D*.

Using the reduction rate information from **Figure 5.1** and **Figure 5.2** and applying an isothermal model fitting approach, a set of kinetic pre-factors are determined ($k \cdot P_{H_2}^n$) and plotted as a function of P_{H_2} . An Avrami—Erofe’ev nucleation and nuclei growth reaction model (AE1.5) was chosen to fit the data. The resulting pre-factors and approximate reaction order n are provided in **Table 5.1**, while the partial pressure relations are included as **Figure D1** in *Appendix D*. The reaction order n for the reduction of $CaMnO_3$ by H_2 is thus largely independent of temperature and centers on an approximate value of 0.73; the presence of an additional and potentially rate-limiting step at 550°C and 500°C (the brownmillerite decomposition) leads to a slight decrease in n for these conditions. The determination of a more precise reaction order for H_2 allows for an improvement of the kinetic model established in *Chapter 4*.

Table 5.1. Kinetic pre-factors $A = k(T) \cdot (P_{H_2})^n$ for reduction of $CaMnO_3$ by H_2 at six temperatures and four P_{H_2} conditions, along with apparent reaction orders n at each temperature.

Temperature	A (0.025 atm)	A (0.05 atm)	A (0.075 atm)	A (0.10 atm)	n
700°C	0.907	1.437	2.021	2.503	0.735
675°C	0.812	1.302	1.804	2.269	0.740
650°C	0.721	1.139	1.605	1.937	0.721
600°C	0.564	0.947	1.239	1.590	0.738
550°C	0.409	0.662	0.850	1.104	0.701
500°C	0.250	0.391	0.495	0.619	0.644

5.3.2. Temperature Dependence of $CaMnO_3$ Reduction Kinetics

The primary focus of this kinetics investigation is on the temperature dependence of $CaMnO_3$ reduction, particularly as a point of comparison with the 20 wt.% $Na_2WO_4/CaMnO_3$ discussed in later sections. Moreover, this study strives to obtain a firm understanding of the variability of the kinetic data. **Figure 5.3** illustrates the dimensionless solid conversion (X) of $CaMnO_3$ by 5% H_2 gas in integral form (X vs. t , **Figure 5.3a**) and differential form (dX/dt vs. X , **Figure 5.3b**). The

data represent an average of five independent data sets across four unique samples, with **Figure 5.3c-h** presenting error bars based on the five data sets. Across the 500°C to 700°C range, the rates of CaMnO₃ reduction by H₂ followed a predictable Arrhenius trend. 95% dimensionless conversion of the perovskite (*i.e.* to CaO/MnO solid solution) was observed within 2 min at most conditions; at lower temperatures ($\leq 600^\circ\text{C}$), a decrease in the reduction rate near $X = 0.4$ likely represented the more energetically difficult decomposition of brownmillerite (Ca₂Mn₂O₅) into CaO and mixed manganese oxides as mentioned previously.

A kinetic model fitting analysis as described next was performed independently on each of the CaMnO₃ reduction data sets and will be shown for the sample CM-03 in **Figure 5.4**, while key kinetic results are tabulated in **Table 5.2**. The underlying experiments cover a range of different operating conditions, cycle programs, and sample histories, representing a more comprehensive examination of the dependence of CaMnO₃ reduction on temperature; for more details on the experiments, see *Appendix D*. The present study evaluated 15 common solid-state kinetic models (**Table D3**), including four power-law relations (F), three geometric contraction models (R), four diffusion equations (D), and four Avrami-Erofe'ev nucleation-nuclei growth models (AE); in all cases, the rate constant k (min⁻¹) served as the single fitting parameter.^[45,49] **Figure 5.4** depicts the application of the best-fitting models of each category to the CaMnO₃ rate data at 700°C (**Figure 5.4a-b**) and 500°C (**Figure 5.4c-d**) in the integral and differential forms. First-order power law (F1), unreacted shrinking core (R3), and nucleation-nuclei growth with Avrami exponent either $n = 1.5$ or 2 (AE1.5 or AE2) all provided satisfactory empirical fits to the reduction rate data across all six temperatures. The combination of the closely related AE1.5 and AE2 models exhibited the overall lowest fitting error across the entire temperature range, and the associated k values and

apparent activation energy E_a should be treated with greatest confidence among the four model types. As shown in the Arrhenius plot for the reduction of CM-03 in H₂ (**Figure D2**), and the accompanying set of kinetic parameters (**Table D4**), the selection of kinetic model did not appreciably affect the value of E_a or the R² of the Arrhenius relation, despite the variations in fitting accuracy of the model predictions to the kinetic data depicted in **Figure 5.4**. This held true for all samples tested.

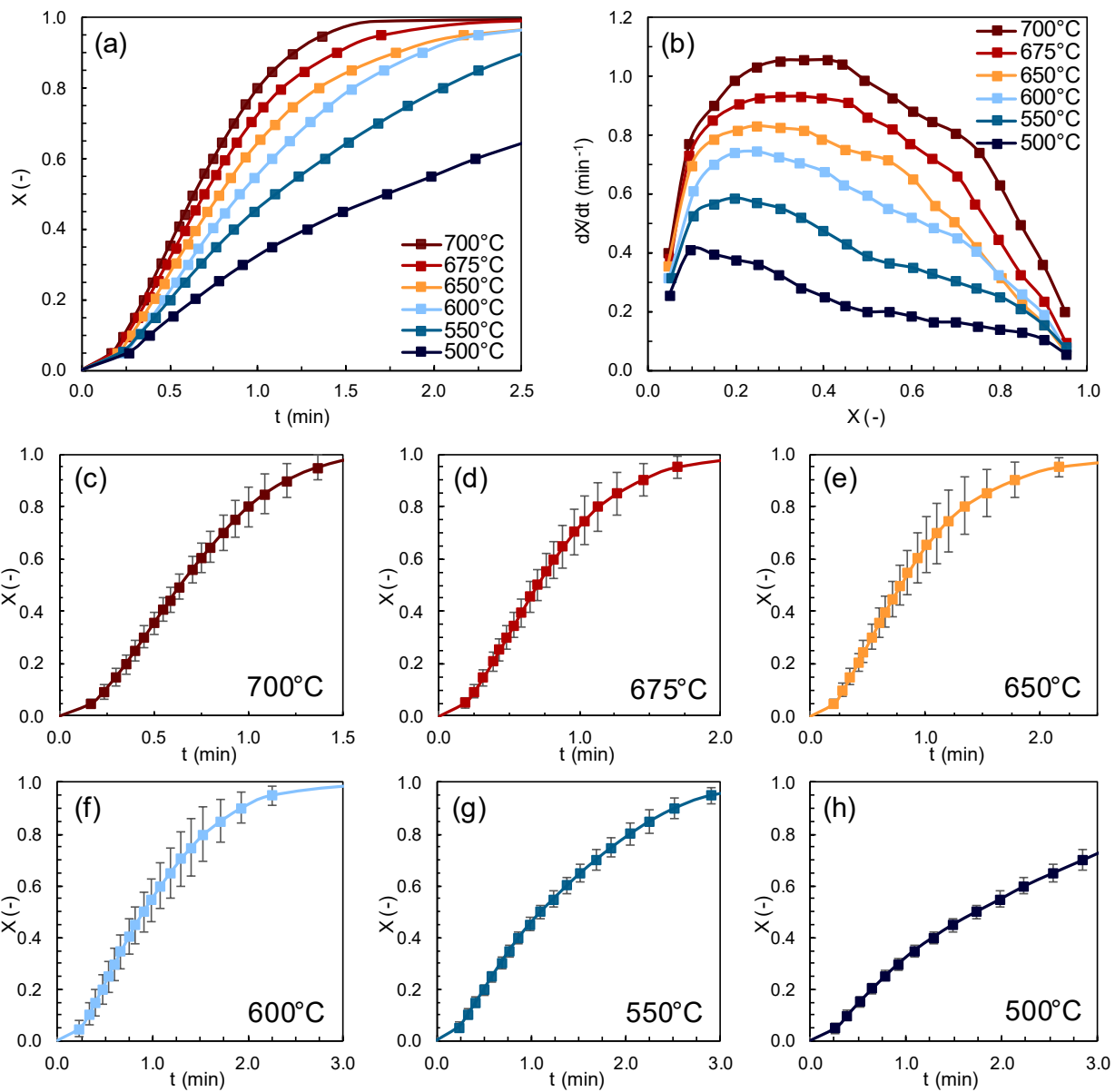


Figure 5.3. Reduction kinetics of CaMnO₃ in 5% H₂. (a) Integral and (b) differential solid conversion plots, representing an average of thermogravimetric data for five independent experiments across four samples (CM-02, CM-03, CM-04, CM-05), for all six temperature conditions. (c)—(h): Individual temperature data sets, with error bars representing one sample standard deviation calculated from the five individual sets.

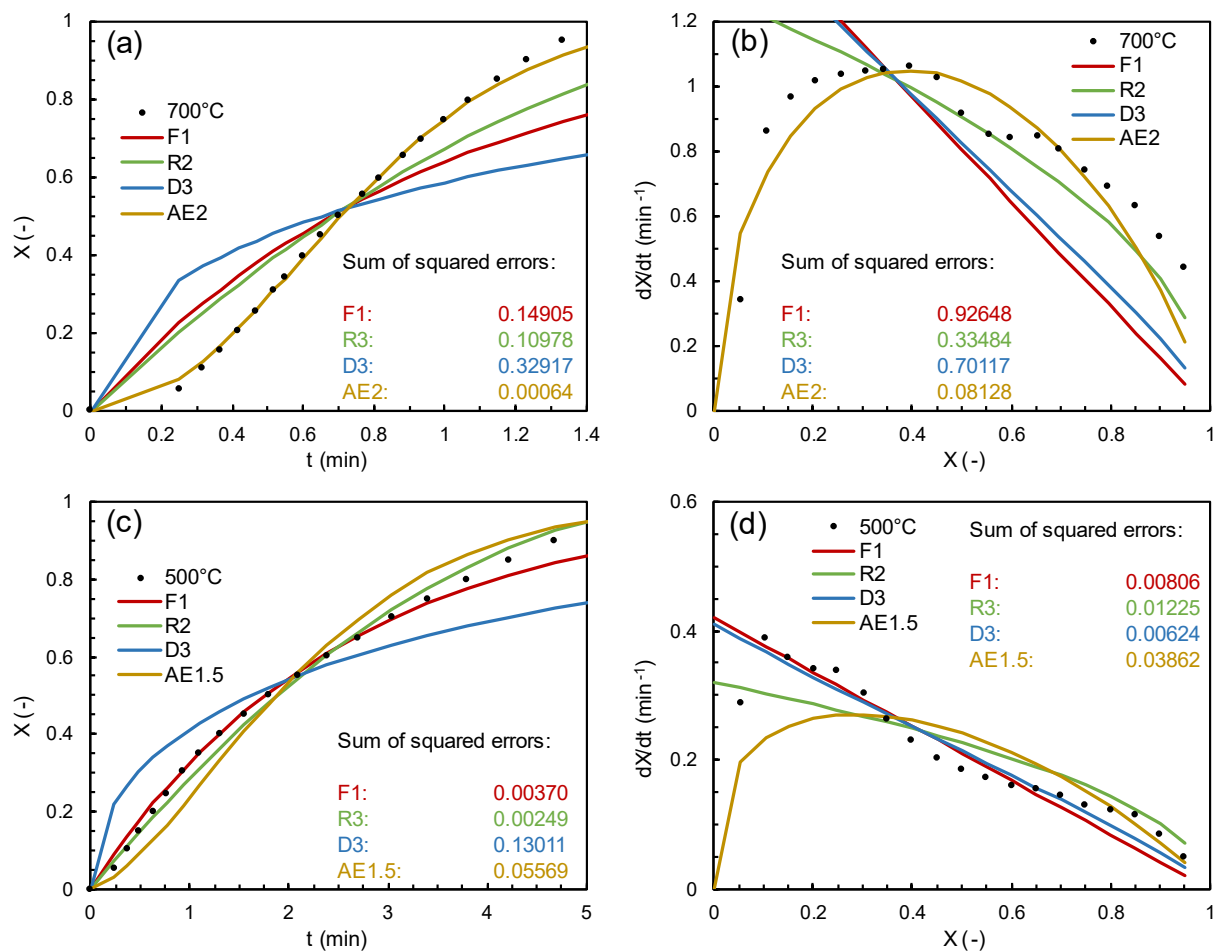


Figure 5.4. Model-fitting method results for CaMnO_3 reduction by 5% H_2 , shown for (a, c) integral and (b, d) differential data at 700°C and 500°C. Four best-fitting kinetic models are presented along with associated sum of squared errors (SSE): first-order power law (F1), three-dimensional unreacted shrinking core (R3), Jander equation for three-dimensional diffusion (D3), and Avrami-Erofe'ev nucleation (AE, $n = 1.5$ or 2). The fitting data are from Experiment 2 on sample CM-03.

The model fitting analysis described above and illustrated in **Figure 5.4** were applied to every individual data set. As can be seen from the range of kinetic parameters obtained across all experiments (**Table 5.2**), there is some variability in the kinetic parameters centered around an average E_a of approximately 39.5 kJ mol^{-1} , which agrees with the apparent value of E_a determined

in the work discussed previously in *Chapter 4* (40.1 kJ mol⁻¹ for CaMnO₃ prepared via the solid state reaction method). Removal of the outlier (30.2 kJ mol⁻¹) results in an average value of 40.6 kJ mol⁻¹, equally close in agreement to the reported value. The results together indicate that preparation method does not significantly affect the apparent E_a for reduction by H₂. One further insight that can be drawn from the data, from the CM-02 sample, is that the order in which the testing was performed did not significantly impact the reduction behavior or the apparent energy barrier; in back-to-back experiments following an increasing order program (500°C to 700°C) and then following a decreasing order program (700°C to 500°C), there was little observed variation.

Table 5.2. List of apparent activation energy and pre-exponential factor values obtained via the reduction of CaMnO₃ by H₂. Avrami-Erofe'ev models (AEn) were selected for parameter fitting.

Sample Name (Experiment)	Testing Order	Gas Environment	# of Previous Cycles	E _a (kJ mol ⁻¹)	k ₀ (s ⁻¹)
CM-01 (1)	<i>Decreasing</i>	10% H ₂	5	37.1	3.49
CM-02 (1)	<i>Decreasing</i>	5% H ₂	5	30.2	0.82
CM-02 (2)	<i>Increasing</i>	5% H ₂	23	39.6	3.99
CM-03 (2)	<i>Decreasing</i>	5% H ₂	24	40.6	1.93
CM-04 (1)	<i>Decreasing</i>	5% H ₂	25	42.9	1.85
CM-05 (1)	<i>Decreasing</i>	5% H ₂	45	40.6	1.58
CM-05 (2)	<i>Decreasing</i>	10% H ₂	66	42.3	8.16
CM-05 (3)	<i>Decreasing</i>	7.5% H ₂	87	43.2	7.34
CM-05 (4)	<i>Decreasing</i>	2.5% H ₂	105	39.4	2.03
CM-05 (5)	<i>Decreasing</i>	5% H ₂	123	39.5	3.33

However, the extent of prior redox cycling potentially had an impact on the redox catalyst working state and in particular on the pre-exponential factor. The two lowest values of the apparent E_a for reduction in H₂ (37.1 kJ mol⁻¹ for CM-01 and the outlier 30.2 kJ mol⁻¹ for CM-02) occurred when the respective samples had been cycled only five times each prior to the experiment, indicating that more extensive redox cycling may have stabilized the activation energy barrier for reduction

over time in the CaMnO_3 system. Moreover, the reduction rates became faster overall with increased cycling; a comparison of the two experiments using 10% H_2 (CM-01 (1) and CM-05 (2)) shows that the value of the pre-exponential factor more than doubled, from 3.49 s^{-1} to 8.16 s^{-1} , possibly as a result of the difference in pre-treatment (five vs. 87 cycles). A similar outcome was observed with CM-02 (1), showing a pre-exponential factor of 0.82 s^{-1} in 5% H_2 , and every other experiment, which provided a range of significantly higher values (3.99, 1.93, 1.85, 1.58, and 3.33), though with no obvious trend. One possible explanation for an increase in the reduction rates with cycling is that the average grain size of CaMnO_3 changed over time. In summary, while bulk CaMnO_3 reduction kinetics did not appear to be affected by testing order (highest temperatures vs. lowest temperatures first), the extent of redox cycling may have impacted the kinetics by bringing the samples to a higher and more stable activation barrier ($\sim 40 \text{ kJ mol}^{-1}$) and increasing the reduction rates of CaMnO_3 over time.

The final aspect to be considered for the bulk or unpromoted CaMnO_3 is the reduction kinetics in ethylene, which serves as an important contrast to the kinetics in H_2 . *Chapter 4* focused heavily on the differences in reduction rates for the various gases. Here, we mention that the reduction rate of CaMnO_3 in 5% C_2H_4 was in line with expectations based on the previously established rate data, with the magnitude of the rates about three to 15 times lower in ethylene than in hydrogen, and that the synthesis method (SSR method in *Chapter 4* vs. modified Pechini method in *Chapter 5*) did not substantially affect the kinetics. As shown in **Figure 5.5**, the reduction rates of bulk CaMnO_3 in 5% C_2H_4 atmosphere were only slightly lower than the reported rates for reduction of bulk CaMnO_3 (via SSR) in 10% C_2H_4 , a finding consistent with the reported low reaction order of $n = 0.28$ for ethylene.^[46] The apparent activation energy barrier was not calculated again for

reduction by C_2H_4 . Two final notes on the ethylene kinetics are that the testing order once again did not significantly impact the reduction rate and that the total extent of reduction of $CaMnO_3$ in C_2H_4 did not reach the minimum achieved under H_2 , which agrees with previous results on the oxygen site dependence of the ethylene combustion reaction and explains the incomplete reduction curves shown in **Figure 5.5**. Ethylene kinetics will not be discussed in much more detail, and the broad focus of this chapter is on the rate differences between $CaMnO_3$ and 20 wt.% $Na_2WO_4/CaMnO_3$ under H_2 , as described next.

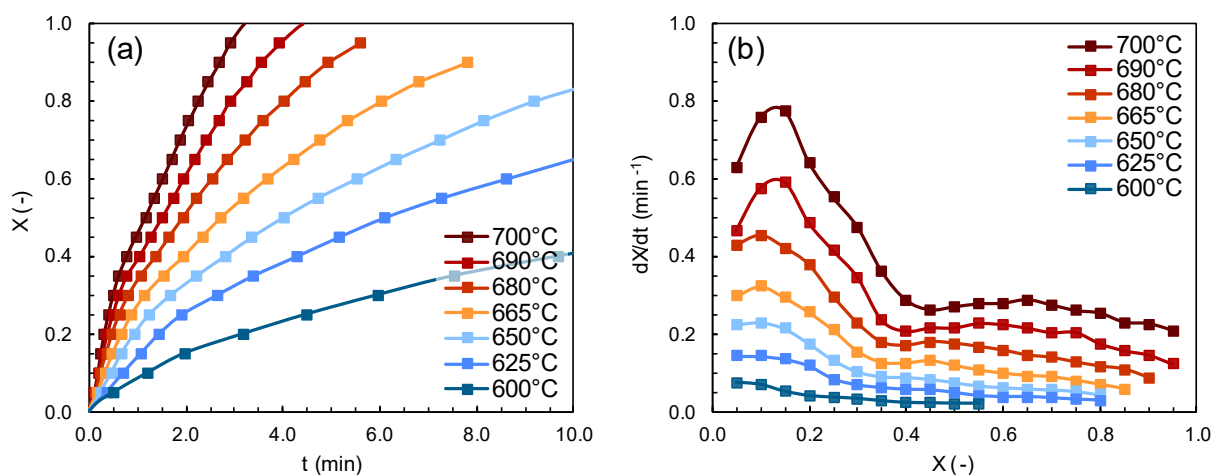


Figure 5.5: Reduction kinetics of $CaMnO_3$ in 5% C_2H_4 ; (a) Integral and (b) differential solid conversion plots.

Data were acquired on sample CM-04.

5.3.3. Reduction Kinetics of $Na_2WO_4/CaMnO_3$: Rate Crossover and Hysteresis Phenomena

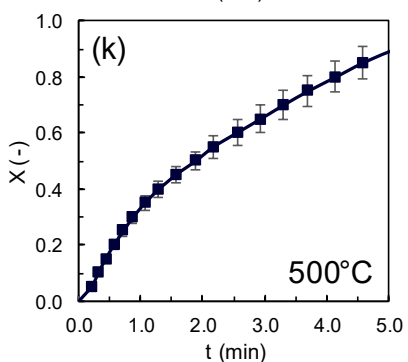
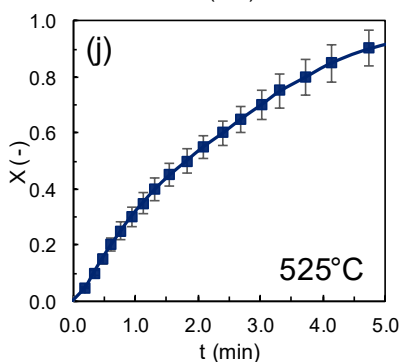
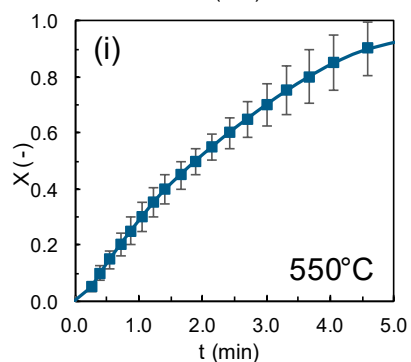
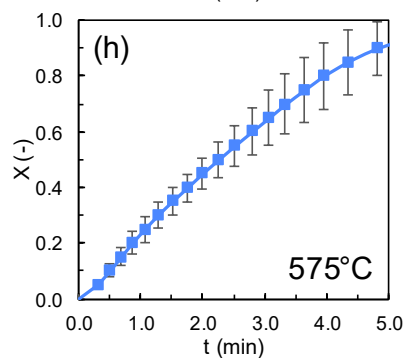
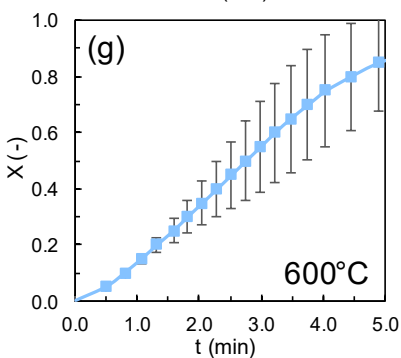
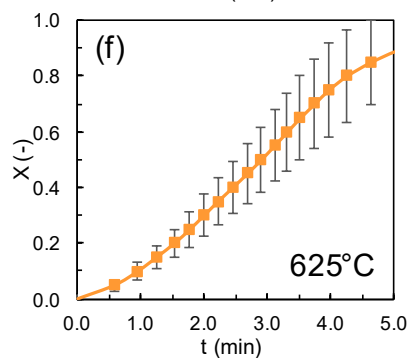
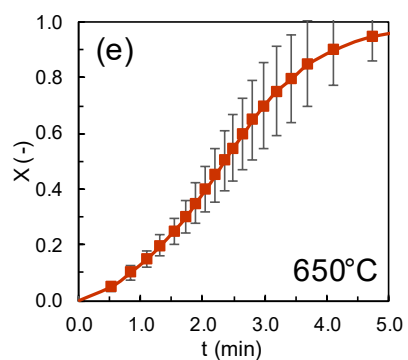
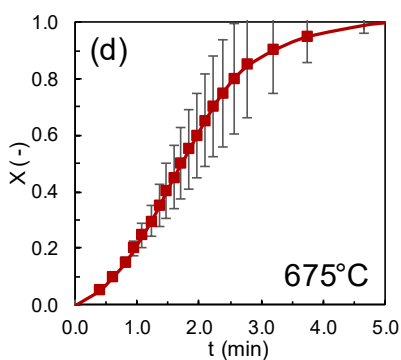
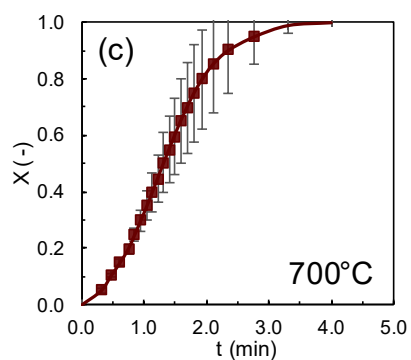
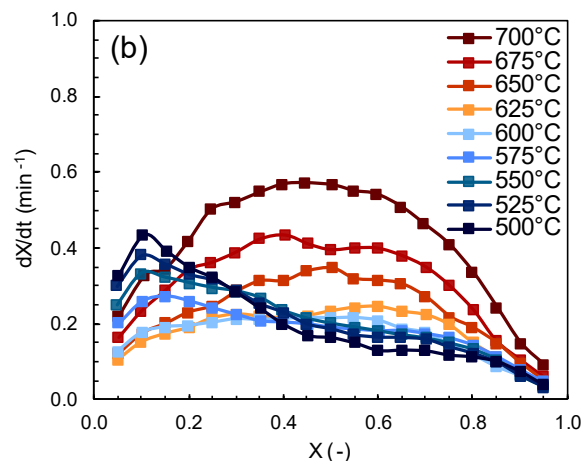
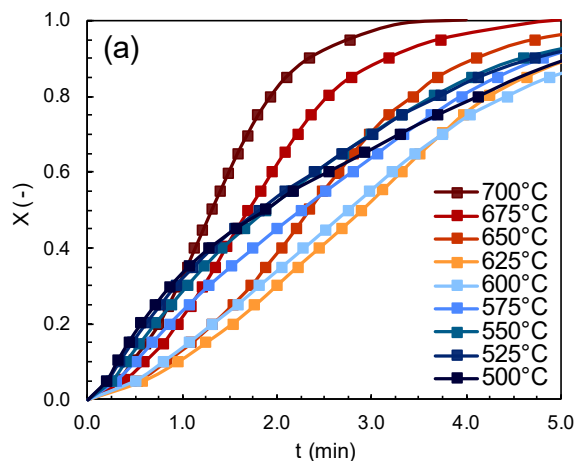
The primary goal of this chapter is to provide a comprehensive view of the reduction kinetics of the high-performing $Na_2WO_4/CaMnO_3$ redox catalyst in hydrogen gas, and to report on a series of interesting properties demonstrated by the material. In our previous work, we reported reduction rates and kinetic parameters for $Na_2WO_4/CaMnO_3$ in both H_2 and C_2H_4 and established that the

high selectivity of this redox catalyst stems from differences in the energy barrier (E_a and T), oxygen site dependence (X), and reaction order (P_{H_2} and $P_{C_2H_4}$). However, the full range of operating temperatures (500°C to 700°C) was not presented for the Na_2WO_4 -promoted $CaMnO_3$ due to a series of interesting, yet highly dynamic rate phenomena which proved difficult to explain from a material standpoint. The rest of this chapter will provide our current level of understanding of the reduction kinetics of $Na_2WO_4/CaMnO_3$, while the concluding chapter of this dissertation will include recommendations on how the system can and should be studied further.

Figure 5.6 illustrates the reduction kinetics of the 20 wt.% $Na_2WO_4/CaMnO_3$ redox catalyst in 5% H_2 over a range of nine temperatures from 500°C to 700°C. In **Figure 5.6a–b**, the integral and differential kinetic plots are shown, respectively; **Figure 5.6c–k** focuses on one temperature condition each and gives error bars constructed from the sample standard deviation of three independent experiments on samples NWCM-05, NWCM-08, and NWCM-09, all of which were pre-treated with five cycles only before the experiments. Moreover, each experiment was conducted in a decreasing temperature order beginning from 700°C. The most notable feature of the $Na_2WO_4/CaMnO_3$ kinetics is the presence of a statistically significant crossover between the high- and low-temperature conditions, particularly at low to intermediate conversion ($X < 0.6$), leading to an unusual phenomenon in which reduction rates increase with decreasing temperature starting at 625°C. Additionally, the rates at the four temperatures from 575°C to 500°C collapse upon one another, suggesting a region in which the apparent activation energy barrier equals zero. While the sample error did become prominent at high conversion due to the cumulative uncertainty throughout each experiment, at low conversions the error is minimal and so the crossover phenomenon should be accepted as repeatable. This phenomenon has also been reproduced across

multiple sample batches, including independent batches of modified Pechini method CaMnO_3 as well as solid state reaction method CaMnO_3 (**Figures D3–D4**) and at concentrations other than 5% H_2 ; the phenomenon was observed almost identically at 10% H_2 as shown in **Figures D3–D5**. All of these experiments agreed qualitatively (*e.g.* the absolute values of the rates were somewhat different, but the internal relations were comparable), and all showed similar crossover temperatures (typically 625°C or 600°C). Due to the lack of a similar rate crossover phenomenon for the unpromoted CaMnO_3 redox catalyst (**Figure 5.3**), the counterintuitive results of **Figure 5.6** can be attributed to the presence of the Na_2WO_4 promoter. Given that some of the potential applications for this redox catalyst involve the selective combustion of hydrogen at or near 650°C (*e.g.* ethane dehydrogenation, ethane dehydroaromatization), it is important to attempt to gain a fuller understanding of the system and of this Na_2WO_4 effect on kinetics within this temperature range. The following paragraphs delve further into various aspects of the reduction kinetics, with derived kinetic parameters E_a (kJ mol^{-1}) and k_0 (s^{-1}) listed in **Table 5.3**.

Figure 5.6: Reduction kinetics of 20 wt.% $\text{Na}_2\text{WO}_4/\text{CaMnO}_3$ in 5% H_2 . **(a)** Integral and **(b)** differential solid conversion plots, representing an average of thermogravimetric data for independent experiments across three samples (NWCM-05, NWCM-08, NWCM-09), for nine temperature conditions. **(c)—(k)**: Individual temperature data sets, with error bars representing one sample standard deviation calculated from the three individual sets. All data were acquired in a decreasing order of temperatures.



The $\text{Na}_2\text{WO}_4/\text{CaMnO}_3$ grows more complex when the testing order of temperature conditions is switched from decreasing order, as in **Figure 5.6**, to increasing order, *i.e.* beginning from 500°C and heating to 700°C . **Figure 5.7** shows the impact of reversing the testing order by examining the sample NWCM-07 in increasing order. (Multiple repetitions of this testing program have resulted in similar trends, but without sufficient quantitative agreement to make a presentation of error bars appropriate.) The rates at 500°C and 525°C , first in the testing order, were not well developed and are not pictured. On examination of **Figure 5.7** and in comparison with **Figure 5.6**, two conclusions can be drawn: (i) the reduction rates are generally faster when the material is tested in increasing order, particularly at 600°C and above, and (ii) no high—low crossover phenomenon occurs as was seen for the decreasing order data sets. The reduction of $\text{Na}_2\text{WO}_4/\text{CaMnO}_3$ by H_2 therefore exhibits thermal hysteresis in addition to the rate crossover during cooling.

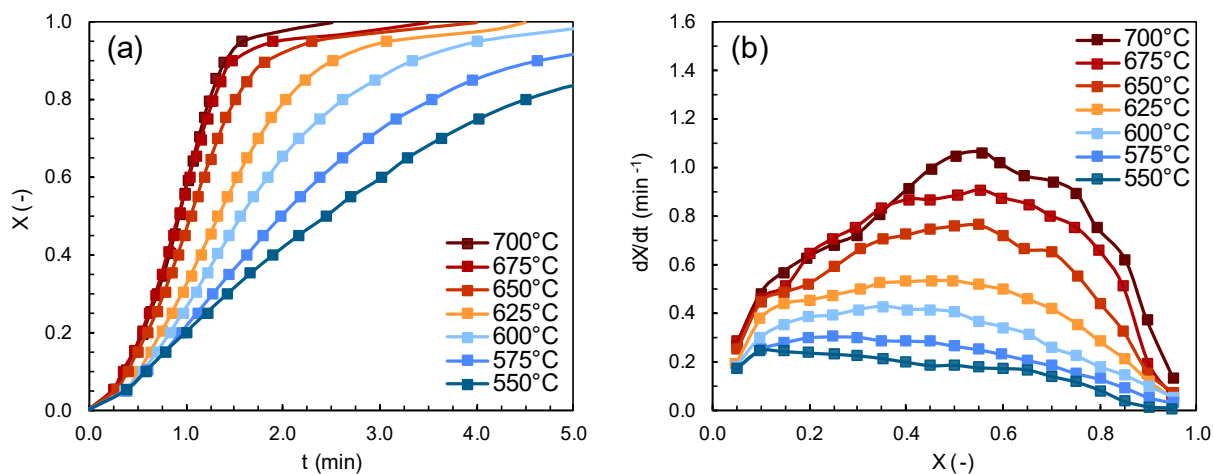


Figure 5.7: Reduction kinetics of 20 wt.% $\text{Na}_2\text{WO}_4/\text{CaMnO}_3$ in 5% H_2 . (a) Integral and (b) differential solid conversion plots for seven temperature conditions, acquired on a single sample (NWCM-07, Experiment 1).

All data were acquired in an increasing order of temperatures.

The hysteresis effect observed for the $\text{Na}_2\text{WO}_4/\text{CaMnO}_3$ system was explored in further detail via two independent experiments on samples NWCM-07 and NWCM-08 after each sample had been cycled more than 30 times (see NWCM-07, Experiment 2A-B and NWCM-08, Experiment 2A-B in *Appendix D*). In one testing program, the sample was heated to 675°C first, tested in decreasing order, then immediately re-tested in increasing order; in the other, the sample was uniformly heated from 525°C and tested in increasing order up to 700°C followed immediately by decreasing order. Dimensionless conversion curves for the two complementary experiments are depicted in **Figure 5.8**.

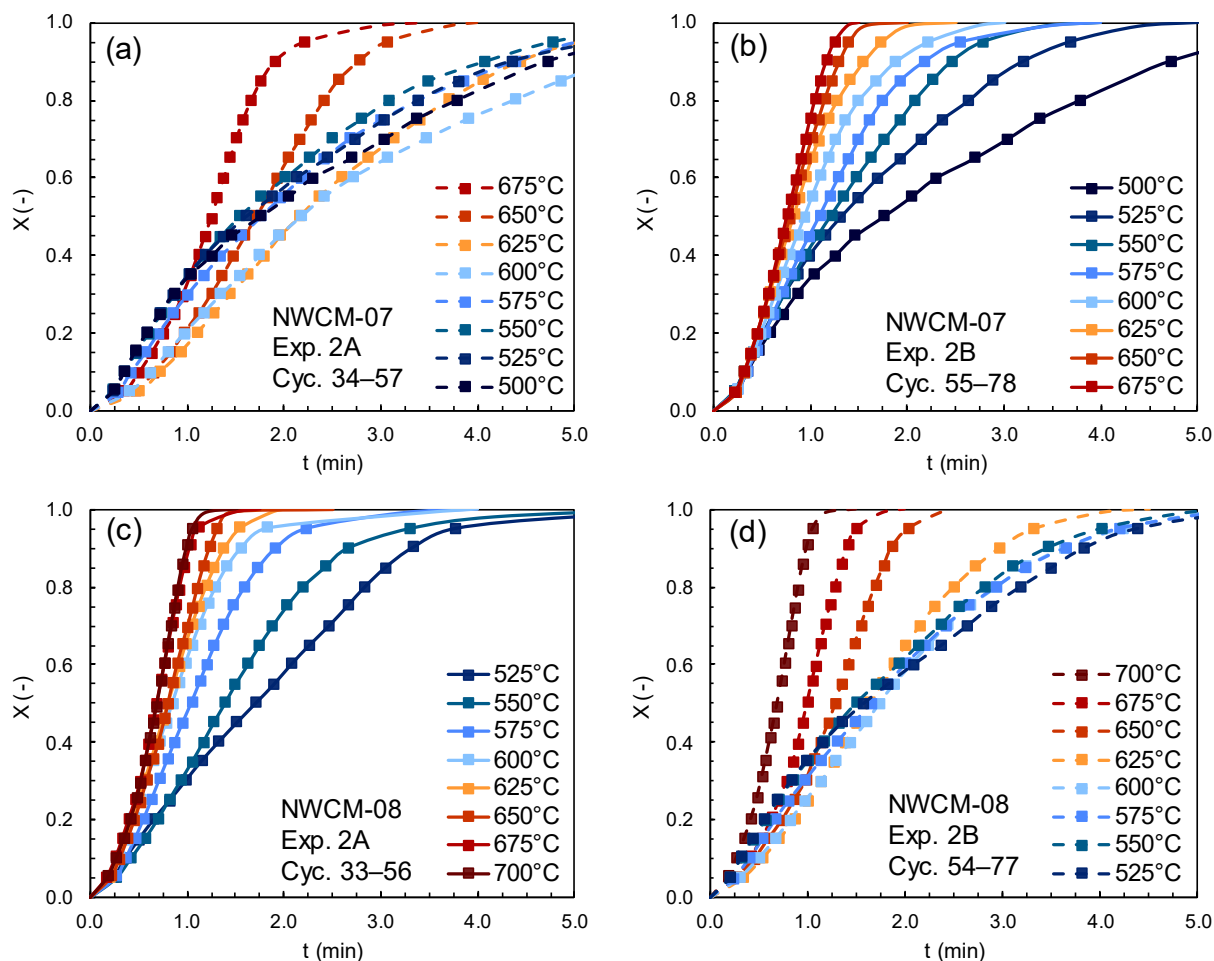


Figure 5.8: Examination of the thermal hysteresis effect on two distinct $\text{Na}_2\text{WO}_4/\text{CaMnO}_3$ samples. **(a)–(b):** Experiments on sample NWCM-07, tested first in decreasing order from 675°C to 500°C (Exp. 2A) and then back to 675°C (Exp. 2B), comprising cycles 34–78 on the sample. **(c)–(d):** Experiments on sample NWCM-08, tested first in increasing order from 525°C to 700°C (Exp. 2A) and then back to 525°C (Exp. 2B), comprising cycles 33–77 on the sample. Dotted lines represent cooling; solid lines represent heating.

The results in **Figure 5.8** clearly demonstrate that the high—low temperature rate crossover phenomenon observed for decreasing order experiments is itself not affected by thermal hysteresis, as this phenomenon occurs regardless of whether the sample is quickly heated to 675°C or 700°C and then tested immediately in decreasing order, or heated gradually to high temperature with

consistent redox cycling during the increasing order testing and then subsequently tested in decreasing order. Similarly, **Figure 5.8** also shows that the hysteresis effect differentiating the results from the two different testing orders will occur regardless of which conditions are performed first. Given the number of repetitions for which these phenomena have been observed as well as their appearance during two different testing protocols, the measurements shown here on the $\text{Na}_2\text{WO}_4/\text{CaMnO}_3$ redox catalyst during reduction with H_2 are likely to be genuine and not an artifact of the apparatus (*e.g.* TG drift).

5.3.4. Effect of Long-Term Redox Cycling on $\text{Na}_2\text{WO}_4/\text{CaMnO}_3$ Reduction Rates

In a final set of experiments testing the reduction of the $\text{Na}_2\text{WO}_4/\text{CaMnO}_3$ redox catalyst over an extended time, one final layer of complexity was revealed; namely, both the thermal hysteresis phenomenon (causing the increasing order and decreasing order rates to differ) and the rate crossover phenomenon (causing higher temperatures to produce lower reduction rates during sample cooling) disappeared gradually over the course of many redox cycles. **Figure 5.9** describes the effect of extended redox cycling on $\text{Na}_2\text{WO}_4/\text{CaMnO}_3$, using the NWCM-08 sample. Three sequential experiments (2, 5, and 6) were performed on this sample using the same testing program, with heating during the first half and cooling during the second half; in all, the sample was cycled in excess of 230 times, though not always with the same reducing gas environment (see *Appendix D* for details). The thermal hysteresis and the zero activation energy phenomenon both appeared during experiment 2A-B on NWCM-08, relatively early in the sample lifetime. However, subsequent experiments 5A-B and 6A-B clearly demonstrate that the hysteresis disappears with increasing cycle count. It is apparent from **Figure 5.9e–f** that after 180 redox cycles, the reduction rates during the increasing order and decreasing order programs have converged; moreover, the

decreasing order data (**Figure 5.9f**) no longer display a rate crossover between high and low temperature, and the rates from 575°C to 500°C are no longer identical, indicating that the apparent activation energy barrier no longer equals zero. Further experiments are needed to determine a material-based explanation for the hysteresis and rate crossover phenomena, as well as the gradual change in redox catalyst activity over time. In the following section we will describe an *in situ* X-ray diffraction investigation of Na₂WO₄/CaMnO₃, undertaken with this purpose in mind.

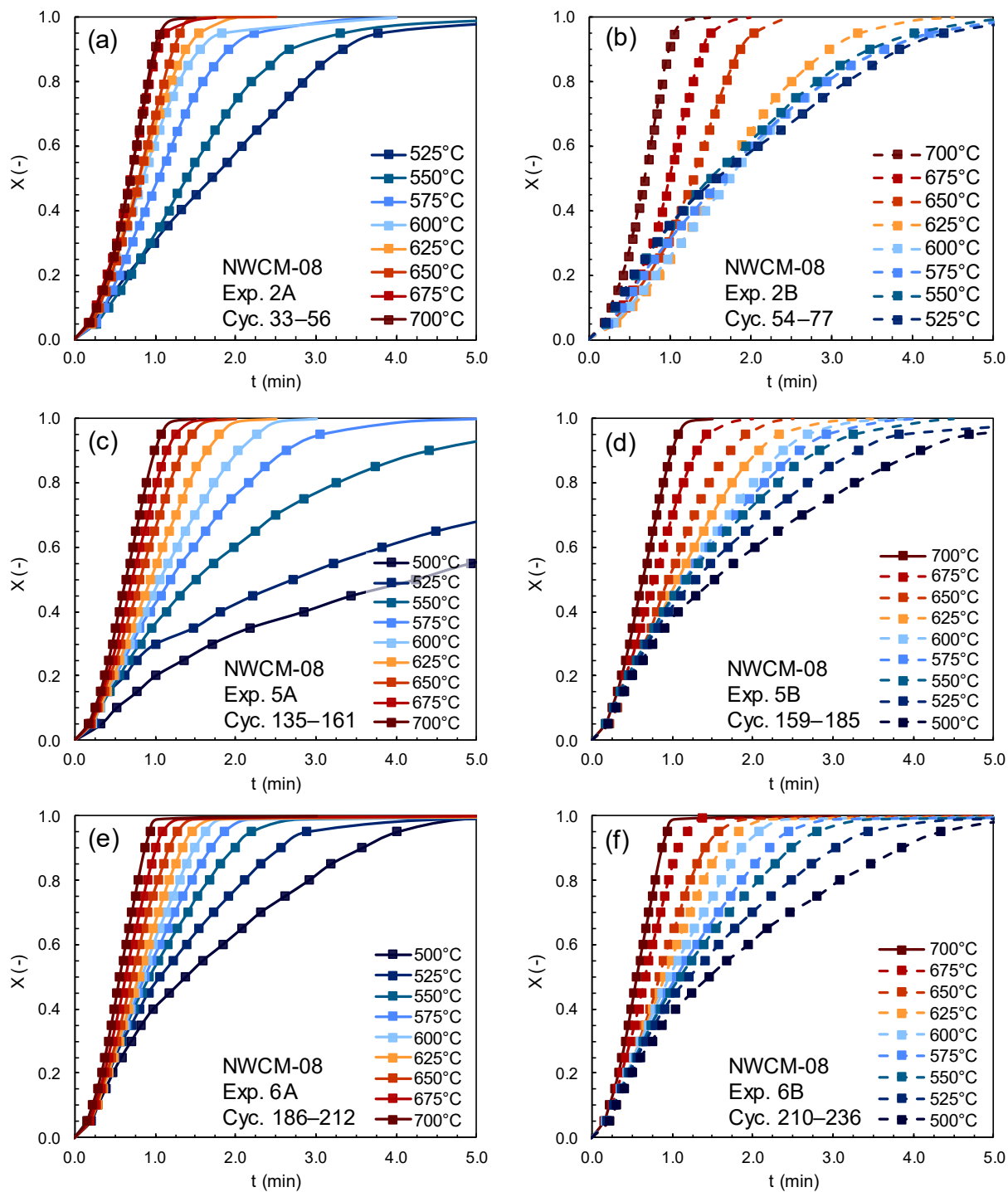


Figure 5.9: Effect of extended redox cycling on the reduction rate crossover and hysteresis phenomena of $\text{Na}_2\text{WO}_4/\text{CaMnO}_3$, all performed on sample NWCM-08: (a) Cycles 33–77; (b) Cycles 135–185; (c) Cycles 186–236. All experiments follow an increasing temperature program from 500°C/525°C to 700°C followed by a decreasing temperature program to 500°C/525°C. Reduction kinetics in 5% H_2 are shown.

We conclude the discussion of the reduction kinetics of $\text{Na}_2\text{WO}_4/\text{CaMnO}_3$ with H_2 by presenting **Table 5.3**, which summarizes the Arrhenius kinetic parameters (E_a , kJ mol^{-1} and k_0 , s^{-1}) from the experiments presented in **Figures 5.6–5.9**. The Avrami-Erofe'ev nucleation and nuclei growth model was used once again to capture the kinetics, as this family of models (particularly with $n = 1.5$ or 2) was determined to be best-fitting in a previous study (*Chapter 4*).^[46] Several key comparisons can be drawn from the data of **Table 5.3**. Firstly, by examining rows 1–3, 5, and 7 (corresponding to the data in **Figure 5.6** and **Figure 5.8a,d**), it is clear that during a cooling temperature program, the reduction kinetics of $\text{Na}_2\text{WO}_4/\text{CaMnO}_3$ are bifurcated around 600°C into a high-temperature region with a high E_a (on the order of 100 kJ mol^{-1}) and a low-temperature region with approximately zero activation energy. Rows 4–7 (**Figure 5.8**) directly compare the differing kinetic parameters obtained from a heating and a cooling program, reproduced on two samples, and clearly illustrate that the energy barriers associated with $\text{Na}_2\text{WO}_4/\text{CaMnO}_3$ reduction are not equal for a heating vs. a cooling program when the sample is still relatively fresh. Finally, an examination of rows 6–11 (**Figure 5.9**), and in particular of rows 7, 9, and 11, shows the steady convergence in apparent activation energy as the sample is progressively cycled, which results in the elimination of both the hysteresis phenomenon and the low-temperature rate convergence observed during the decreasing-order testing program.

Table 5.3. List of apparent activation energy and pre-exponential factor values obtained via the reduction of $\text{Na}_2\text{WO}_4/\text{CaMnO}_3$ by 5% H_2 . The Avrami-Erofe'ev model (AE1.5 or AE2) was selected for parameter fitting.

Experiments are separated into Low Temperature (575°C and below) and High Temperature (625°C and above) to capture the bifurcation of kinetics around 600°C for certain samples.

Row	Sample (Experiment)	Testing Order	# Prev. Cycles	E_a (kJ mol ⁻¹)		k_0 (s ⁻¹)	
				Low T	High T	Low T	High T
1	NWCM-05 (1)	<i>Dec</i>	5	0.0	71.7	5.0×10^{-4}	5.4×10^1
2	NWCM-08 (1)	<i>Dec</i>	5	8.3	88.0	2.0×10^{-2}	6.9×10^2
3	NWCM-09 (1)	<i>Dec</i>	5	0.0	74.4	2.0×10^{-3}	1.1×10^2
4	NWCM-07 (2A)	<i>Inc</i>	33	33.8		1.5×10^1	
5	NWCM-07 (2B)	<i>Dec</i>	54	4.6	111.7	1.0×10^{-2}	1.8×10^4
6	NWCM-08 (2A)	<i>Inc</i>	32	36.0		1.9×10^0	
7	NWCM-08 (2B)	<i>Dec</i>	53	0.5	100.6	1.0×10^{-2}	5.9×10^3
8	NWCM-08 (5A)	<i>Inc</i>	134	47.3		8.3×10^0	
9	NWCM-08 (5B)	<i>Dec</i>	158	24.4	61.7	4.2×10^{-1}	4.6×10^1
10	NWCM-08 (6A)	<i>Inc</i>	185	41.6	41.3	5.8×10^0	4.4×10^0
11	NWCM-08 (6B)	<i>Dec</i>	209	29.9	59.9	8.7×10^{-1}	4.3×10^1

5.3.5. In Situ X-Ray Diffraction Study

In an attempt to explain the thermal hysteresis and rate crossover phenomena on $\text{Na}_2\text{WO}_4/\text{CaMnO}_3$, we turned to *in situ* powder X-ray diffraction (XRD) to characterize changes in phase composition and crystal structure of the redox catalyst as a function of both temperature and gas environment. **Figure 5.10** displays *in situ* XRD data for the $\text{Na}_2\text{WO}_4/\text{CaMnO}_3$ redox catalyst during a heating program (**5.10a**) and cooling program (**5.10b**). The phase composition of the sample is largely consistent with previous reports for this material, with the reflections at $2\theta = 24^\circ$, 33° and 48° corresponding to the cubic CaMnO_3 phase (nominally 80 wt.% of the sample) and those at $2\theta = 16^\circ$, 28° , and 32° indicating the presence of cubic crystalline Na_2WO_4 . Upon heating the sample from room temperature to 700°C, the diffractions for crystalline Na_2WO_4 disappeared at approximately 600°C; this phase transition is in good agreement with previous *in*

situ characterization of Na₂WO₄.^[24,32,36,37] The melting point of Na₂WO₄ (695°C) is also well-established and has been observed via *in situ* techniques in multiple literature reports,^[32,33] as well as in **Figure 5.10**, which features a second set of diffraction peaks disappearing at approximately 680°C. However, there is uncertainty within the literature about the identity of the transitional phase which exists between 600°C and 680°C. According to Pistorius, the Na—W—O system at ambient pressure re-crystallizes from cubic to orthorhombic Na₂WO₄ at 600°C before melting at 695°C.^[33] Werny *et al.* attributed a phase in this 600°C to 680°C region, with peaks $2\theta = 17^\circ, 21^\circ, 26.5^\circ, 27.5^\circ, 28.5^\circ, 31^\circ, \text{ and } 32^\circ$, to the orthorhombic structure of Na₂WO₄.^[32] Interestingly, these authors reported different diffraction patterns when Na₂WO₄ was heated under 10% O₂ environment vs. pure He; they did not identify the different phase which persisted during heating under inert He ($2\theta = 17^\circ, 18.5^\circ, 19.5^\circ, 20.5^\circ, 23^\circ, 25.5^\circ, 26.5^\circ, 27^\circ, 28^\circ, 29.5^\circ, 31.5^\circ$) and also did not comment on whether it was one or potentially multiple transition phases.^[32] The diffraction peaks reported here in **Figure 5.10** resemble more closely the orthorhombic Na₂WO₄ described by Werny *et al.* In contrast, Hao *et al.*, studying the same Na₂WO₄/CaMnO₃ system as in this work, attributed a similar set of peaks in this region to Na₂W₂O₇.^[24] In the absence of more reliable diffraction data from the literature, it is difficult to rule out either phase, but it is evident that the Na₂WO₄ promoter undergoes a phase transition into a non-cubic crystalline phase within the same temperature range that the hysteresis effect appears in the reduction kinetics of Na₂WO₄/CaMnO₃. However, the *in situ* XRD data from heating and cooling do not appear to show significant hysteresis in the melting and recrystallization behavior; the aforementioned transitional peaks appear faintly in **Figure 5.10b** before disappearing at approximately 575°C. This slight amount of hysteresis is in fact less significant than the hysteresis previously reported for this system, where cubic Na₂WO₄ did not recrystallize until 450°C. It is therefore difficult to conclude anything about

the melting and recrystallization of the Na_2WO_4 , and its impact on the observed rate crossover and hysteresis phenomena, from the heating and cooling data alone.

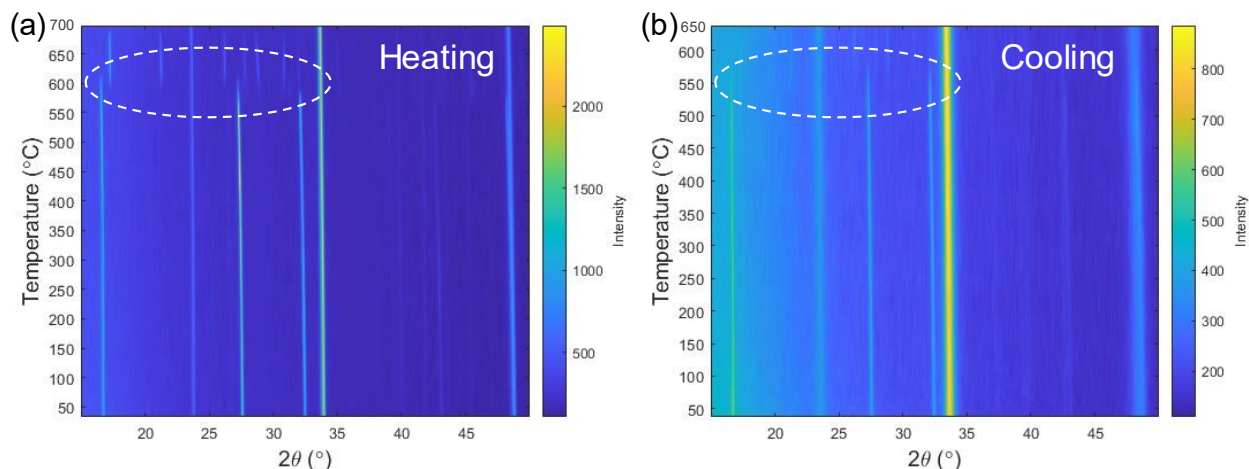


Figure 5.10: *In situ* XRD patterns for $\text{Na}_2\text{WO}_4/\text{CaMnO}_3$ redox catalyst. (a) Heating from RT to 700°C, prior to redox cycling. (b) Cooling from 650°C to RT, following redox cycling.

To complement the *in situ* XRD data from heating and cooling, *in situ* XRD measurements were also taken at six isothermal conditions: 550°C, 600°C, 625°C, 650°C, 675°C, and 700°C. In these experiments, sample powder of $\text{Na}_2\text{WO}_4/\text{CaMnO}_3$ was alternated between 3% H_2 (balance N_2) and air environments, with inert N_2 serving as the purge gas. **Figure 5.11** shows the XRD patterns collected at all six conditions during redox cycling. The reduction step begins at approximately $t = 10$ min for each condition, with some variability, and lasts for a duration of between 45–90 minutes, with lower temperatures requiring a longer exposure to reduce completely. The greater intensity of the diffraction peaks in **Figure 5.11a** and **5.11f** (550°C and 700°C) are a result of fresh sample being used for these runs; in addition, the higher temperature runs generally maintained higher crystallinity and displayed more intense peaks as a result. All six measurements clearly show the signature peaks of CaMnO_3 at $2\theta = 24^\circ$, 33° and 48° . However, crystalline Na_2WO_4

appears only for the fresh samples which are present at the beginning of the runs pictured in **Figure 5.11a** and **5.11f**, and it is worth mentioning that Na_2WO_4 evidently does not reappear in crystalline form following re-oxidation even if the operating temperature is below the melting point of Na_2WO_4 (695°C). At all six temperatures, the reduction of the $\text{Na}_2\text{WO}_4/\text{CaMnO}_3$ redox catalyst results almost immediately in the appearance of crystalline Ca_3WO_6 at $2\theta = 18.5^\circ, 19^\circ, 22^\circ, 31.5^\circ,$ and 38.5° (see **Figure D6** of *Appendix D*). This phase has been reported previously during the reduction of this redox catalyst.^[6] Notably, this Ca_3WO_6 persists even after re-oxidation when the temperature is low (less than 650°C), such that the material likely begins with surface Ca_3WO_6 at the beginning of each redox cycle when the redox catalyst is operated below 650°C . It is possible that the Ca_3WO_6 phase factors into the rate crossover phenomenon; for example, if Ca_3WO_6 (which has a melting point far above these temperatures) has oxygen conductivity higher than orthorhombic Na_2WO_4 (or $\text{Na}_2\text{W}_2\text{O}_7$) but lower than that of cubic Na_2WO_4 , the reduction rate could increase due to the prevalence of surface Ca_3WO_6 as the temperature is lowered from 700°C . An explanation of the thermal hysteresis phenomenon is more elusive. Oxide ionic conductivity measurements for Na_2WO_4 , $\text{Na}_2\text{W}_2\text{O}_7$, and Ca_3WO_6 collected across the temperature range 500°C to 700°C (in which range the sodium tungstates are molten) could be useful in explaining the hysteresis, as the movement of oxygen ions (O^{2-}) through the surface layer of the redox catalyst likely plays a major role in the overall reduction kinetics of the material. Additional *in situ* or operando techniques, such as *in situ* Raman spectroscopy, could also shed light on the working state of the redox catalyst and better inform the study of the reduction kinetics.^[30]

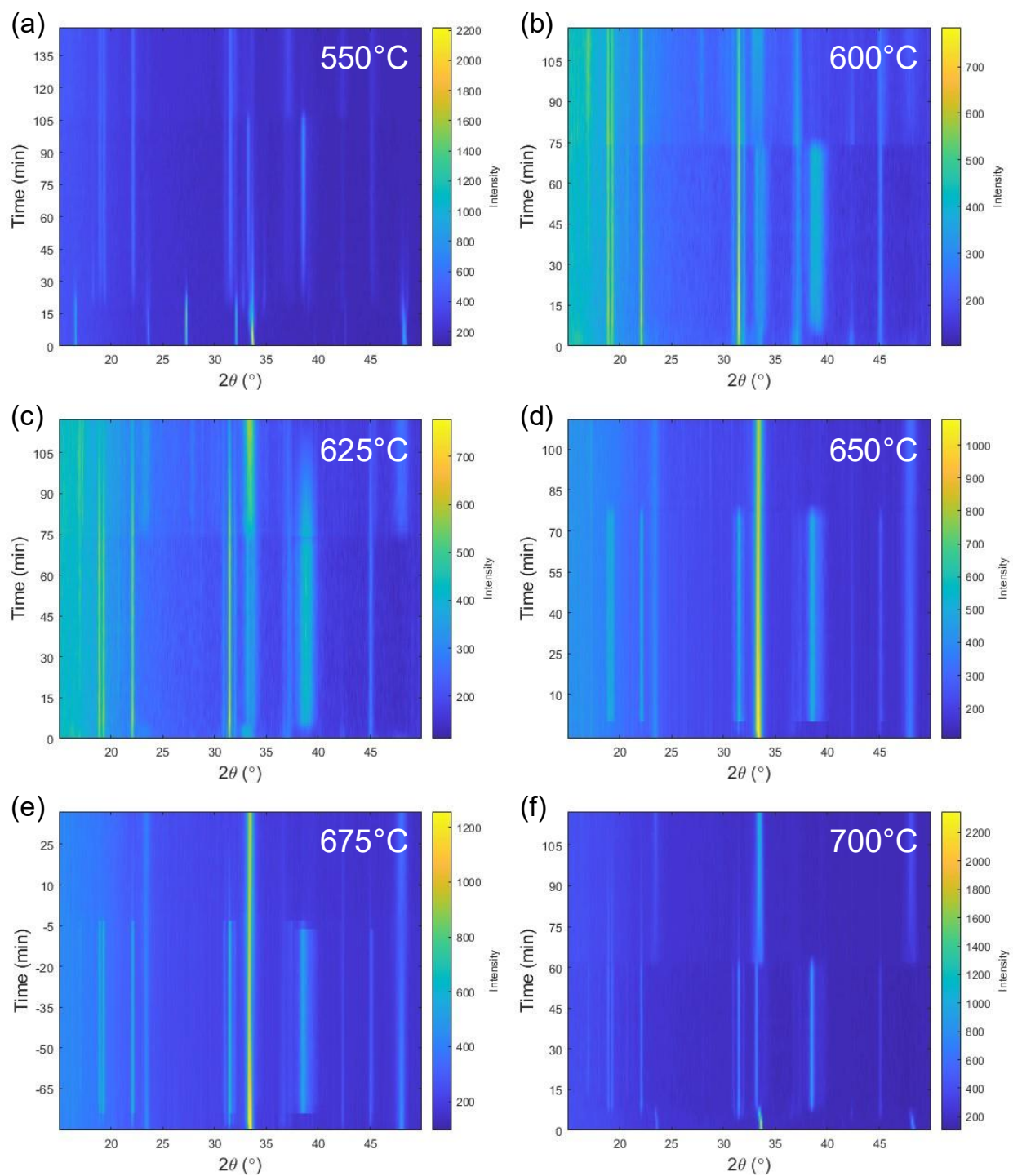


Figure 5.11: *In situ* XRD patterns for $\text{Na}_2\text{WO}_4/\text{CaMnO}_3$ redox catalyst at six operating temperatures during redox cycling. Beginning at $t = 0$ under inert N_2 flow, the sample is switched to a 3% H_2 environment for 45 to 90 minutes, purged in N_2 , and then re-oxidized with air.

5.4. Conclusions

In this study, we further investigated the reduction kinetics of both the unpromoted and 20 wt.% Na_2WO_4 -promoted CaMnO_3 redox catalysts for application in the CL-ODH of ethane and related applications involving the selective combustion of H_2 . Multiple experiments were conducted on CaMnO_3 to determine a more precise P_{H_2} and T dependence and to improve the previously reported model for the reduction kinetics of CaMnO_3 in H_2 gas. For the $\text{Na}_2\text{WO}_4/\text{CaMnO}_3$ redox catalyst, two repeatable phenomena were observed which may have interesting implications in applying the material for ethane CL-ODH. Firstly, thermal hysteresis was observed in which the temperature order of the kinetics experiments (increasing or decreasing) had a significant effect on the kinetic parameters and reduction rates for $\text{Na}_2\text{WO}_4/\text{CaMnO}_3$. Secondly, when $\text{Na}_2\text{WO}_4/\text{CaMnO}_3$ was tested with a cooling (decreasing temperature) program, the rates at four conditions between 575°C and 500°C converged on one another, and all of the low-temperature reduction rates were faster than the rates at higher temperature (600°C and above). Both phenomena gradually disappeared as the sample was cycled more extensively (> 200 cycles). *In situ* XRD results indicated a lack of significant hysteresis in the melting and recrystallization behavior of the Na_2WO_4 promoter, but also revealed a crystalline Ca_3WO_6 phase which could potentially be involved in the rapid reduction of the $\text{Na}_2\text{WO}_4/\text{CaMnO}_3$ redox catalyst at lower temperatures. Further investigations are needed to assess material changes (such as phase composition) of the material over many redox cycles and the impact of the changes on the reduction kinetics.

5.5. References

- [1] X. Zhu, Q. Imtiaz, F. Donat, *Energy Environ. Sci.* **2020**, *13*, 772–804.
- [2] V. P. Haribal, L. M. Neal, F. Li, *Energy* **2017**, *119*, 1024–1035.
- [3] C. A. Gartner, A. C. Van Veen, J. A. Lercher, *ChemCatChem* **2013**, *5*, 3196–3217.
- [4] L. M. Neal, S. Yusuf, J. A. Sofranko, F. Li, *Energy Technol.* **2016**, *4*, 1200–1208.
- [5] S. Yusuf, L. M. Neal, F. Li, *ACS Catal.* **2017**, *7*, 5163–5173.
- [6] R. B. Dudek, Y. Gao, J. Zhang, F. Li, *AIChE J.* **2018**, *00*, 1–10.
- [7] J. Adanez, A. Abad, F. Garcia-Labiano, P. Gayan, L. F. De Diego, *Prog. Energy Combust. Sci.* **2012**, *38*, 215–282.
- [8] L. Zeng, Z. Cheng, J. A. Fan, L. Fan, J. Gong, *Nat. Rev. Chem.* **2018**, *2*, 349–364.
- [9] J. G. Tsikoyiannis, D. L. Stern, R. K. Grasselli, **1999**, *86*, 77–86.
- [10] S. Al-Ghamdi, M. Volpe, M. M. Hossain, H. De Lasa, *Appl. Catal. A Gen.* **2013**, *450*, 120–130.
- [11] S. A. Al-Ghamdi, H. I. De Lasa, *Fuel* **2014**, *128*, 120–140.
- [12] I. A. Bakare, S. A. Mohamed, S. Al-ghamdi, S. A. Razzak, M. M. Hossain, H. I. De Lasa, *Chem. Eng. J.* **2015**, *278*, 207–216.
- [13] A. H. Elbadawi, M. S. Ba-shammakh, S. Al-ghamdi, S. A. Razzak, M. M. Hossain, *Chem. Eng. J.* **2016**, *284*, 448–457.
- [14] S. Chen, L. Zeng, R. Mu, C. Xiong, Z. Zhao, C. Zhao, C. Pei, L. Peng, J. Luo, L. Fan, et al., *J. Am. Chem. Soc.* **2019**, *141*, 18653–18657.
- [15] P. Novotný, S. Yusuf, F. Li, H. H. Lamb, *Catal. Today* **2018**, 1–6.
- [16] S. Yusuf, V. Haribal, D. Jackson, L. Neal, F. Li, *Appl. Catal. B Environ.* **2019**, *257*, 117885.

- [17] Y. Gao, L. M. Neal, F. Li, *ACS Catal.* **2016**, *6*, 7293–7302.
- [18] Y. Gao, F. Haeri, F. He, F. Li, *ACS Catal.* **2018**, 1757–1766.
- [19] Y. Gao, X. Wang, J. Liu, C. Huang, K. Zhao, Z. Zhao, X. Wang, F. Li, **2020**, 1–10.
- [20] S. Yusuf, L. Neal, Z. Bao, Z. Wu, F. Li, *ACS Catal.* **2019**, *9*, 3174–3186.
- [21] S. Yusuf, L. Neal, V. Haribal, M. Baldwin, H. H. Lamb, F. Li, *Appl. Catal. B Environ.* **2018**, *232*, 77–85.
- [22] R. B. Dudek, X. Tian, M. Blivin, L. M. Neal, H. Zhao, F. Li, *Appl. Catal. B Environ.* **2019**, *246*, 30–40.
- [23] X. Tian, R. B. Dudek, Y. Gao, H. Zhao, F. Li, *Catal. Sci. Technol.* **2019**, 2211–2220.
- [24] F. Hao, Y. Gao, L. Neal, R. B. Dudek, W. Li, C. Chung, B. Guan, P. Liu, X. Liu, F. Li, *J. Catal.* **2020**, *385*, 213–223.
- [25] Z. C. Jiang, C. J. Yu, X. P. Fang, S. B. Li, H. L. Wang, *J. Phys. Chem.* **1993**, *97*, 12870–12875.
- [26] Z. Q. Yu, X. M. Yang, J. H. Lunsford, M. P. Rosynek, *J. Catal.* **1995**, *154*, 163–173.
- [27] D. J. Wang, M. P. Rosynek, J. H. Lunsford, *J. Catal.* **1995**, *155*, 390–402.
- [28] S. Pak, P. Qiu, J. H. Lunsford, *J. Catal.* **1998**, *179*, 222–230.
- [29] S. Arndt, T. Otremba, U. Simon, M. Yildiz, H. Schubert, R. Schomäcker, *Appl. Catal. A, Gen.* **2012**, *425–426*, 53–61.
- [30] D. Kiani, S. Sourav, J. Baltrusaitis, I. E. Wachs, *ACS Catal.* **2019**, *9*, 5912–5928.
- [31] S. Hou, Y. Cao, W. Xiong, H. Liu, Y. Kou, *Ind. Eng. Chem. Res.* **2006**, *45*, 7077–7083.
- [32] M. J. Werny, Y. Wang, F. Girgsdies, R. Schlögl, A. Trunschke, *Angew. Chemie Int. Ed.* **2020**, *59*, 14921–14926.
- [33] C. W. F. T. Pistorius, *J. Chem. Phys.* **1966**, *44*, 4532.

- [34] M. A. Cortes-Jacome, C. Angeles-Chavez, M. Morales, E. Lopez-Salinas, J. A. Toledo-Antonio, *J. Solid State Chem.* **2007**, *180*, 2682–2689.
- [35] C. Luz Lima, G. D. Saraiva, P. T. C. Freire, M. Maczka, W. Paraguassu, F. F. de Sousa, J. Mendes Filho, *J. Raman Spectrosc.* **2011**, *42*, 799–802.
- [36] K. Takanabe, A. M. Khan, Y. Tang, L. Nguyen, A. Ziani, B. W. Jacobs, A. M. Elbaz, S. M. Sarathy, F. F. Tao, *Angew. Chemie Int. Ed.* **2017**, *56*, 10403–10407.
- [37] J. Wang, J. L. You, A. A. Sobol, L. M. Lu, M. Wang, J. Wu, X. M. Lv, S. M. Wan, *J. Raman Spectrosc.* **2017**, *48*, 298–304.
- [38] J. Xu, Y. Li, J. Wang, H. Bao, J. Wang, C. Zhu, *Adv. Electron. Mater.* **2018**, *4*, 1800352.
- [39] K. E. Sedor, M. M. Hossain, H. I. De Lasa, *Can. J. Chem. Eng.* **2008**, *86*, 323–334.
- [40] I. Iliuta, R. Tahoces, G. S. Patience, S. Rifflart, F. Luck, *AIChE J.* **2010**, *56*, 1063–1079.
- [41] L. Han, Z. Zhou, G. M. Bollas, *Chem. Eng. Sci.* **2014**, *113*, 116–128.
- [42] T. Mattisson, A. Järnäs, A. Lyngfelt, *Energy and Fuels* **2003**, *17*, 643–651.
- [43] Z. Zhou, L. Han, G. M. Bollas, *Int. J. Hydrogen Energy* **2014**, *9*, 8535–8556.
- [44] M. S. C. Chan, H. G. Baldovi, J. S. Dennis, **2018**, 887–897.
- [45] A. Khawam, D. R. Flanagan, *J. Phys. Chem. B* **2006**, *110*, 17315–17328.
- [46] R. B. Dudek, Y. Tian, G. Jin, M. Blivin, F. Li, *Energy Technol.* **2019**, *1900738*, 1–12.
- [47] Y. Tian, R. B. Dudek, P. R. Westmoreland, F. Li, *Chem. Eng. J.* **2020**, *398*, 125583.
- [48] L. M. Neal, V. P. Haribal, F. Li, *iScience* **2019**, *19*, 894–904.
- [49] Z. Zhou, L. Han, G. M. Bollas, *Int. J. Hydrogen Energy* **2014**, *39*, 8535–8556.

CHAPTER 6: CONCLUSIONS AND OUTLOOK

6.1. Conclusions

As global demand grows for ethylene and propylene, more sustainable and intensified processes are needed to supply these critical building blocks to the chemicals sector while reducing energy consumption and mitigating carbon emissions. Oxidative dehydrogenation (ODH) is a promising process alternative to replace the energy- and carbon-intensive steam cracking of ethane due to its net exothermicity, higher equilibrium ethylene yields, and minimal coke deposition. Similarly, oxidative cracking (OC) provides a path for lower-temperature conversion of naphtha to both light olefins, ethylene and propylene. However, the implementation of both processes is difficult due to the necessity for pure O₂ from costly air separation and the inherently dangerous requirement for oxygen—hydrocarbon co-feed. Adopting a chemical looping (CL) approach for both ODH and OC eliminates these core disadvantages while preserving the main energetic and environmental benefits of each process in comparison with steam cracking. In both chemical looping oxidative dehydrogenation (CL-ODH) and redox oxidative cracking (ROC), two half-reactions proceed in spatially separate reactors, linked together by a solid oxygen-donating intermediate phase known as a redox catalyst. In the ODH (OC) reactor, also referred to as the reducer, the feed hydrocarbon (ethane or naphtha) undergoes gas-phase pyrolysis to form a mixture of light olefins, hydrogen gas, and unreacted feedstock. As the product mixture comes into contact with the metal oxide redox catalyst, the co-produced H₂ is selectively combusted by the redox catalyst to form water, supplying *in situ* high-grade heat and shifting the equilibrium towards the production of olefins. In the regenerator reactor, the depleted redox catalyst becomes exposed to air and extracts the O₂ due to the P_{O₂} difference between the air and the solid, enabling a thermodynamically driven, high-

temperature reactive separation scheme. The redox catalyst, capable of becoming reduced and re-oxidized over thousands of cycles, is of central importance to CL-ODH and ROC.

The property of selective hydrogen combustion (SHC) – the ability of a redox catalyst material to oxidize H₂ out of a hydrocarbon gas mixture without reacting with other compounds to form CO or CO₂ – is critical to the success of any CL-ODH or ROC reaction and to any process operating on similar principles. Thus, the first body of work presented here focused on the screening of a set of redox catalysts for SHC properties in the context of CL-ODH of ethane. A series of low-cost, environmentally benign redox catalysts using manganese (Mn) and an assortment of alkaline earth metals (Mg, Ca, Sr), with and without an alkali salt promoter (sodium tungstate, Na₂WO₄), were selected for SHC testing across the temperature range 550–850°C. Unpromoted variants of the rock salt-structured Mg₆MnO₈ and perovskite oxide-structured CaMnO₃ and SrMnO₃ exhibited inherent selectivity towards H₂ combustion in the presence of C₂H₄; in general, H₂ conversion rose and selectivity towards H₂ combustion (S_H) fell with increasing temperature. The addition of 20 wt.% Na₂WO₄ to each metal oxide substrate via wet impregnation resulted in much more selective redox catalysts which combusted H₂ more selectively even in the presence of equimolar C₂H₄. Characterization of the six samples via XPS revealed that Na₂WO₄ inhibits the surface expression of Mn, which correlated well with the increase in S_H. Na and W, in contrast, were over-expressed in the near-surface regions of the promoted samples, suggesting an enrichment of Na₂WO₄ to the redox catalyst surface. The high-performing Na₂WO₄/CaMnO₃ redox catalyst was tested for 50 cycles at 850°C and found to have satisfactory cycling stability. Additionally, Na₂WO₄/CaMnO₃ was evaluated for SHC in the presence of an ethane dehydrogenation co-catalyst (Cr₂O₃/Al₂O₃) and combusted 84% of the produced H₂ while limiting CO_x yield to below 2% on a carbon basis.

The three promoted materials – $\text{Na}_2\text{WO}_4/\text{Mg}_6\text{MnO}_8$, $\text{Na}_2\text{WO}_4/\text{CaMnO}_3$, and $\text{Na}_2\text{WO}_4/\text{SrMnO}_3$ – were found to be exceptional redox catalysts for SHC across a range of operating temperatures.

Perovskite oxide-based redox catalysts $\text{Na}_2\text{WO}_4/\text{CaMnO}_3$ and $\text{Na}_2\text{WO}_4/\text{SrMnO}_3$ were examined in closer detail for the redox oxidative cracking (ROC) of naphtha to light olefins, using *n*-hexane as a model compound for naphtha. (A subsequent study by these authors utilizes cyclohexane as a naphtha model compound and finds similar results.)^[1] Both Na_2WO_4 -promoted redox catalysts gave superior olefin yields compared to thermal cracking and also compared favorably with literature reports of olefin and CO_x yields from oxidative cracking; at 725°C and 4500 h^{-1} and over 25 redox cycles, $\text{Na}_2\text{WO}_4/\text{CaMnO}_3$ provided olefin yields 72% higher than thermal cracking and combusted all available H_2 while generating less than 3% CO_x , and $\text{Na}_2\text{WO}_4/\text{SrMnO}_3$ showed CO_x as low as 0.28%. The selective hydrogen combustion (SHC) by the redox catalysts, and consequently the preservation of high yields of ethylene and propylene, was primarily attributed to the presence of Na_2WO_4 as a surface-enriched promoter, which significantly altered the surface properties of the CaMnO_3 and SrMnO_3 bulk oxides. The unpromoted oxides generated excessive CO_2 and lower olefin yields as a result. An array of characterization techniques revealed a core-shell arrangement of the $(\text{Ca},\text{Sr})\text{MnO}_3$ and Na_2WO_4 components; data from low-energy ion scattering (LEIS) along with XPS near-surface chemical composition data clearly showed Na_2WO_4 enriched in the near-surface and constituting the first several layers of the redox catalyst surface. Hao *et al.* confirmed via transmission electron microscopy (TEM) and energy dispersive X-ray spectroscopy (EDS) in a follow-up study that molten Na_2WO_4 coats the exterior of CaMnO_3 . Non-selective surface oxygen species such as hydroxides (OH^-) and carbonates (CO_3^{2-}) were suppressed by the Na_2WO_4 promoter, which correlated with a 97% and a 90% suppression in CO_x selectivity

on the SrMnO₃ and CaMnO₃ systems, respectively.^[1] Similarly, the thermal uncoupling of oxygen from the lattice of CaMnO₃ was inhibited by the tungstate promoter, further benefiting the selectivity towards H₂ combustion. Na₂WO₄/CaMnO₃ and Na₂WO₄/SrMnO₃ redox catalysts were shown to be promising redox catalysts for the ROC of naphtha for intensified olefin production, and a combination of reaction testing and characterization methods emphasized the importance of the Na₂WO₄ surface layer to the overall function of the redox catalysts. As with the previous study, Na₂WO₄/CaMnO₃ showed the highest performance for ROC – in this case, the highest olefin yield – among all the materials tested, and so Na₂WO₄/CaMnO₃ was selected for a detailed investigation.

To facilitate the rational design and optimization of redox catalysts in chemical looping processes, a firm understanding of redox catalyst kinetics must be obtained – therefore, the remainder of this work focused on the reduction and re-oxidation of Na₂WO₄/CaMnO₃ at the particle level. Treating selective hydrogen combustion as a consequence of particle-level differences in the reduction of a redox catalyst by H₂, C₂H₄, and other feedstock or product molecules, we examined the reduction kinetics of CaMnO₃ and Na₂WO₄/CaMnO₃, first with a focus on fitting kinetic models to the solid conversion by H₂ and C₂H₄ (*Chapter 4*), and then with a deeper look at the kinetics with H₂ over a wider temperature range with more complex material phenomena occurring (*Chapter 5*). For unpromoted CaMnO₃, it was determined that the kinetics of C₂H₄ oxidation depended to a greater extent on the available oxygen site concentration, related to solid conversion X, leading to dynamic selectivity behavior over time in a fixed-bed reactor as the redox catalyst became more reduced. Promotion of CaMnO₃ with Na₂WO₄ resulted in a two-orders-of-magnitude suppression in the rate of reduction in C₂H₄ as compared to the unpromoted sample, giving the high S_H we have repeatedly observed for that redox catalyst. Upon closer study of the Na₂WO₄/CaMnO₃ redox catalyst, we

uncovered a number of unexpected phenomena affecting the reduction kinetics of the material near its phase transition temperatures (600°C cubic to orthorhombic transition; 695°C melting point of Na₂WO₄). Firstly, thermal hysteresis in the kinetics – seemingly due to the Na₂WO₄ salt – led to rates and kinetic parameters with markedly different values depending on whether the sample had recently been heated or cooled. Secondly, for experiments in which the conditions were tested in decreasing order of temperature, the redox catalyst upon molten salt recrystallization gave kinetics which were insensitive to temperature (i.e. exhibiting zero activation energy) between 575°C and 500°C, as well as reduction rates which crossed over to give higher reduction rates as temperature decreased. *In situ* XRD revealed the presence of a Ca₃WO₆ phase which persisted after reoxidation at low temperature, which could be a contributing factor to the phenomena. However, the Na₂WO₄-promoted CaMnO₃ redox catalyst system should be investigated further in order to fully describe the changes in reduction kinetics and assess their importance in a scaled-up reactor.

6.2. Outlook

The central theme of this work has been the development of highly selective redox catalysts for use in chemical looping processes for the intensification of olefin production from hydrocarbon feedstocks. CL-ODH of ethane (775–850°C) and ROC of naphtha (725–800°C) were selected as representative examples of processes in which an alkane feedstock (ethane or *n*-hexane as a model compound) is cracked at high temperature to form olefins and H₂, followed by a redox catalyst performing selective hydrogen combustion (SHC). We note that multiple other processes use the same principle of balancing heat requirements and lifting thermodynamic yield restrictions via the combustion of hydrogen, and in such processes the redox catalysts presented here may find suitable application. In the applications tested – high- and low-temperature ethane CL-ODH (with thermal

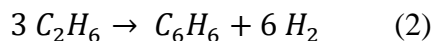
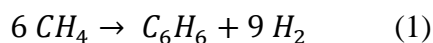
cracking and co-catalytic dehydrogenation, respectively) and the ROC of naphtha – redox catalysts consisting of a Mn-containing metal oxide core with a Na_2WO_4 promoter shell were demonstrated to be highly effective for SHC in the presence of ethylene, propylene, and additional high-value olefins. The design principle of metal oxide surface modification using a molten alkali tungstate salt can be extended to use alternative alkali cations (*e.g.* Li_2WO_4) or oxyanions (*e.g.* Na_2MoO_4 , Li_2CO_3); similarly, a wide range of oxide substrates could be used for the core material, including Mn- or Fe-based perovskite oxides, spinels, Ruddlesden-Popper phases, rock salts, or Mn ores.^[2,3] Numerous process simulation studies on this topic have shown that CL-ODH and ROC can provide significantly reduced energy and emissions intensity compared to ethane or naphtha steam cracking, respectively, when a highly selective and stable redox catalyst is employed.^[4–6] Therefore, future research should strive to develop a deeper understanding of the redox catalyst materials both from a fundamental standpoint (*e.g.* probing kinetic mechanisms) and from an applied perspective (*e.g.* testing at rigorous conditions over long sample lifetimes). In parallel with such efforts, the SHC redox catalyst materials should be evaluated in further applications. In the next section, a few potentially valuable directions of future work are presented.

6.3. Future Work

6.3.1. Oxidative Aromatization (OA) of Methane and Ethane

As discussed in *Chapter 1*, a small subset of chemicals in the manufacturing sector are responsible for a large portion of energy consumption and carbon emissions; while this dissertation focused on the light olefins ethylene and propylene, the BTX class of compounds – benzene, toluene, and xylene – are a similarly attractive target for process intensification. A highly promising application for the SHC redox catalysts developed throughout this work is the oxidative aromatization (OA)

of methane and ethane from natural gas directly to form aromatics such as benzene and toluene. The OA concept builds upon existing research on dehydroaromatization (DHA) of methane and ethane, which typically proceeds over a Mo/HZSM-5 catalyst^[7,8] or a Ga-Pt/HZSM-5 catalyst,^[9–11] respectively, according to the following reactions:



As with catalytic dehydrogenation and steam cracking processes, the methane and ethane DHA reactions are both highly endothermic and equilibrium-limited.^[7] However, DHA reactions also evolve a significant amount of hydrogen gas, creating the same opportunity for selective hydrogen combustion to provide *in situ* heat to balance the endothermicity of the DHA reaction while lifting thermodynamic constraints on the equilibrium via the removal of H₂ product (**Table 6.1**). Multiple studies by Bhan *et al.* have demonstrated a similar concept of enhancing aromatics yield from methane DHA by removing H₂ with a “scavenger bed” made up of Zr metal downstream of the DHA bed.^[12,13] In these studies, the resulting ZrH_{1.75} compound was regenerated by exposure to higher-temperature inert flow to release the H₂ from the hydride phase. However, attempting the same principle with a composite catalyst system comprising a DHA catalyst and a metal oxide for SHC would potentially give the same benefits while also producing steam to actively suppress coke formation, which is a major problem for DHA catalysts.^[14] Zhang *et al.* recently reported on this topic using a Gd-doped cerium oxide for SHC in combination with DHA in a composite bed configuration.^[15]

Table 6.1: Effect of selective hydrogen combustion (shown as H₂ conversion) on the overall heat of reaction (positive = endothermic) and equilibrium conversion of the feed (methane or ethane) for DHA at 650°C.

	H ₂ Conversion	ΔH_R (650°C)	Equil. Conv.
Methane DHA	0%	+592.9 kJ	8.0%
	96%	-1631.9 kJ	74.9%
Ethane DHA	0%	+374.9 kJ	85.0%
	96%	-1108.3 kJ	99.9%

We have produced preliminary data using a composite DHA+SHC bed to enhance yields of aromatics from ethane, shown in **Figure 6.1**. Compared to a single bed containing a DHA catalyst (2.5% Ga / 0.5% Pt supported on ZSM-5), a composite bed consisting of the same DHA catalyst plus a downstream SHC bed of Na₂WO₄/CaMnO₃ resulted in significantly higher instantaneous benzene and toluene yields (**Figure 6.1a, 6.1c**). The SHC material was capable of combusting H₂ produced during the DHA reaction (**Figure 6.1b**). Future research efforts will focus on improving synergy between zeolite-supported metal catalysts for DHA and manganese-based redox catalysts for SHC in order to provide enhanced yields of aromatics from methane and ethane, which could be a highly impactful chemical process for the valorization of stranded methane and natural gas liquid (NGL) reserves. The potential benefits of designing a single composite core-shell catalyst (SHC@DHA) for the OA process, in which the highly selective Na₂WO₄ surface layer on CaMnO₃ will be replaced with a shape-selective zeolite shell containing the DHA active metal sites, will also be evaluated as a part of this ongoing and future effort (**Figure 6.2**).

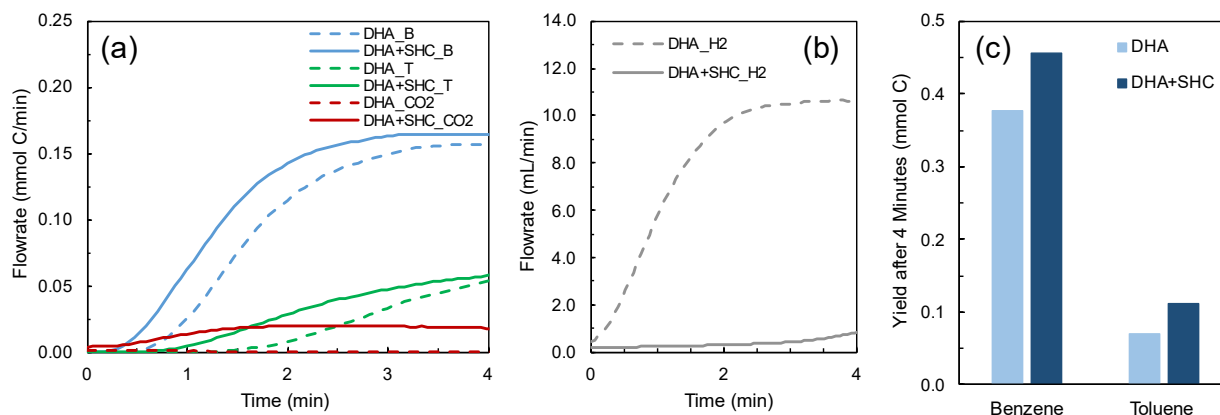


Figure 6.1: Oxidative aromatization using a DHA+SHC approach with either a single DHA bed (dotted line) or a DHA bed upstream followed by an SHC bed downstream. **(a)** Yields of benzene (B), toluene (T), and CO₂ from DHA. **(b)** Hydrogen effluent flowrate from the reaction with and without the SHC bed. **(c)**

Instantaneous benzene and toluene yields in DHA vs. DHA+SHC.



Figure 6.2: Core-shell composite catalyst design for the oxidative aromatization (OA) of methane or ethane using a combined SHC@DHA approach. In this OA catalyst system, a perovskite oxide (e.g. CaMnO_3) with optimal oxygen donation properties is covered by a shape-selective zeolite shell exchanged with active metal sites (e.g. Mo, Ga, Pt), rather than by a chemical promoter such as Na_2WO_4 . Alkane feedstock enters the pore network of the zeolite and is activated to form aromatics and H_2 ; at the zeolite-perovskite interface, the SHC core selectively combusts hydrogen, and the resulting steam permeates through the zeolite shell, burning off coke in the process.

6.3.2. Towards an Improved Understanding of $\text{Na}_2\text{WO}_4/\text{CaMnO}_3$ Reduction Kinetics

The primary focus of *Chapter 4* and *Chapter 5* was the kinetic modeling of the $\text{Na}_2\text{WO}_4/\text{CaMnO}_3$ redox catalyst in H_2 and C_2H_4 reducing environments. While the efforts described throughout this work represent significant progress in the understanding of redox catalyst kinetics for selective hydrogen combustion (SHC), there are still many unknowns that must be adequately studied and addressed in order to utilize the redox catalysts in increasingly large-scale and complex operations such as CL-ODH. One particular area that should receive focus is the extent of prior redox cycling on the redox catalyst kinetics. Multiple studies,^[6] including the one described in *Chapter 3*, have shown that $\text{Na}_2\text{WO}_4/\text{CaMnO}_3$ and related redox catalysts such as $\text{Na}_2\text{MoO}_4/\text{CaMn}_{0.9}\text{Ti}_{0.1}\text{O}_3$ are

highly stable over many redox cycles in fixed-bed and fluidized-bed reactor applications. However, the kinetic parameters for this system were shown to be highly dynamic, even after 200 cycles (**Table 5.3**). A potential explanation for the gradual increase in activity and decrease in selectivity over time is that the sodium leached into the quartz crucible in which the experiments; the use of a ceramic crucible, such as one constructed from yttria-stabilized zirconia (YSZ), would help to address this issue. Whatever the explanation, the material properties of the system should be more fully understood. As the dynamics of the $\text{Na}_2\text{WO}_4/\text{CaMnO}_3$ system become clear with further investigations, the presence or absence of (i) the rate crossover phenomenon and (ii) the thermal hysteresis phenomenon should be revisited. The kinetics studies reported in this work can also be expanded upon by utilizing different reducing gases relevant to the applications which have been discussed, such as propylene (for propane CL-ODH or naphtha CL-OC processes) or benzene (for oxidative aromatization of methane or ethane).

6.4. References

- [1] F. Hao, Y. Gao, L. Neal, R. B. Dudek, W. Li, C. Chung, B. Guan, P. Liu, X. Liu, F. Li, *J. Catal.* **2020**, *385*, 213–223.
- [2] F. Li, L. M. Neal, Y. Gao, *WO 2018/232133 A1*, **2018**.
- [3] F. Li, L. M. Neal, Y. Gao, S. Yusuf, R. Dudek, *US 2020/0215515 A1: Oxygen Carrying Materials with Surface Modification for Redox-Based Catalysis and Methods of Making and Uses Thereof*, **2020**.
- [4] V. P. Haribal, L. M. Neal, F. Li, *Energy* **2017**, *119*, 1024–1035.
- [5] V. P. Haribal, Y. Chen, L. Neal, F. Li, *Engineering* **2018**, *4*, DOI <https://doi.org/10.1016/j.eng.2018.08.001>.
- [6] L. M. Neal, V. P. Haribal, F. Li, *iScience* **2019**, *19*, 894–904.
- [7] K. Sun, D. M. Ginosar, T. He, Y. Zhang, M. Fan, R. Chen, **2018**, DOI [10.1021/acs.iecr.7b04707](https://doi.org/10.1021/acs.iecr.7b04707).
- [8] I. Vollmer, I. Yarulina, F. Kapteijn, J. Gascon, **2019**, 39–52.
- [9] A. Samanta, X. Bai, B. Robinson, H. Chen, J. Hu, *Ind. Eng. Chem. Res.* **2017**, *56*, 11006–11012.
- [10] B. Robinson, X. Bai, A. Samanta, V. Abdelsayed, D. Shekhawat, J. Hu, **2018**, DOI [10.1021/acs.energyfuels.8b01516](https://doi.org/10.1021/acs.energyfuels.8b01516).
- [11] X. Bai, A. Samanta, B. Robinson, L. Li, J. Hu, **2018**, DOI [10.1021/acs.iecr.7b05094](https://doi.org/10.1021/acs.iecr.7b05094).
- [12] A. Kumar, K. Song, L. Liu, Y. Han, A. Bhan, *Angew. Chemie - Int. Ed.* **2018**, *57*, 15577–15582.
- [13] N. K. Razdan, A. Kumar, A. Bhan, *J. Catal.* **2019**, *372*, 370–381.
- [14] N. Kosinov, F. J. A. G. Coumans, E. Uslamin, F. Kapteijn, E. J. M. Hensen, **2016**, 15086–

15090.

- [15] Y. Zhang, H. Jiang, *Chem. Commun.* **2018**, 54, 10343–10346.

APPENDICES

Appendix A: Supplementary Information for Chapter 2

Definition and Calculation of Key Reaction Terms

H₂ conversion and SHC selectivity are referred to throughout this study as the key metrics for selective hydrogen combustion (SHC) performance. Both terms are calculated using gas chromatography results and an atomic balance approach on carbon and hydrogen.

H₂ conversion on a molar basis (by the redox catalyst) is defined using a balance on H₂:

$$H_2 \text{ conversion} = (H_2)_{in} - (H_2)_{out}$$

Hydrogen is converted in small amounts by side reactions; however, in most cases we observed more hydrogen generation (i.e. by CO_x formation) than hydrogen consumption in side reactions.

C₂H₄ conversion on a molar basis (by the redox catalyst) is defined slightly differently, by knowing that CO_x is produced only by combustion with the redox catalyst:

$$C_2H_4 \text{ conversion} = [(C_2H_4)_{in} - (C_2H_4)_{out}] (S_{CO} + S_{CO_2})$$

Where S_{CO} and S_{CO₂} are selectivity to CO and CO₂, respectively, on a carbon basis. Alternative forms of ethylene conversion (e.g. an equilibrium reaction with H₂ to form C₂H₆) are not considered in this definition, as they take place in the gas phase.

SHC selectivity is finally defined as the molar H₂ conversion divided by the sum of molar H₂ conversion and C₂H₄ conversion (as defined above):

$$SHC \text{ selectivity} = \frac{H_2 \text{ conversion}}{H_2 \text{ conversion} + C_2H_4 \text{ conversion}}$$

Complete TPR Data for All SHC Redox Catalysts

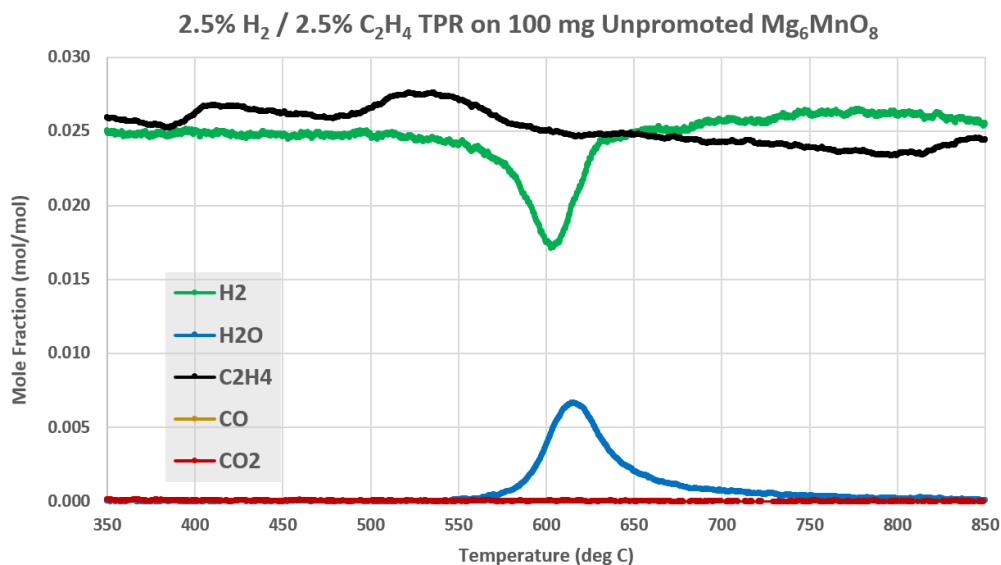


Figure A1: Complete H₂/C₂H₄ TPR results for the Mg₆MnO₈ redox catalyst, including H₂ (m/z = 2), H₂O (m/z = 18), C₂H₄ (m/z = 26) CO (m/z = 28), and CO₂ (m/z = 44).

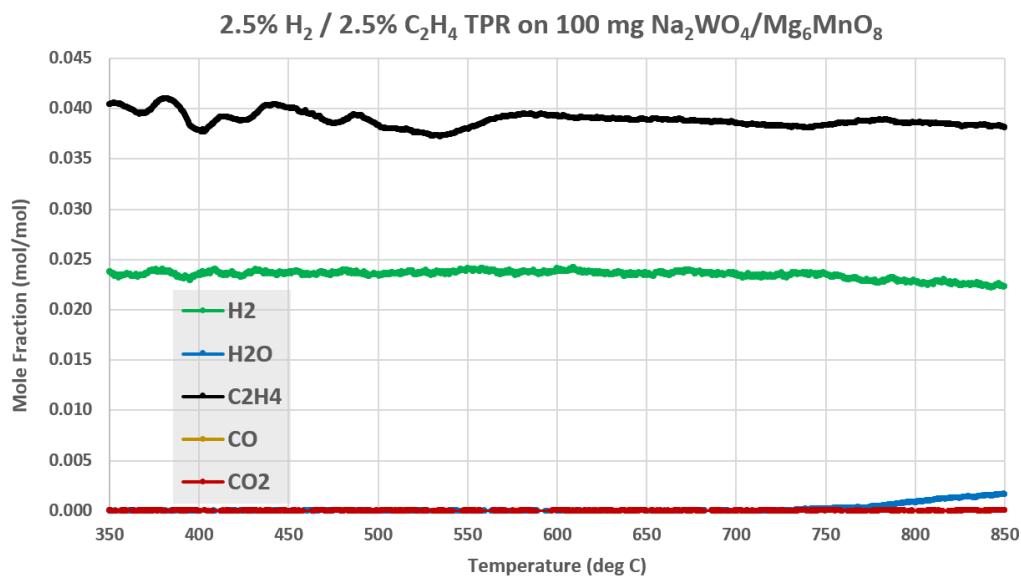


Figure A2: Complete H₂/C₂H₄ TPR results for the Na₂WO₄-promoted Mg₆MnO₈ redox catalyst, including H₂ (m/z = 2), H₂O (m/z = 18), C₂H₄ (m/z = 26) CO (m/z = 28), and CO₂ (m/z = 44).

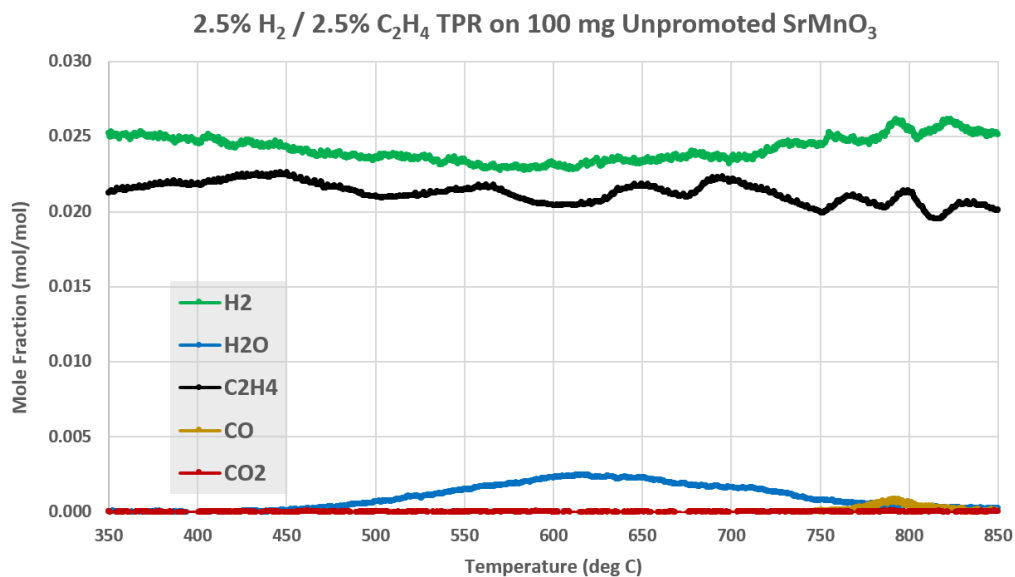


Figure A3: Complete H₂/C₂H₄ TPR results for the SrMnO₃ redox catalyst, including H₂ (m/z = 2), H₂O (m/z = 18), C₂H₄ (m/z = 26) CO (m/z = 28), and CO₂ (m/z = 44).

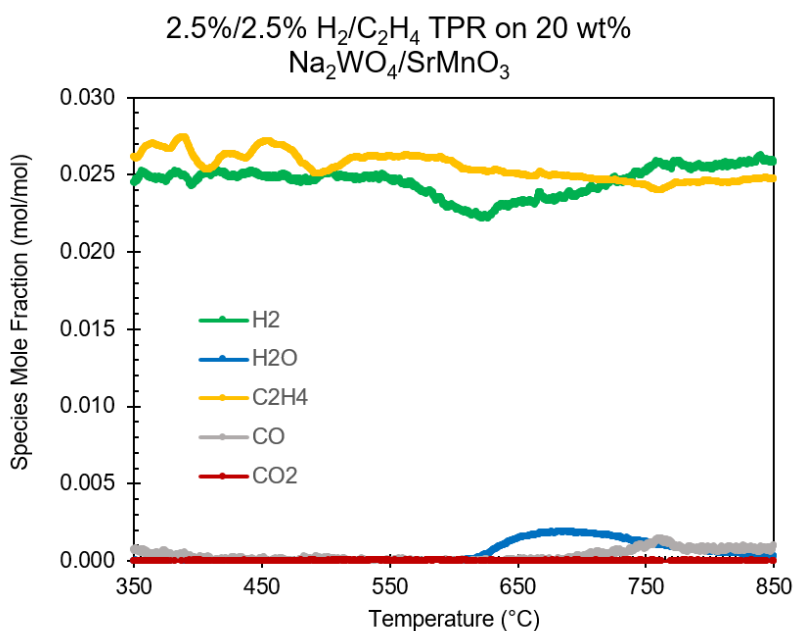


Figure A4: Complete H₂/C₂H₄ TPR results for the Na₂WO₄-promoted SrMnO₃ redox catalyst, including H₂ (m/z = 2), H₂O (m/z = 18), C₂H₄ (m/z = 26) CO (m/z = 28), and CO₂ (m/z = 44).

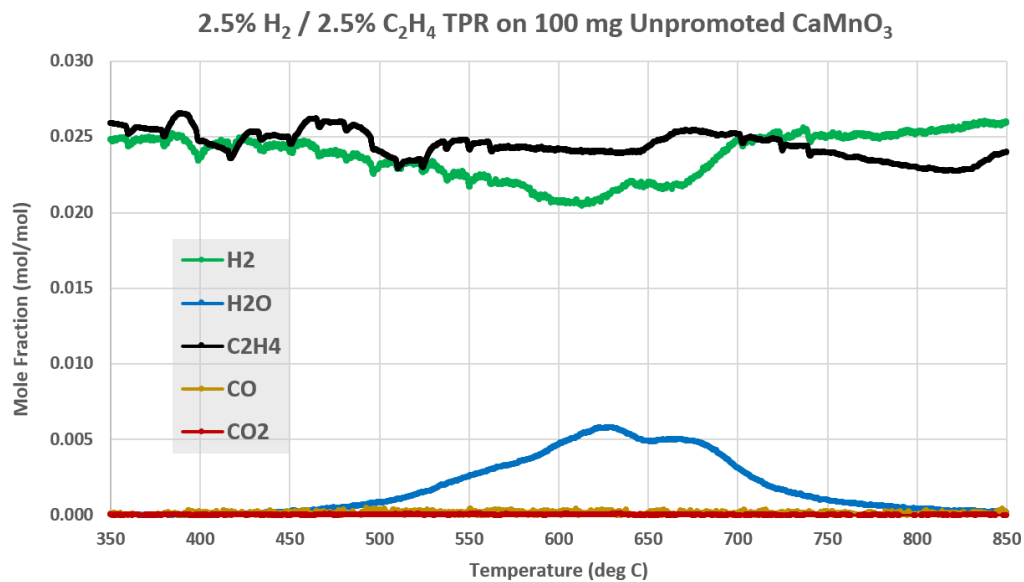


Figure A5: Complete H₂/C₂H₄ TPR results for the CaMnO₃ redox catalyst, including H₂ (m/z = 2), H₂O (m/z = 18), C₂H₄ (m/z = 26) CO (m/z = 28), and CO₂ (m/z = 44).

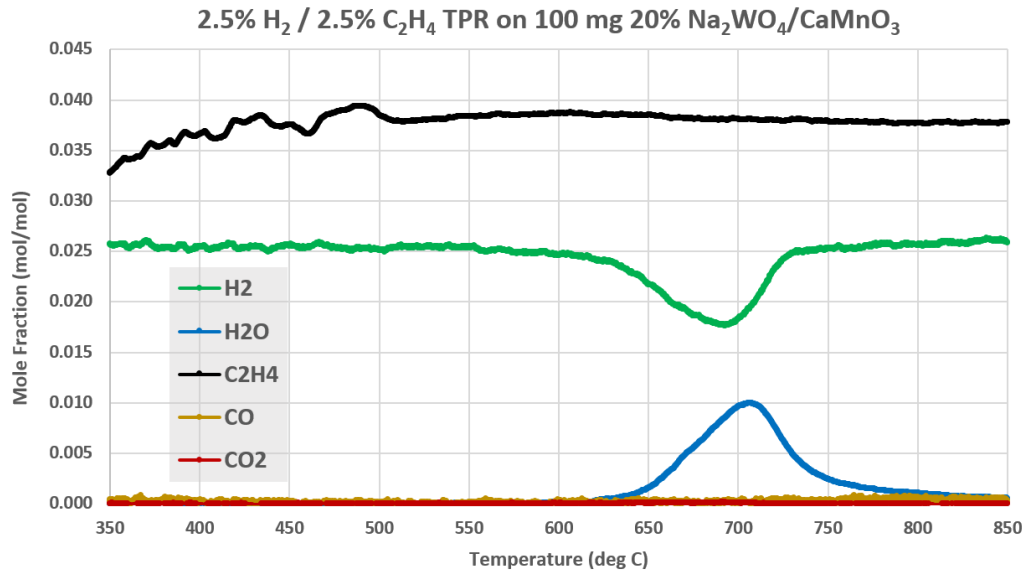


Figure A6: Complete H₂/C₂H₄ TPR results for the Na₂WO₄-promoted CaMnO₃ redox catalyst, including H₂ (m/z = 2), H₂O (m/z = 18), C₂H₄ (m/z = 26) CO (m/z = 28), and CO₂ (m/z = 44).

Oxygen Storage Capacity for Redox Catalysts

Approximations of oxygen storage capacity (i.e. oxygen released during the experimental duration which are a measure of, but not the true value of, the oxygen capacity), for each of the six redox catalysts are included in **Figures A7 through A9**. Values are calculated based on atomic C, H, and O material balances on the entire step volume of the SHC experiments and derived from the GC data. See dissertation *Section 2.3.3* for more experimental details.

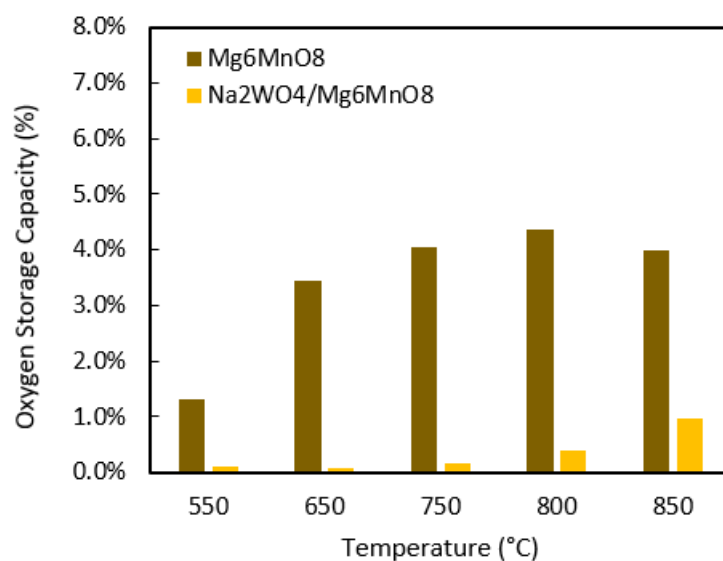


Figure A7: Approximation of oxygen storage capacity (OSC, wt.%) for the Mg₆MnO₈ pair of materials, based on material balances calculation on the GC control volume and product distribution. Conditions: m = 100 mg,

F = 100 mL/min, H₂:C₂H₄ = 40%:40% v/v in Ar, pulse duration = 10 s.

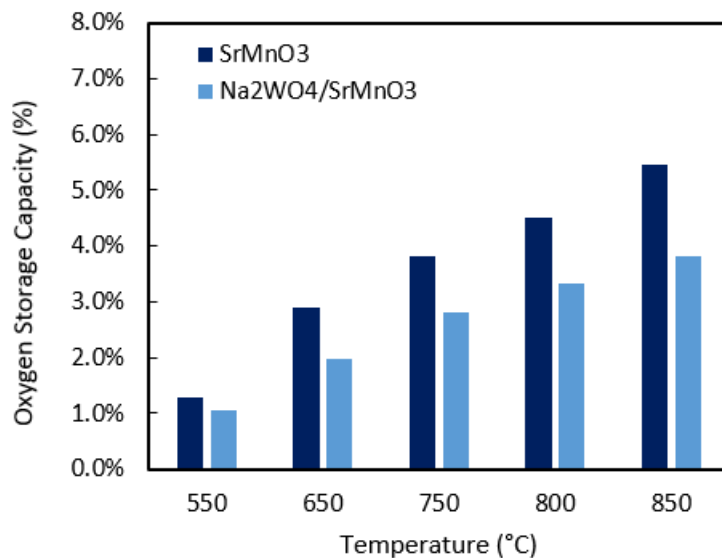


Figure A8: Approximation of oxygen storage capacity (OSC, wt.%) for the SrMnO₃ pair of materials, based on material balances calculation on the GC control volume and product distribution. Conditions: m = 100 mg,

F = 100 mL/min, H₂:C₂H₄ = 40%:40% v/v in Ar, pulse duration = 10 s.

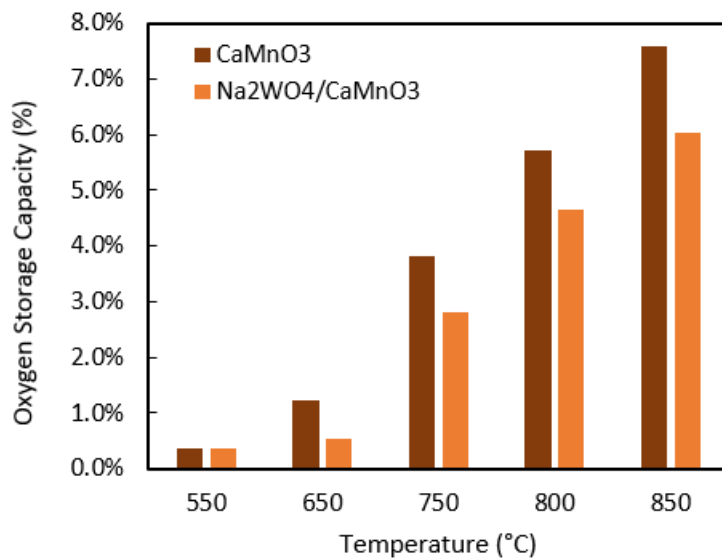


Figure A9: Approximation of oxygen storage capacity (OSC, wt.%) for the CaMnO₃ pair of materials, based on material balances calculation on the GC control volume and product distribution. Conditions: m = 100 mg,

F = 100 mL/min, H₂:C₂H₄ = 40%:40% v/v in Ar, pulse duration = 10 s.

Surface Enrichment and Suppression

A complete set of enrichment and suppression values for each redox catalyst (obtained from XPS) are provided in **Table A1**.

Table A1: Enrichment and suppression values for each metal present in the redox catalysts. Enrichment (greater than 1) indicates a higher metal content than the bulk formulation, while suppression (less than 1) indicates a lower than expected content.

Redox Catalyst	Mg	Sr	Ca	Mn	Na	W
Mg ₆ MnO ₈	0.69	--	--	2.84	--	--
Na ₂ WO ₄ /Mg ₆ MnO ₈	0.51	--	--	1.44	3.50	5.01
SrMnO ₃	--	1.46	--	0.54	--	--
Na ₂ WO ₄ /SrMnO ₃	--	1.43	--	0.50	0.98	1.49
CaMnO ₃	--	--	1.35	0.65	--	--
Na ₂ WO ₄ /CaMnO ₃	--	--	1.00	0.53	1.56	3.73
CaMnO ₃ , <i>cycled 25 times</i>	--	--	1.58	0.42	--	--
Na ₂ WO ₄ /CaMnO ₃ , <i>cycled 75 times</i>	--	--	1.67	0.48	0.00	1.82

Mn 2p 3/2 XPS Discussion

XP spectra in the Mn 2p region for the CaMnO₃ redox catalysts are presented in **Figure A10**.

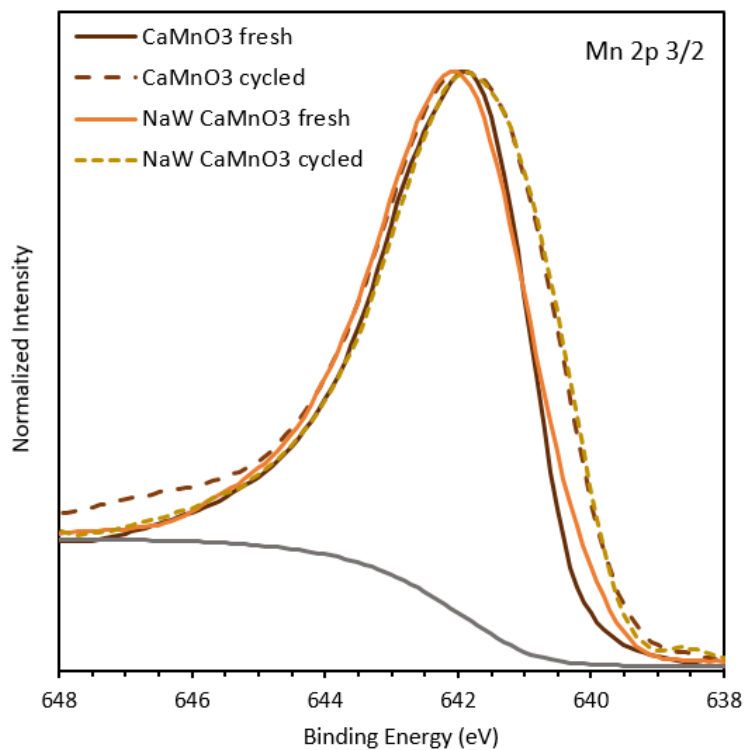


Figure A10: XPS narrow scans over the range of the Mn 2p 3/2 peak for fresh and cycled variants of the CaMnO₃ and Na₂WO₄/CaMnO₃ redox catalysts. Each spectrum was normalized by its maximum and minimum value, i.e. peak amplitude is not indicative of relative manganese content.

Appendix B: Supplementary Information for Chapter 3

Oxygen Donation Calculation

Approximate oxygen donation by a redox catalyst during a step experiment (not to be confused with oxygen capacity, which is the maximum theoretical oxygen content which can be withdrawn from the redox catalyst) was calculated using a material balance on the gas injection. Volumes of combustion products H₂O, CO, and CO₂ were determined, and from these a mmol O donation number was calculated. Oxygen donation in wt.% was then estimated by converting to mg O and dividing by the redox catalyst loading. An example formula is presented below for a redox catalyst donating oxygen under an H₂/C₂H₄ atmosphere as presented in manuscript **Figure 3.1**, where Y_j refers to yield of a product. For an *n*-hexane injection, F_{C₆H₁₄} replaces F_{C₂H₄}.

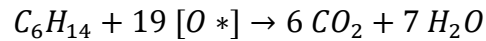
Oxygen donated (mmol)

$$\begin{aligned} &= \frac{t_{inj}(s)}{60 \frac{s}{min}} \left\{ \left[\frac{2 * F_{C_2H_4} \left(\frac{mL}{min} \right)}{22.4 \frac{mL}{mmol}} (Y_{CO}(\%) + 2 * Y_{CO_2}(\%)) \right] \right. \\ &\quad \left. + \left[\frac{F_{H_2} \left(\frac{mL}{min} \right)}{22.4 \frac{mL}{mmol}} \left(\frac{H_{2, fed} + H_{2, prod}}{H_{2, fed}} \right) (Y_{H_2O}(\%)) \right] \right\} \end{aligned}$$

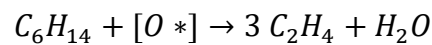
$$\text{Oxygen donation by redox catalyst} = \frac{\text{Oxygen donated (mmol)} * \left(\frac{16 \text{ mg O}}{1 \text{ mmol O}} \right)}{\text{redox catalyst loading (mg)}}$$

Lattice Oxygen Utilization

In chemical looping combustion (CLC), the oxygen donation required by a redox catalyst is high due to the total combustion of the fuel. If *n*-hexane were used as a feedstock for CLC, the total combustion would require 19 lattice oxygen atoms (shown as [O*]) per C₆H₁₄ molecule combusted:



However, redox oxidative cracking (ROC) of *n*-hexane represents a partial oxidation approach, and therefore the redox catalyst needs only to donate one lattice oxygen atom per C₆H₁₄ molecule undergoing reaction:



Therefore, lattice oxygen from a redox catalyst can be used up to 19 times more efficiently in the ROC of *n*-hexane compared to traditional CLC.

Table B1. Specific surface areas (m^2/g) from BET method for redox catalysts. The same preparation and characterization methods were used for CaMnO_3 , SrMnO_3 and Na_2WO_4 -promoted forms in both this work and

Dudek et al. 2018.

Redox Catalyst	Surface Area (m^2/g)
SrMnO_3	6.8
$\text{Na}_2\text{WO}_4/\text{SrMnO}_3$	3.1
CaMnO_3	2.2
$\text{Na}_2\text{WO}_4/\text{CaMnO}_3$	2.0

Table B2. Supplemental reaction data for four thermal cracking background cases at $T = 725^\circ\text{C}$ and 750°C ,

$\text{GHSV} = 4500 \text{ h}^{-1}$ and 9000 h^{-1} . Accompanying **Results and Discussion**.

	725°C , 4500 h^{-1}	725°C , 9000 h^{-1}	750°C , 4500 h^{-1}	750°C , 9000 h^{-1}
Conversion (mol %)				
<i>n</i> -hexane	39.9	33.6	62.1	48.0
Selectivity (carbon mol %)				
CH_4	10.0	9.7	10.7	10.3
C_2H_4	36.8	36.9	41.4	39.6
C_3H_6	25.7	25.9	25.1	25.1
butenes	14.8	15.9	11.3	13.8
1,3-butadiene	2.4	1.9	3.6	2.7
$\text{C}_2\text{-C}_4$ paraffins	4.6	4.2	4.4	4.4
C_{5+} (paraffins, olefins)	4.3	4.8	2.6	3.6

Table B3. Supplemental reaction data for four redox catalyst materials at GHSV = 9000 h⁻¹ and T = 725°C to 775°C. Accompanying **Figure 3.5** of **Results and Discussion**.

Redox Catalyst	T (°C)	<i>n</i> -hexane Conv (%)	Olefin Yield (%)	CO _x Yield (%)	Coke Yield (%)	H ₂ Conv (%)	SHC (%)
SrMnO ₃	725	81.78	28.70	43.21	3.89	100.00	37.79
	750	88.22	29.43	45.65	5.93	100.00	39.64
	775	93.32	30.60	46.18	7.42	100.00	40.24
Na ₂ WO ₄ /SrMnO ₃	725	53.24	43.19	3.19	0.00	100.00	70.98
	750	72.03	58.52	3.58	0.00	90.02	69.48
	775	85.20	67.64	5.04	0.00	90.81	62.86
CaMnO ₃	725	57.35	35.55	15.42	0.00	95.37	35.30
	750	70.46	40.74	22.08	0.00	97.13	33.94
	775	85.70	42.15	34.23	0.00	98.30	27.88
Na ₂ WO ₄ /CaMnO ₃	725	49.42	42.23	0.56	0.00	89.01	90.74
	750	65.67	55.20	1.04	0.00	100.00	88.41
	775	81.65	67.24	2.25	0.00	88.98	78.80

Table B4. Reaction data for 500 mg 20 wt.% Na₂WO₄/CaMnO₃ redox catalyst using two particle size ranges to verify similarity of performance.

Particle Size	Condition	Hexane Conv. (%)	Olefin Sel. (%)	CO _x Sel. (%)
250–425 μm	725°C, 4500 h ⁻¹	60.1	83.7	1.8
	725°C, 9000 h ⁻¹	50.8	84.2	1.8
	750°C, 9000 h ⁻¹	65.9	83.8	2.4
425–850 μm	725°C, 4500 h ⁻¹	55.1	83.9	1.7
	725°C, 9000 h ⁻¹	47.8	83.8	2.1
	750°C, 9000 h ⁻¹	63.0	84.2	2.0

Table B5. Carbon balance on reaction data for SrMnO₃ and 20 wt.% Na₂WO₄/CaMnO₃ at the conditions of 725°C and 4500 h⁻¹; these tests best illustrate the prevalence of coke for SrMnO₃ and the absence of coke formation on Na₂WO₄/CaMnO₃.

Product (C%)	SrMnO ₃	Na ₂ WO ₄ /CaMnO ₃
unreacted <i>n</i> -hexane	11.3	33.1
methane	5.1	6.7
C ₂ -C ₅ olefins	27.5	54.8
C ₂ -C ₅ paraffins	1.7	2.8
CO and CO ₂	46.0	1.7
coke	8.3	0.0

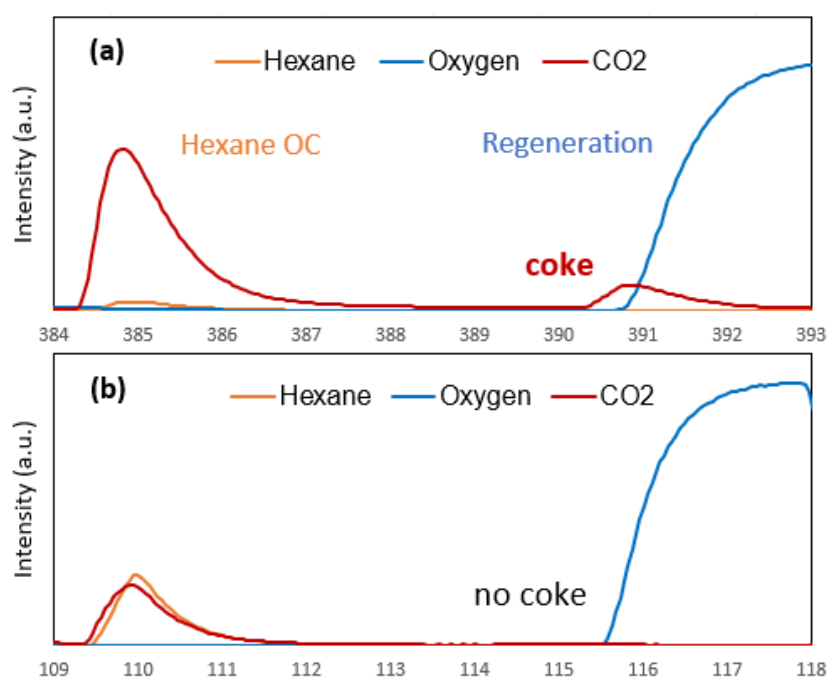


Figure B1. An illustration of how coke formation is detected in this system via on-stream MS analysis, for (a) SrMnO₃ (heavy coking) and (b) 20 wt.% Na₂WO₄/CaMnO₃ (no coking). During regeneration, deposited coke (C) is combusted by O₂ to form CO₂. The relative amounts of CO₂ during reduction and regeneration are combined with gas chromatography analysis of the reduction half-cycle in order to close the carbon balance around the process.

Table B6. XPS peak positions (in eV) for Sr 3*d* spectra on SrMnO₃-based redox catalysts, accompanying

Figure 3.7 of Results and Discussion.

	Lattice Sr 3 <i>d</i> _{5/2}	Lattice Sr 3 <i>d</i> _{3/2}	Surface Sr 3 <i>d</i> _{5/2}	Surface Sr 3 <i>d</i> _{3/2}
SrMnO ₃	132.3	134.0	132.8	134.5
Na ₂ WO ₄ /SrMnO ₃	132.2	134.0	132.6	134.3

Table B7. XPS peak positions (in eV) for Ca 2*p* spectra on CaMnO₃-based redox catalysts. Accompanying

Figure 3.7 of Results and Discussion.

	Lattice Ca 2 <i>p</i> _{3/2}	Lattice Ca 2 <i>p</i> _{1/2}	Surface Ca 2 <i>p</i> _{3/2}	Surface Ca 2 <i>p</i> _{1/2}
CaMnO ₃	345.2	348.7	346.6	350.0
Na ₂ WO ₄ /CaMnO ₃	345.3	348.8	346.6	350.1

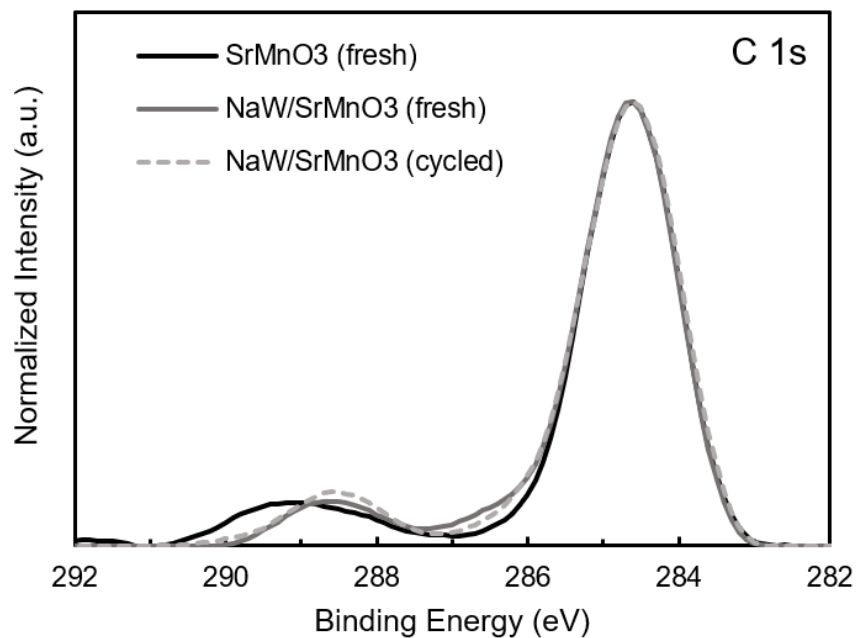


Figure B2. XPS C 1s spectra for SrMnO₃ redox catalysts.

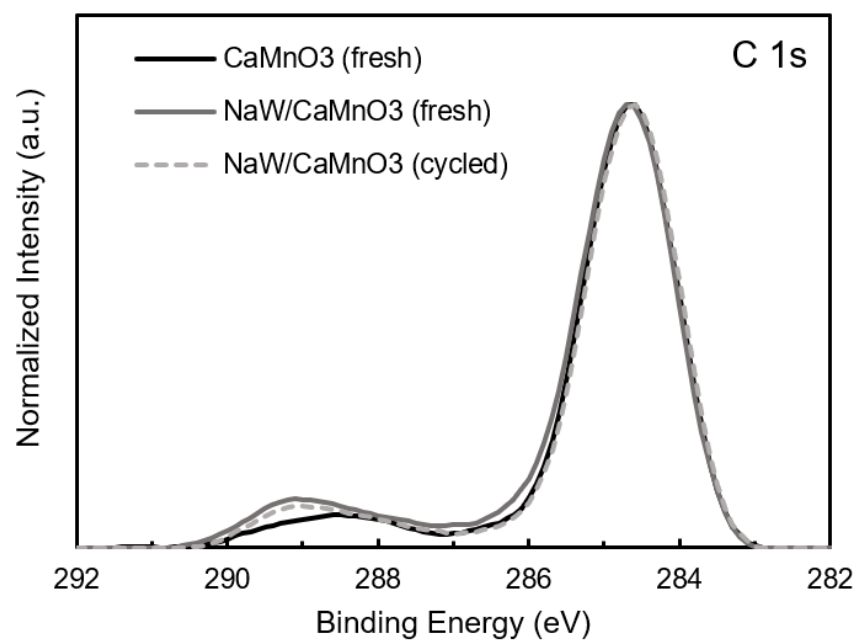


Figure B3. XPS C 1s spectra for CaMnO₃ redox catalysts.

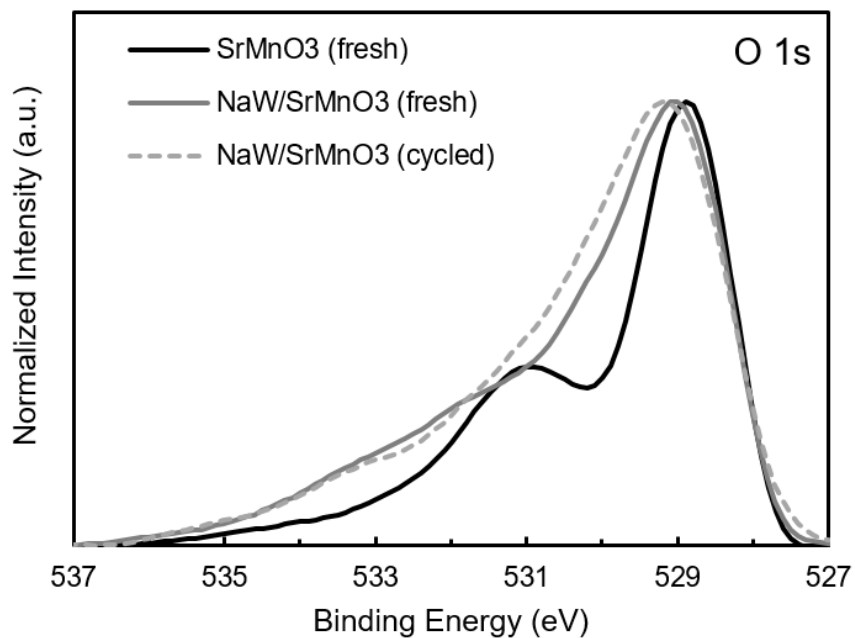


Figure B4. XPS O 1s spectra for SrMnO₃ redox catalysts.

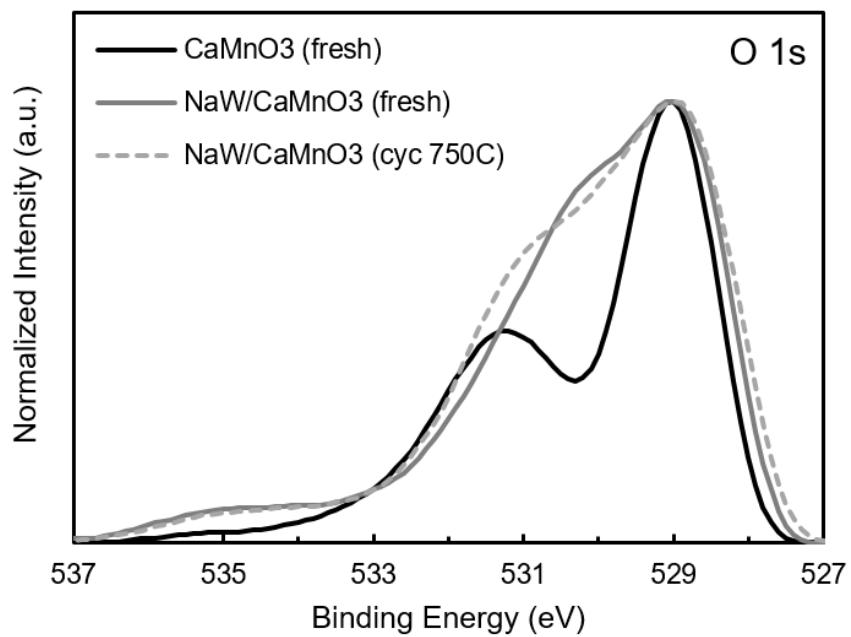


Figure B5. XPS O 1s spectra for SrMnO₃ redox catalysts.

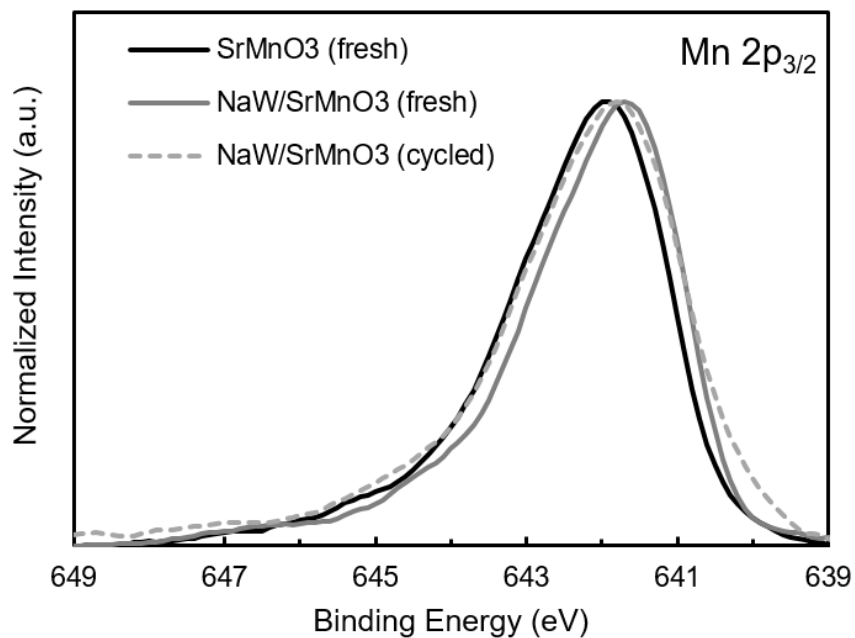


Figure B6. XPS Mn 2p_{3/2} spectra for SrMnO₃ redox catalysts.

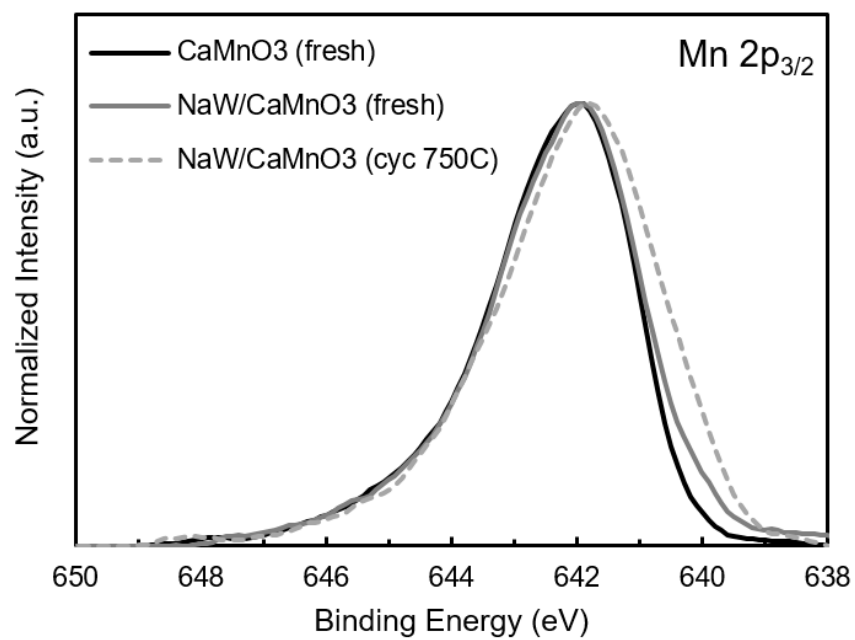


Figure B7. XPS Mn 2p_{3/2} spectra for CaMnO₃ redox catalysts.

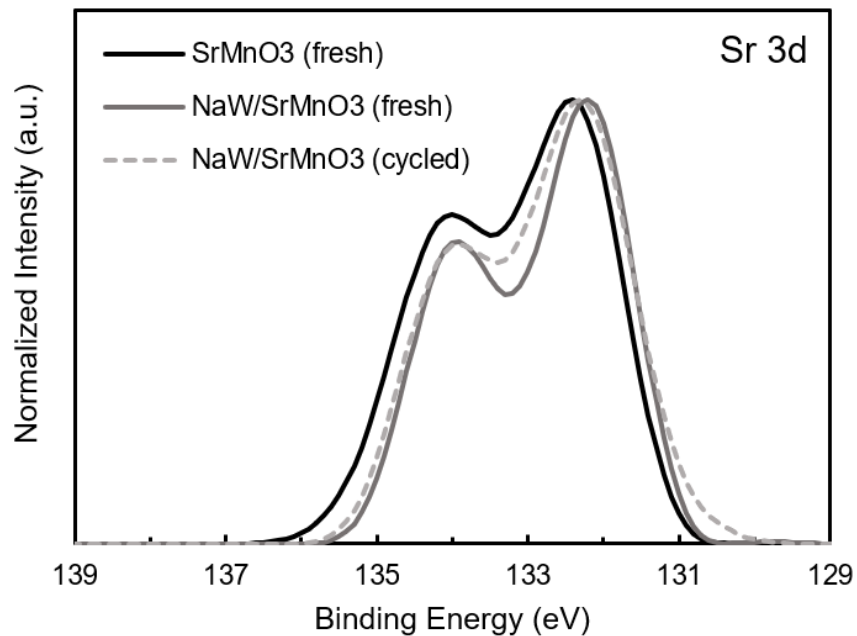


Figure B8. XPS Sr 3d spectra for SrMnO₃ redox catalysts.

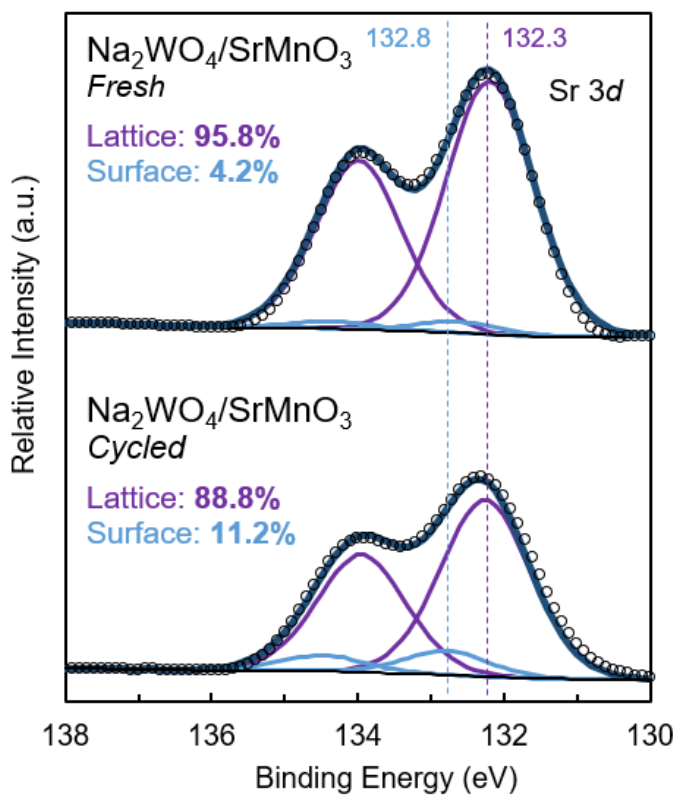


Figure B9. Deconvolution of XPS Sr 3d spectra for fresh and cycled Na₂WO₄/SrMnO₃.

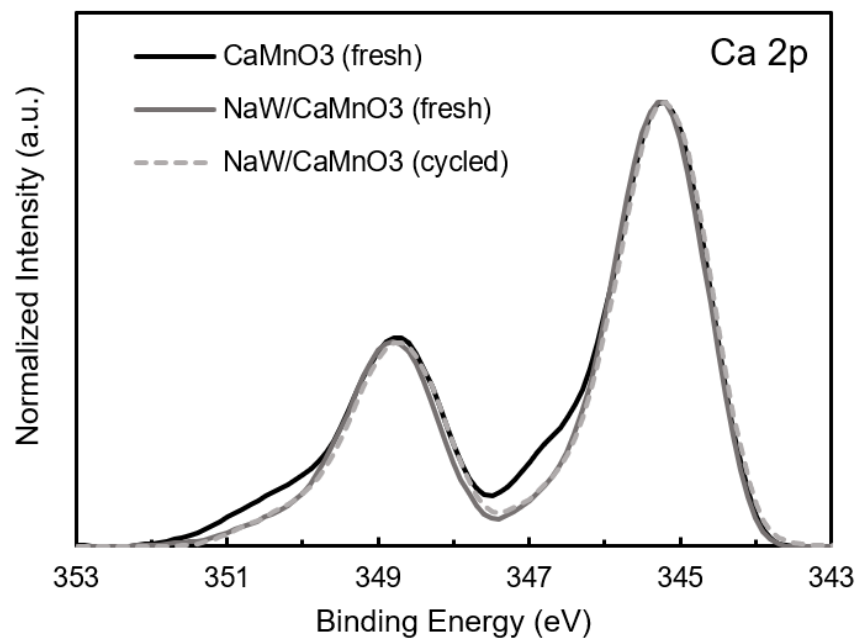


Figure B10. XPS Ca 2p spectra for CaMnO₃ redox catalysts.

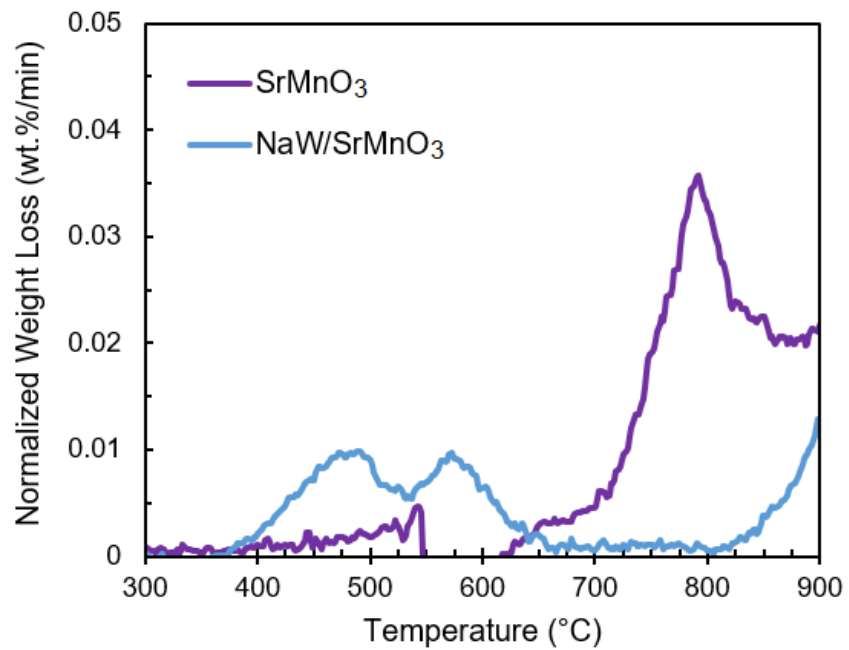


Figure B11. CO₂-TPD results for SrMnO₃ and 20 wt.% Na₂WO₄/SrMnO₃.

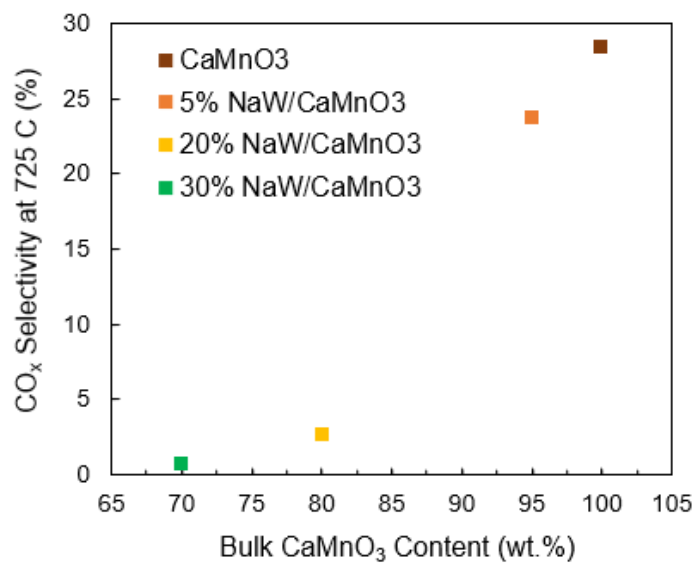


Figure B12. Relationship between bulk CaMnO₃ content of the redox catalysts (wt.%), which is an indicator for the prevalence of surface-type Ca species, and CO_x selectivity in the *n*-hexane ROC reaction (pictured at 725°C and 4500 h⁻¹).

Appendix C: Supplementary Information for Chapter 4

Tables C1–C4 provide statistical indicators for the kinetic model fitting of CaMnO_3 and $\text{Na}_2\text{WO}_4/\text{CaMnO}_3$ reduction by H_2 and by C_2H_4 . **Figures C1** and **C2** discuss the application of models of different categories to the reduction of CaMnO_3 . **Figures C3–C4** demonstrate the reaction order of CaMnO_3 reduction by H_2 , and **Figures C5–C6** provide analogous information for C_2H_4 . **Figure C7** shows the original data and fitting of the AE0.5 model to the reduction of $\text{Na}_2\text{WO}_4/\text{CaMnO}_3$ by ethylene. **Figure C8** provides XRD patterns for the as-prepared redox catalysts. **Figures C9–C11** provide additional experiments verifying the absence of mass transfer limitations on the measured kinetics.

Table C1: GRG nonlinear regression statistics for 15 kinetic model predictions, based on experimental data, for the reduction of CaMnO_3 (SSR) by H_2 . Bolded figures indicate the top five best fits (by RSS) for each method ($X - t$, $dX/dt - X$), while the figure in green indicates the overall best-fit kinetic model. Particular solutions for the D2 and D4 kinetic models (*i.e.* in the integral form $X - t$) were not calculated.

Method	Model	RSS (evaluated for $0.15 \leq X \leq 0.6$)			
		500°C	550°C	600°C	650°C
$X - t$	F1	0.00763	0.03507	0.04130	0.01907
	F1.5	0.03005	0.06933	0.07080	0.03932
	F2	0.07277	0.10957	0.10351	0.06316
	F3	0.18602	0.19411	0.16939	0.11327
	R1	0.08410	0.01332	0.01189	0.00688
	R2	0.01907	0.01307	0.01931	0.00622
	R3	0.01042	0.01852	0.02544	0.00936
	D1	0.15538	0.17186	0.15134	0.09801
	D2	--	--	--	--
	D3	0.26023	0.24359	0.20606	0.14083
	D4	--	--	--	--
	AE0.5	0.31361	0.27768	0.23167	0.16120
	AE1.5	0.16485	0.02251	0.00970	0.01267
	AE2	0.59883	0.17086	0.09473	0.09903
	AE3	1.77982	0.71220	0.45803	0.40785
$dX/dt - X$	F1	0.20271	0.05696	0.12814	0.11005
	F1.5	0.07853	0.09586	0.18120	0.47112
	F2	0.14969	0.45975	0.69650	1.42988
	F3	0.71205	1.79376	2.58201	4.33346
	R1	1.08701	1.15934	1.69253	1.74403
	R2	0.54226	0.40820	0.62894	0.51460
	R3	0.40509	0.24579	0.39787	0.28810
	D1	0.15368	0.67871	1.10997	1.80207
	D2	0.39533	1.27882	1.95380	3.11193
	D3	0.24290	0.09224	0.18153	0.13383
	D4	0.47180	0.33023	0.52073	0.41174
	AE0.5	1.29074	3.03203	4.39621	6.64212
	AE1.5	0.80703	0.67120	0.97170	0.82345
	AE2	1.23501	1.24846	1.77857	1.73700
	AE3	1.71136	1.94870	2.75879	2.92317

Table C2: GRG nonlinear regression statistics for 15 kinetic model predictions, based on experimental data, for the reduction of CaMnO_3 (SSR) by C_2H_4 . Bolded figures indicate the top five best fits (by RSS) for each method ($X - t$, $dX/dt - X$), while the figure in green indicates the overall best-fit kinetic model. Particular solutions for the D2 and D4 kinetic models (*i.e.* in the integral form $X - t$) were not calculated.

Method	Model	RSS (evaluated for $0.15 \leq X \leq 0.5$)					
		650°C	665°C	675°C	685°C	695°C	700°C
$X - t$	F1	0.01889	0.01011	0.00742	0.00746	0.00468	0.00192
	F1.5	0.00446	0.00164	0.00151	0.00241	0.00155	0.00126
	F2	0.00142	0.00151	0.00205	0.00292	0.00280	0.00425
	F3	0.01770	0.01735	0.01573	0.01486	0.01387	0.01709
	R1	0.09873	0.06489	0.04826	0.04243	0.03060	0.02006
	R2	0.04869	0.02995	0.02206	0.02000	0.01372	0.00759
	R3	0.03676	0.02186	0.01605	0.01484	0.00994	0.00504
	D1	0.03206	0.03029	0.02816	0.02491	0.02377	0.02703
	D2	--	--	--	--	--	--
	D3	0.06422	0.05646	0.05062	0.04496	0.04119	0.04394
	D4	--	--	--	--	--	--
	AE0.5	0.08210	0.07075	0.06272	0.05572	0.05042	0.05270
	AE1.5	0.22943	0.15603	0.12387	0.11102	0.08585	0.06303
	AE2	0.56819	0.40132	0.32089	0.28460	0.22599	0.17988
	AE3	1.32358	0.95865	0.76705	0.67521	0.54474	0.45718
$dX/dt - X$	F1	0.10365	0.11384	0.11877	0.11409	0.13806	0.18078
	F1.5	0.07093	0.06574	0.07902	0.12151	0.13699	0.17231
	F2	0.05990	0.05025	0.07719	0.16623	0.18015	0.21588
	F3	0.09458	0.10452	0.16937	0.34214	0.36905	0.42276
	R1	0.23429	0.30723	0.31599	0.22561	0.29030	0.37516
	R2	0.15850	0.19505	0.19818	0.14828	0.18854	0.24763
	R3	0.13780	0.16438	0.16732	0.13210	0.16603	0.21862
	D1	0.03610	0.03941	0.08842	0.20356	0.19045	0.20985
	D2	0.06315	0.08413	0.16203	0.31392	0.31763	0.34893
	D3	0.10946	0.12270	0.12651	0.11491	0.13983	0.18411
	D4	0.14590	0.17662	0.17909	0.13722	0.17289	0.22805
	AE0.5	0.17128	0.25141	0.39257	0.60723	0.65805	0.72793
	AE1.5	0.22865	0.29649	0.31365	0.22965	0.30891	0.39261
	AE2	0.30838	0.41393	0.44590	0.33046	0.44455	0.55582
	AE3	0.44707	0.54122	0.59201	0.45182	0.60340	0.74539

Table C3: GRG nonlinear regression statistics for 15 kinetic model predictions, based on experimental data, for the reduction of Na₂WO₄/CaMnO₃ (SSR) by H₂. Bolded figures indicate the top five best fits (by RSS) for each method (X – t, dX/dt – X), while the figure in green indicates the overall best-fit kinetic model. Particular solutions for the D2 and D4 kinetic models (*i.e.* in the integral form X – t) were not calculated.

Method	Model	RSS (evaluated for 0.15 ≤ X ≤ 0.6)		
		625°C	650°C	675°C
X – t	F1	0.35421	0.29484	0.18429
	F1.5	0.47503	0.38867	0.24994
	F2	0.59328	0.48025	0.31484
	F3	0.81272	0.65028	0.43689
	R1	0.12724	0.11534	0.06306
	R2	0.23555	33.95115	23.50345
	R3	0.27445	0.23251	0.14134
	D1	0.84949	0.69531	0.46929
	D2	--	--	--
	D3	1.01979	0.82665	0.56513
	D4	--	--	--
	AE0.5	1.09676	0.88607	0.60869
	AE1.5	0.03694	0.04175	0.01988
	AE2	0.05209	0.04959	0.04883
	AE3	0.69831	0.53902	0.43825
dX/dt – X	F1	0.60607	1.11629	1.60169
	F1.5	0.96322	1.61745	2.33979
	F2	1.33893	2.11836	3.08239
	F3	2.05197	3.02396	4.43111
	R1	0.09968	0.29622	0.41987
	R2	0.30414	0.65748	0.93385
	R3	0.39606	0.80248	1.14372
	D1	1.45025	2.26554	3.37872
	D2	1.83376	2.75449	4.10448
	D3	0.55088	1.03594	1.48504
	D4	0.34857	0.72851	1.03739
	AE0.5	2.56145	3.64735	5.42494
	AE1.5	0.17456	0.43799	0.60479
	AE2	0.05811	0.21006	0.28394
	AE3	0.01287	0.06989	0.10000

Table C4: Rate constants (k , min^{-1}) for the selected best-fit kinetic models. Model fitting was performed independently for the integral TGA data (X vs. t) and for the processed derivative data (dX/dt vs. X). The k values used in Arrhenius analysis and parameter estimation were an average of the k values from the integral and differential methods (k_{avg}).

Solid / Gas (Model Fit)	T (°C)	k (X-t)	k (dX/dt-X)	k (avg)
CaMnO ₃ / H ₂ (F1)	500	0.544	0.610	0.577
	550	0.793	0.994	0.893
	600	1.013	1.343	1.178
	650	1.502	1.817	1.659
CaMnO ₃ / C ₂ H ₄ (F1.5)	650	0.358	0.360	0.359
	665	0.477	0.490	0.484
	675	0.561	0.573	0.567
	685	0.630	0.626	0.628
	695	0.728	0.745	0.737
	700	0.794	0.845	0.819
Na ₂ WO ₄ /CaMnO ₃ / H ₂ (AE2)	625	0.297	0.260	0.279
	650	0.367	0.324	0.346
	675	0.556	0.473	0.515
Na ₂ WO ₄ /CaMnO ₃ / C ₂ H ₄ (AE0.5)	600	0.000058	--	0.000058
	625	0.000086	--	0.000086
	650	0.000168	--	0.000168
	675	0.000252	--	0.000252

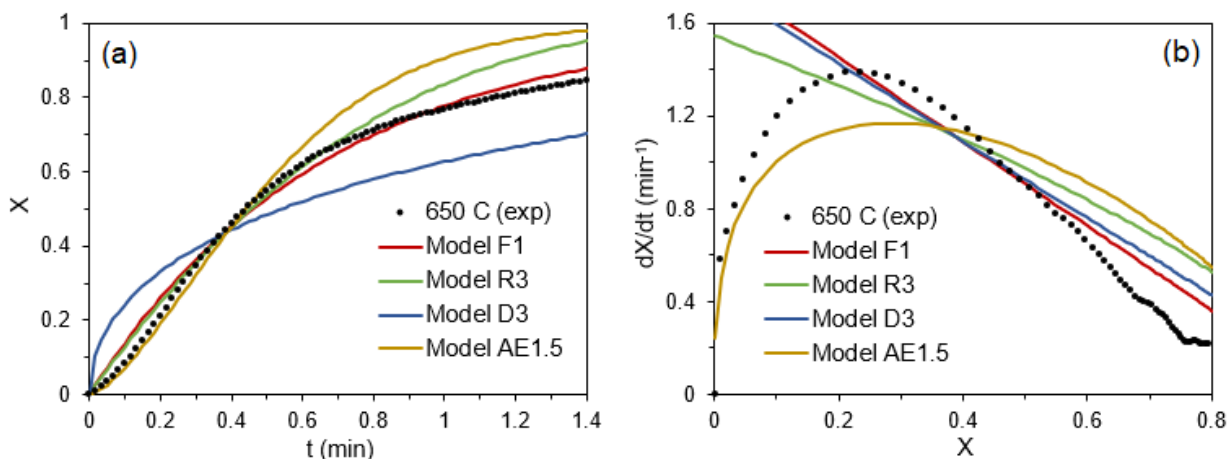


Figure C1: (a) Kinetic model fitting of X vs. t data, and (b) kinetic model fitting of dX/dt vs. X data, for the reduction of 20 mg CaMnO_3 by H_2 at 650°C . The best kinetic model of each of the four categories is plotted: F1 (first-order reaction order), R3 (contracting volume), D3 (three-dimensional diffusion; the Jander equation), AE1.5 (three-halves order Avrami-Erofe'ev nucleation and nuclei growth). Model F1 provided the overall best fit. Conditions: $m_0 = 20$ mg, $150\text{--}250$ μm , $T = 650^\circ\text{C}$, $P = 1$ atm, $F_{\text{total}} = 200$ mL/min (20 mL/min H_2 , 180 mL/min He).

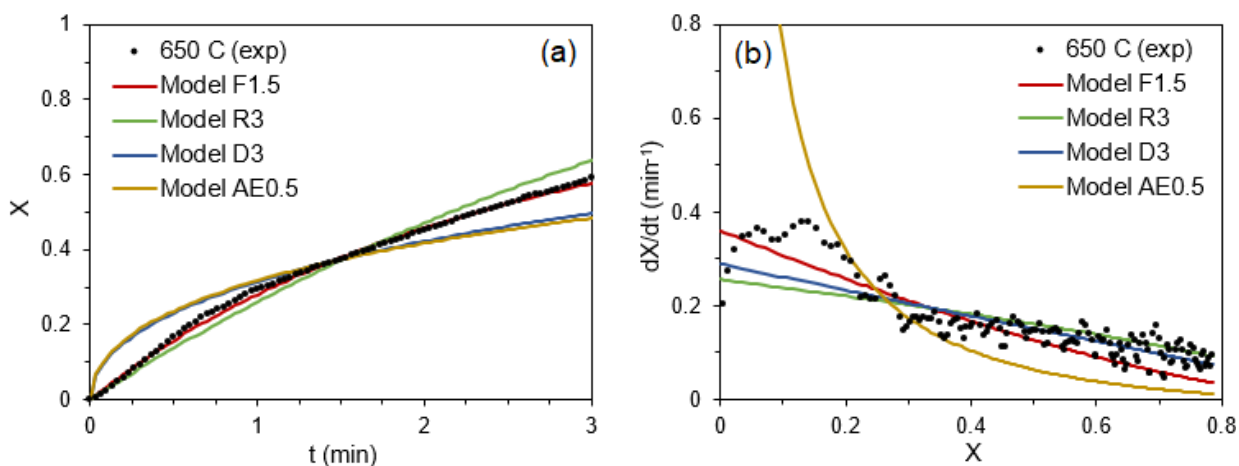


Figure C2: (a) Kinetic model fitting of X vs. t data, and (b) kinetic model fitting of dX/dt vs. X data, for the reduction of 20 mg CaMnO_3 by C_2H_4 at 650°C . The best kinetic model of each of the four categories is plotted: F1.5 (three-halves reaction order), R3 (contracting volume), D3 (three-dimensional diffusion; the Jander

equation), AE0.5 (one half-order Avrami-Erofe'ev nucleation and growth). Model F1.5 provided the overall best fit. Conditions: $m_0 = 20$ mg, $150\text{--}250$ μm , $T = 650^\circ\text{C}$, $P = 1$ atm, $F_{\text{total}} = 200$ mL/min (20 mL/min C_2H_4 , 180 mL/min Ar).

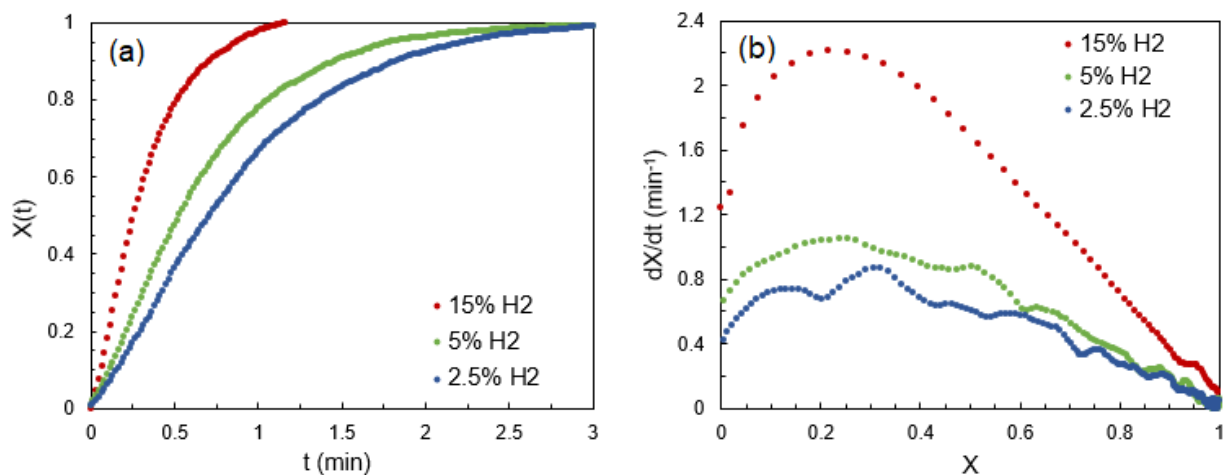


Figure C3: Reduction of 20 mg CaMnO_3 with H_2 at differing partial pressures; $y_{\text{H}_2} = 0.025, 0.05, 0.15$. (a) X vs. t , (b) dX/dt vs. X . Conditions: $m_0 = 20$ mg, $150\text{--}250$ μm , $T = 650^\circ\text{C}$, $P = 1$ atm, $F_{\text{total}} = 200$ mL/min (5, 10, or 30 mL/min H_2 ; 195, 190, or 170 mL/min He).

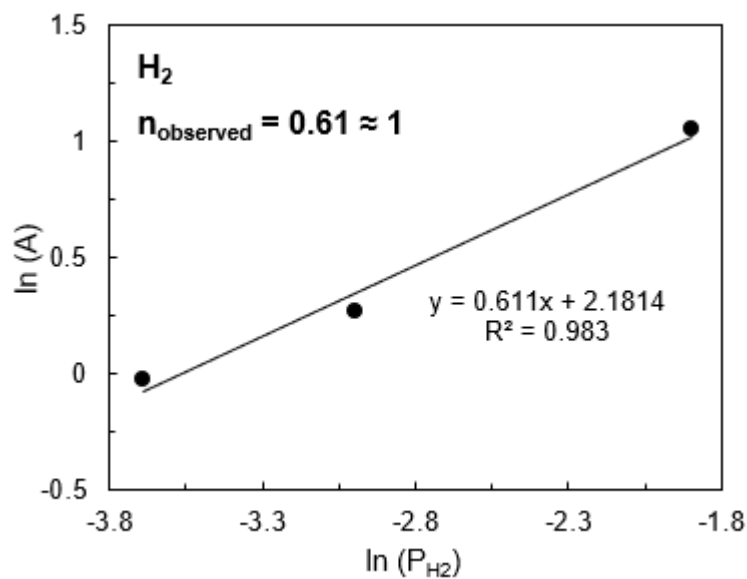


Figure C4: Logarithmic plot of hydrogen partial pressure (P_{H_2}) against the combined rate constant A , where $A = k(T) h(P_{H_2}) = k_0 \exp(-E_a/RT) (P_{H_2})^n$. Values of A were approximated from the rate data of Figure S01 by assuming an F1 reaction model, as discussed in the main document. The slope of the plot is approximately equal to the reaction order, n , of H_2 in the reduction reaction of $CaMnO_3$ by H_2 . Rounded to the nearest integer, the reduction reaction is approximately 1st order in P_{H_2} . Conditions: $m_0 = 20$ mg, 150–250 μ m, $T = 650^\circ\text{C}$, $P = 1$ atm, $F_{\text{total}} = 200$ mL/min (5, 10, or 30 mL/min H_2 ; 195, 190, or 170 mL/min He).

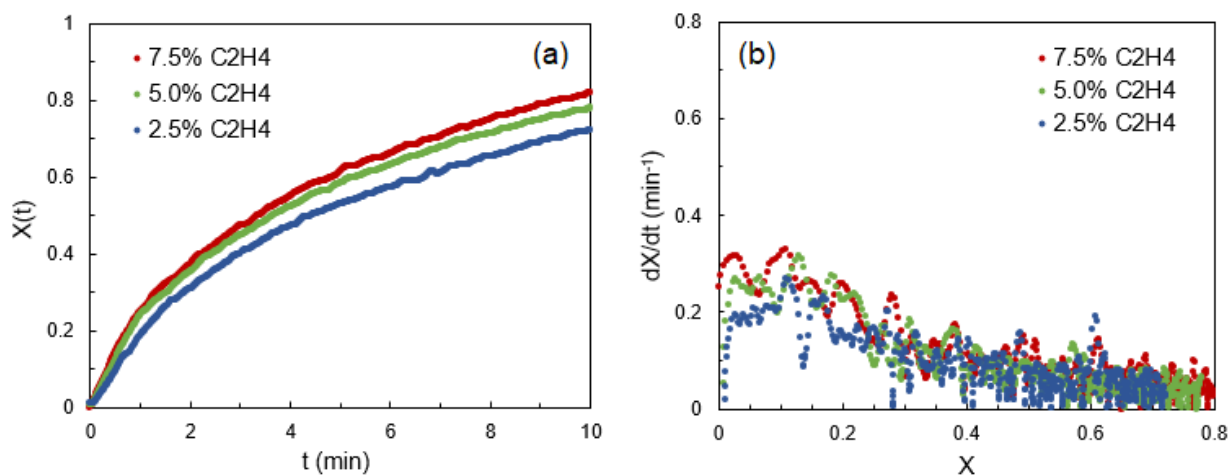


Figure C5: Reduction of 20 mg $CaMnO_3$ with C_2H_4 at differing partial pressures; $y_{C_2H_4} = 0.025, 0.05, 0.075$. (a) X vs. t , (b) dX/dt vs. X . Conditions: $m_0 = 20$ mg, 150–250 μ m, $T = 650^\circ\text{C}$, $P = 1$ atm, $F_{\text{total}} = 200$ mL/min (5, 10, or 15 mL/min C_2H_4 ; 195, 190, or 185 mL/min Ar/He).

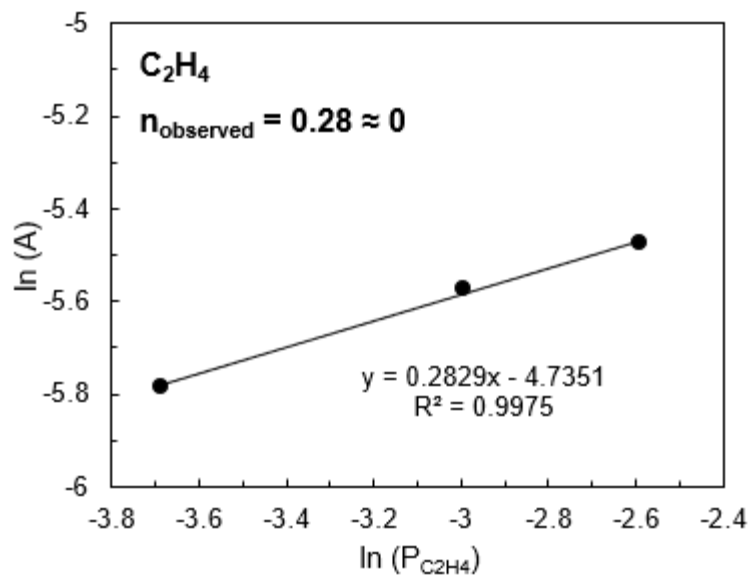


Figure C6: Logarithmic plot of ethylene partial pressure ($P_{\text{C}_2\text{H}_4}$) against the combined rate constant A , where $A = k(T) h(P_{\text{C}_2\text{H}_4}) = k_0 \exp(-E_a/RT) (P_{\text{C}_2\text{H}_4})^n$. Values of A were approximated from the rate data of Figure S03 by assuming an F1.5 reaction model, as discussed in the main document. The slope of the plot is approximately equal to the reaction order, n , of C_2H_4 in the reduction reaction of CaMnO_3 by C_2H_4 . Rounded to the nearest integer, the reduction reaction is approximately 0th order in $P_{\text{C}_2\text{H}_4}$. Conditions: $m_0 = 20$ mg, 150–250 μm , $T = 650^\circ\text{C}$, $P = 1$ atm, $F_{\text{total}} = 200$ mL/min (5, 10, or 15 mL/min C_2H_4 ; 195, 190, or 185 mL/min Ar/He).

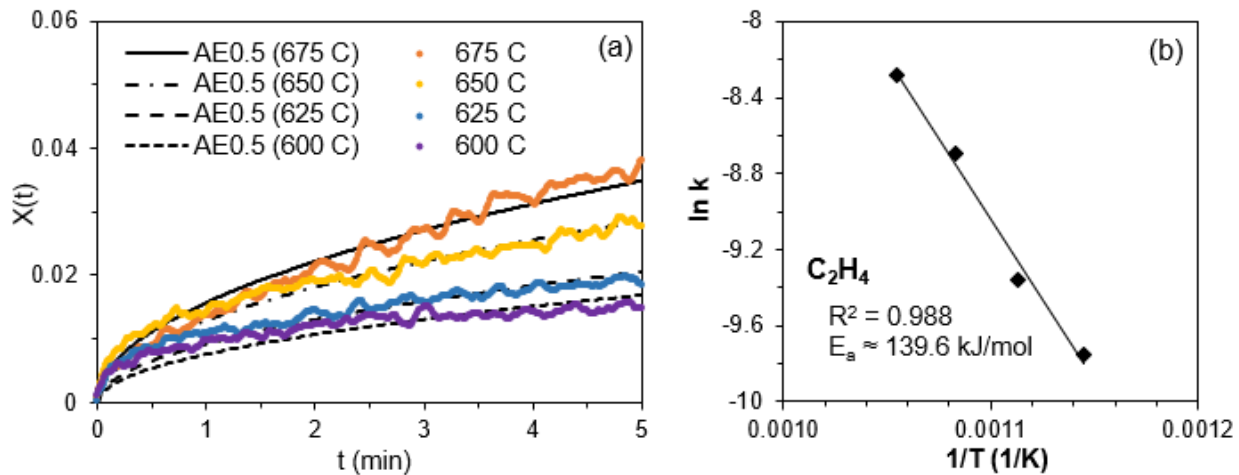


Figure C7: (a) Kinetic model fitting of X vs. t data, and (b) Arrhenius analysis for the reduction of 20 mg $\text{Na}_2\text{WO}_4/\text{CaMnO}_3$ by C_2H_4 . The one half-order Avrami-Erofe'ev kinetic model (AE0.5) was selected for the fitting based on its providing the best statistical indicators, though the Jander equation (model D3) provided similar rate parameters. Conditions: $m_0 = 20$ mg, $150\text{--}250$ μm , $T = 600^\circ\text{C}$ to 675°C , $P = 1$ atm, $F_{\text{total}} = 200$ mL/min (20 mL/min C_2H_4 , 180 mL/min Ar).

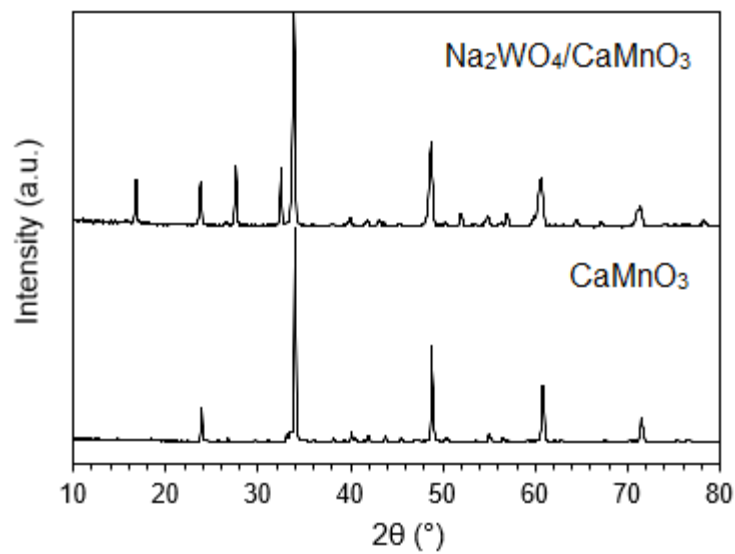


Figure C8: XRD patterns for two as-prepared redox catalysts, CaMnO_3 and 20 wt.% $\text{Na}_2\text{WO}_4/\text{CaMnO}_3$. Diffraction peaks for CaMnO_3 are located at $2\theta = 24^\circ, 34^\circ, 40^\circ, 42^\circ, 49^\circ, 55^\circ, 61^\circ,$ and 72° ; Na_2WO_4 contributes to $2\theta = 16^\circ, 28^\circ, 32^\circ, 52^\circ, 55^\circ, 64^\circ,$ and 67° . Patterns were collected on a Rigaku SmartLab X-ray diffractometer operated at 40 kV and 44 mA with a monochromatic $\text{Cu K}\alpha$ radiation source ($\lambda = 0.1542 \text{ nm}$).

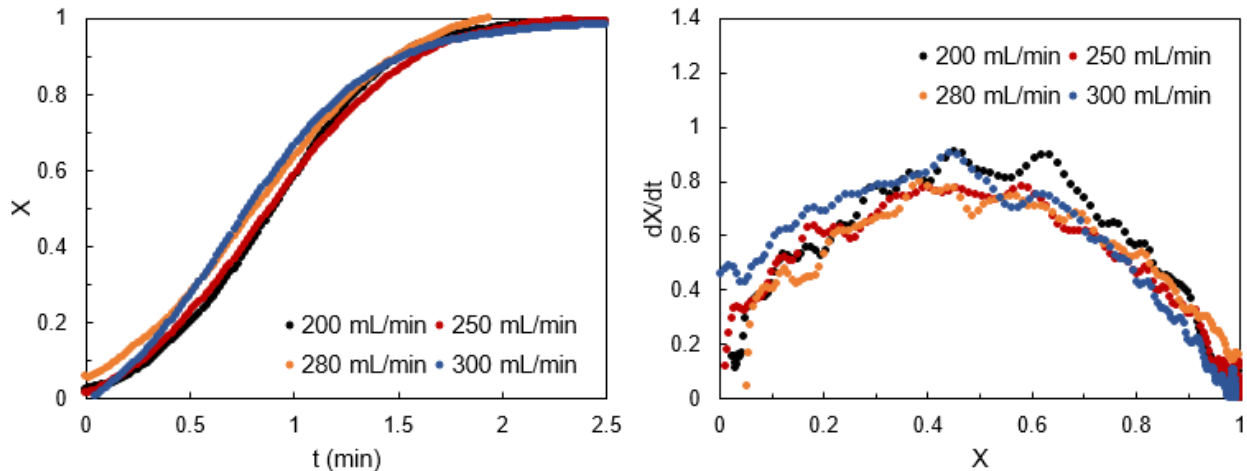


Figure C9: Reduction kinetics of 20 mg $\text{Na}_2\text{WO}_4/\text{CaMnO}_3$ under 10% H_2 at $T = 650^\circ\text{C}$, with data taken at four different total flowrates (200, 250, 280, and 300 mL/min), demonstrating that measured kinetics are not affected by external mass transfer limitations.

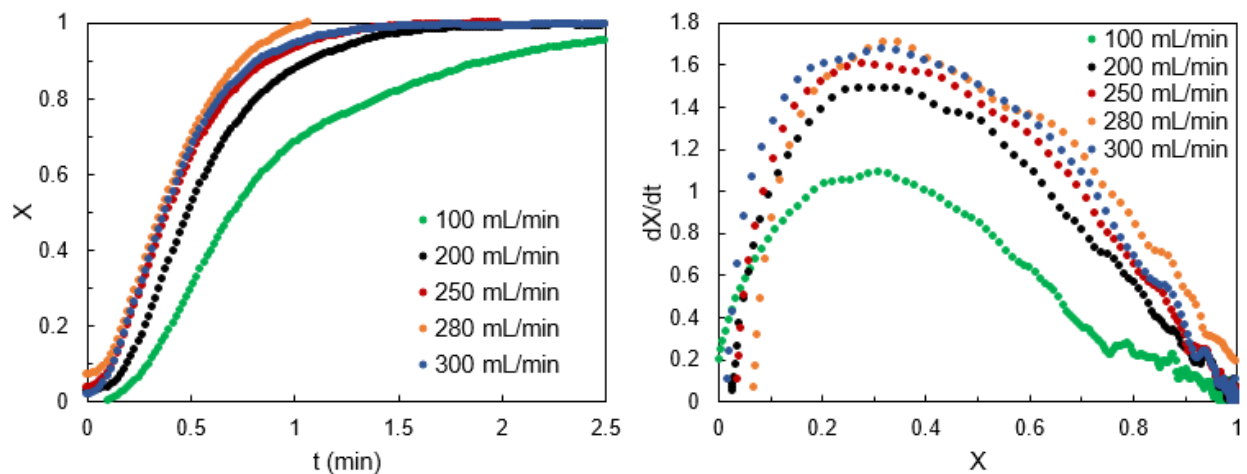


Figure C10: Reduction kinetics of 20 mg CaMnO_3 under 10% H_2 at $T = 650^\circ\text{C}$ (featuring the most rapid rates present in this study), with data taken at five different total flowrates (100, 200, 250, 280, and 300 mL/min), demonstrating that measured kinetics are affected by external mass transfer at the 100 mL/min condition but such effects are largely avoided at the chosen flowrate of 200 mL/min and absent at temperatures below 650°C .

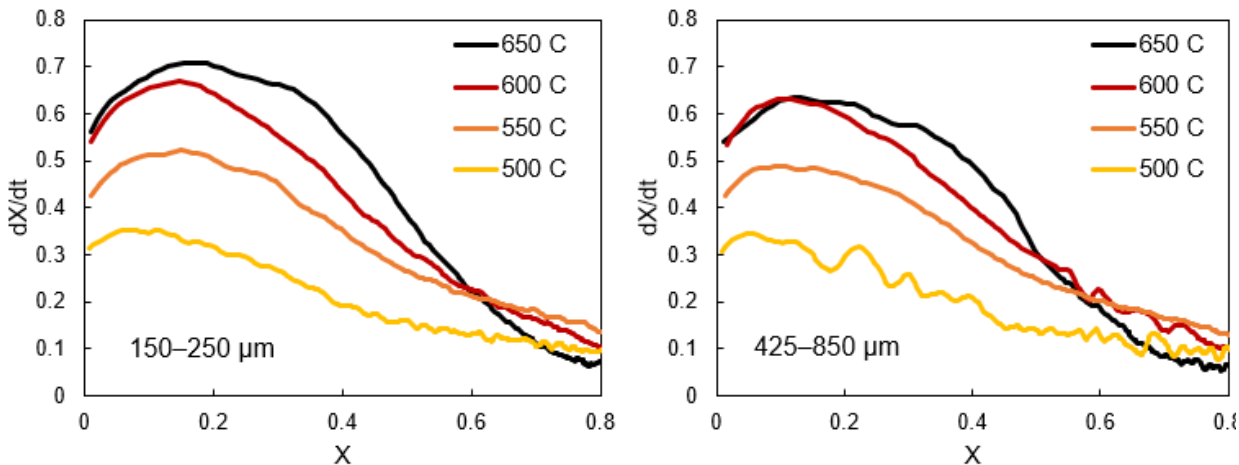


Figure C11: Comparison of CaMnO_3 reduction kinetics in H_2 at four temperatures and two different particle sizes: (1) 150–250 μm ; (2) 425–850 μm . Intraparticle mass transfer effects on measured kinetic rates are limited at $T = 650^\circ\text{C}$ (decreasing the maximum rate by $\sim 10.2\%$ from the smaller to the larger particle size) and entirely absent at 600°C and lower. Particle size of 150–250 μm was utilized for all kinetics calculations in this study to minimize such intraparticle effects.

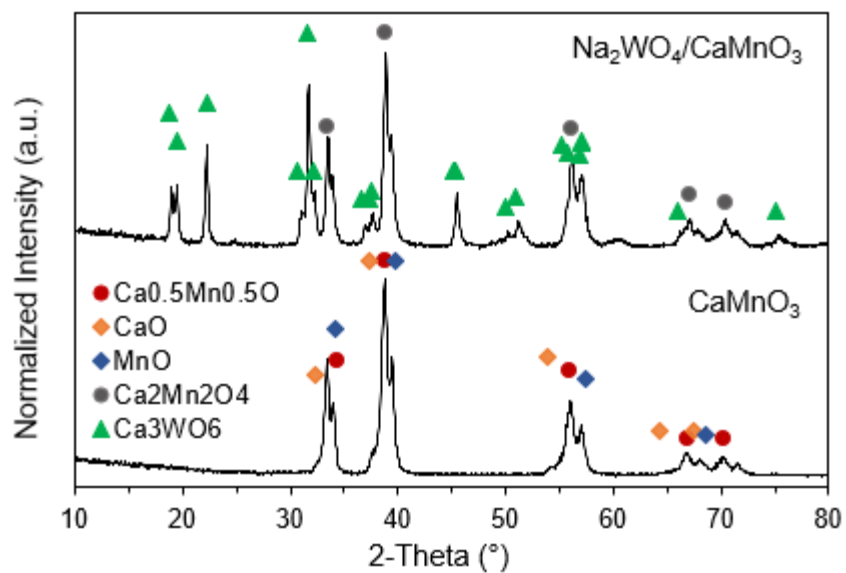


Figure C12. XRD patterns of CaMnO₃ and 20 wt.% Na₂WO₄/CaMnO₃ redox catalysts, after five “break-in” redox cycles in 10% H₂/O₂ at 750°C, followed by two and one-half cycles at 650°C to end the materials in the reduced state. Powders with size less than 150 microns were used for XRD analysis. Phase markers indicate best-fit phases as determined via matching analysis in HighScore Plus using the ICDD database.

Appendix D: Supplementary Information for Chapter 5

Table D1: Descriptions of all kinetics experiments conducted on CaMnO₃ and discussed in this work.

Sample / Experiment	Batch	Date	Cycles	T (°C)	P _{H₂} (atm)	P _{C₂H₄} (atm)
<u>CM-01 / Experiment 1</u> Cyc 1–5 [Break-In] Cyc 6–23 [10% H ₂ , <i>Decreasing T</i>]	Sol b.6A	05/20/19	1–5	750	0.10	--
			6–8	700	0.10	
			9–11	675	0.10	
			12–14	650	0.10	
			15–17	600	0.10	
			18–20	550	0.10	
			21–23	500	0.10	
<u>CM-01 / Experiment 2</u> Cyc 24–37 [10% C ₂ H ₄ , <i>Decreasing T</i>]	Sol b.6A	05/21/19	24–26	700	--	0.10
			27–29	695		0.10
			30–32	685		0.10
			33–35	675		0.10
			36–37	665		0.10
<u>CM-02 / Experiment 1</u> Cyc 1–5 [Break-In] Cyc 6–23 [5% H ₂ , <i>Decreasing T</i>]	Sol b.6A	06/17/20	1–5	750	0.05	--
			6–8	700	0.05	
			9–11	675	0.05	
			12–14	650	0.05	
			15–17	600	0.05	
			18–20	550	0.05	
			21–23	500	0.05	
<u>CM-02 / Experiment 2</u> Cyc 24–47 [5% H ₂ , <i>Increasing T</i>]	Sol b.6A	06/19/20	24–26	500	0.05	--
			27–29	550	0.05	
			30–32	600	0.05	
			33–35	625	0.05	
			36–38	650	0.05	
			39–41	675	0.05	
			42–44	700	0.05	
			45–47	725	0.05	
<u>CM-03 / Experiment 1</u> Cyc 1–6 [Break-In] Cyc 7–24 [5% H ₂ , <i>Increasing T</i>]	Sol b.6A	06/26/20	1–6	750	0.05	--
			7–9	500	0.05	
			10–12	550	0.05	
			13–15	600	0.05	
			16–18	650	0.05	
			19–21	675	0.05	
			22–24	700	0.05	
<u>CM-03 / Experiment 2</u> Cyc 25–42 [5% H ₂ , <i>Decreasing T</i>]	Sol b.6A	06/27/20	25–27	700	0.05	--
			28–30	675	0.05	
			31–33	650	0.05	
			34–36	600	0.05	
			37–39	550	0.05	
			40–42	500	0.05	

Table D1 (continued).

<u>CM-04 / Experiment 1</u> Cyc 1–25 [Break-In] Cyc 26–46 [5% H ₂ , <i>Decreasing T</i>]	Sol b.6A	07/02/20	1–25	750	0.05	--
			26–28	700	0.05	
			29–31	675	0.05	
			32–34	650	0.05	
			35–37	625	0.05	
			38–40	600	0.05	
			41–43	550	0.05	
<u>CM-04 / Experiment 2</u> Cyc 47–67 [5% C ₂ H ₄ , <i>Decreasing T</i>]	Sol b.6A	07/20/20	44–46	500	0.05	
			47–49	700	--	0.05
			50–52	690		0.05
			53–55	680		0.05
			56–58	665		0.05
			59–61	650		0.05
			62–64	625		0.05
<u>CM-04 / Experiment 3</u> Cyc 68–88 [5% C ₂ H ₄ , <i>Increasing T</i>]	Sol b.6A	07/21/20	65–67	600		0.05
			68–70	600	--	0.05
			71–73	625		0.05
			74–76	650		0.05
			77–79	665		0.05
			80–82	680		0.05
			83–85	690		0.05
<u>CM-05 / Experiment 1</u> Cyc 1–45 [Break-In] Cyc 46–66 [5% H ₂ , <i>Decreasing T</i>]	Sol b.6A	07/04/20	86–88	700		0.05
			1–45	750	0.05	--
			46–48	700	0.05	
			49–51	675	0.05	
			52–54	650	0.05	
			55–57	625	0.05	
			58–60	600	0.05	
<u>CM-05 / Experiment 2</u> Cyc 67–87 [10% H ₂ , <i>Decreasing T</i>]	Sol b.6A	07/07/20	61–63	550	0.05	
			64–66	500	0.05	
			67–69	700	0.10	--
			70–72	675	0.10	
			73–75	650	0.10	
			76–78	625	0.10	
			79–81	600	0.10	
<u>CM-05 / Experiment 3</u> Cyc 88–105 [7.5% H ₂ , <i>Decreasing T</i>]	Sol b.6A	07/09/20	82–84	550	0.10	
			85–87	500	0.10	
			88–90	700	0.075	--
			91–93	675	0.075	
			94–96	650	0.075	
			97–99	600	0.075	
			100–102	550	0.075	
			103–105	500	0.075	

Table D1 (continued).

<u>CM-05 / Experiment 4</u> Cyc 106–123 [2.5% H ₂ , <i>Decreasing T</i>]	Sol b.6A	07/13/20	106–108	700	0.025	--
			109–111	675	0.025	
			112–114	650	0.025	
			115–117	600	0.025	
			118–120	550	0.025	
			121–123	500	0.025	
<u>CM-05 / Experiment 5</u> Cyc 124–144 [5% H ₂ , <i>Decreasing T</i>]	Sol b.6A	07/30/20	124–126	700	0.05	--
			127–129	675	0.05	
			130–132	650	0.05	
			133–135	625	0.05	
			136–138	600	0.05	
			139–141	550	0.05	
			142–144	500	0.05	
<u>CM-05 / Experiment 6</u> Cyc 145–165 [5% H ₂ , <i>Increasing T</i>]	Sol b.6A	08/05/20	145–147	500	0.05	--
			148–150	550	0.05	
			151–153	600	0.05	
			154–156	625	0.05	
			157–159	650	0.05	
			160–162	675	0.05	
			163–165	700	0.05	
<u>CM-05 / Experiment 7</u> Cyc 166–186 [5% H ₂ , <i>Decreasing T</i>]	Sol b.6A	08/06/20	166–168	700	0.05	--
			169–171	675	0.05	
			172–174	650	0.05	
			175–177	625	0.05	
			178–180	600	0.05	
			181–183	550	0.05	
			184–186	500	0.05	

Table D2: Descriptions of all kinetics experiments conducted on Na₂WO₄/CaMnO₃ and discussed in this work.

Designation	Batch	Date	Cycles	T (°C)	P_{H2} (atm)	P_{C2H4} (atm)
<u>NWCM-01 / Experiment 1</u> Cyc 1–5 [Break-In] Cyc 6–17 [10% H ₂ , <i>Decreasing T</i>]	Sol b.3	03/04/19	1–5	750	0.10	--
			6–8	650	0.10	--
			9–11	625	0.10	
			12–14	600	0.10	
			15–17	575	0.10	
<u>NWCM-02 / Experiment 1</u> Cyc 1–5 [Break-In] Cyc 6–20 [10% C ₂ H ₄ , <i>Decreasing T</i>]	Sol b.6A	05/28/19	1–5	750	0.10	--
			6–8	700	--	0.10
			9–11	695		0.10
			12–14	685		0.10
			15–17	675		0.10
			18–20	665		0.10
<u>NWCM-03 / Experiment 1</u> Cyc 1–5 [Break-In] Cyc 6–32 [10% H ₂ , <i>Decreasing T</i>]	Sol b.6A	06/07/19	1–5	750	0.10	--
			6–8	700	0.10	
			9–11	675	0.10	
			12–14	650	0.10	
			15–17	625	0.10	
			18–20	600	0.10	
			21–23	575	0.10	
			24–26	550	0.10	
			27–29	525	0.10	
			30–32	500	0.10	
<u>NWCM-04 / Experiment 1</u> Cyc 1–5 [Break-In] Cyc 6–32 [5% H ₂ , <i>Increasing T</i>]	Sol b.6A	03/04/20	1–5	750	0.05	--
			6–8	500	0.05	
			9–11	525	0.05	
			12–14	550	0.05	
			15–17	575	0.05	
			18–20	600	0.05	
			21–23	625	0.05	
			24–26	650	0.05	
			27–29	675	0.05	
			30–32	700	0.05	
<u>NWCM-05 / Experiment 1</u> Cyc 1–5 [Break-In] Cyc 6–32 [5% H ₂ , <i>Decreasing T</i>]	Sol b.6A	03/11/20	1–5	750	0.05	--
			6–8	700	0.05	
			9–11	675	0.05	
			12–14	650	0.05	
			15–17	625	0.05	
			18–20	600	0.05	
			21–23	575	0.05	
			24–26	550	0.05	
			27–29	525	0.05	
			30–32	500	0.05	
<u>NWCM-06 / Experiment 1</u> Cyc 1–5 [Break-In] Cyc 6–30 [5% H ₂ , 650°C → 700°C → 650°C]	Sol b.6A	03/19/20	1–5	750	0.05	--
			6–10	650	0.05	
			11–15	700	0.05	
			16–30	650	0.05	

Table D2 (continued).

NWCM-07 / Experiment 1 Cyc 1–6 [Break-In] Cyc 7–33 [5% H ₂ , <i>Increasing T</i>]	Sol b.6A	06/20/20	1–6	750	0.05	--
			7–9	500	0.05	
			10–12	525	0.05	
			13–15	550	0.05	
			16–18	575	0.05	
			19–21	600	0.05	
			22–24	625	0.05	
			25–27	650	0.05	
			28–30	675	0.05	
			31–33	700	0.05	
NWCM-07 / Experiment 2A-B Cyc 34–57 [5% H ₂ , <i>Decreasing T</i>] Cyc 55–78 [5% H ₂ , <i>Increasing T</i>]	Sol b.6A	06/30/20	34–36	675	0.05	
			37–39	650	0.05	
			40–42	625	0.05	
			43–45	600	0.05	
			46–48	575	0.05	
			49–51	550	0.05	
			52–54	525	0.05	
			55–57	500	0.05	
			58–60	525	0.05	
			61–63	550	0.05	
			64–66	575	0.05	
			67–69	600	0.05	
			70–72	625	0.05	
			73–75	650	0.05	
76–78	675	0.05				
NWCM-07 / Experiment 3A-B Cyc 79–102 [5% C ₂ H ₄ , <i>Increasing T</i>] Cyc 100–123 [5% C ₂ H ₄ , <i>Decreasing T</i>]	Sol b.6A	07/27/20	79–81	575	--	0.05
			82–84	600		0.05
			85–87	625		0.05
			88–90	650		0.05
			91–93	665		0.05
			94–96	680		0.05
			97–99	690		0.05
			100–102	700		0.05
			103–105	690		0.05
			106–108	680		0.05
			109–111	665		0.05
			112–114	650		0.05
			115–117	625		0.05
			118–120	600		0.05
121–123	575		0.05			

Table D2 (continued).

NWCM-07 / Experiment 4A-B Cyc 124–143 [5% H ₂ + 5% C ₂ H ₄ , <i>Increasing T</i>] Cyc 140–159 [5% H ₂ + 5% C ₂ H ₄ , <i>Decreasing T</i>]	Sol b.6A	08/10/20	124–127	600	0.05	0.05
			128–131	625	0.05	0.05
			132–135	650	0.05	0.05
			136–139	675	0.05	0.05
			140–143	700	0.05	0.05
			144–147	675	0.05	0.05
			148–151	650	0.05	0.05
			152–155	625	0.05	0.05
			156–159	600	0.05	0.05
NWCM-08 / Experiment 1 Cyc 1–5 [Break-In] Cyc 6–32 [5% H ₂ , <i>Decreasing T</i>]	Sol b.6A	06/24/20	1–5	750	0.05	--
			6–8	700	0.05	
			9–11	675	0.05	
			12–14	650	0.05	
			15–17	625	0.05	
			18–20	600	0.05	
			21–23	575	0.05	
			24–26	550	0.05	
			27–29	525	0.05	
30–32	500	0.05				
NWCM-08 / Experiment 2A-B Cyc 33–56 [5% H ₂ , <i>Increasing T</i>] Cyc 54–77 [5% H ₂ , <i>Decreasing T</i>]	Sol b.6A	06/28/20	33–35	525	0.05	--
			36–38	550	0.05	
			39–41	575	0.05	
			42–44	600	0.05	
			45–47	625	0.05	
			48–50	650	0.05	
			51–53	675	0.05	
			54–56	700	0.05	
			57–59	675	0.05	
			60–62	650	0.05	
			63–65	625	0.05	
			66–68	600	0.05	
			69–71	575	0.05	
72–74	550	0.05				
75–77	525	0.05				
NWCM-08 / Experiment 3A-B Cyc 78–83 [5% H ₂ , <i>Increasing T</i>] Cyc 84–89 [5% H ₂ , <i>Decreasing T</i>]	Sol b.6A	07/22/20	78–80	600	0.05	--
			81–83	625	0.05	
			84–86	625	0.05	
			87–89	600	0.05	

Table D2 (continued).

NWCM-08 / Experiment <u>4A-B</u> Cyc 90–113 [5% C ₂ H ₄ , <i>Increasing T</i>] Cyc 111–134 [5% C ₂ H ₄ , <i>Decreasing T</i>]	Sol b.6A	08/03/20	90–92	575	--	0.05
			93–95	600		0.05
			96–98	625		0.05
			99–101	650		0.05
			102–104	665		0.05
			105–107	680		0.05
			108–110	690		0.05
			111–113	700		0.05
			114–116	690		0.05
			117–119	680		0.05
			120–122	665		0.05
			123–125	650		0.05
			126–128	625		0.05
			129–131	600		0.05
132–134	575		0.05			
NWCM-08 / Experiment <u>5A-B</u> Cyc 135–161 [5% H ₂ , <i>Increasing T</i>] Cyc 159–185 [5% H ₂ , <i>Decreasing T</i>]	Sol b.6A	08/07/20	135–137	500	0.05	--
			138–140	525	0.05	
			141–143	550	0.05	
			144–146	575	0.05	
			147–149	600	0.05	
			150–152	625	0.05	
			153–155	650	0.05	
			156–158	675	0.05	
			159–161	700	0.05	
			162–164	675	0.05	
			165–167	650	0.05	
			168–170	625	0.05	
			171–173	600	0.05	
			174–176	575	0.05	
177–179	550	0.05				
180–182	525	0.05				
183–185	500	0.05				

Table D2 (continued).

<u>NWCM-08 / Experiment 6A-B</u> Cyc 186–212 [5% H ₂ , <i>Increasing T</i>] Cyc 210–236 [5% H ₂ , <i>Decreasing T</i>]	Sol b.6A	08/12/20	186–188	500	0.05	--
			189–191	525	0.05	
			192–194	550	0.05	
			195–197	575	0.05	
			198–200	600	0.05	
			201–203	625	0.05	
			204–206	650	0.05	
			207–209	675	0.05	
			210–212	700	0.05	
			213–215	675	0.05	
			216–218	650	0.05	
			219–221	625	0.05	
			222–224	600	0.05	
			225–227	575	0.05	
			228–230	550	0.05	
			231–233	525	0.05	
234–236	500	0.05				
<u>NWCM-09 / Experiment 1</u> Cyc 1–15 [Break-In] Cyc 16–42 [5% H ₂ , <i>Decreasing T</i>]	Sol b.6A	09/02/20	1–15	750	0.05	--
			16–18	700	0.05	
			19–21	675	0.05	
			22–24	650	0.05	
			25–27	625	0.05	
			28–30	600	0.05	
			31–33	575	0.05	
			34–36	550	0.05	
			37–39	525	0.05	
			40–42	500	0.05	

Table D3: Fifteen solid-state reaction models tested for the fitting of CaMnO_3 and $\text{Na}_2\text{WO}_4/\text{CaMnO}_3$ reduction kinetics, from four families of models: reaction-order models (F); geometric contraction models (R); diffusion-limited models (D); Avrami–Erofe’ev nucleation models (AE).

Name	Reaction model description	Differential form $f(X) = 1/k \, dX/dt$	Integral form $g(X) = kt$
F1	First-order or Avrami–Erofe’ev ($n = 1$)	$(1-X)$	$-\ln(1-X)$
F1.5	Three-halves order	$(1-X)^{3/2}$	$2[[(1-X)^{-1/2} - 1]$
F2	Second-order	$(1-X)^2$	$1/(1-X) - 1$
F3	Third-order	$(1-X)^3$	$(1/2)[(1-X)^{-2} - 1]$
R1	Zero-order	1	X
R2	Contracting area	$2(1-X)^{1/2}$	$1 - (1-X)^{1/2}$
R3	Contracting volume	$3(1-X)^{2/3}$	$1 - (1-X)^{1/3}$
D1	1-D diffusion	$1/(2X)$	X^2
D2	2-D diffusion, Valensi equation	$1/[-\ln(1-X)]$	$(1-X) \ln(1-X) + X$
D3	3-D diffusion, Jander equation	$3(1-X)^{1/3}/[2(1-X)^{-1/3} - 1]$	$[1 - (1-X)^{1/3}]^2$
D4	Ginstling–Brounshtein equation	$3/[2(1-X)^{-1/3} - 1]$	$1 - 2X/3 - (1-X)^{2/3}$
AE0.5	Avrami–Erofe’ev ($n = 0.5$)	$(1/2)(1-X)[-\ln(1-X)]^{-1}$	$[-\ln(1-X)]^2$
AE1.5	Avrami–Erofe’ev ($n = 1.5$)	$(3/2)(1-X)[-\ln(1-X)]^{1/3}$	$[-\ln(1-X)]^{2/3}$
AE2	Avrami–Erofe’ev ($n = 2$)	$2(1-X)[-\ln(1-X)]^{1/2}$	$[-\ln(1-X)]^{1/2}$
AE3	Avrami–Erofe’ev ($n = 3$)	$3(1-X)[-\ln(1-X)]^{2/3}$	$[-\ln(1-X)]^{1/3}$

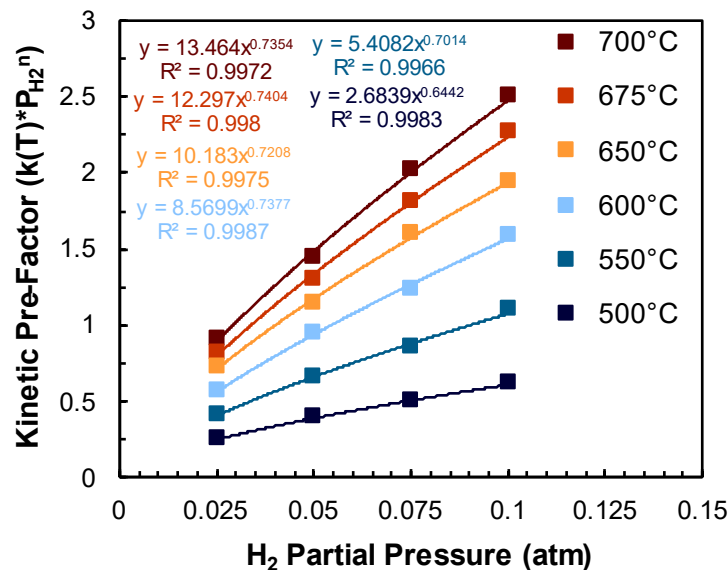


Figure D1: Reduction kinetic pre-factors ($k \cdot P_{\text{H}_2}^n$) of CaMnO_3 (sample CM-05) plotted as a function of H_2 partial pressure for the determination of the reaction order n (the exponent of the power-law trendlines).

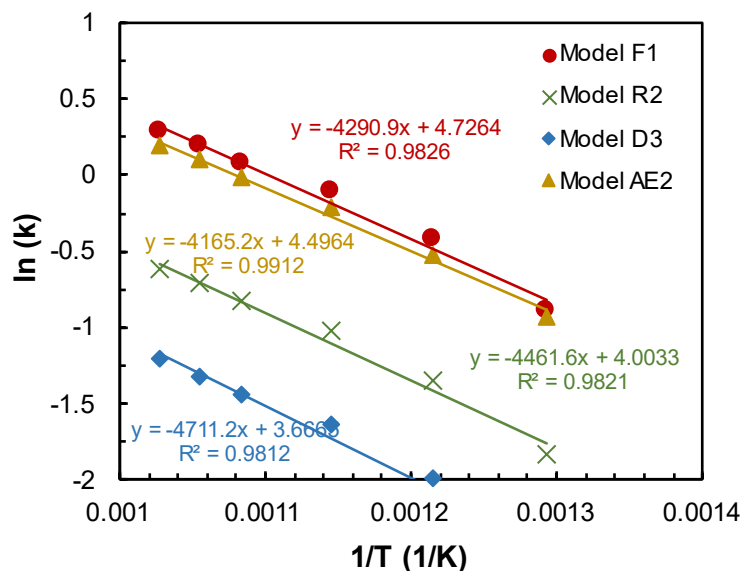


Figure D2: A representative example of an Arrhenius plot developed in this work for the reduction of CaMnO_3 or Na_2WO_4 . The pictured data are from the reduction of sample CM-03 by 5% H_2 and are associated with **Figure 3** and **Figure 4** in the main text.

Table D4: Resulting temperature-dependent kinetic parameters for the reduction of CaMnO_3 (CM-03), associated with **Figure D2** above and **Figure 3** and **Figure 4** in the main text, illustrating the minimal influence of model selection on Arrhenius plot linearity and derived parameters.

	Model F1	Model R2	Model D3	Model AE2
E_a (kJ mol^{-1})	35.7	37.1	39.2	34.6
k_o (s^{-1})	1.88	0.91	0.65	1.49
R^2	0.9826	0.9821	0.9812	0.9912

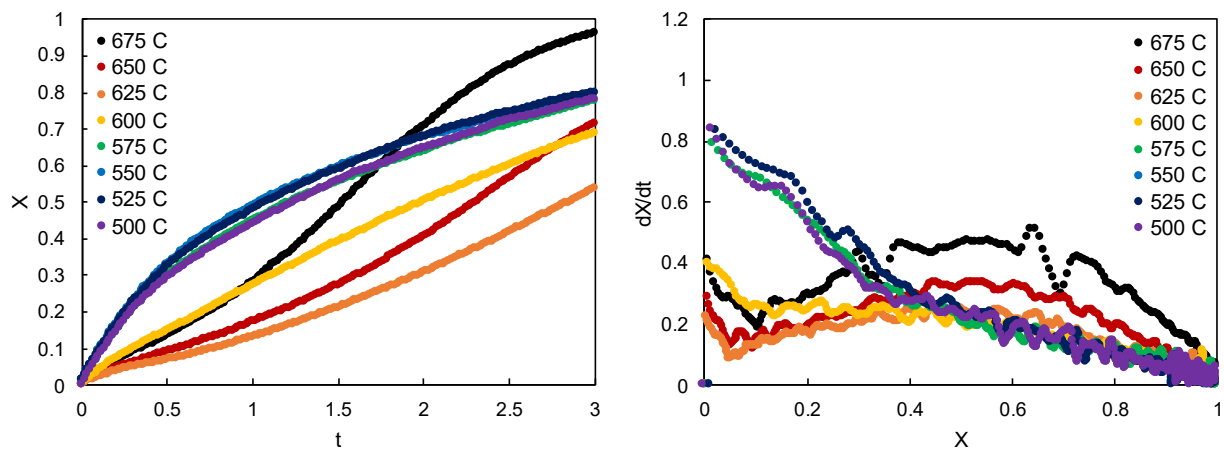


Figure D3: Reduction kinetics of $\text{Na}_2\text{WO}_4/\text{CaMnO}_3$ (prepared via solid state reaction or SSR method) by 10% H_2 . The data shown are the same as those featured in Dudek *et al.* with the lower temperatures included.

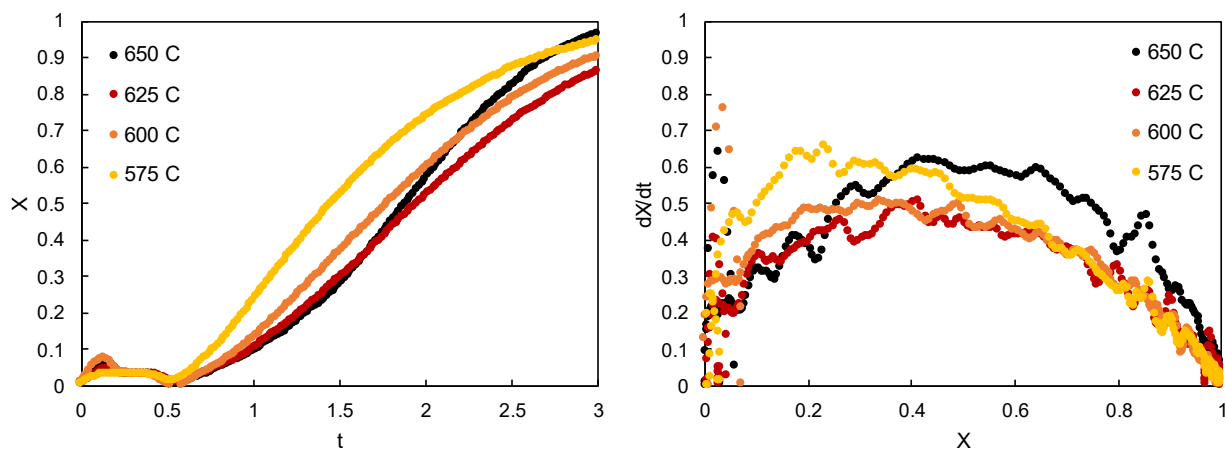


Figure D4: Reduction kinetics of $\text{Na}_2\text{WO}_4/\text{CaMnO}_3$ (prepared via modified Pechini method) by 10% H_2 . The data shown correspond to NWCM-01 (Experiment 1) described in **Table D2**.

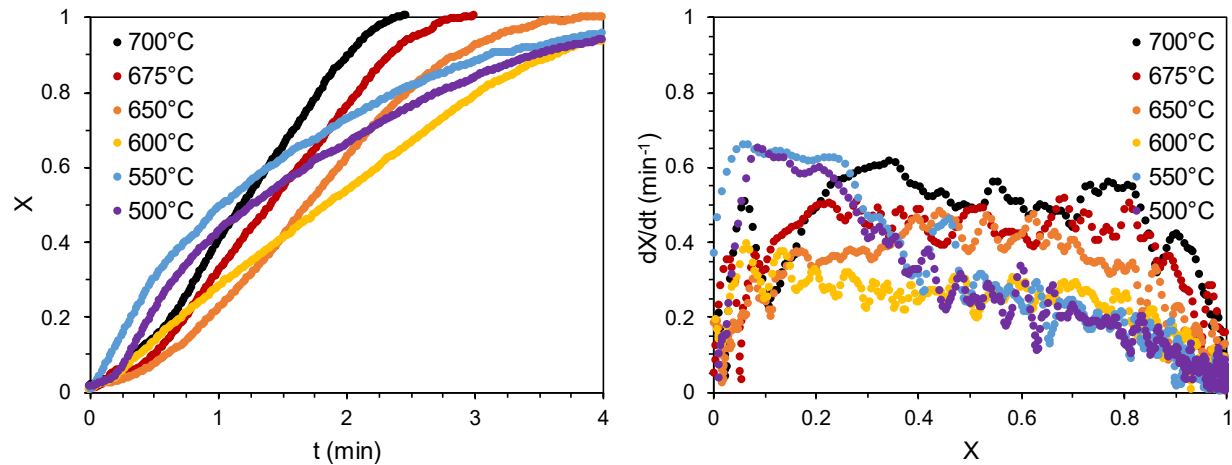


Figure D5: Reduction kinetics of $\text{Na}_2\text{WO}_4/\text{CaMnO}_3$ (prepared via modified Pechini method) by 10% H_2 . The data shown correspond to NWCM-03 (Experiment 1) described in **Table D2**.

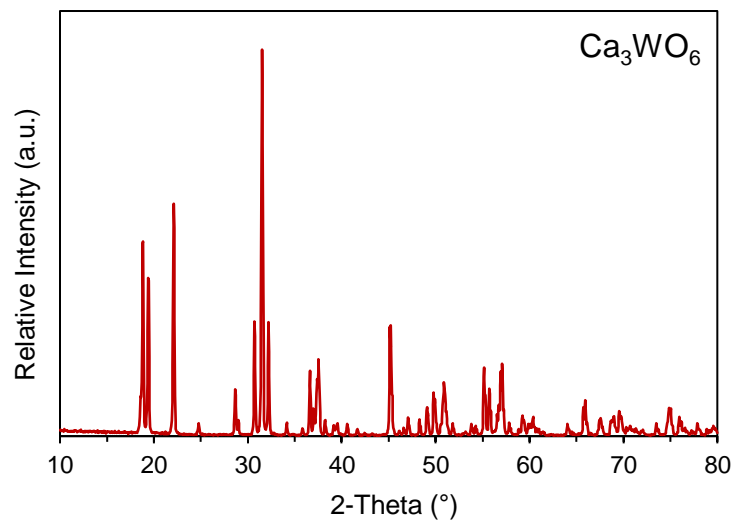


Figure D6: Reference X-ray diffraction (XRD) pattern for Ca_3WO_6 .